

EXPLORATION OF VILLARRICA GEOTHERMAL SYSTEM USING
GEOPHYSICAL AND GEOCHEMICAL TECHNIQUES

Zur Erlangung des akademischen Grades eines

DOKTORS DER NATURWISSENSCHAFTEN

von der Fakultät für

Bauingenieur-, Geo- und Umweltwissenschaften
des Karlsruher Instituts für Technologie (KIT)

genehmigte

DISSERTATION

von

M.Sc. Sebastian Held

aus Dortmund

Tag der mündlichen Prüfung: 10.11.2017

Referent: Prof. Dr. Thomas Kohl

Korreferent: Prof. Dr. Diego Morata

Karlsruhe 2018

Abstract

The International Energy Agency projects a significant contribution of geothermal energy to the future energy mix. Geothermal energy has the potential to substitute fossil energies due to its baseload capacity, combined with a decentralized and permanently available energy production. To the present day, geothermal development concentrates on the exploitation of high-enthalpy, conventional systems that are related to active volcanism, magmatism and active rifting. Yet, for South American Countries geothermal development just started with the first power plant being installed in Chile in 2017. In Chile, basically high geothermal potentials are related to the active volcanic arc of the Andean Cordillera. In order to reach national and international expectations besides the development of high-enthalpy resources low and medium-enthalpy resources shall be exploited for energy supply.

Low-enthalpy-geothermal reservoirs globally and in Chile are often related to major fault zones or particular lithologies. Resource identification and quantification require an adopted exploration strategy, which are generally developed for high-enthalpy systems. The goal of this thesis is the development and application of an exploration strategy to investigate the potential of low/medium-enthalpy systems. Therefore the Villarrica geothermal system in the Andean Cordillera of Southern Chile is selected due to the occurrence of major fault zones in combination with a significant lithological contrast and the active Villarrica volcano. In order to characterize the spatial distribution and also conditions of the reservoir, a multidisciplinary approach is selected combining geochemical and geophysical techniques.

Geophysical studies target the investigation of the major fault zones, identified as key features of the geothermal circulation system. The Liquiñe-Ofqui Fault system (LOFS), an arc parallel, >1000 km long strike-slip fault system is intersected by the Mocha-Villarrica fault zone (MVFZ). The two fault zones are investigated with geophysical (gravity and magnetotelluric) profiles perpendicular to their progression. High-resolution broad band magnetotelluric measurements reveal for both tectonic structures a resistivity reduction resulting from circulation of geothermal fluids and/or hydrothermal alteration products. Fault zone geometry and depth extension are investigated indicating at least for the MVFZ a connection to a mid-crustal conductor. For LOFS, a sub-vertical conductor reaching at least the brittle-ductile transition zone is depicted from inversion and forward modeling results. The gravity survey, following the location of the MT campaign, allows for a joint data interpretation. For LOFS, a significant gravity reduction is detected. This negative anomaly coincides spatially with the reduced resistivity from MT measurements. Applying Butterworth Filtering and forward modeling, the gravity anomaly is used to disclose fault zone geometry and density contrast. In a final joint interpretation, fault zone properties in terms of clay mineral fillings and porosity are determined in order to estimate the fault zone permeability.

Geochemical techniques are used to characterize the geothermal reservoir processes. The hot springs discharging the Villarrica area are used as a proxy to subsurface revealing fluid origin and genesis. The geothermal fluids originated from equilibrated water-rock interaction of meteoric fluids with crystalline rocks. Major input of magmatic volatiles or fluids, degassing from the Villarrica magma chamber, as observed for high-enthalpy fields related to active volcanism, cannot be identified. Subsequently water-rock interaction is investigated by a joint study of geochemical fluid and rock composition. The significant lithological contrast between plutonic rocks of North Patagonian Batholith (NPB) south of the volcanic chain and volcano-sedimentary rocks of Cura-Mallín formation north of it can be traced in the fluids by application of $^{87}\text{Sr}/^{86}\text{Sr}$ isotope ratios. Variations of geothermal fluid circulation inside both lithologies is investigated by analysis of chlorofluorocarbon (CFC) species and oxygen isotopes fractionation of $\text{SO}_4\text{-H}_2\text{O}$ system. For NPB a channeled fluid flow along the LOFS is derived while a more ramified fluid movement along secondary fault and fractures is deduced for the Cura-Mallín formation. The application of different CFC species enables the quantification of shallow meteoric dilution of geothermal fluids during ascent. Thus the in-situ brine composition can be revealed allowing a profound estimation of reservoir properties.

The Villarrica geothermal system has an exploitable geothermal potential. Geothermal fluids can ascent on major fault zones generating reservoirs in feasible depth. Especially Cura-Mallín formation, due to the branched circulation system, has the capacity of a good subsurface heat exchanger guaranteeing long-term operability. Maximum reservoir temperatures of 140–180 °C would enable the construction of a district heating system for the city of Pucón.

Zusammenfassung

Für den globalen, zukünftigen Energiemix prognostiziert die internationale Energieagentur (IEA) einen erheblichen Beitrag aus geothermischer Energie. Dabei soll die grundlastfähige, dezentrale und permanent verfügbare Energiequelle helfen, fossile Energieträger zu ersetzen. Aktuell konzentriert sich die Erschließung geothermischer Lagerstätten vor allem auf konventionelle High-Enthalpy Ressourcen, die oftmals in Zusammenhang mit Vulkanismus oder Magmatismus an aktiven Kontinentalrändern oder Rifting-Prozessen auftreten. Die aktiven Kontinentalränder, die den Pazifik umspannen (auch "pazifischer Feuerring" genannt), werden von vielen Anrainern geothermisch genutzt. Lediglich in der Andenregion konnten bislang keine nennenswerten geothermischen Ressourcen erschlossen werden. Chile hat, nach Inbetriebnahme des ersten geothermischen Kraftwerks, begonnen das geothermische Potential systematisch zu entwickeln. Dabei sollen, um eine nachhaltige Energieversorgung zu gewährleisten, neben der Erschließung von High-Enthalpy Lagerstätten auch Low/Medium-Enthalpy Reservoirs genutzt werden.

Global gesehen sind Low/Medium-Enthalpy Reservoirs oft an große Störungssysteme oder geothermische geeignete Gesteinsformationen gebunden. Zur Auffindung und Charakterisierung der Lagerstätten bedarf es einer angepassten Explorationsstrategie, da klassische geothermische Exploration auf High-Enthalpy Ressourcen ausgelegt ist. Im Rahmen dieser Doktorarbeit soll eine Explorationsstrategie für Low/Medium Enthalpy Geothermiereservoirs in Chile entwickelt werden. Als Forschungsstandort wurde das Geothermalsystem am Vulkan Villarrica gewählt, da der Erfolg der Explorationsstrategie zur Charakterisierung des komplexen Störungszonensystems und eines markanten Lithologie Wechsel getestet werden kann. Um sowohl die Reservoirgeometrie als auch Reservoirprozesse quantifizieren zu können, wurde ein interdisziplinärer Ansatz gewählt, der geochemische und geophysikalische Methoden koppelt.

Störungszonensysteme besitzen eine übergeordnete Bedeutung zur Ausbildung des geothermischen Zirkulationssystems und somit zur Bildung der Lagerstätte. Der Forschungsstandort ist gekennzeichnet durch das Schneiden zweier überregionaler Störungszonen, der Liquiñe-Ofqui Störungssystem (LOFS) und der Mocha-Villarrica Störungszone (MVFZ), die mit geophysikalischen Methoden untersucht werden. Mit Hilfe hoch aufgelöster magnetotellurischer Messungen können beide Störungszonen durch verminderte elektrische Widerstände identifiziert werden. Diese Widerstandsreduktion wird durch das Auftreten von leitfähigen geothermischen Tiefenwässern und/oder hydrothermalen Alterationsprodukten hervorgerufen werden. Für die MVFZ zeigen die Untersuchungen eine nordwärts einfallende Störungszone, die mit einer Zone erhöhter elektrischer Leitfähigkeit in der mittleren Kruste verbunden ist. Der Ausbiss der Störungszone fällt mit der Lage der Villarrica-Quetripillán-Lanín Vulkankette zusammen. Die LOFS zeigt sich als vertikale Zone erhöhter Leitfähigkeit, die sich von der Erdoberfläche bis zum Spröd-Duktilen Übergang erstreckt. Ein mögliches

Eindringen in den duktilen Bereich mit potentieller Verbindung zu einer vorhandenen Zone erhöhter Leitfähigkeit in der mittleren Kruste wird durch erhöhte Leitfähigkeiten der duktilen Kruste maskiert. Parallel zu den MT Profilen werden gravimetrische Messungen durchgeführt. Die LOFS zeichnet sich durch eine markante negative Bouguer Anomalie aus, die räumlich mit den erhöhten Leitfähigkeiten übereinstimmt. Die Anwendung von Butterworth Filtern in Kombination mit gravimetrischer Modellierung ermöglicht die Bestimmung der Störungszonengeometrie und die Quantifizierung des Dichtekontrasts. In einer gemeinsamen Interpretation magnetotellurischer und gravimetrischer Daten können die Eigenschaften der LOFS in Bezug auf Tonmineralgehalt und Porosität berechnet werden um die Permeabilität der Störungszone abzuschätzen.

Mit Hilfe geochemischer Methoden sollen die Reservoirprozesse charakterisiert werden. Dazu werden die Thermalwasseraustritte als Fenster zum Untergrund genutzt um den Ursprung und die Genese der Thermalwässer zu bestimmen. Es kann gezeigt werden, dass die Thermalwässer meteorische Ursprungs sind und durch intensive Reaktion mit Kristallin Gestein entstehen. Obwohl räumliche Nähe zu aktiven Vulkanen besteht, kann kein substantieller Einfluss magmatischer Fluide oder Gase festgestellt werden. Nachfolgend werden die Gesteins-Wasser Wechselwirkungen durch eine vergleichende Studie der Thermalwässer und möglicher Reservoirgesteine untersucht. Dabei wird der markante Lithologie Kontrast, zwischen plutonischen Gesteinen des Nord Patagonischen Batholiths (NPB) und vulkano-klastischen Gesteinen der Cura-Mallín Formation, durch die Analyse von Strontium Isotopen nachgezeichnet. Durch Analyse von FCKW Spezies und Sauerstoff Isotopen des $\text{SO}_4\text{-H}_2\text{O}$ Systems kann gezeigt werden, dass in beiden Formationen unterschiedliche Fluidzirkulationssysteme auftreten. Im NPB kommt es zu einer Konzentration der Thermalwasserzirkulation auf Hauptstörungszonen, wohingegen für die Cura-Mallín Formation eine verzweigtere Fluidzirkulation nachgewiesen werden kann. Die Analyse der verschiedenen FCKW Spezies ermöglicht die Quantifizierung der Vermischungsprozesse im Untergrund und kann so genutzt werden um die in-situ Thermalwasserzusammensetzung zu ermitteln. Erst diese ermöglicht eine genaue Bestimmung der Reservoirbedingungen und des geothermischen Potentials.

Der Villarrica Geothermalsystem besitzt ein erhöhtes geothermisches Potential. Durch Thermalwasseraufstieg entlang der Hauptstörungszonen bilden sich Reservoir in erschließbarer Tiefe. Als unterirdischer Wärmetauscher eignet sich vor allem die Cura-Mallín Formation durch das verzweigte Fließfeld. Maximale Reservoirtemperaturen $140\text{--}180^\circ\text{C}$ eignen sich beispielsweise zur Wärmeversorgung der Stadt Pucón durch eine Fernwärmesystem.

Contents

1. Introduction	1
1.1. Energy sector of Chile	2
1.2. Geothermal energy in Chile	3
1.3. Motivation: The role of fault zones and lithology variation in low/medium geothermal systems	5
1.4. Villarrica geothermal system	6
1.5. Thesis structure	7
2. Geological setting	11
2.1. Andean orogenic development	11
2.2. Characteristics of the Andean orogeny	12
2.3. Magmatism	15
2.4. Neotectonics	17
2.5. Regional geology of the magmatic arc of southern Chile	20
2.6. Scientific exploration of geothermal reservoirs in SVZ	22
3. Principles of geothermal exploration	25
3.1. Geophysical Exploration	25
3.1.1. Magnetotellurics	25
3.1.1.1. Electromagnetic field sources	26
3.1.1.2. Conductivity of rocks and fluids of the earth crust	27
3.1.1.3. Basic equations	29
3.1.1.4. Data processing	30
3.1.1.5. Interpretable outputs: Impedance tensor, apparent resistivity and phase	32
3.1.1.6. Induction at discontinuities	34
3.1.1.7. Dimensionality	36
3.1.2. Gravimetry	38
3.1.2.1. Basic concepts	38
3.1.2.2. Gravity correction and Bouguer Anomaly	39
3.1.2.3. Density ranges of rocks	41
3.2. Geochemical Exploration	41
3.2.1. Strontium isotope analysis	42
3.2.2. Chlorofluorocarbon analysis	42
3.2.3. Geothermometry using the oxygen isotope fractionation of the sulfate-water system	46
4. Geological and Tectonic Settings Preventing High-Temperature Geothermal Reservoir Development at Mt. Villarrica (Southern Volcanic Zone): Clay Mineralogy and Sulfate-Isotope Geothermometry	49
4.1. Introduction	50
4.2. Geological setting	51

4.3. Methods and sampling procedure	52
4.4. Results	54
4.5. Discussion	55
4.6. Outlook	58
5. Resistivity distribution from mid-crustal conductor to near-surface across the 1200 km long Liquiñe-Ofqui Fault System, Southern Chile	61
5.1. Introduction	62
5.2. Geological setting	63
5.3. Data acquisition	65
5.4. Data processing and results	66
5.4.1. Directionality and dimensionality analysis	66
5.4.2. Vertical magnetic field data	68
5.4.3. Phase tensor	69
5.5. Inversion of MT and vertical magnetic field data	71
5.6. Discussion	74
5.7. Conclusions	76
6. Fault zone characterization using gravimetric techniques	79
6.1. Introduction	79
6.2. Methods	81
6.2.1. Acquisition of gravity and GPS data	81
6.2.2. Data processing	82
6.2.3. Butterworth filtering	84
6.2.4. Gravity modeling	84
6.3. Results	85
6.3.1. Processing of gravity data	85
6.3.2. Results from Butterworth filtering	86
6.3.3. Gravity forward modelling	87
6.4. Discussion	89
6.5. Conclusion	92
7. Hydrochemistry of the hot spring fluids of Villarrica geothermal system in the Andes of Southern Chile	95
7.1. Introduction	96
7.2. Geological setting	97
7.3. Materials and Methods	98
7.4. Hydrochemistry of geothermal springs	100
7.4.1. Main components	100
7.4.2. Equilibrium state	103
7.4.3. Stable isotopes	105
7.5. Conclusion and outlook	106
8. Geochemical characterization of the geothermal system at Villarrica volcano, Southern Chile; Part 1: Impacts of lithology on the geothermal reservoir	109
8.1. Introduction	110
8.2. Geological setting	111
8.3. Materials and methods	113
8.4. Results and discussion	115
8.4.1. Analysis of reservoir rock analogues: Potential host rocks of the geothermal system	115
8.4.2. Deduction of reservoir rock type using Rb/Sr and $^{87}\text{Sr}/^{86}\text{Sr}$ isotope ratios	117

8.4.3. Temperature dependent oxygen isotope fractionation of the SO ₄ -H ₂ O system	120
8.4.4. Estimating Surficial Dilution using chlorofluorocarbons (CFCs)	121
8.4.5. Comprehensive discussion and conceptual model	125
8.5. Conclusion	128
9. Comprehensive discussion and outlook	131
Bibliography	137
References	162
Appendix	163
A. Academic Curriculum Vitae	163
B. Declaration of authorship	164
C. Publications	166
D. Presentations with abstracts	168
E. Acknowledgements	169

1. Introduction

At the 21st United Nations Climate Change Conference in Paris 2015 the representatives reached an agreement on the reduction of climate change. The agreement came into force on 4th November 2016 after 57 countries ratified the contract, representing >55 % of worldwide greenhouse gas emissions. The signatories committed themselves to limit the global mean temperature increase to no more than 2 °C compared to pre-industrial conditions. In order to reach this goal a series of measures have to be taken including the substitution of fossil-based by renewable energies. That substitution of fossil or atomic energy, generating the majority of base-load power, requires renewable energy forms capable of supplying base-load energy. In contrast to the majority of the fluctuating renewables, geothermal energy is able to generate CO₂ neutral, permanent energy of widespread spatial availability.

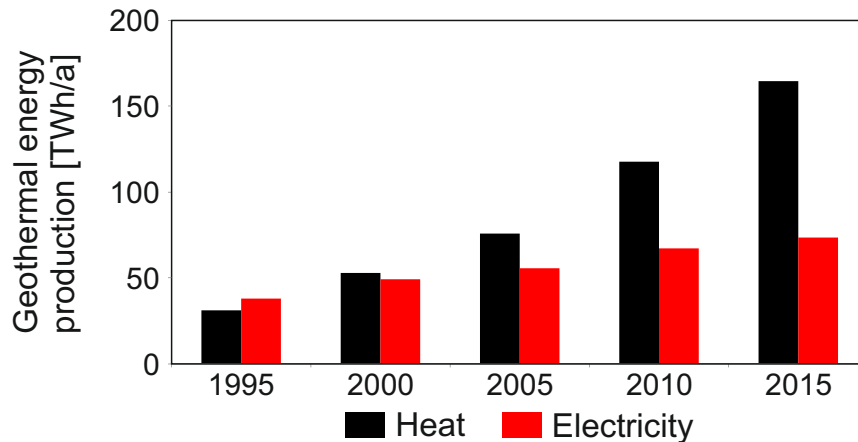


Figure 1.1.: Development of geothermal energy production. Data from [Lund & Boyd \(2016\)](#) and [Bertani \(2016\)](#)

For the future energy mix, the International Energy Agency estimates a geothermal energy production of 1400 TW h a⁻¹ electric and 1600 TW h a⁻¹ thermal by 2050 ([IEA, 2011](#)). Although the installed capacity of geothermal resources and thus, produced energy is increasing (Figure 1.1) it needs further efforts to increase the share of geothermal to 3.5 respectively 3.9 % of the global energy demand.

Considering the worldwide occurrence of installed capacity (Bertani, 2016) the dominance of exploitation of conventional geothermal resources becomes obvious. In 2015, 98.9% of produced electricity is generated in geothermal systems based on conventional resources. Enhanced geothermal systems (EGS), although accounting for a majority of worldwide resource estimates, are poorly exploited due to their high initial investment costs resulting mainly from extensive drilling operations (IEA, 2011).

Conventional resources are characterized by easy accessibility (low depth of the geothermal reservoir) of the high-enthalpy geothermal resource. low levelized costs of energy (LCOE) can be realized. To fulfill the IEA predictions an initial, rapid expansion of conventional resources is predicted followed by exploitation of deeper resources in a second development step. Conventional resources are limited to areas of elevated geothermal gradient often related to magmatism at plate boundaries (Harvey et al., 2016). The so-called “Pacific Ring of Fire”, a synonym for active plate boundaries surrounding the Pacific Ocean, hosts >60% of worldwide geothermally produced electricity (status 2015 from Bertani (2016)). In South America exists a huge, so far untapped geothermal potential. Especially Chile with >4000 km long, active plate boundary, possess enormous resources without major geothermal production.

1.1. Energy sector of Chile

In spring 2017 the inauguration of the first geothermal power plant - Cerro Pabellon - in Chile and whole South America was announced (press release: ThinkGeoenergy 31.03.2017). The plant of 48 MW_{el} installed capacity, operated by Enel Green power, is constructed in an altitude of >4500 m in the Atacama desert of Northern Chile. It is the first successful installation in Chile after a few failed attempts (e.g. abandoned projects of El Tatio and Tolhuaca).

Chilean energy production, distribution and demand are controlled mainly by the particular geography of the country. The elongated country is governed by two cordilleras, Coastal Cordillera and Andean Cordillera. Both cordilleras enclose the Longitudinal Valley, which has a high population density and, thus, a high energy demand. Further high quantities of energy are required by the mining sector in the desert regions of Northern Chile.

The Chilean energy mix (Figure 1.2) depends strongly on fossil fuels. Having no own fossil energy resources, Chile depends strongly on energy imports mostly from neighboring countries. The Argentinian gas supply crisis in 2007, where Argentina stopped the gas exports to Chile as a consequence of own shortages, highlights the problematic nature of this import dependency. Besides fossil fuels, hydroelectric power contributes to a large extend to the energy mix with huge facilities installed in the humid south of the country. The beginning resistance of Chilean people against further installations of hydroelectric power facilities (e.g. press release: The New York Times 16.06.2011) and the distance to consumers restricts its further expansion.

The Chilean government has recognized that renewable energies enable, besides the obvious environmental advantages, the solution of Chilean energy sector problems, such as import dependency and distribution complexity. By law the government set the objective to generate 20% of its electricity in 2025 by renewable energies (IRENA, 2015). This political will is demonstrated by the foundation of research centers associated with development of renewable energies, e.g. Centro de Excelencia en Geotermia de los Andes (CEGA) or Solar Energy Research Center (SERC). Additionally, laws came into force (Law 19.657 in

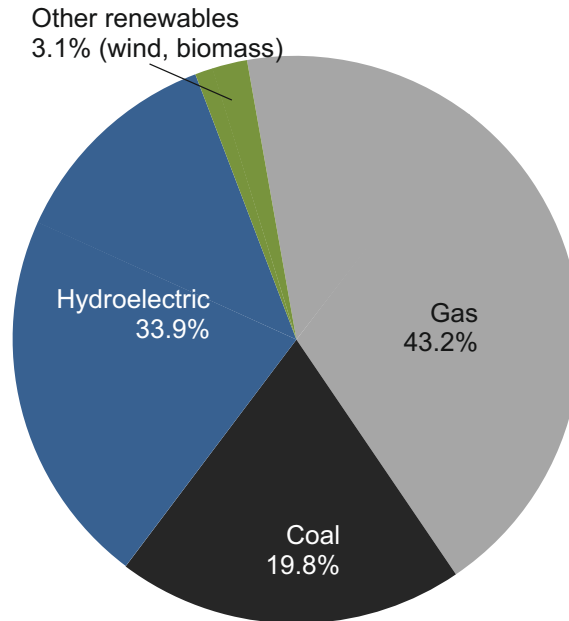


Figure 1.2.: Chilean Energy Mix. Data from [Ministerio de Energía \(2012\)](#)

2000 and Short law 20.698 in 2013) regulating production and feed-in of geothermal energy ([IRENA, 2015](#))

The Chilean renewable energy potential is enormous due its diversified geography ([Woodhouse & Meisen, 2011](#)). Higher potentials for wind power are located at the coast, solar power can be harnessed efficiently in the Atacama desert, while biomass production benefits from humid climate in the south of the country. Geothermal resources, with reservoir temperatures allowing for electricity generation, are situated within the active volcanic chain. Chile has an estimated geothermal potential of $16 \text{ GW}_{\text{el}}$ ([Lahsen et al., 2010](#)). Even conservative potential determinations, based on the already explored prospects, estimate a potential of $1.3 \text{ GW}_{\text{el}}$ for resources in Northern Chile ([Procesi, 2014](#)) and $1.4 \text{ GW}_{\text{el}}$ for Southern Chile ([Aravena & Lahsen, 2012](#)). Thus, geothermal energy can contribute to a major extend to the Chilean energy sector with a total installed capacity of $22 \text{ GW}_{\text{el}}$ ([Minierstio de Energía, 2016](#)).

1.2. Geothermal energy in Chile

Chilean geothermal development started at the beginning of the 19th century with the drilling of shallow wells in the El Tatio geothermal field in the Atacama Desert by researchers from Larderello, Italy. In the 1970s during the global energy crisis, geothermal power production was promoted by a United Nations Development program, resulting in the exploration of first concessions (e.g. [Cusicanqui et al., 1975](#); [Lahsen, 1976](#)). Even though feasibility was proven, the sites were not explored due to a change in energy policy abandoning further geothermal research. With the beginning of the new century, environmental awareness and increasing energy demand triggered a re-thinking of energy policy resulting in the enactment of a geothermal energy laws (first law passed 2000) and the funding of geothermal research (e.g. CEGA funded in 2011).

In Chile, geothermal resources are associated to recent volcanic activity within the Andean cordillera. The Cordillera contains > 200 potentially active volcanoes located in four

separated segments, three of them are situated within Chile: the Central (CVZ: 14–28°S), Southern (SVZ: 33–34°S) and Austral (AVZ: 49–55°S) Volcanic Zones (Stern, 2004). Volcanism is generated by the subduction of the Nazca Plate beneath the South America Plate and associated magma ascent. The Chilean geological survey - SERNAGEOMIN - tenders 51 geothermal concessions (status June 2017), eight of them are granted for exploitation (Figure 1.3).

Aravena et al. (2016b) outline the progress in Chilean geothermal development. Nine geothermal concessions with advanced exploration activities including slimhole wells (Apacheta, El Tatio, La Lorta, Tolhuaca, Puchuldiza, Tinguiririca, Mariposa, Nevados de Chillán, Cordon Caulle) have proven high-enthalpy geothermal reservoirs. From these sites, Apacheta has a completed power plant in operation (Cerro Pabellon) and two sites - Tolhuaca and El Tatio - were abandoned after the drilling of the first production wells. Eight further sites have a high probability of hosting high-enthalpy geothermal reservoirs as estimated by geophysical and/or geochemical measurements. Additionally 57 sites are marked by “Areas of higher Interest” basically determined by outflow conditions $>50^{\circ}\text{C}$.

Sánchez-Alfaro et al. (2015) analyze the barriers of Chilean geothermal development. Uncertainties in the regulatory framework hinder an acceleration of geothermal development as they a) cause conflicts between geothermal developers and local entities, b) allow the usage of concessions for financial speculation and c) cause delays through impractical concession policy. Whether these legal impediments can be removed by revision of existing law, furthermore, the authors list major infrastructural or geographic barriers. High enthalpy resources are located inside the volcanic arc at high altitudes, which gives rise to cost-intensive infrastructure measures in terms of road construction and connection to the electricity grid. Furthermore, the wet climate in the south of the country in combination with severe winter times limits the construction period. In combination with the scarcity of drilling equipment for geothermal purposes, higher investment costs arise for the exploitation of “greenfield” Chilean geothermal resources. The failure of previous projects (El Tatio, Tolhuaca) also deters private investors. As a consequence, besides the exploitation of remote high-enthalpy resources, the exploration of low to medium-enthalpy (forthcoming abbreviated low/medium-enthalpy) reservoirs comes into focus.

Industrial exploration of high-enthalpy geothermal reservoirs in Chile follows a standard approach at least for the above mentioned fields of proven geothermal potential (Melosh et al., 2012; Hickson et al., 2011; Tassi et al., 2010; Cumming et al., 2002; Clavero et al., 2011; Sepulveda et al., 2005, 2006). If high-enthalpy geothermal manifestations in terms of hot springs, fumaroles, or wide-spread alteration products exist, reservoir temperatures are estimated using fluid or gas thermometry. In a few cases, fluid origin and genesis determination complements hydrochemical surveys. If sufficient reservoir temperatures are encountered, magnetotelluric campaigns are conducted focusing on clay cap identification to quantify reservoir expansion. Sometimes, further geophysical techniques (e.g. gravimetry, aeromagnetism, remote sensing) are applied in order to study lithology and especially hydrothermal alteration. In a last step before exploitation, slimhole wells are drilled confirming reservoir characteristics obtained from geophysical and geochemical surveys.



Figure 1.3.: Location of stratovolcanos (red triangles) and geothermal concessions (blue squares) awarded from SERNAGEOMIN; status June 2017

1.3. Motivation: The role of fault zones and lithology variation in low/medium geothermal systems

In times of worldwide rising demand of renewable energies the exploitation of geothermal resources is expected to increase its contribution to a sustainable energy mix. Exploitation concentrates so far on high-enthalpy geothermal systems of magmatic origin as higher energy output raises also economic output. The discrepancy between distribution of energy demand and high-enthalpy geothermal reservoirs (e.g. Baria et al., 2017) in combination with increasing global energy prices provoke the interest in exploitation of low/medium enthalpy geothermal systems. Temperatures, which are usually below 200 °C (Sveinbjörnsson, 2016;

Stober & Bucher, 2013), can be used for heating purposes (district heating, process heat, etc.) or, in terms of medium-enthalpy reservoirs, electricity production operating presumably binary power plants. Low-medium enthalpy systems occur in a wide range of different geological settings: sedimentary basins, crystalline basement, pull-apart basins, graben systems just to name a few. The importance of fault zones acting as a fluid conduit or barrier is a common feature of those different settings (Harvey et al., 2016). The fault zones enable convectional fluid flow locally increasing the geothermal gradient. That results in the formation of temperature anomalies in exploitable depth ranges. The second key factor for reservoir development is the lithology and its ability to act as a subsurface heat exchanger. Primary porosity or secondary porosity in form of small-scale fractures are required to allow a branched reservoir fluid circulation guaranteeing long-term fluid heating. Well studied fault-zone related systems are documented in the Upper Rhine Graben (URG), SW Germany (e.g. Genter et al., 2010), the Büyük Menderes Graben, SW Turkey (Karakuş & Şimşek, 2013) and Basin and Range province, USA (Blackwell et al., 1999).

The exploration strategy has to be adapted to the characteristics of those geothermal systems. For conventional systems, identification of the resource extension is accomplished by the application of magnetotelluric measurements targeting the clay cap of enhanced conductivity. As a clay cap is often missing in non-magmatic, low/medium enthalpy systems, magnetotelluric exploration targets the identification of possible aquifer formations, enhanced in conductivity by saline brine (Muñoz, 2014). Due to the importance of fault zones in low/medium enthalpy systems, MT exploration has to focus the identification of fault zone orientation, geometry and depth penetration thus characterizing major circulation pathways. Further geophysical techniques (e.g. gravimetry or seismics) can complement the fault zone characterization by revealing hydraulic or mineralogical properties.

Geochemical exploration methods have to be updated for low/medium enthalpy resources. The classical exploration tools are developed for conventional systems focusing on the identification of classical reservoir features like upflow zone, fluid separation processes, etc. Above all geothermometer equations are calibrated at high-enthalpy reservoirs increasing its uncertainties when applied at lower temperatures (Fournier, 1979; Nitschke, 2017). Methods have to be selected or adopted to be valid for the special characteristics of low/medium enthalpy, where the hydrochemical composition depends more on rock-water interaction and, thus, lithology than on magmatic degassing processes. Fluid genesis has to be evaluated considering mixing of different groundwater bodies and the heat source itself.

For the development of an adopted exploration strategy, a research area in the Andean Cordillera of southern Chile was selected. Although located inside the magmatic arc, the occurrence of a high-enthalpy system is doubted (Sánchez et al., 2013). Yet, the regionally elevated geothermal gradient generates a low/medium geothermal system. The site contains the intersection of major fault zones and a prominent lithology change enabling us to study their impacts in a kind of natural laboratory. Furthermore, a high number of hot springs can be used as a windows to the subsurface to investigate reservoir processes.

1.4. Villarrica geothermal system

The research area is located 650 km south of the Chilean capital Santiago inside the Andean cordillera. Subpolar oceanic climate prevails, comparable with northern Germany or Southern England, with all-the-year humid conditions (precipitation $>2000 \text{ mm a}^{-1}$) and strong rainfall in winter times. Central component of the Villarrica geothermal system is the

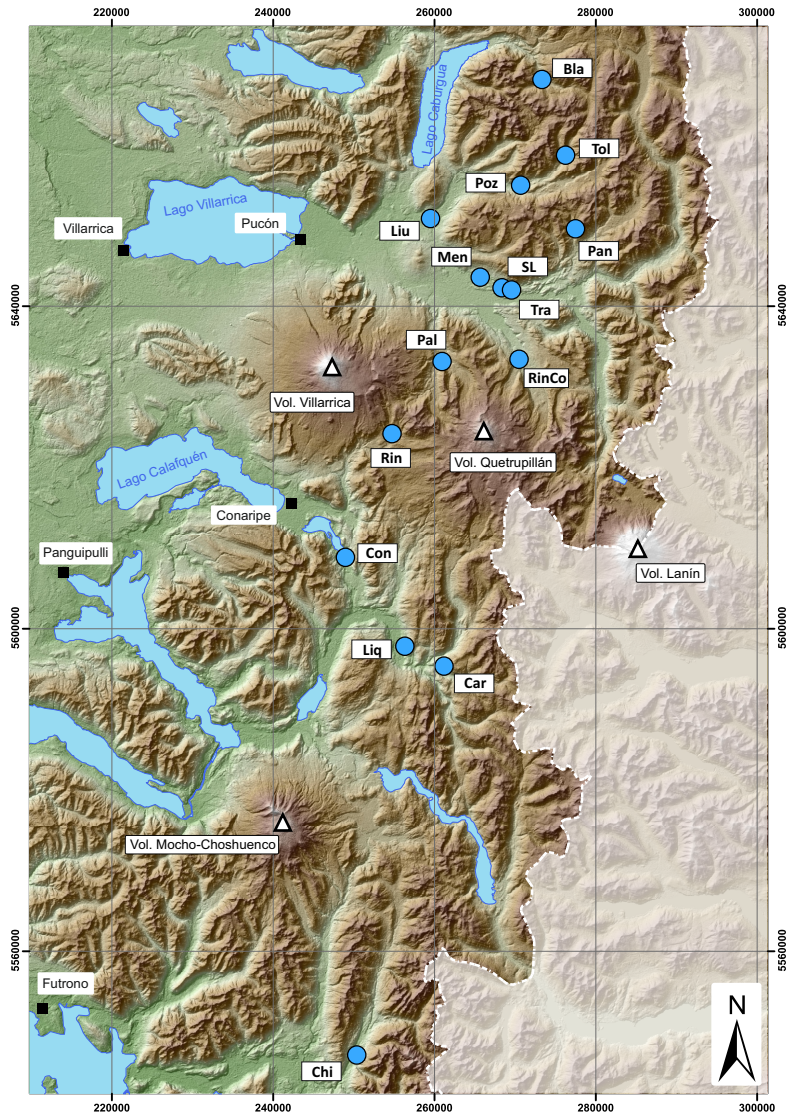


Figure 1.4.: Topographical map of the Villarrica geothermal system and its surroundings including major stratovolcanoes and the location of sampled thermal springs. Topographic data derived from CGIAR-CSI version of SRTM data.

WNW-ESE aligned volcanic chain of three major stratovolcanoes: Villarrica, Quetrupillán and Lanín. The area has a strong relief between the valleys (around 300 masl) and the summits of the volcanoes Villarrica (2847 masl) and Lanín (3747 masl) (Figure 1.4). Villarrica volcano is an active volcano with frequent eruptions, the last occurred in 2015. Most of the valleys of the rural area are used for agricultural purposes. The population lives in small communities (<10'000 inhabitants) with the biggest towns being Pucón (14'000 inhabitants) and Villarrica (50'000 inhabitants). Besides agriculture, tourism is a major source of income of the local population focusing on adventure tourism and balneology in the numerous hot springs. On overview of the locations of the sampled springs is given in Figure 1.4.

1.5. Thesis structure

In the context of expedited geothermal development in Chile this study investigates the characteristics of low/medium enthalpy systems. A resource adapted exploration strategy

is developed revealing the key characteristics of geothermal reservoirs. This strategy shall answer key questions arising during reservoir exploration: (1) Is it possible to determine the location of the reservoir and reveal site-specific geologic features forming the reservoir and define its characteristics (2) What is the geometry and extension of the geothermal reservoir? (3) Can fluid origin, genesis and reservoir processes be identified? (4) Is a quantification of the shallow processes in order to determine in-situ conditions feasible? And (5) as fault zones are often of major importance for low/medium enthalpy systems is it possible to characterize fault zone properties from surface measurements? Since the explorations strategy is developed and applied at the Villarrica geothermal system in the Andean Cordillera of Southern Chile, a brief overview of the geology of the volcanic arc of Southern Chile is given in Chapter 2. The multidisciplinary exploration strategy contains geochemical and geophysical techniques. The fundamentals of the used techniques are provided in Chapter 3. The results of geothermal exploration are presented in form of individual manuscripts, which are published (Chapter 5) or prepared for submission (Chapter 8 and 6) to international journals. Two studies appeared in peer-reviewed Conference Proceedings (Chapter 4 and 7). The following outline provides an overview of the investigation of Villarrica geothermal system using the multidisciplinary exploration strategy.

Determination of reservoir characteristics (Chapter 4)

The first study documents the findings of the first field inspection to the Villarrica geothermal system. The main geological features are inspected and analyzed in terms of relevance for the geothermal system. First estimations of reservoir temperature using oxygen isotope fractionation in the $\text{SO}_4\text{-H}_2\text{O}$ system are conducted. Investigations of clay mineralogy target on the evaluation of the presence of a cap rock. The absence of cap rock in combination with reservoir temperature estimates confirm the assumption of low/medium enthalpy reservoir. Characteristics affecting the geothermal system are highlighted and evaluated in comparison with further geothermal systems of Southern Chile. Based on these findings the exploration strategy is adopted to the site-specific geological characteristics (e.g. fault zone related reservoir, lithological contrast, etc.).

The chapter documents preliminary findings of an early phase of the exploration of the Villarrica geothermal system. Later work, documented in chapter 5 - 8, update and partly revise these early findings. Especially the term “Alpine-type” geothermal system would, considering the complete investigations, be translated to fault-dominated geothermal system. Yet as the chapter is published in the Proceedings of the World Geothermal Congress and furthermore as it documents a step towards understanding of the geothermal reservoirs, I decided to leave the manuscript untouched.

This chapter has been published in: S. Held, E. Schill, P. Sánchez, T. Neumann, K. Emmerich, D. Morata and T. Kohl [2015]: Geological and Tectonic Settings Preventing High-Temperature Geothermal Reservoir Development at Mt. Villarrica (Southern Volcanic Zone): Clay Mineralogy and Sulfate-Isotope Geothermometry; *Proceedings World Geothermal Congress 2015*, Melbourne, Australia

Localization and geometry of fault zone related reservoir (Chapter 5)

Fault zones are identified as major geological structures effecting fluid circulation in the Villarrica geothermal system. The geometry and depth expansion of the major fault zones are studied using the magnetotelluric method. The method reveals fault zones by increased

conductivities detectable in the electromagnetic depth signal. Small inter-station distances and a broad frequency band guarantee high-resolution data that are able to reveal fault zone geometry from shallow to greater depth. The two intersecting fault zones are clearly detected in inversion results of processed MT data. LOFS is identified as a sub-vertical fault intersecting a resistive crust. Fault signal can be traced down to the brittle-ductile transition where a possible connection to an existing mid-crustal conductor is masked by low resistive ductile crust. Fault zone width is investigated by forward modelling indicating a flower structure with variable width being the most reliable model for the LOFS. MVFZ is characterized as a northward dipping fault zone connected to a mid-crustal conductor. Fault zone location coincides with the run of the Villarrica-Quetrupillán-Lanín volcanic chain.

This chapter has been published in: S. Held, E. Schill, M. Pavez, D. Díaz, G. Muñoz, D. Morata and T. Kohl [2016]: Resistivity distribution from mid-crustal conductor to near-surface across the 1200 km long Liquiñe-Ofqui Fault System, Southern Chile; *Geophysical Journal International* (207), 1387-1400

Quantification of fault zone porosity and clay mineral content (Chapter 6)

A second geophysical survey studies fault zone characteristics in terms of clay mineral content and porosity generated by shearing and hydrothermal alteration processes. Gravity measurements are conducted along the MT profiles to investigate the effects of fault zones to subsurface density distribution. A high-resolution survey of 220 gravity measurements reveal negative Bouguer Anomalies for the LOFS. In case of the MVFZ no negative gravity anomaly is detectable at fault locations identified by MT measurements. Butterworth filtering techniques confirm depth expansion revealed by MT inversion. Gravity forward modeling transfers determined gravity anomalies to density contrasts. Finally in a joint evaluation of gravity and MT results the porosity and clay mineral content of LOFS can be quantified.

Analysis of fluid origin and genesis (Chapter 7)

The hot springs of Villarrica geothermal system are studied to identify the fluid origin and genesis. Especially the contribution of the Villarrica magma chamber in terms of input of magmatic fluids or volatiles is investigated. 15 hot spring fluids are analyzed for chemical composition and stable isotopes focusing especially on the interpretation of conservative elements and equilibrium state. The fluids are of meteoric origin and are generated by water-rock interaction with crystalline rocks. A minor magmatic input is documented for hot springs in vicinity of the volcanic chain, which possesses slightly increased B concentrations.

This chapter has been published in: S. Held, F. Nitschke, E. Schill, D. Morata, E. Eiche and T. Kohl [2017]: Hydrochemistry of the hot spring fluids of Villarrica geothermal system in the Andes of Southern Chile; *Geothermal Research Council Transactions* (41)

Characterization of lithological impact on fluid circulation (Chapter 8)

The impact of the lithological change from plutonic rocks of NPB to volcano-sedimentary Cura-Mallín formation is studied by a comparative analysis of geochemical fluid and rock compositions. Additional to sampled fluids, 31 reservoir rock analogues are collected and analyzed in terms of geochemical rock composition to evaluate water-rock interaction. The

two igneous rock formations vary only slightly in terms of element composition. Hence Sr isotope studies are used to trace the lithological transition in the fluids. Subsequently the circulation systems of the two lithologies are investigated using anthropogenic tracers and the temperature depended oxygen fractionation of the $\text{SO}_4\text{-H}_2\text{O}$ system. For the NPB a strongly channeled fluid circulation is evident, while for the Cura-Mallín formation a more ramified circulation can be derived. Note that this study is part of a joint hydrochemical study of the Villarrica geothermal system. Nitschke et al. (2018), in Part B, re-evaluates classical solute geothermometry based on the findings of the here presented Part A. A significant decrease of geothermometer uncertainties can be achieved.

This chapter has been published in: S. Held, E. Schill, J. Schneider, F. Nitschke, D. Morata, T. Neumann and T. Kohl [2018]: Geochemical characterization of the geothermal system at Villarrica volcano, Southern Chile; Part 1: Impacts of lithology on the geothermal reservoir; *Geothermics* (74), 226-239

2. Geological setting

The Andes are part of the “Pacific Ring of Fire”, a system of active plate margins and associated magmatism. Although similar tectonic processes generate the Andean orogeny, significant variations along the run of the Andean mountain belt are detectable. Within this chapter the geological setting is outlined starting with the geological framework of the Andean orogeny following Charrier et al. (2007), Parada et al. (2007), Stern (2004), Cembrano et al. (2002), Cembrano et al. (2007) and Oncken et al. (2006). Subsequently Andean Magmatism and tectonics is presented supplemented by an introduction into the regional geology of southern Chile, where the research area is located.

2.1. Andean orogenic development

The geology and tectonics of Chile is governed by the subduction of the oceanic Nazca Plate and subordinately the Antarctic Plate below the continental South American Plate. The western continental margin of South America, as western part of Gondwana, was an active plate boundary during most of the geological history. Between Late Proterozoic - Devonian times the accretion of smaller terranes is documented by a few early Paleozoic outcrops. First widespread occurrence of metamorphic and magmatic rocks of the Gondwanan tectonic cycle between Devonian and Permian are related to the continental assembly of Gondwana (Charrier et al., 2007). While outcrops exposing rocks of this time in Northern Chile are exposed throughout the complete width of the country, in Southern Chile rocks are limited to the Coastal Cordillera. A metamorphic series, accumulated as an accretionary prism, is accompanied by the magmatic rocks of the Coastal Batholith to the east. South of 38°S the Coastal Batholith bends away from the coast towards the Andean Cordillera (see Figure 2.4). Prior to Gondwana break-up the final phase of continent consolidation was characterized by an interruption of subduction and crustal warping. The continental drift stopped and heat accumulated in the mantle. Sedimentary and volcanic rocks were deposited in NNW-SSE extensional basins.

The Andean subduction cycle begun with the break-up of Gondwana through the opening of the Southern Atlantic Ocean in Jurassic times. Successively oceanic Phoenix (or Aluk)-, Farallon and Nazca Plate were or in case of the Nazca-Plate are subducted under the South America Plate. Continuous magmatism generated the Andean Cordillera today's appearance. Extensional and compressional tectonic regimes alternate, with major

plutonism and volcanic deposits occurring in extensional phases. Compressional phases were often followed by an eastward shift of magmatic activity. The Andean cycle can be separated into three individual phases: First stage (Jurassic - lower Cretaceous), Second stage (Upper Cretaceous - Eocene) and Third stage (Oligocene - Present). In the first stage the magmatic arc was located west of the Carboniferous - Permian magmatic arc in the Coastal Cordillera. Extensional tectonics evoke intensive magmatic activity documented by huge batholith complexes in the magmatic arc. At this time the arc remains close to sea level, with a shallow-marine back-arc basin located at today's Central Depression. In the following stages the arc moved continuously eastwards reaching its present-day position in Neogene times. The first and second stage of Andean evolution are divided by a period of uplifting and erosion caused by accelerated contradictional plate movement and a shallow subduction angle probably related to increased production rate of oceanic crust (Larson, 1991; Coira et al., 1982). In the second stage with the eastward migrating arc a continental foreland basin develops east of the arc accompanied by a fore-arc region west of it. Extensional tectonics, related to highly oblique subsidence and low convergence rates, caused intense magmatic activity resulting in the formation of major plutonic bodies and widespread volcanic formations. Strong subsidence is indicated by the great thickness of volcanic and non-marine sedimentary deposits behind the fore-arc. Again, the second stage was terminated by a major compressive deformation event, called main Incaic phase, in Eocene times leading to tectonic inversion of the arc and basin deposits and thrusting of the foreland basin (Cornejo et al., 2003; Reutter, 2001). During the third stage the present configuration of the Andean range was developed. An extensional period was followed by a compressional event in Miocene (Cembrano et al., 2007). Through the breakup of the Farallon Plate into the Cocos and Nazca Plate (Cande & Leslie, 1986) convergence accelerated and changed to a nearly orthogonal subduction (Pardo-Casas & Molnar, 1987; Somoza, 1998; Pilger, 1984), leading to tectonic shortening, uplift and decreased magmatic activity. Before compressional tectonics in Oligocene volcanic material interbedded with continental sediments were deposited in extensional intra-arc basins between 28°-39°S (Radic et al., 2002; Suarez & Emparan, 1995; Klohn, 1960; Jordan et al., 2001) forming the Cura-Mallín and Abanico formation in Southern Chile. In the following compressional tectonic period the basin deposits were uplifted and folded (Radic et al., 2002). Since Miocene times continuous rapid subduction generates compressional tectonics that result in the uplift of the Andean Cordillera (Pardo-Casas & Molnar, 1987). In the last 5 Ma convergence rate has decreased to present values of 7–9 cm a⁻¹ (Norabuena, 1998; Angermann et al., 1999; Cembrano et al., 2007). In fact, the current, shallow- dip subduction with high interplate coupling has its type localization in the Chilean Andes therefore called Chilean-type subduction.

2.2. Characteristics of the Andean orogeny

The present-day status of the Andean orogeny is generated through the continuous subduction since Miocene times. Currently the Nazca Plate is moving with 7–9 cm a⁻¹ (Norabuena, 1998; Angermann et al., 1999) against the South American Plate, while the Antarctic Plate has a velocity of 2 cm a⁻¹ relative to South American Plate (DeMets et al., 1990). Along the Chilean trench the Nazca-Plate is moving with an orientation of N75°-78°E (Pardo-Casas & Molnar, 1987; Somoza, 1998) and a dip of 19-35° (Barazangi & Isacks, 1976; Bohm et al., 2002; Husen et al., 1999) under the South American Plate. Considering the whole Chilean margin, a uniform convergence can be observed (Hoffmann-Rothe et al., 2006).

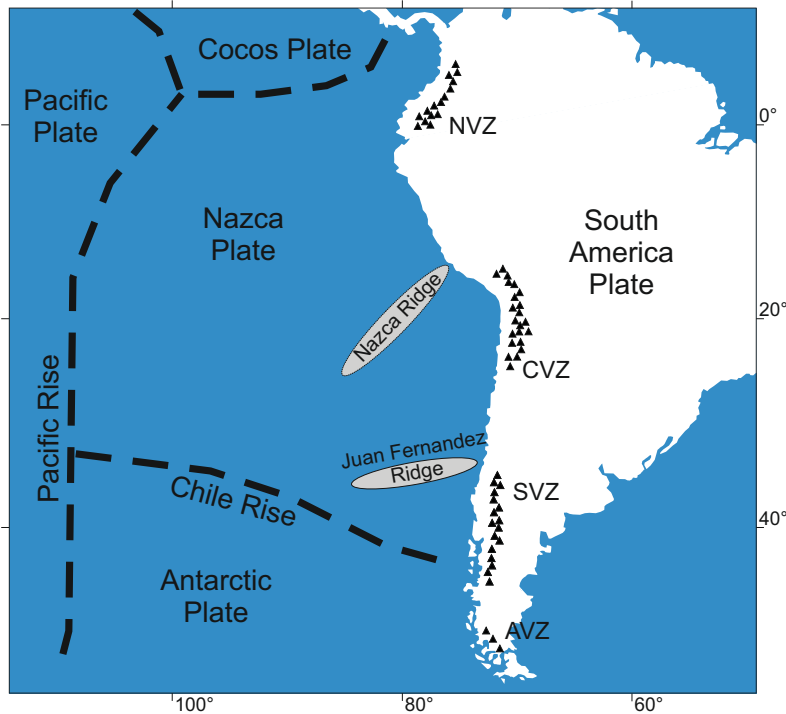


Figure 2.1.: Schematic overview of the plate arrangement at the western margin of South America including major geologic features.

Collision between the approximately N10°E striking South America plate margin and the NE moving Nazca Plate results in an obliquity of 26° of the subduction (Jarrard, 1986). In fact, since initiation of continuous subduction in Jurassic times the subduction was always oblique solely changing its subduction angle (Somoza, 1998). The subduction generates two different types of orogens along the western margin of Chile: A) a plateau-orogen with high crustal thickness and B) a non-plateau orogeny in the Southern Chilean Andes with average crustal thickness (Haschke et al., 2006).

The Nazca and Antarctic Plate are separated by the active Chile Rise, which is split in several segments by transform faults (Tebbens et al., 1997). The oceanic transform faults continue as large scale fault zones with NW-SE orientation in the continental crust (Figure 2.2) (Potent, 2003). At the triple junction between Nazca, Antarctic and South American plate the Chile rise is subducted below the South American plate. Subduction of the Chile rise and continuous northward movement of the triple junction towards its current position at approx. 46°S continues since middle Miocene (Forsythe & Nelson, 1985). At the triple junction recent oceanic crust is subducted getting older towards the north until reaching an maximum age of 48 Ma at the Peru-Chile border (Müller et al., 1997). Two further prominent features on Nazca Plate are two ridges being subducted below the South American Plate (Figure 2.1). The Juan Fernández Ridge consists of chain of large seamounts, originating from stationary Juan Fernández hot spot. Subduction began in Miocene time starting in northern Chile and migrated southwards to its present collision location (32-33°S) (Yáñez et al., 2001, 2002). The Nazca Ridge is a 1000 km long submarine, aseismic ridge originating from the Cenozoic Pacific-Nazca spreading center (Pilger & Handschumacher, 1981; Woods & Okal, 1994). The first contact between ridge and trench started 12.5 Ma ago moving continuously eastward to the current position (Hampel et al., 2004).

The subduction determine the geomorphological structure of Chile, partitioning the country in three major features. Towards the Pacific Ocean the Coastal Cordillera rise to maximum altitudes of 3114 masl exceeding rarely 1500 masl in Southern Chile. There the mountain range consists of Late Paleozoic-Mesozoic igneous and partly metamorphic rocks. The Central Depression, bordering the Coastal Cordillera to the east, is a downwarp filled with Mesozoic and Quaternary sediments. Both features, in their described form, continue south until the Triple Junction. The current volcanic arc is located east of the Central Depression, accompanied in Northern Chile by the Pre-cordillera and the Altiplano and Puna plateaus. Altiplano and Puna in northern Chile and southern Bolivia reach averages altitudes of 3000–4500 masl with the summit elevations of the volcanoes exceeding sometimes 6000 masl. Formation of the high plateaus is related to 250 km crustal shortening, appearing mostly behind the volcanic front in the Puna/Altiplano region, and resulting in a crustal thickness of up to 70 km (Haschke et al., 2006; Swenson et al., 2000; Dorbath & Paul, 1996; Beck et al., 1996). The crustal thickening cannot be related to one process alone but rather originates from a combination of processes, where tectonic shortening, magmatic addition, lithospheric thinning, hydration of the lithospheric wedge and tectonic underplating are the dominant ones (Isacks, 1988; Giese et al., 1999; Allmendinger et al., 1997; Kley et al., 1999). The Coastal Cordillera and Central depression are less effected by crustal deformation and crustal downwarp in northern Chile (Reutter et al., 1994). In southern Chile the formation of a high plateau is lacking. The volcanoes seldomly exceed elevations of 3500 masl, while the average elevations are below 1500 masl. Crustal thickness is reduced to 40 km at 39°S (Lüth et al., 2003) and 30–35 km for the southern part of SVZ (Lowrie & Hey, 1981). Unlike the northern section the deformation concentrates on the central part of the volcanic arc. The fore-arc is affected by trench orthogonal shortening, while the trench parallel component is adsorbed within the volcanic arc by large intra-arc fault zones (Dewey & Lamb, 1992; Chinn & Isacks, 1983; Cifuentes, 1989, e.g.). While the volcanic arc in northern Chile is located on the western margin of the high plateaus in southern Chile the volcanic arc is located in the center of the main cordillera, shifting to western positions towards the south.

Many of the differences between the Andean cordillera of northern and southern Chile can be attributed to the difference in subduction process. Northern Chile, as well as the whole northern part of the western margin of South America is affected by subduction erosion since Miocene time (Kukowski & Oncken, 2006). As the rates of magmatic addition are lower than the erosion process, the northern Chilean margin is an area of net loss of continental crust. The areas of ridge subduction (Juan Fernandez Ridge, Nazca Ridge, Chile rise) have even an increased rate of subduction erosion. In southern Chile subduction erosion was ongoing until 3 Ma (Kukowski & Oncken, 2006). With the climatically induced increased input of terrestrial sediments, subduction erosion was decreased dramatically until an accretion of an accretionary prism was initiated. For the area south of the collision of Juan Fernandez Ridge, with the exception of an area around the triple junction, sediment accretion can be observed (Ranero et al., 2006). The origin of the differences in subduction process are not finally solved. Discrepancies might be provoked by the variations in age of the oceanic crust and hence temperature and density, the roughness of crust and the coverage with sediments (Davies, 1999). Yet the difference in climatic conditions, especially considering the rainfall, and its consequences for erosion processes and sediment transport are significant and will affect the subduction process (Bangs & Cande, 1997).

Asch et al. (2006) use seismic data to characterize the Wadati-Benioff zone of the Nazca

subduction and differentiate between northern (transect at 21°S) and southern (36°-40°S) Chile. In northern Chile the Nazca Plate has a dip of 19°-20° in the first 40 km depth and at greater depth a higher angle of 35° (Husen et al., 1999). In southern Chile lower angles of 10° in the upper part and 30° in greater depth are observed (Bohm et al., 2002). Maximum release of seismicity of Wadati-Benioff zone in northern Chile can be recorded up to greater depth (80–110 km) than in southern Chile (50–70 km), that is attributed to the greater age and, hence, colder temperatures of the oceanic crust (Asch et al., 2006). While in northern Chile the seismicity is spread over a wider area in fore-arc, main cordillera and back-arc, in southern Chile the seismicity is concentrated in the fore-arc area (Cahill & Isacks, 1992). Often the location of seismicity correlates with major NW-SE striking fault zones (Gastre, Bío-Bío) in the fore-arc.

2.3. Magmatism

Since the beginning the subduction of the oceanic plates beneath South American plate causes the generation of magmatism that resulted in the deposition of volcanic or plutonic rocks. There are different periods of magmatism that occur in times of extensional tectonics (Parada et al., 2007). In northern Chile (18°-28°S) magmatic arc activity concentrates between Jurassic and Early Cretaceous time on the area of today's Coastal Cordillera. Volcanic-, sedimentary successions and huge plutons with thicknesses of up to 10 km alternated and were deposited in subaerial to shallow marine intra-arc basin environments (Scheuber & Gonzalez, 1999). In central Chile (28°-38°S) several magmatic cycles appear between Carboniferous and Cenozoic times decreasing in age towards the east. In Mesozoic times two plutonic belts, the High Andes Batholith (28°-31°S) and the Coastal batholith (28°-38°S), were generated followed by two belts in Cenozoic times between 30°-38°S (Parada et al., 1988). These two belts are located east of the Coastal Batholith along the Andean range (Figure 2.4). The western Paleogene belt, limited between 30°-32°S, consists of diorite and leucogranites, while the eastern Miocene - Neogene belt has higher petrological variations between gabbro and granite (Parada et al., 2007). Major porphyry deposits in southern Chile are related to those formations. South of 38°S the occurrence of plutonic rocks increase forming a continuous body south of 39.5°S called the North Patagonian Batholith (NPB). The NPB is a prominent lithological feature that is, together with its continuation in the Southern Patagonian Batholith, one of the world's largest cordilleran plutonic complexes located between 40°-47°S (Pankhurst et al., 1999). The emplacement of NPB occurred episodically between Cretaceous - Tertiary time (Suárez & de la Cruz, 2001) related to extensional tectonics. The NPB is described briefly in chapter 2.5. In the SVZ south of 37°S volcanic and subvolcanic rocks of Cenozoic age occur inside the main Cordillera, the Central Depression and also the Coastal Cordillera. Extensional settings in Oligocene and early Miocene leading to strong magmatism provoke widespread subsidence coupled with the formation of extensional basins (Niemeyer & Muñoz, 1983; Jordan et al., 2001; Radic et al., 2002). Hence, the Oligocene volcanic deposits, forming as part of an island arc volcanism, are interbedded with continental sediments of intra arc setting or marine sediments forming thick volcano-sedimentary formations (Parada et al., 2007).

Recent volcanism characteristics are related to the subduction process. Andean volcanism can be grouped into four volcanic zones: Northern Volcanic Zone (NVZ, 5°N-2°S, Colombia and Ecuador), Central Volcanic Zone (CVZ, 14°-27°S, Peru and Chile), Southern Volcanic Zone (SVZ, 33°-46°S, Chile) and Austral Volcanic Zone (AVZ, 49°-55°S, Chile) (Stern, 2004). The volcanic zones are interrupted by zone of volcanic absence. Those areas are

associated with shallow subduction angles that are related to the subduction of thickened oceanic crust (Nur & Ben-Avraham, 1983; Yáñez et al., 2001, 2002; Kirby et al., 1996; Cahill & Isacks, 1992; Gutscher, 2002). The Pampean Flat slab segment (27°-33°S) and the Patagonian Volcanic Gap (46°-49°S) are both marked by the subduction of an oceanic ridge, Juan Fernández Ridge and Chile Rise respectively. For the Pampean Flat slab segment volcanic activity stopped after the impingement of the Juan Fernández Ridge around 14 Ma (Kay et al., 2002) causing lithospheric thickening. Combined with the lack of volcanic activity morphological variations, as the Central depression, is absence.

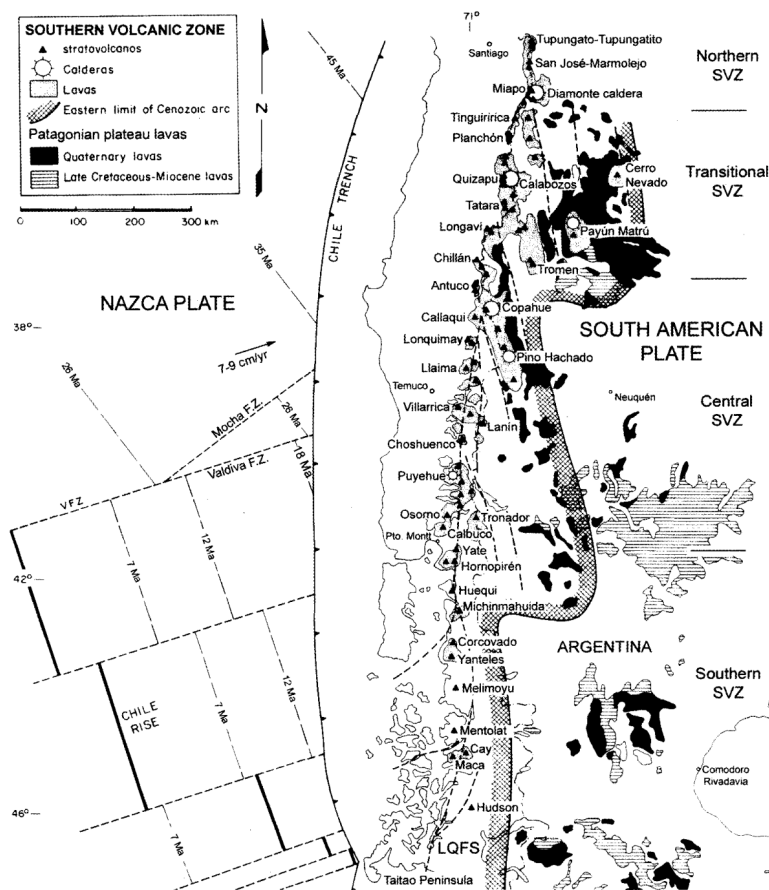


Figure 2.2.: Location of the major stratovolcanos and caldera complexes in the Southern Volcanic Zone. Map taken from Stern (2004). LOFS indicated by almost N-S oriented, dashed line.

Chilean CVZ and SVZ are characterized by active stratovolcanoes, ignimbritic caldera systems and a high number of minor eruptive centers. Thorpe (1984) studied the Andean subduction process and concluded that subduction originate by dehydration of oceanic crust triggering partial melting of the overlying mantle wedge. Continental assimilation is precluded yielding mafic mantle derived magmas similar to magmatism along oceanic convergent plate boundaries. In the CVZ the volcanic arc is located 120 km above the subducted slab at a distance of 240–300 km east of the trench. The depth of the subduction slab below the active SVZ is 90–120 km and the arc is located 270–290 km east of the trench. While the volcanic rocks in SVZ are deposited on top of Paleozoic - Mesozoic basement rocks and Oligocene volcano-sedimentary units (Munizaga et al., 1988; Nelson et al., 1999), CVZ volcanic rocks lie on top of Late Oligocene - recent volcanic rocks. SVZ

contains at least 60 volcanos of historical activity, three caldera complexes (Diamante, Calabozos, Copahue) and numerous minor eruptive centers (Stern, 2004). Unlike CVZ the caldera systems in SVZ are all younger than 1.1 Ma (Stern, 2004). The SVZ is being divided by its volcanological characteristics into four major segments: Northern SVZ (33°-34.5°), Transitional SVZ (34.5°-37°S), Central SVZ (37°-41.5°S) and Southern SVZ (41.5°-46°S) (Hildreth & Moorbath, 1988; López Escobar et al., 1995; López-Escobar et al., 1993; Hickey-Vargas et al., 1986). For the SVZ the locations of major stratovolcanoes are depicted in Figure 2.2. Over the length of SVZ crustal thickness is decreasing from 55km in northern SVZ to 30 km in southern SVZ, accompanied by a decline of the base of arc volcanoes from >3000 masl to <1000 masl. The northern SVZ is a N-S oriented volcanic belt of three stratovolcanoes located east of the general trend of SVZ volcanoes. The transitional SVZ contains a more NNE-SSW striking volcanic chain moving the volcanic activity towards the western margin of the main Cordillera (Stern, 2004). In northern and transitional SVZ stratovolcanoes overlie an uplifted Pre-Quaternary units of plutonic and sedimentary rocks that is partly deformed by faulting and folding (Hickey-Vargas et al., 2016; Cembrano & Lara, 2009). SiO₂-rich rocks prevail in northern and transitional SVZ above the deformed, thickened crust with basaltic andesites, andesites and dacites predominate documenting an incorporation of continental crust (Hickey-Vargas et al., 2016; Futa & Stern, 1988; Davidson et al., 1991; Francis & Hawkesworth, 1994). The northern sector of central SVZ shows a wide arc similar to transitional SVZ narrowing towards the south. In the central and southern SVZ Mesozoic/Cenozoic plutonic rocks of the NPB and low-grade metamorphic rocks form the basement of the volcanic arc (Herve et al., 2007). Völker et al. (2011) determine maximum volcanic activity to occur in the central SVZ. Petrologically magmas of tholeiitic, basaltic and basaltic-andesitic composition prevail (Hickey-Vargas et al., 1986; Futa & Stern, 1988; López-Escobar et al., 1993). Herron et al. (1981) assume that the discrepancies can be related to the age of subducted oceanic crust that decreasing from north to south with steps occurring at the transform faults of Chile Rise (López Escobar et al., 1995). Later authors (Hickey-Vargas et al., 2016) differentiate the characteristics of SVZ to two subgroups situating the transition at 38°S, where LOFS splay from N-S direction to NE-SW orientation forming a horse tail structure next to Callaqui volcano. López Escobar et al. (1995) proves that the LOFS triggers the location of major stratovolcanoes along its run. Magmatism south of 38°S is affected by the thinned crust and also by the LOFS, both facilitated magma ascent to surface, thus, resulting in the generation of magmas without much crustal contamination. The magmas generated in the northern segment, without enhanced vertical permeability, undergo lithospheric overprinting.

2.4. Neotectonics

In Paleogene times tectonics was characterized by low convergence rate (8 cm a^{-1}) and oblique subduction (Cembrano et al., 2007). With the break up of the Farallon plate convergence increased to a maximum in Miocene of 14 cm a^{-1} and a reduced convergence angle (10-20°). After the maxima the convergence rate was reduced stepwise reaching today's $7-9 \text{ cm a}^{-1}$ and remaining small values of obliquity. The recent stress pattern has a maximal horizontal stress trending N60°E and subhorizontal minimum stress (Lavenue & Cembrano, 1999; Rosenau et al., 2006). Neogene tectonics generate typical geomorphical structures. Close to the trench a fore-arc region develops, consisting in southern Chile of the Coastal Cordillera and the Central Depression, followed to the east by the Main

Cordillera, containing the magmatic arc, completed by the foreland zone in Argentina also possessing active back-arc volcanism. In northern Chile a second inner fore-arc is added consisting of the Precordillera and Pre-Andean Depression west of the Western (magmatic) Cordillera. To the east the high plateaus of Altiplano and Puna follows bordered by the Eastern Cordillera towards the Amazonas lowland. The subduction causes the generation of major N-S oriented, large-scale (>1000 km) fault systems that are partly active since Mesozoic times. Margin-parallel strike-slip faults, related to magmatic arcs are observed for other subduction zones with oblique convergence (e.g. [Jarrard, 1986](#)). The Atacama Fault System is located in the Coastal Cordillera of northern Chile. As extensional tectonics prevail normal faulting dominates ([Brown et al., 1993](#)). The Precordillera and Western Cordillera of northern Chile undergo compressional tectonics generating fold and thrust belts. Inside the Precordillera the Domeyko fault system ([Lindsay et al., 1995](#)), also called Falla Oeste, consists of high angle reverse faults controlling the location of shallow silicic plutons hosting today's porphyry copper deposits ([Tomlinson & Blanco, 1997](#); [Ossandón C. et al., 2001](#)). The Domeyko Fault system can be traced to depth using magnetotelluric techniques ([Brasse, 2002](#); [Echternacht et al., 1997](#); [Hoffmann-Rothe, 2002](#)).

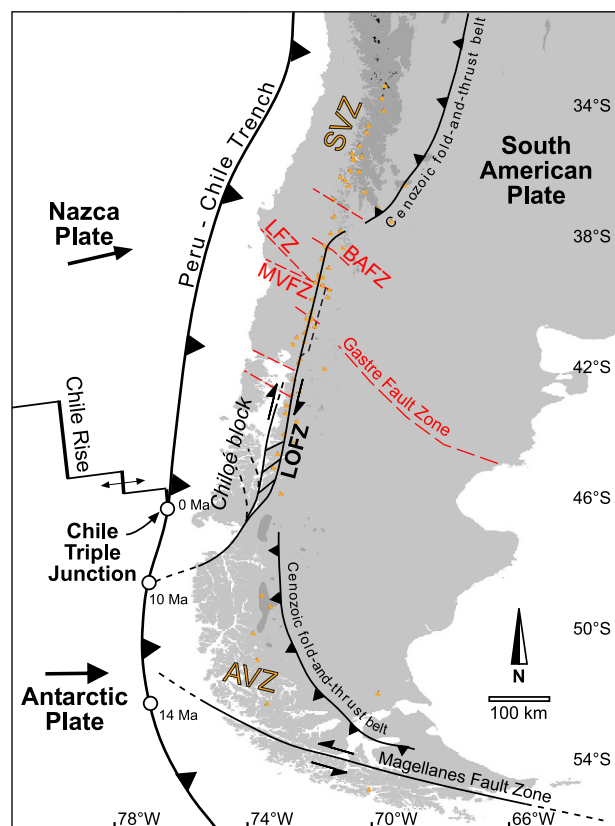


Figure 2.3.: Plate tectonic setting of the southern Andes modified after [Rosenau et al. \(2006\)](#), [Pérez-Flores et al. \(2016\)](#) and [Cembrano & Lara \(2009\)](#). LOFZ: Liquiñe-Ofqui fault system, BAFZ: Bío-Bío Alumine Fault System, MVFZ: Mocha-Villarrica Fault Zone, LFZ: Lanahue Fault zone

In southern Chile no major N-S oriented fault zone is located in the Coastal Cordillera even if strong earthquake activity (e.g. Valdivia 1960: $M_w=9.5$ ([Plafker & Savage, 1970](#))) and continuous seismic activity ([Bohm et al., 2002](#)) is located at the plate interface. Yet at the

border between the Central Depression and the Main (magmatic) Cordillera major fault systems are located. Close to Santiago the west-vergent San Ramon thrust fault separates the Central Depression from the Main Cordillera, while south of 37°S the Liquiñe-Ofqui fault system (LOFS) runs at the western margin of the Main Cordillera. The LOFS is a 1200 km long, intra-arc fault zone (Cembrano & Herve, 1993) running from the Triple Junction (47°S) parallel to the volcanic arc up to Copahue volcano, where it bends and continues in the Antiñir-Copahue Fault system (Cembrano et al., 1996; Folguera et al., 2004) towards a NE direction (Figure 2.3). The LOFS is a set of NNE oriented, margin-parallel lineaments (Rosenau et al., 2006) associated with NE aligned normal faults that splay off the master faults (Pérez-Flores et al., 2016). Partly this combination of parallel running faults in combination with NE-SE aligned en echelon faults, form duplex structures (Cembrano et al., 1996). Oblique subduction and transpressional tectonics generate dextral strike slip movement on the LOFS (Cembrano et al., 1996) decoupling the fore-arc sliver from the back-arc block (Lavenu & Cembrano, 1999; Nelson et al., 1994; Hervé, 1976). Block rotation west (counterclockwise) and east (clockwise) of the LOFS is documented (Beck Jr. et al., 1993; Rojas et al., 1994) with additional uplift of the blocks located east of LOFS (Diraison et al., 1997). Along the fault zone indications for both brittle and ductile deformation are documented pointing on temporal variations of the tectonic regime (Cembrano & Herve, 1993; Pankhurst et al., 1992; Munizaga et al., 1988; Cembrano et al., 1996). Shallow, crustal seismic activity on the SVZ can be related to the trace of LOFS often also detected at fault zone segments in the vicinity of major stratovolcanos (Haberland et al., 2006; Lange et al., 2008). To the north the LOFS continues in form of Antiñir-Copahue Fault system towards Argentina forming an east vergent set of high angle fault zones in form of an active fan or horsetail structure (Folguera et al., 2004; Potent, 2003) without intense seismic activity recorded. Additional to LOFS several Andean Transverse Faults (ATF) occur in southern Chile (Figure 2.3) (Pérez-Flores et al., 2016). These discrete NW-striking faults originate from pre-Andean time (e.g. Radic, 2010; Rapela & Pankhurst, 1992). Geophysical and remote sensing investigations indicate lithospheric-scale structures (e.g. Yañez et al., 1998) controlling partially the paleo and recent fluid movement (Tardani et al., 2016; Sánchez et al., 2013; Lara et al., 2006). In southern Chile Lanalhue Fault Zone, Mocha-Villarrica Fault Zone and Bío-Bío Alumine Fault System are the most prominent ATFs, with some of them having continuous seismic activity with elevated magnitudes (Pérez-Flores et al., 2016; Haberland et al., 2006; Aron et al., 2013). In Argentina the Paleozoic/Mesozoic Gastre Fault Zone crosses the complete South American continent reaching the Andean Cordillera at 40°S (around the Puyehue/Cordon Caulle volcanic complex). In SVZ the LOFS and ATFs controls the location and characteristics of volcanic centers (López Escobar et al., 1995). Cembrano & Lara (2009) study the tectonic control of stratovolcanoes and minor eruptive centers for SVZ in detail revealing that besides LOFS and ATF also NE- to ENE- striking tension cracks trigger and effect volcanic centers. Location and geochemical characteristics, especially in terms of magma type and composition, depend strongly on the triggering tectonic feature. NE-, N- or ENE-striking master faults or secondary tension cracks usually trigger volcanic edifices of mafic composition, while stratovolcanoes above ancient NW-aligned fault zones have a more variable composition producing also felsic magmas.

2.5. Regional geology of the magmatic arc of southern Chile

The basement of the volcanic arc in the northern part (33°-38°S) of SVZ consists of thick series of volcano-sedimentary rocks, while south of 39.5° volcano-sedimentary outcrops are lacking and the Holocene volcanoes lie directly on plutonic basement rocks of the North Patagonian Batholith (NPB) (Figure 2.4). Between 38°-39.5°S the area is marked by a gradual transition from plutonic to volcano-sedimentary basement rocks. The emplacement of NPB occurred episodically between Cretaceous - Tertiary time (Suárez & de la Cruz, 2001) related to extensional tectonics. Three main plutonic events can be dated to Cretaceous, early Miocene and late Miocene - Pliocene times (Parada et al., 2007). Plutonic rocks are deposited on top of metasedimentary rocks, outcropping partly at the western margin of NPB. The NPB, following calc-alkaline magma series, has a wide spectrum of occurring plutonic rocks. Even as individual plutons are difficult to distinguish due to similarity in their lithology, for Cretaceous intrusives granodioritic to tonalitic composition can be determined, while geochemical composition of Tertiary plutonic rocks have a stronger variation between gabbro and granit (Pankhurst et al., 1999, 1992; Parada et al., 1987). East and West margin of the NPB show intrusive contacts to underlying bedrock. Intrusion locus of NPB show no temporal variations (Parada et al., 2007). LOFS runs within the central part of the NPB often being the contact between different aged intrusive rocks. It is assumed that the fault zone controls the spatial emplacement of intrusive rocks since Mesozoic times (Hervé, 1994; Munizaga et al., 1988). In the research area major outcrops of plutonic rocks can be found south of the Villarrica-Quetrupillán-Lanín volcanic chain but also north of it e.g. east of Caburgua Lake or at the northern flank of Villarrica volcano.

During the Eocene-Miocene extensional tectonic interval (Pardo-Casas & Molnar, 1987; Melnick et al., 2006) in the SVZ a series of asymmetric basins occur (Radic et al., 2002; Niemeyer & Muñoz, 1983; Muñoz & Niemeyer, 1984). The basin deposits, known as Cura-Mallín group in the southern part and Abanico formation (Charrier 2002) respectively in the northern part, contain of volcanoclastic and non-marine sedimentary rocks reaching thickness of up to 3000 m (Suarez & Emparan, 1995; Radic et al., 2002). Cura-Mallín group overlies Jurassic sedimentary and volcanic as well as Cretaceous magmatic rocks. While various subdivisions proposed (Utgé et al., 2009; Niemeyer & Muñoz, 1983) Suarez & Emparan (1995) subdivide the group into two interfingering sub-series, the volcanic Guapitrio and the sedimentary Rio Pedregoso formation. The Guapitrio series contains lava deposits and volcanoclastic rocks, while Rio Pedregoso formation consists of fluvial, lacustrine and (Gilbert-type) deltaic sediments. Marine sediments are absent due to the intra-arc character of the basins separated by the volcanic arc from the fore-arc (Suarez & Emparan, 1995). Overlapping ages demonstrate the interfingering character of the formations. In Miocene times the intra arc basins were, due to accelerated convergence and thus compression, inverted and uplifted (Jordan et al., 2001; Vergara et al., 1997). Between 33°- 38° volcano-sedimentary deposits are located inside the current volcanic arc moving gradually eastward towards positions inside the Argentinian back-arc (Jordan et al., 2001) south of 39°. Radic (2010) described the depocenters as half-graben, sub-basins separated by accommodation zones, coinciding with Pliocene volcanic activity. Hervé (1984) assume that the northward continuation of LOFS formed the Cura-Mallín basins as pull-apart basins. An effect of basin structure to the occurrence of recent volcanism is documented (Radic, 2010). It is assumed that the Cura-Mallín group is a possible target of geothermal exploration as the geothermal reservoirs are assumed to be hosted by these rocks (Sánchez-Alfaro et al., 2016). The Cura-Mallín group is conformably overlain by the volcanic

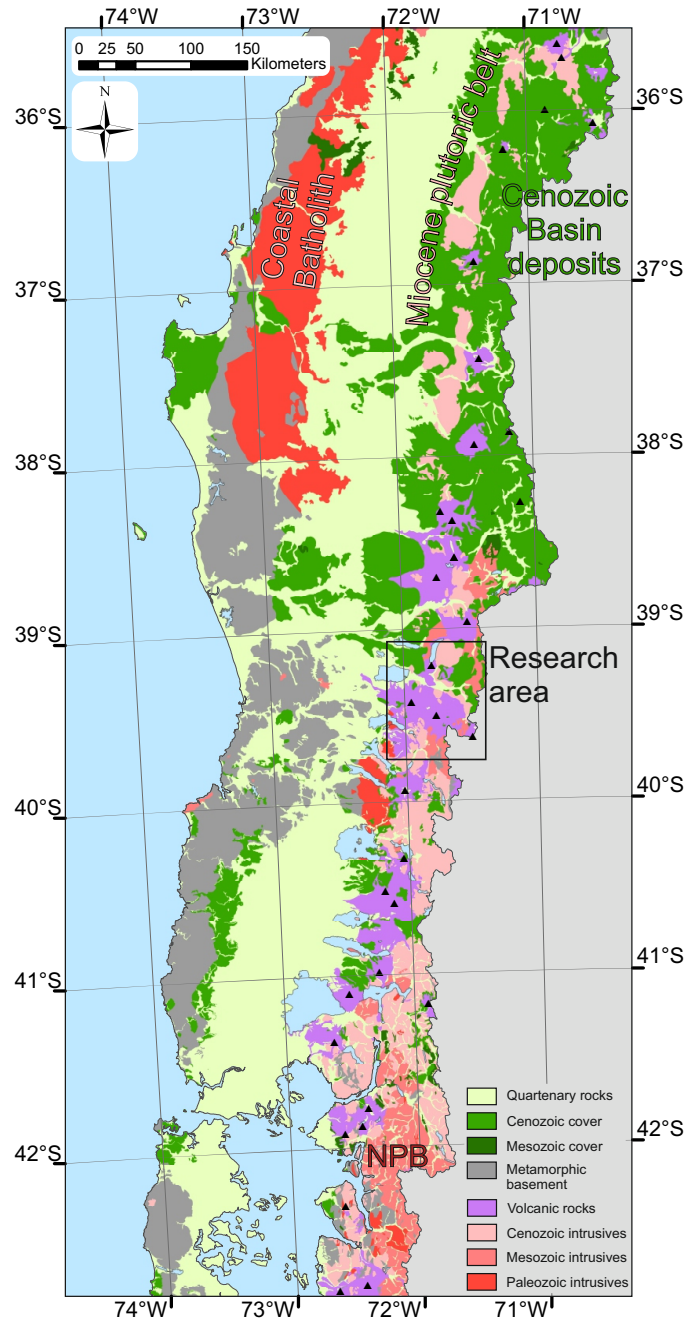


Figure 2.4.: Geological map of the Southern Chile between 36°S - 42°S, modified from 1:1.000.000 scale map, Servicio Nacional de Geología y Minería, Chile considering also the finding of Cembrano & Lara (2009); Sánchez et al. (2013); Pérez-Flores et al. (2016).

Trapa-Trapa formation, called Farellones in the northern sector of SVZ (Charrier et al., 2007). A differentiation between overlaying volcanic formation and Guapitrio formation is sometimes challenging. In the research area around Villarrica volcano-sedimentary rocks outcrop west of Caburgua Lake and around the city of Curarrehue, NE of Quetrupillán volcano. Furthermore isolated lenses of volcano-sedimentary material occur hinting on a more wide-spread appearance below quaternary deposits or fresh volcanic rocks.

The active Villarrica volcano belongs to the WNW-ESE oriented volcanic chain that runs oblique to the volcanic arc. The volcanic chain runs parallel to Mocha Villarrica

Fault zone (Spalletti & Salda, 1996; Rapela & Pankhurst, 1992; Hackney et al., 2006). Unlike Quetrupillán and Lanín, Villarrica exhibits a strong, frequent activity of Hawaiian - Strombolian type with >20 major eruptions per century (Petit-Breuilh & Lobato, 1994; Clavero & Moreno, 2004; Ortiz, 2003). Latest major eruptions are observed in 1948/49 (generating small pyroclastic flows), 1963/64, 1971/72 and 1984. Evolution of Villarrica continues since Pleistocene. Generally the formation of a stratocone was followed by a caldera collapse erupting huge ignimbritic deposits. Caldera collapses are documented for 100 ka, 13.7 ka (forming Lican ignimbrite) and 3.7 ka (forming Pucón ignimbrite) (Clavero & Moreno, 2004; Moreno & Clavero, 2006). Since the last collapse a new stratocone generates and continues having an almost permanent lava lake of fluctuating depth in the summit crater (Moreno & Clavero, 2006). The ancestral as well as the current stratocone are built of basaltic to basaltic andesite lavas. The ignimbritic rocks, basaltic to andesitic in composition, formed during a period of increased explosivity show pyroclastic and lahar depositional characteristics (Moreno & Clavero, 2006). While Lanín has a similar mineralogical composition Quetrupillán shows more silicic magmas with dacites and high-SiO₂ andesites occurring (Hickey-Vargas et al., 1989). The volcanic chain is surrounded by 20 monogenetic cones located inside the volcanic chain or in a segment S and SE of Caburgua lake (Lara et al., 2004). Those scoria cones have a pure basaltic composition with very low ⁸⁷Sr/⁸⁶Sr signatures. Through the REE composition and the mafic character of the rocks of the scoria cones Hickey-Vargas et al. (2016) conclude on a mantle origin without strong crustal assimilation. A strong coupling with the trace of the LOFS is determined (Cembrano & Lara, 2009). From isotopic studies magma chambers below the stratovolcanoes are assumed in shallow depth (Hickey-Vargas et al., 1989), neglecting in contrast the presence of major chambers below the small eruptive centres.

2.6. Scientific exploration of geothermal reservoirs in SVZ

Within the last decade geothermal energy supply in Chile came into focus resulting in the systematic approach to investigate geothermal reservoirs. Within this last chapter we want to highlight new findings relevant for the exploration and understanding of geothermal reservoirs in the SVZ. As mentioned above Cembrano & Lara (2009) reveal that the type and structure of volcanic manifestations is related to the fault zone characteristics especially in terms of orientation towards the main stress field. Sánchez et al. (2013) prove similar correlation between the characteristics of geothermal reservoirs and fault zones for their study of Villarrica geothermal system. Using geochemical techniques different geochemical signatures can be observed for springs discharging in the vicinity of NW-SE aligned ATFs and springs related to N-S master faults of LOFS. For the LOFS domain enhanced permeability in combination with deep convection cells is assumed with the heat originating from conduction from host rock. For the compressional ATF domain a higher probability of hosting magma or geothermal reservoirs is derived. A more horizontal fluid flow is assumed while magmatic input (vapour or fluids) will effect heating additionally. Tardani et al. (2016) and Wrage et al. (2017) confirm the findings concerning the two tectonic domains and their effect on geothermal fluid circulation by their more regional geochemical studies. Wrage et al. (2017) additional reveal that the subsurface fluid flow is affected also by lithology with enhanced horizontal permeability related to volcano-sedimentary formations while in granodioritic rocks vertical permeability prevail. Roquer et al. (2017) using microstructural analysis of fracture samples from the different tectonic domains postulates that the intersection of ATF and LOFS fault zones generates higher probabilities

of enhanced hydrothermal activity. The tectonics of the fault zones in SVZ and their effects on geothermal reservoirs are investigated intensively by Pérez-Flores et al. (2016, 2017b,a). Between Copahue and Llaima volcano (37.7°S - 38.7°S) they study the structural geology of the LOFS and ATF domain and derive a regional structural model. Their investigations show that LOFS domain faults act as fluids pathways while AFT domain faults could host geothermal reservoirs with a dense fault-fracture network (Pérez-Flores et al., 2016). Those findings are in accordance with Tardani et al. (2016) using isotope geochemistry to study the effects of the different fault zone set on the hydrothermal fluid chemistry. The effects of fracturing on the rock permeability of SVZ rocks are investigated in Pérez-Flores et al. (2017b) and show a tremendous increase of permeability enabling convective heat transport. For the Tolhuaca geothermal system that was the first system in the SVZ that was explored and exploited under economic considerations, hydrothermal activity can be expected for NE and NW oriented fault zones (Pérez-Flores et al., 2017a). It could be shown that the proven high enthalpy reservoir (Temp >300 °C) developed through hydrothermal alteration products sealing the reservoir as a cap rock (Sánchez-Alfaro et al., 2016). The existence of such clayly cap rocks is used for geothermal exploration in the SVZ as done e.g. for the Tolhuaca geothermal system (Melosh et al., 2012) or for the Laguna del Maule prospect (Reyes-Wagner et al., 2017).

3. Principles of geothermal exploration

In the following chapter the, principles of geothermal exploration are introduced, which will be used for the exploration of low/medium-enthalpy Villarrica geothermal system. Since various methods of different disciplines are used within this study, basic concepts (e.g. classical fluid composition analysis) are excluded. Principles of the magnetotelluric concept bases on the works of [Simpson & Bahr \(2005\)](#), [Caldwell et al. \(2004\)](#) and [Vozoff \(1991\)](#). Fundamentals of gravity measurements were mainly taken from [Lowrie \(2007\)](#), [Telford et al. \(2012\)](#) and [Clauser \(2004\)](#). The concept of the application of chlorofluorocarbons as anthropogenic tracers follow the monography of [Plummer & Busenberg \(2006\)](#) and the review paper of [Turnadge & Smerdon \(2014\)](#). For the fundamentals of Strontium isotopes the work of [Faure & Powell \(1986\)](#) was consulted.

3.1. Geophysical Exploration

Geophysical exploration for identification geothermal resources allows reservoir evaluation previous to cost-intensive drilling. Application of a variety of different methods is possible. The selection of appropriate techniques depends strongly on the exploration target but also on the presumed geology. Petroleum exploration uses in most cases active seismics as typical trapping structures in sedimentary sequences can be easily detected. Within this study we have decided to use electromagnetic techniques (Magnetotellurics) as geothermal targets, hot saline fluids, can be visualized by conductivity contrast. Electromagnetics are accompanied by gravimetrical measurements revealing major tectonic structures (in particular fault zones) by density differences.

3.1.1. Magnetotellurics

Electromagnetic techniques reveal subsurface structure using differences in electrical conductivity. Magnetotellurics (MT) is a passive electromagnetic exploration technique using fluctuations in the natural terrestrial magnetic field as a power source penetrating into the earth. Thus it can be distinguished to active geoelectric techniques, where an electric source is injected into the earth to measure the conductivities underneath.

MT utilize fluctuations of the natural geomagnetic field (see chapter 3.1.1.1 for introduction of source mechanisms) penetrating into the earth and generating response, that is measured

in order to calculate rock conductivity (see chapter 3.1.1.3 for detailed description of subsurface processes). Basic theory of MT was discovered in the 1950's by Tikhonov (1950) and cited Cagniard 1953 revealing the possibility to derive complex impedance out of simultaneous measurements of electromagnetic waves enabling to determine rock conductivity.

Electromagnetic waves are damped during motion in solid rocks according to their frequency and hence wavelength. High frequency waves are subject to rapid damping resulting in shallow penetration depth, whereas waves of low frequency (= long wavelength) are less damped, thus, penetrating deeper into the earth. This tenet is expressed in the electromagnetic skin depth $p(T)$ (Eq. 3.1) describing the exponential decay of the diffusion process.

$$p(T) = \sqrt{T/\pi\mu\bar{\sigma}} \quad (3.1)$$

where T is the selected period, μ the magnetic permeability (often simplified by free-space permeability $\mu_0 = 4\pi \cdot 10^{-7} \text{Hm}^{-1}$) and $\bar{\sigma}$ the average conductivity of cumulated rock mass. As a consequence theoretically enlarging the sounding period enables measurements to any depth. In practice even long sounding periods cannot resolve very large depth as the sufficient signal to noise ratio are often lacking (Brasse & Soyer, 2001). Besides sounding period, equation 3.1 display the dependency of penetration depth from conductivity of overlying rock.

The received electromagnetic depth signal allows determination of averaged conductivity values. The averaging entails smooth conductivity curves out of MT data as also sharp boundary contrasts are smoothed by the integrated approach. Interpretation, to say it bold and simple, is done by extracting conductivity information frequency after frequency beginning with high frequencies.

3.1.1.1. Electromagnetic field sources

Earth's magnetic field consist of stationary and transient parts. The stationary part is generated inside the liquid outer core by magnetohydrodynamic process, as convection of liquid metals producing electricity and hence a magnetic field (geodynamo theory). This magnetic field fluctuates in time scales far below the periods of MT measurements and can be considered as a stationary magnetic dipole within the purpose of MT. Transient earth's magnetic field is superimposed by (1) metrological phenomena evoking electromagnetic fluctuations and (2) interaction between earth magnetic field and solar storms. Metrology effecting EM field mainly by thunderstorm and lighting activity generating co-called "Sferics". These strong impulses of broad frequency range (<100 kHz) can be considered as being continuous emitted due to constant equatorial thunderstorm activity considering the global perspective. Electromagnetic waves of frequencies <30 kHz propagate from equatorial regions to higher latitudes guided by earth-ionosphere waveguide enabling huge travelling distances. Electromagnetic waves guided at the ionosphere generate the so-called Schumann resonances occurring at specific frequencies: 7.8, 14.1, 20.3, 26.3, and 32.5 Hz (Madden & Thompson, 1965). Those resonances provide main energy component at the transition between metrological and geomagnetic origin of transient EM field (Tzanis, 1987).

EM field flucuations at lower frequencies (<1 Hz) are induced by interactions between solar winds (especially in times of geomagnetic storms) and the magnetosphere of the earth. Continuous coronal plasma radiation towards the earth generates an EM-field due to splitting of charges at the terrestrial magnetic field. Transient character of EM-field

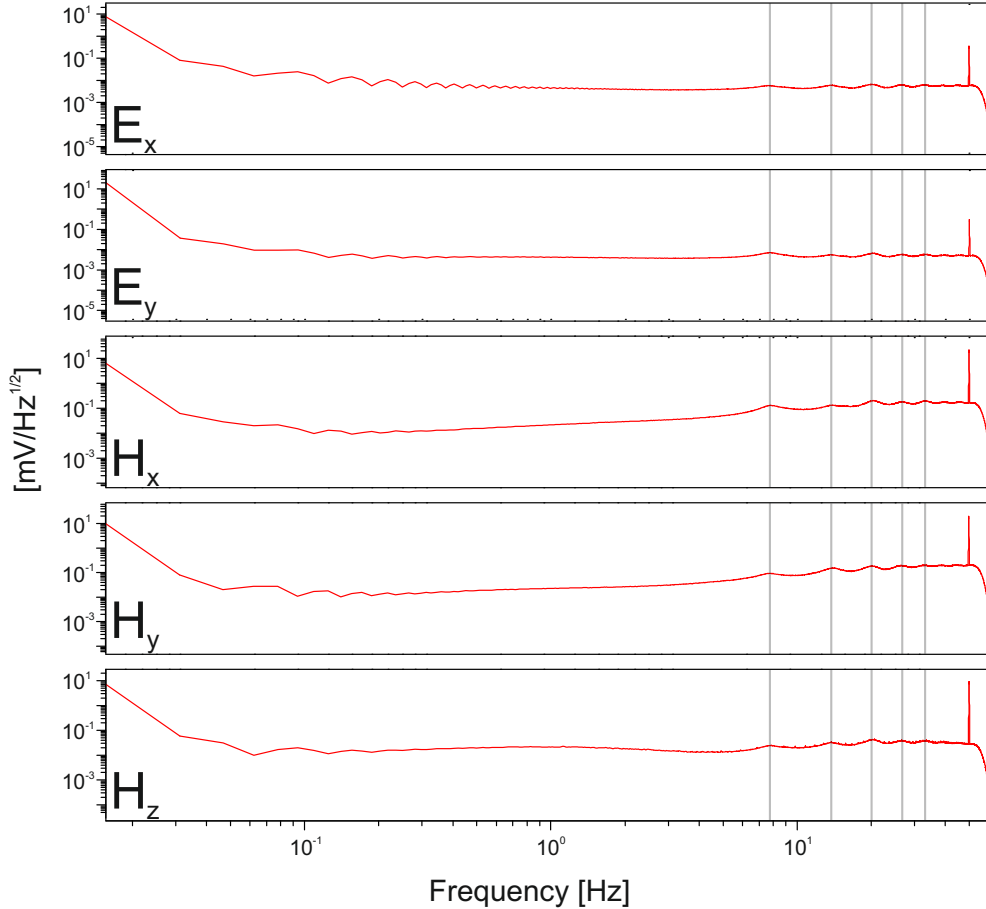


Figure 3.1.: Schumann resonances at 7.8, 14.1, 20.3, 26.3, and 32.5 Hz recorded at remote reference station during MT survey at Villarrica volcano (compare chapter 5). Schuman resonance frequencies highlighted by grey lines. Amplitude maxima through 50 Hz utility frequency.

is evoked by variations of the emitted plasma in terms of density, velocity and intensity. Strength of transient distortions of the Earth's magnetosphere is display using the K-index (Bartels et al., 1939).

Superposition of both input signals allows recording of a huge frequency range (10^5 – 10^{-5} Hz) and as a consequence a broad depth range. Both power spectra do not overlap but rather enclose an amplitude low, the so-called dead-band, between 0.5–5 Hz (Simpson & Bahr, 2005). In fact transfer functions from field surveys suffer often from low data quality at even broader ranges between 1-10 s (Figure 3.2).

3.1.1.2. Conductivity of rocks and fluids of the earth crust

EM depth soundings contain information about the electrical conductivity of the subsurface. Thus, geological subsurface structure can be explored by linking electrical conductivity to physicochemical parameters.

In porous, solid materials the movement of free charge carriers is related to one of the following conduction processes: electronic, semi-conduction and electrolytic. Electronic conduction is characterized by free electrons, which can move in metallic matrix transporting charge. In nature this mechanism accounts for some ore minerals, graphite and for the

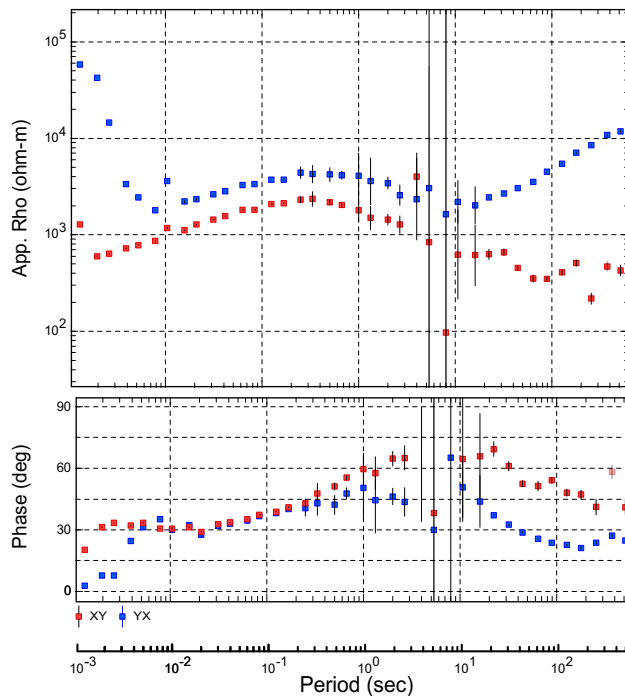


Figure 3.2.: Effect of MT dead band on data quality of Transfer function displayed at Station 7 from MT survey at Villarrica volcano (compare chapter 5). Data quality minima are located between 3-20 s

metallic earth inner core. In semi-conductors conduction arise from a limited number of charge carriers as not all electrodes are able to move freely and hence contributing to conduction. This process governs mantle resistivity as major mantle minerals (e.g. olivine) are affected by semi-conduction. Electrolytic conduction occurs in solutions, where free charge carriers can move freely in the liquid phase. Saline groundwater, often documented for geothermal systems and partial melting generate their decreased resistivity by electrolytic conduction inside a solution moving in a solid media.

Figure 3.3 presents a list of different earth materials and their varying electric resistivity. Rocks and especially fresh rocks have high resistivities. Nevertheless their bulk rock resistivity can differ from matrix resistivity due to saline fluids in pore space. As a consequence the occurrence of circulating saline brines can predominate bulk rock resistivity in dependence of porosity and especially interconnected porosity, hence permeability. Whereas seawater has an almost constant resistivity of $0.2 \Omega\text{m}$, fluids in geological formations differ over three orders of magnitude in resistivity according to their aqueous mineral load. The amount of dissolved ions depends i.a. strongly on circulation time and water-rock interaction and hence the fluid genesis. Furthermore fluid resistivity is temperature dependent (Ussher et al., 2000; Dakhnov, 1962). Besides saline brines in the natural system electrolytic conduction predominated the resistivity of molten material. Resistivities of melt vary between $0.05\text{--}1 \Omega\text{m}$. Even if only small percentages of rock mass are molten, the bulk rock resistivity of the partial melt can be lowered by orders (e.g. Rippe et al., 2013; Hill et al., 2009). Clay minerals are incorporated in the listing due to their relevance for geothermal exploration. The majority of clay minerals possess resistivities comparable to sedimentary rocks (Losito & Muschietti, 1998) but the smectite group has significantly

lower resistivities (Emerson & Yang, 1997). As this mineral forms classically in geothermal cap rocks above high-enthalpy geothermal systems (Inoue et al., 1992), it is a prior target in geothermal exploration using electromagnetic techniques. In nature electronic conduction is limited to some ore minerals and graphite. Graphite can be found in various geological environments reducing the resistivities by orders. Black shales, containing higher graphite content, possess reduced resistivities (Mareschal et al., 1991). Furthermore some rock samples, formed under mid-crustal conditions, possess graphite in their rock matrix (Frost et al., 1989; Haak et al., 1991). Those findings have contributed to the discussion, whether the decreased resistivity in lower crustal depth is related to the occurrence of saline fluids or graphite (Yardley & Valley, 1997, 2000; Wannamaker, 2000) as many authors observed the phenomena of crustal conductors worldwide at depths between 10-20 km (i.a. Shankland & Ander, 1983; Haak & Hutton, 1986; Jones, 1992; Vanyan et al., 2001). Possible explanations for conductive mechanism are discussed e.g. by Gough (1986); Jones (1992); Jödicke (1992).

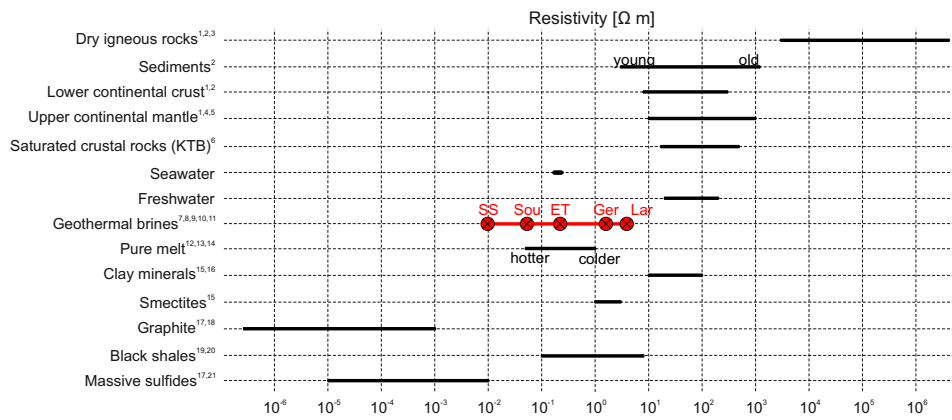


Figure 3.3.: Selection of electric resistivities ranges of rocks and further common materials. References: ¹Jones (1992), ²Simpson & Bahr (2005), ³Duba & Shankland (1982), ⁴Heinson & Lilley (1993), ⁵Lizarralde et al. (1995), ⁶Duba et al. (1994), ⁷Ussher et al. (2000), ⁸Sanjuan et al. (2016), ⁹Cortecci et al. (2005), ¹⁰Karakuş & Şimşek (2013), ¹¹Duchi et al. (1986), ¹²Tyburczy & Waff (1983), ¹³Ni et al. (2011), ¹⁴Presnall et al. (1972), ¹⁵Emerson & Yang (1997), ¹⁶Losito & Muschietti (1998), ¹⁷Olhoeft (1981), ¹⁸Parkhomenko (1967), ¹⁹Jödicke (1992), ²⁰Korja et al. (2008), ²¹Pearce (2006); SS = Salton Sea (USA), Sou = Soultz-sous-Fôrets (France), ET = El Tatio (Chile), Ger = Germencik (Turkey), Lar = Lardarello (Italy)

3.1.1.3. Basic equations

The basis of MT technique is the assumption of the electromagnetic wave as being a planar wave. This assumption is valid at least at mid-latitudes with sufficient distance to local disturbance at equatorial or boreal regions. Yet Madden & Nelson (1986) show that plane wave assumption is limited to periods <10 000 s. The plane wave propagated normal to the earth surface and can be described by equation 3.2.

$$X = X_0 e^{i\omega t - kz} \quad (3.2)$$

where X is a placeholder for either electric (E) or magnetic (B) field, X₀ the original amplitudes, ω the angular frequency and k the wavenumber. From the equation time variance of exciting source can be derived, which is a major requirement for induction processes in the

subsurface. Interaction of electromagnetic waves with polarizable, magnetisable material is described by Maxwell's equations:

$$\nabla \cdot D = \rho \quad (3.3)$$

$$\nabla \cdot B = 0 \quad (3.4)$$

$$\nabla \times E = -\frac{\partial B}{\partial t} \quad (3.5)$$

$$\nabla \times H = J_c + \frac{\partial D}{\partial t} \quad (3.6)$$

where D is the electric flux density [in $C\ m^{-2}$], ρ the electric charge density [in $C\ m^{-3}$], B the magnetic flux density [in T], E the electric field intensity [in $V\ m^{-1}$], H the magnetic field strength [in $A\ m^{-1}$] and J_c the electric current density [in $A\ m^{-2}$]. Equations 3.3 and 3.4 are the Gauss equations stating that electric charges can only cumulate at conductivity discontinuities and that magnetic monopoles do not exist. Faraday's equation (Eq. 3.5) states that a time-varying magnetic field induces an electric field. Finally Ampere's law (Eq. 3.6) states that a closed loop of electrical current generates a magnetic field of transient proportional magnitude. In terms of the natural system the Maxwell equations reveal that a transient magnetic field induces an electrical field, which again induces a secondary magnetic field. From Maxwell's equations and incorporation of Ohm's law one can derive diffusion equations of both electric and magnetic fields:

$$\nabla^2 X = i\omega\mu_0\sigma X \quad (3.7)$$

where μ_0 is the free space magnetic permeability [$\mu_0 = 1.2566 \times 10^{-6}\ Hm^{-1}$] and σ the electric conductivity of the rock [in $S\ m^{-1}$]. Initial frequency-dependent excited energy diffuses through the earth and is dampened depending on frequency. Because of the diffusive propagation the recorded signal displays the averaged response of a rock body. Unlike gravity measurements, which also record a complete rock volume by skalar potential, magnetotelluric methode yields vector fields describing the subsurface. From equation 3.7 one can derive that measuring of the secondary electromagnetic field allows determination of frequency dependent subsurface conductivity enabling to reveal geological relevant information.

3.1.1.4. Data processing

Electromagnetic signals are recording continuously over time. Electromagnetic fields are recorded by two pairs of non-polarizable electrodes, installed perpendicular to each other with a spacing of 100 m (ideal) recording E_x and E_y components of the electric field, and three magnetic coils, installed perpendicular to each other recording all components of magnetic field (H_x , H_y and H_z). The five different signals are recorded using analogue-to-digital (A/D) converter. Conversion of time-varying electromagnetic signals into an interpretable format is known as data processing. Thereby data in time-domain are converted into frequency-domain before forming transfer function, which enables subsequent interpretation. Nyquist frequency (Eq.3.8) determines smallest interpretable frequency, that is not effected by aliasing. Hence during field campaign, sampling rate has to be

adapted to striven sounding depth. Frequencies above Nyquist frequency are removed from data by anti-aliasing filters prior to digitization (Simpson & Bahr, 2005).

$$f_{signal} < f_{Nyquist} = \frac{1}{2} f_{sampling} \quad (3.8)$$

Time-to-frequency conversion is carried out by a Fournier transformation (FT). In plain words the input signal is decomposed and partitioned in participating frequencies. Each frequency contributing to the signal has an amplitude corresponding to the strength of participation of that frequency to original signal. Frequency depended calibration files of induction coils has to be considered in Fourier transformation. Observations in frequency-domain from discretized time windows are stacked to increase data accuracy.

Noise in electromagnetic measurements can be subdivided into geologic and anthropogenic noise (McCracken et al., 1986). Whether geologic noise has to be investigated and evaluated further during interpretation, anthropogenic noise has to be removed during processing at its best. Szarka (1988) lists sources of anthropogenic noise,

- railway lines
- power, cable or pipelines including anti-corrosion currents
- vibrations of anthropogenic or plant origin (root movement through wind load)
- EM wave transmitters
- moving metal vehicles
- utility frequency
- cattle fences

to name only a few. Anthropogenic noise can often be easily identified by displaying the EM signal in frequency domain (Figure 3.4). If affected frequency is known or can be identified, special filters techniques can be applied to eliminate the noise limited to certain frequencies (e.g. Fontes et al., 1988). In the case that anthropogenic noise cannot be resolved easily, robust remote reference technique improves signal-to-noise ratio during transfer function calculation.

Transfer function \bar{Z} is the ratio between time-varying electric input field and induced time-varying magnetic field.

$$E_x(\omega) = Z_{xx}(\omega)H_x(\omega) + Z_{xy}(\omega)H_y(\omega) + \delta Z(\omega) \quad (3.9)$$

$$E_y(\omega) = Z_{yx}(\omega)H_x(\omega) + Z_{yy}(\omega)H_y(\omega) + \delta Z(\omega) \quad (3.10)$$

whereas the δZ displays the measurement errors and noise in this case in the electrical field component. Remote reference technique (Gamble et al., 1979) minimizes the remaining error statistically by correlation of the EM signal of the measuring site with a remote station installed at a (quasi) noise free location in a certain distance to the measuring site. Coherency is expected for the natural electromagnetic field at least over a certain distance, whereas noise of local origin shall be incoherent between those two stations. Thus, cross-correlation of measuring and remote station shall remove local noise from the

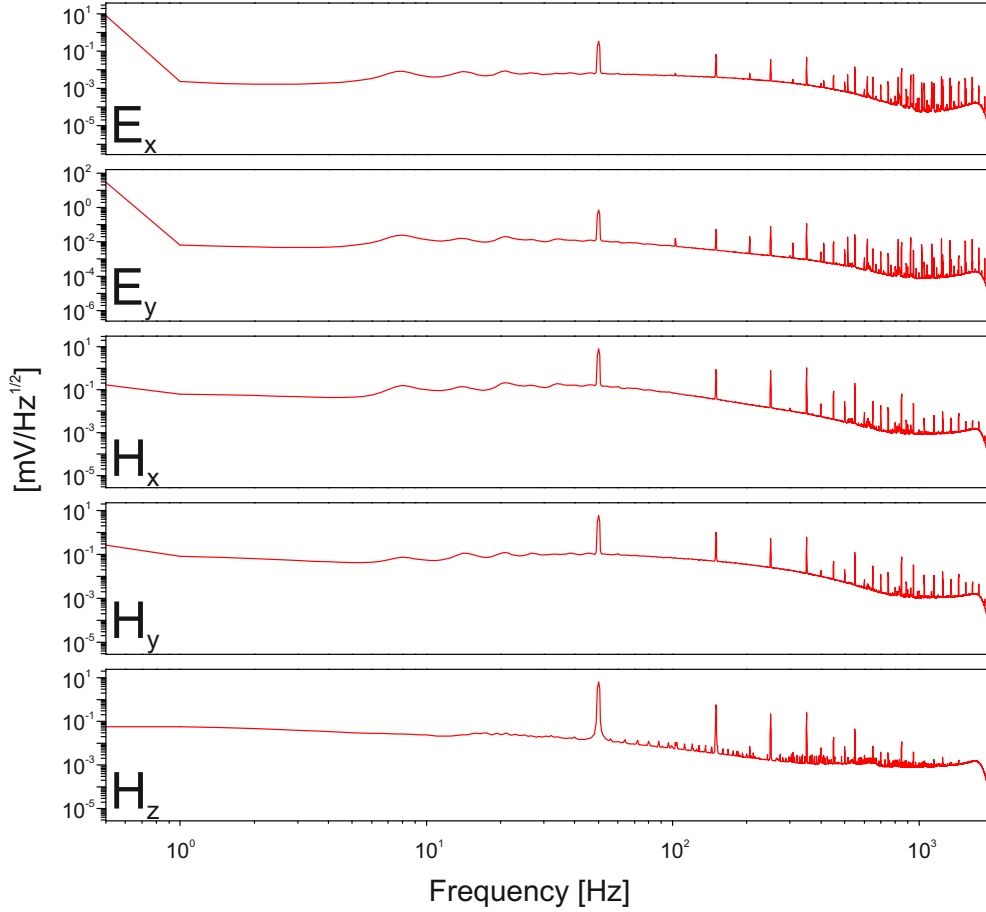


Figure 3.4.: Noisy EM signal of Station 2 from the MT survey at Villarrica geothermal system (compare chapter 5) displayed in frequency domain showing 50 Hz utility frequency and corresponding harmonics.

data without affecting the subsurface EM signal. Usually remote reference method based on the magnetic field is selected due to invulnerability to lateral subsurface resistivity heterogeneities and the general lower noise level compared to the electric field.

3.1.1.5. Interpretable outputs: Impedance tensor, apparent resistivity and phase

The passive MT method uses the transmitted electromagnetic signal to determine the resistivity distribution of the subsurface. The measured horizontal electric and magnetic fields can be linked by the impedance tensor $\overline{\overline{Z}}$:

$$\begin{bmatrix} E_x \\ E_y \end{bmatrix} = \begin{bmatrix} Z_{xx} & Z_{xy} \\ Z_{yx} & Z_{yy} \end{bmatrix} \begin{bmatrix} \frac{B_x}{\mu_0} \\ \frac{B_y}{\mu_0} \end{bmatrix} \quad (3.11)$$

where each component can be calculated from the detected signal by

$$Z_{ij}(\omega) = \frac{E_i(\omega)}{H_j(\omega)} \quad (3.12)$$

Sometimes relationship between measured electric and magnetic fields can be expressed

using Schmucker-Weidelt transfer function C (Weidelt, 1972; Schmucker, 1973):

$$C = \frac{E_x}{i\omega B_y} = -\frac{E_y}{i\omega B_x} \quad (3.13)$$

where the relationship between C and Z for the 1-D case is given by:

$$|Z_{xy,1D}| = |Z_{yx,1D}| = i\mu_0\omega C \quad (3.14)$$

EM wave propagation in the subsurface can be described by equation 3.7. Using the solution of that second order differential equation and considering Maxwell equations (3.3 - 3.6) relationship between measured impedance tensor and subsurface resistivity can be established.

$$Z_{xy}(\omega) = \frac{1-i}{\sqrt{2}} \sqrt{\frac{i\mu_0\omega}{\sigma}} \quad \text{or} \quad C = \frac{1}{i\mu_0\omega\sigma} \quad (3.15)$$

Description of physical assumptions and mathematical transformations can be found e.g. in Simpson & Bahr (2005). This equations allows determination of the electrical conductivity in a case that the subsurface can be considered as an uniform half-space. The assumption is only valid until the wavelength exceeds the thickness of the first layer of constant resistivity. Later on we will discuss discontinuities in the subsurface (see chapter 3.1.1.6). Frequency depended resistivity can be expressed as:

$$\rho_{a,ij}(\omega) = \frac{1}{\mu_0\omega} |Z_{ij}(\omega)|^2 \quad \text{or} \quad \rho_a(\omega) = |C(\omega)|^2 \mu_0\omega \quad (3.16)$$

ρ_a is known as apparent resistivity as the value describing the average resistivity of the rock body defined by the penetration depth depending on the considered frequency (Eq. 3.1). It gives an average of the resistivities detected by a certain frequency. Vertical changes in resistivity, also abrupt discontinuities, are displayed by smooth resistivity shifts own the diffusive behavior of the EM field.

As the impedance tensor is complex, impedance phase can be calculated, displaying the phase lag between electric and magnetic field evoked by conductivity-dependent induction mechanism.

$$\Phi_{ij} = \tan^{-1} \left(\frac{\Im Z_{ij}}{\Re Z_{ij}} \right) \quad \text{or} \quad \Phi = \tan^{-1} \left(\frac{\Im C}{\Re C} \right) \quad (3.17)$$

Apparent resistivity and impedance phase are typically displayed as the function of frequency allowing a first interpretation of the data (Figure 3.5). Therefore evaluation frequencies are selected. Phases illustrate changes in resistivity. If the phase = 45°, describing equal real and imaginary parts of the transfer function, the subsurface do not contain any resistivity change and can be considered as homogenous at least for the considered frequency range. Phases deviating from 45° depict changed in resistivity. Magnetotelluric phases >45° indicate substrate of decreasing resistivities, whereas phases <45° display increasing resistivities in the subsurface.

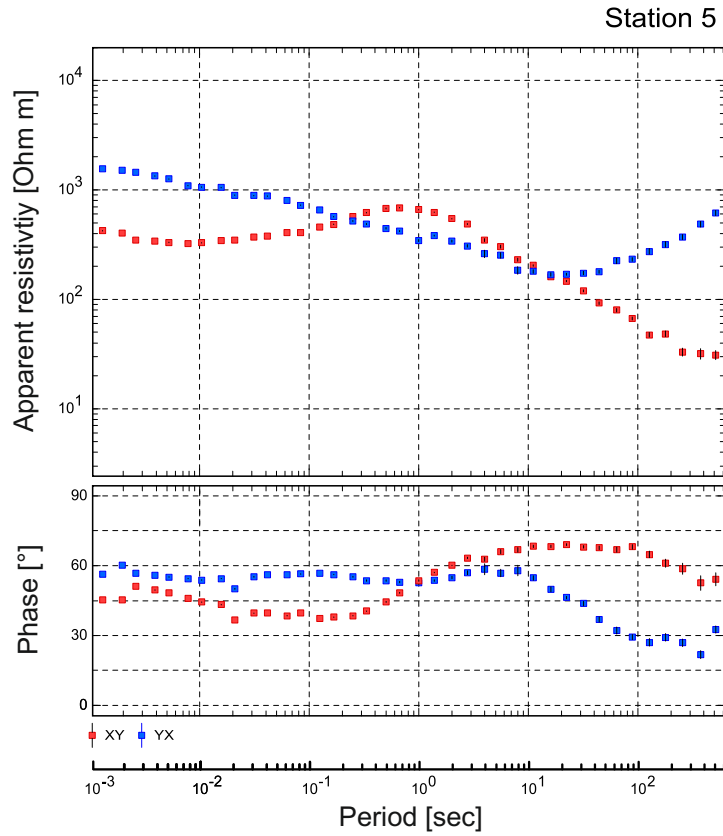


Figure 3.5.: Apparent resistivity and impedance phase of Station 5 from the MT survey at Villarrica geothermal system (compare chapter 5). Presented are TE (red) and TM (blau) modi

3.1.1.6. Induction at discontinuities

The assumption of a uniform half-space, used in the derivation of the impedance tensor, is usually not valid considering complex substrata. Geoelectric discontinuities and their effects on EM signal have to be assessed further. In the beginning we assume a horizontally layered earth, where resistivity varies only in z -direction. Transfer function of the n th layer would be computed using:

$$C_n(\omega) = \frac{E_{xn}(\omega)}{i\omega B_{yn}(\omega)} \quad (3.18)$$

Wait (1954) found an analytical solution for the transfer function for the n th-layer, known as Wait's recursive formula (Eq. 3.19).

$$C_n(z_n - 1) = \frac{1}{q_n} \frac{q_n C_{n+1}(z_n) + \tanh(q_n l_n)}{1 + q_n C_{n+1}(z_n) \tanh(q_n l_n)} \quad (3.19)$$

where $q = \sqrt{i\mu_0\sigma_n\omega}$ and l is the layer thickness. Determination of transfer function starts from the lowermost layer N , considered as uniform half-space, and calculates the transfer function for each layer iteratively. Apparent resistivity and phase for each layer can then be calculated using equations 3.16 and 3.17.

After dealing with horizontal discontinuities, problems becoming two-dimensional by including vertical discontinuities, that might be generated by fault zones or discordances. The vertical contact separates formations of different conductivities. According to Ohm's law (displayed in Figure 3.6) the discontinuity evokes a discontinuous electric field perpendicular

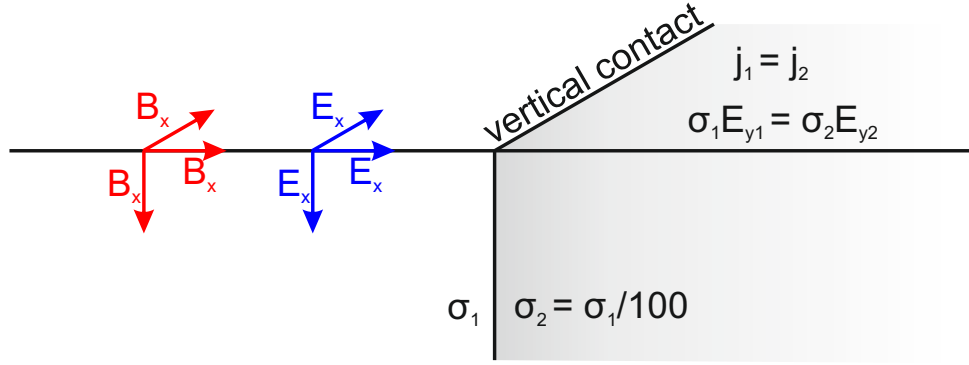


Figure 3.6.: Two-dimensional resistivity model with vertical contact in x-direction separating two regions of different conductivity. The vertical contact may be evoked by a fault zone segregating different geological formations. Following Ohm's law the contact generates a discontinuity in perpendicular electric field, while electric field parallel to the contact and magnetic fields remain continuous.

to the contact (E_y), while the magnetic fields and the electric field parallel to the contact remain continuous. The displayed scenario can be considered as 2-D case, if the vertical contact has an along-strike extension that exceeds the penetration depth. Electromagnetic homogeneity in x-direction and hence $\frac{\partial}{\partial x} = 0$ allow a simplification of Faraday's and Ampere's law. In component form decoupled Maxwell can be displayed and sorted in transverse electric (TE) mode and transverse magnetic (TM) mode:

$$TE : \quad \frac{\partial E_x}{\partial y} = i\omega B_z \quad ; \quad \frac{\partial E_x}{\partial z} = -i\omega B_y \quad ; \quad \frac{\partial B_z}{\partial y} - \frac{\partial B_y}{\partial z} = \mu_0 \sigma E_x \quad (3.20)$$

$$TM : \quad \frac{\partial B_x}{\partial y} = \mu_0 \sigma E_z \quad ; \quad \frac{-\partial B_x}{\partial z} = \mu_0 \sigma E_y \quad ; \quad \frac{\partial E_z}{\partial y} - \frac{\partial E_y}{\partial z} = i\omega B_x \quad (3.21)$$

TE mode describes components of the electromagnetic field, where currents flow parallel to the strike of the vertical contact, whereas TM mode analyzes currents crossing the vertical strike. Hence discontinuity in E_y is revealed by the impedances of TM mode (Z_{yy} and Z_{yx}) yielding a sharp resolution of the lateral resistivity boundary by, in the ideal case, a jump in $\rho_{a,yx}$.

Besides the separation in TE and TM modes the 2-D approach comprises another important feature of magnetotelluric investigations: the concept of geoelectric strike. 2-D interpretation and hence reasonable mode segregation require a strict orientation of the mutually orthogonal electric and magnetic field components orthogonal and parallel towards the main geoelectric strike. Thus usually the layout of MT surveys is oriented in accordance to the main geoelectric strike, provoked through dominant often scale-dependent geological features (e.g. major fault zones, subduction zones, etc.). If the geoelectric strike is unknown prior to survey design, rotation of impedance tensor after data collection allows orientation orthogonal to main strike direction. Occasionally the MT data are biased by several strike directions often affecting different frequency ranges (Simpson & Bahr, 2005). For determination of prevailing geoelectric strike out of impedance tensor, which in most of the cases have four non-zero, independent components owed to local distortion and/or misorientation to geoelectric strike, several techniques are available (Swift, 1967; Groom & Bailey, 1989; Jones & Groom, 1993; Becken et al., 2008).

As plane wave assumption limits the incident EM wave to propagate in z-direction, secondary EM fields are induced in horizontal direction. At lateral resistivity discontinuities, however, vertical magnetic fields are generated through differing along-strike electric currents (compare Eq. 3.20). The complex magnetic transfer function T connects the vertical anomalous induced magnetic field to the inducing horizontal magnetic field (Eq. 3.22):

$$B_z(\omega) = (T_x(\omega) \ T_y(\omega)) \begin{pmatrix} B_x(\omega) \\ B_y(\omega) \end{pmatrix} \quad (3.22)$$

The components of magnetic transfer function are often displayed as induction arrows, by projecting the real part of the vector on a horizontal plane using the following equations to describe magnitude M and angle ϕ of the arrow:

$$M = \sqrt{\Re T_x^2 + \Re T_y^2} \ ; \ \phi = \tan^{-1} \left(\frac{\Re T_y}{\Re T_x} \right) \quad (3.23)$$

On a 1-D earth, where no vertical discontinuities exist, vertical magnetic fields do not occur, hence induction arrows are zero. At a vertical discontinuity (2-D earth) induction arrows occur with the magnitude proportional to the conductivity contrast (Jones & Price, 1970). Arrow magnitude decreases with increasing distance from discontinuity in both media. Arrows point towards/away from the conductive anomaly after the convention of Wiese/Parkinson (Wiese, 1962; Parkinson, 1959)

3.1.1.7. Dimensionality

From the impedance tensor Z information about dimensionality can be derived (Table 3.1). Complete independence of the four components, remaining even after tensor rotation, indicates three-dimensional geoelectric of the substrata. If dependencies between the components or even zero diagonal components exist a simpler geometry can be assumed. Often those similarities or zero diagonal components cannot be determined due to (1) data errors, (2) local small-scale 3-D distortions or (3) real 3-D geoelectric geometry. From impedance tensor simple allocation to case 1)-3) is on a pure scientific base impossible. Thus a variety of techniques exists analyzing the dimensionality of the substrata (e.g. Swift, 1967; Larsen, 1975; Bahr, 1988; Groom & Bailey, 1989). Simpson & Bahr (2005) evaluate the mentioned techniques and create a scheme from the combination of the different approached to determine the dimensionality of the substrata. If evidences for simplified geometry exist, a rotation angle can be calculated maximizing off-diagonal components of impedance tensor thus allowing for interpretation based on an approach valid for simplified geometries.

Table 3.1.: Dimensionality derivations from impedance tensor

1-D	2-D	3-D
$\begin{pmatrix} 0 & Z_n \\ -Z_n & 0 \end{pmatrix}$	$\begin{pmatrix} Z_{xx} = -Z_{yy} & Z_{\parallel} \\ Z_{\perp} & Z_{yy} = -Z_{xx} \end{pmatrix}$	$\begin{pmatrix} Z_{xx} & Z_{xy} \\ Z_{yx} & Z_{yy} \end{pmatrix}$

The raise the complexity, dimensionality of a substrata can be frequency depend. A local finite geological body can disturb geoelectric geometry in shallow depth, but with increasing period the effect of the local distribution vanishes enabling simplified geometries. On the contrary simple geometries in shallow depth can be turned to complex 3-D geometry, if increasing penetration depth detects complex geological geometries in greater distance. An

intensive evaluation of dimensionality and directionality is of intrinsic importance for a succeeding modelling.

Caldwell et al. (2004) presented the concept of magnetotelluric phase tensors, which enable the evaluation of geoelectric geometry of substrata. The phase tensor is a non-symmetric, second ranked tensor determined from impedance tensor:

$$\begin{bmatrix} \Phi_{11} & \Phi_{12} \\ \Phi_{21} & \Phi_{22} \end{bmatrix} = \frac{1}{\det(X)} \begin{bmatrix} X_{22}Y_{11} - X_{12}Y_{21} & X_{22}Y_{12} - X_{12}Y_{22} \\ X_{11}Y_{21} - X_{21}Y_{11} & X_{11}Y_{22} - X_{21}Y_{12} \end{bmatrix} \quad (3.24)$$

where with X and Y being real and imaginary part of the impedance tensor. Estimations of substrata dimensionality are not necessitated but can either be obtained from the evaluation of phase tensors. Bibby (1986) introduce a format of displaying a second rank tensor using its coordinate invariants. Adaption to the phase tensor results in:

$$\Phi = R^T(\alpha - \beta) \begin{bmatrix} \Phi_{max} & 0 \\ 0 & \Phi_{min} \end{bmatrix} R(\alpha + \beta) \quad (3.25)$$

where R is the rotation matrix and R^T the transposed rotation matrix.

$$R = \begin{bmatrix} \cos(\alpha + \beta) & \sin(\alpha + \beta) \\ -\sin(\alpha + \beta) & \cos(\alpha + \beta) \end{bmatrix} \quad (3.26)$$

The non-symmetric 2-D tensor is depicted by an ellipse, with magnitude of major and minor axes according to coordinate invariants (Φ_{max} , Φ_{min}). The major axis of the ellipse is rotated by the angle $\alpha - \beta$, where

$$\beta = \frac{1}{2} \tan^{-1} \left(\frac{\Phi_{12} - \Phi_{21}}{\Phi_{11} + \Phi_{22}} \right) \quad (3.27)$$

$$\alpha = \frac{1}{2} \tan^{-1} \left(\frac{\Phi_{12} + \Phi_{21}}{\Phi_{11} - \Phi_{22}} \right) \quad (3.28)$$

The coordinate invariant skew angle β is measure for the asymmetry of the tensor (Caldwell et al., 2004). For symmetric phase tensors, meaning in case of 1-D or 2-D geoelectric geometry, $\beta = 0$, hence rotation of the phase tensor is governed by α alone. In this case the coordinate invariants are equal to the eigenvalues of the phase tensor. α represents the tensor's dependency of the coordinate system (Caldwell et al., 2004) and often governs the orientation of the phase tensor ellipse.

For the simple 1-D geometry, phase tensor is depicted as a circle of uniform radius. Variations of radius occur with varying frequency depending on resistivity development with depth. Through the cylindrical symmetry β is zero and α undefined. In case of 2-D resistivity distribution β remains 0 but circle transforms into an ellipse, with major axes aligned parallel or perpendicular to geoelectric strike. Orientation of the ellipse, hence α , is related to geoelectric strike, but as ambiguity of the orientation of the tensor towards the geoelectric strike exists. The geoelectric strike can be determined from phase tensor just with a 90° ambiguity. Consideration of induction arrows, identifying conductive bodies, solves this ambiguity. A 2-D geoelectric geometry can be identified by consistency in the

direction of principal axes over the reasearch area. Galvanic distortion, meaning shallow, small-scale bodies of varying conductivity channeling currents, cause distortion of the impedance tensor resulting in a assumption of 3-D geometry, even if simpler geometries prevail. The phase tensor evaluation benefits from the disreagard of galvanic distortion allowing an advanced estimation of substrata dimensionality. 3-D resistivity distributions are characterized by variations in orientation of phase tensor ellipse, while skew angle β can possess higher values or remain small. The principle axes are aligned parallel and perpendicular to the flow direction of currents thus enable the estimation of geoelectric strike direction.

3.1.2. Gravimetry

Besides seismic, magnetic and electromagnetic methods gravimetry is a fundamental exploration method in applied geophysics. The method investigates the density distribution of the subsurface and can reveal geological structures by its density contrasts. Gravity surveys are widespread used for instance in the exploration of mineral deposits or hydrocarbon reservoirs or the determination of the extent of sedimentary basins or salt domes. In geothermal exploration gravity surveys are used to explore the fault zone pattern, detect areas of high hydrothermal alteration or investigate the location and characteristics of potential reservoirs (e.g. Kohn et al., 2011; Santos & Rivas, 2009; Altwegg, 2015).

Gravimetric measurements base on the accurate determination of the vertical component of the earth's gravitational field. The development of portable, highly accurate equipment allows the determination of subsurface gravity response within a short time. Each measured data point reflects the superposition of gravity anomalies within the subsurface and thus requires an intensive data treatment and interpretation. In a first step various, natural gravitational effects have to be removed, e.g. tidal effects, elevation and topographic effects, instrumental drifts, before the remaining Bouguer anomaly can be used to reveal the subsurface density structure. Often modeling approaches are selected to compare Bouguer Anomaly with geological models.

3.1.2.1. Basic concepts

Newton's law of gravitation describes the interaction between two masses by a force F directly proportional to the product of their masses M , m (Eq. 3.29).

$$F = -G \frac{m \cdot M}{r^2} \hat{r} \quad (3.29)$$

In this equation G is the gravitational constant $G = 6.67384 \cdot 10^{-11} m^3 kg^{-1} s^{-2}$, r the distance between the two masses and \hat{r} the radial unit vector. The gravitational field, in physics more important than the force itself, describes the attraction of a mass M towards a unit mass depending on its position. The gravitational field can be expressed by the gravitational acceleration a_G affecting each mass within its environment (Eq. 3.30).

$$a_G = -G \frac{M}{r^2} \hat{r} \quad (3.30)$$

Commonly used units for the gravitational acceleration is $1 \text{ mGal} = 10 \mu\text{m s}^{-2}$. The potential energy E_p of a unit mass m inside a gravitational potential of a mass M can be described by the gravitational potential U_G (Eq. 3.31). Work $-dW$, required to move a

mass inside the field, is equal to change of potential energy $dE_p = -dW$.

$$U_G = -G \frac{M}{r} = E_P/m \quad (3.31)$$

Using above stated equations the gravitational potential on a punctual mass in a gravitational field can be calculated. Locations of equal gravitational potential can be combined along equipotential surfaces or, in case of the earth, spheres.

Rotation of the earth adds a centripetal acceleration opposing gravitational acceleration. However strength of centripetal acceleration depends on distance to the rotation axis thus becoming smaller towards the poles. These acceleration variations result in the deviation of the earth shape from a sphere towards an oblate ellipsoid or spheroid. The dimensions of this ellipsoid were established 1980 by the International Association of Geodesy and summarized in the Geodetic Reference System (GRS80). Based on the ellipsoid dimensions theoretical gravity value at any location (Latitude) of the ellipsoid can be calculated using the equation 3.32, being a simplification of the series expansion reproducing Somigliana equation (Heiskanen & Moritz, 1967).

$$g_\phi = g_0(1 + \alpha \sin^2(\phi) - \beta \sin^2(2\phi)) \quad (3.32)$$

where g_ϕ is the gravity acceleration at latitude ϕ , g_0 the gravity at the equator and α and β being constants updated within the years as computing capabilities increase (Heiskanen & Moritz, 1967; Moritz, 1980; Hofmann-Wellenhof & Moritz, 2006).

3.1.2.2. Gravity correction and Bouguer Anomaly

In geophysical exploration, gravity measurements (g_{obs}) are affected by several effects depending on spatial and temporal variations, which have to be considered before data interpretation. Measured gravity data are processed by several corrections adjusting the data to a consistent reference level. The residual gravity anomaly, known as Bouguer Anomaly, characterizes subsurface density contrasts originating purely from geological phenomena. In the following we will outline each gravity reduction step yielding in total the Bouguer Anomaly g_{BA} (Eq. 3.33).

$$g_{BA} = g_{obs} - g_\phi + \Delta g_F - \Delta g_{BP} + \Delta g_T \quad (3.33)$$

where Δg_F is the free-air correction, Δg_{BP} the Bouguer Plate reduction and Δg_T the topographic correction.

Temporal variations: g_ϕ calculates acceleration generated by the earth, but the measuring equipment is effects also by other celestial bodies, mainly the moon. As the earth, the moon attracts masses on the earth according the Newton's law provoking vertical displacement. The effect on Earth becomes obvious in terms of daily tides reaching maximum disturbance of 0.3 mGal in amplitude. The tidal effects are well understood hence their time-depending effects can be removed easily from measured data.

The recordings of gravimeters, commonly used for geophysical exploration, possess small temporal variations. This instrumental drift originates from modifications of the elastic properties of the gravimeter spring. Yet the effect can be compensated by a drift correction. Measurements at selected locations are repeated constantly, quantifying the instrument

drift, enabling to adjust interim measurements by comparison to drift curve.

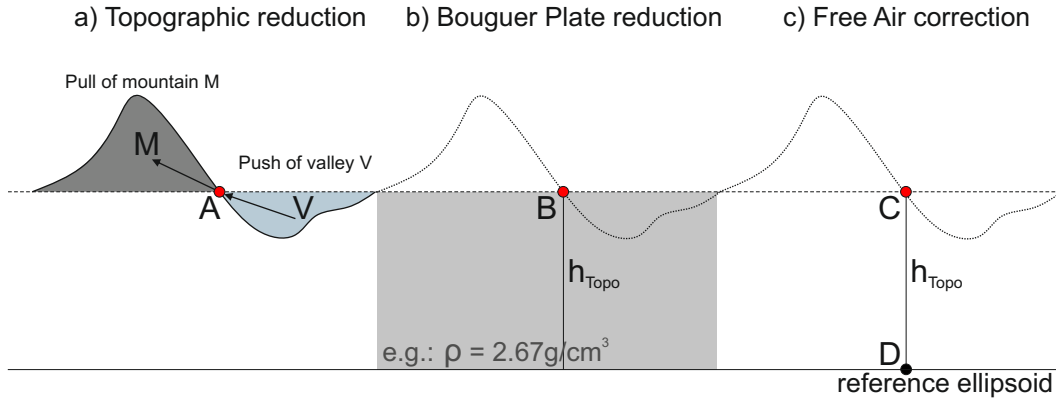


Figure 3.7.: Schematic presentation of gravity measurement reductions yielding Bouguer Anomaly

Free-Air correction: Free-Air correction accounts for the decrease of the gravitational acceleration with increasing distance to attracting earth mass, hence the difference in elevation between measuring point and reference ellipsoid (Figure 3.7c). Virtually the correction computes and reduces the effect of density of the air between measuring location and reference ellipsoid. Free-Air correction can be deduced directly from Newton's law by derivation with respect to the radius (Eq. 3.34).

$$\frac{\partial a_G}{\partial r} = \frac{\partial}{\partial r} \left(-G \frac{M_E}{r^2} \right) = -\frac{2}{r} g = 0.3086 \text{ mGal/m} \quad (3.34)$$

Inserting the radius of the Earth ($r = 6371 \text{ km}$) and the average value of gravity ($981\,000 \text{ mGal}$) resulting in the correction of 0.3086 mGal/m . Uncertainties in elevation determination of $>3 \text{ m}$ result in rather high uncertainties of Bouguer Anomaly of $>0.9 \text{ mGal}$.

Bouguer Plate correction: Bouguer Plate correction compensates the gravitational effect of the rock mass between reference ellipsoid and observation point (Figure 3.7b). This effect is independent of the difference between attracting mass and observations point. In order to reduce the gravity data from extra mass of additional rock formation, the gravitational acceleration of a solid disk of density ρ , infinite radius and thickness equal to the elevation difference on the observation point in its center is determined. Gravitational acceleration of a horizontal prism with the radius r can be computed using equation 3.35.

$$\Delta g_{BP} = 2\pi G \rho \left(h_{Topo} - \left(\sqrt{r^2 + h_{Topo}^2} - r \right) \right) \quad (3.35)$$

Increasing the radius r to infinity reduces the term in brackets to h_{Topo} (Eq. 3.36). Insertion of physical constants yields the correction factor depending on density and elevation.

$$\lim_{r \rightarrow \infty} \Delta g_{BP} = 2\pi G \rho h_{Topo} = 0.00004193 \rho h_{Topo} [\text{mGal}] \quad (3.36)$$

The correction is subtracted if $H_{Topo} > 0$ (observation point above reference ellipsoid) and added if located below the reference ellipsoid. Combination of Bouguer Plate and Free-Air

corrections yield a single elevation correction (Eq. 3.37).

$$(0.3086 - 0.00004193\rho) h_{Topo} [mGal] \quad (3.37)$$

Terrain correction: Terrain correction computes the effect of mass excesses (hills) or deficiencies (valleys) located around the point of observation. Vividly, valleys are filled and hills are removed, leveling the topography allowing a comparison of the different gravity measuring locations (Figure 3.7a). Therefore topography is separated into vertical prisms and the gravitational acceleration on the observation point is calculated for each prism. Both, mass excess and deficit, have an upward acceleration opposing gravity. Thus terrain correction has to be added to Bouguer Anomaly. Originally relief of research area was subdivided in numerous vertical prisms for which the gravitational effect was calculated manually. Today, given the possibilities of digital elevation models (DEM) and increased computing capabilities, terrain correction is computed numerically based nowadays on rectangular grids prescribed by the DEM.

3.1.2.3. Density ranges of rocks

Densities of rocks can be measured on site by borehole logging tools or estimated from seismic velocities. Often outcrop samples are used to determine rock densities in the laboratory. Yet measured densities deviate from true bulk rock density as the sample may be affected by stress release, alteration or dehydration. Density ranges of rocks possibly occurring in the Andean Cordillera are displayed in Figure 3.8. The density of each rock type vary significantly depending on rock-specific mineral composition, porosity, etc. Often different rock formations overlap each other. In general sedimentary rocks possess lower densities than igneous or metamorphic rocks. The wide range of sedimentary rocks is attributable mainly to variations in porosity. For igneous rocks, porosity is of subordinate importance except for fresh lavas, which might possess higher porosity values. Density depends primary on minerals composition and recrystallization processes. Although, igneous rocks have generally a high bulk density, intense fracturation can decrease density significantly (Telford et al., 2012) especially when fracturing is related to major fault zone systems.

3.2. Geochemical Exploration

In geothermal exploration geochemical methods are applied to investigate the subsurface processes affecting the thermal fluids. At early project stages the cost-efficient method is applied to evaluate the geothermal potential. Often geothermal manifestations (hot springs, fumaroles, mud pools, etc.) are used as a window to identify and describe reservoir processes. For this purpose hydrochemical fluid or gas composition is used to describe the geothermal system in terms of physicochemical reservoir properties (temperature, pH, salinity,...), fluid origin and genesis, circulation pattern, reservoir processes (thermodynamic phase changes, hydrothermal alteration, reservoir temperature,...) as well as for predicting of operational risks (e.g. scaling or corrosion potential). For reservoir rock deduction geothermal fluids are investigating in terms of water rock interaction governing the fluid composition. In the following I will introduce selected geochemical techniques, which are nonstandard in geothermal exploration. The common geochemical techniques (major constituents, oxygen/hydrogen isotopy, solute geothermometry), used in this study are introduced shortly in the individual chapters or can be found in Arnórsson (e.g. 2000).

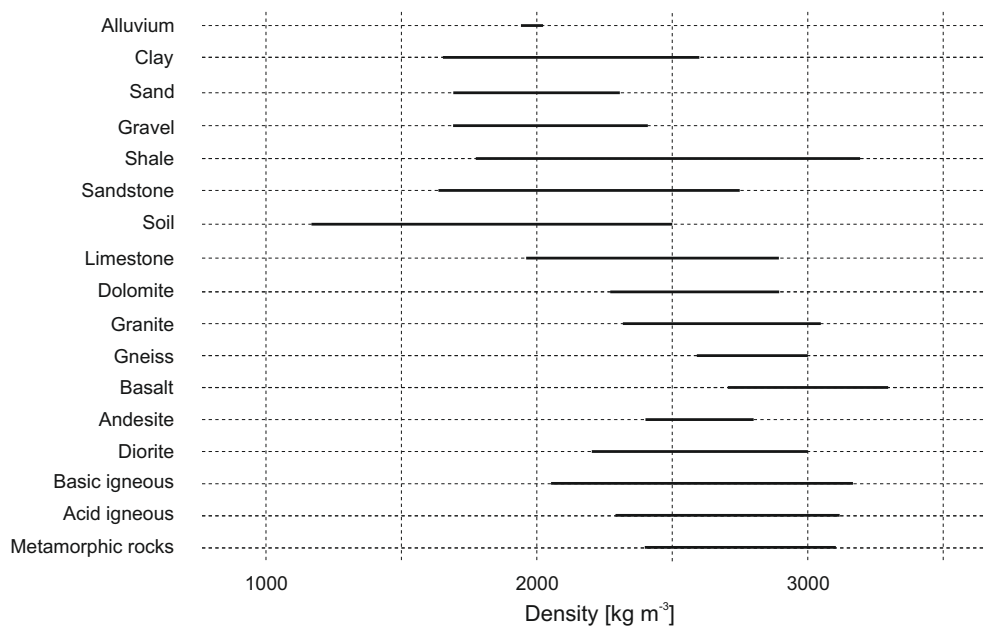


Figure 3.8.: Density ranges of selected rock formations and further earth materials. Density values adopted from Telford et al. (2012) with modifications by Lowrie (2007) and Altwegg (2015)

3.2.1. Strontium isotope analysis

In nature Sr is occurring in four stable isotopes (^{84}Sr , ^{86}Sr , ^{87}Sr , ^{88}Sr), where ^{88}Sr is the most abundant (82.58 %). In earth science the $^{87}\text{Sr}/^{86}\text{Sr}$ ratio is principally used as a measure for age determination or rock affiliation. The ratio is constantly effected by the radioactive β -decay of ^{87}Rb to ^{87}Sr . As the consequence, the $^{87}\text{Sr}/^{86}\text{Sr}$ ratio reflects the (1) decay time and/or the (2) concentrations of Rb and Sr in the original rock matrix. As Rb and Sr, part of the alkali- and alkaline-earth-metal group respectively substitute elements with similar atomic radius and identical charge in the mineral structure, K-rich rocks contain also higher Rb concentrations, while Ca-rich rocks are normally enriched in Sr (Faure & Powell, 1972). Magma fractionation, water-rock interaction processes or sedimentary processes control Rb/Sr and thus $^{87}\text{Sr}/^{86}\text{Sr}$ ratio. Typical $^{87}\text{Sr}/^{86}\text{Sr}$ ratios of different geological environments are presented in Figure 3.9 including also isotope compositions for the research area (compare chapter 8). In conclusion $^{87}\text{Sr}/^{86}\text{Sr}$ ratio can be applied for geochronology and as a geochemical tracer identifying source or genesis of the analyzed sample.

In terms of geothermal exploration Sr isotope analysis is applied to determine the reservoir rock of collected geothermal fields. During water rock interaction the $^{87}\text{Sr}/^{86}\text{Sr}$ ratio of geothermal fluids adopts the signature of the reservoir rock. As Sr is not further fractionated by hydrothermal processes, the comparison of rock and fluid signatures indicates the reservoir rock. Applications in geothermal systems are reported i.a. from Rotorua, New Zealand (Graham, 1992) and El Tatio, Chile (Cortecci et al., 2005).

3.2.2. Chlorofluorocarbon analysis

Environmental tracers are chemical and isotopic substances measured to characterize groundwater flow and genesis. Environmental tracers are radiogenetically produced or emitted in the atmosphere and entering the subsurface by precipitation. The atmospheric, initial concentration is more or less constant or has a known temporal development.

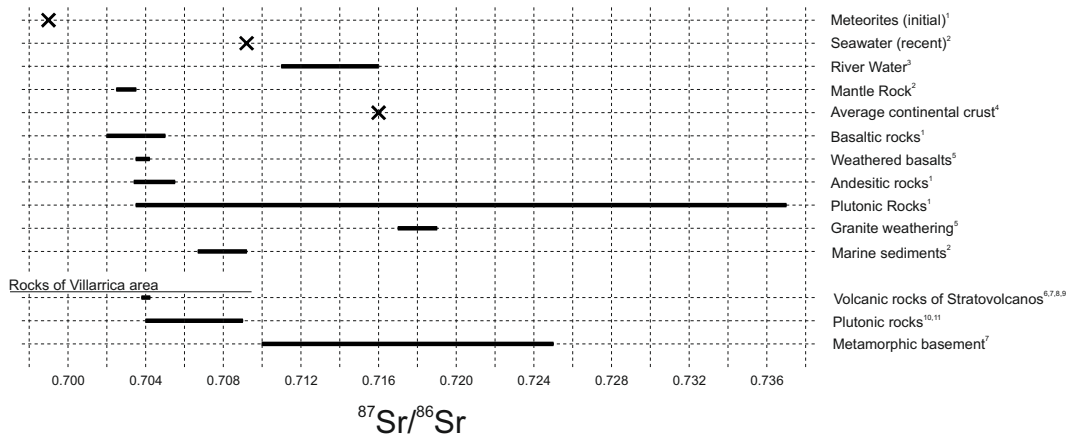


Figure 3.9.: Selection of Strontium isotope ($^{87}\text{Sr}/^{86}\text{Sr}$) composition of rocks. References: ¹Faure & Powell (1986), ²Elderfield (1986), ³Palmer & Elderfield (1985), ⁴Veizer & Compston (1974), ⁵Brass (1976), ⁶Hickey-Vargas et al. (1989), ⁷Davidson (1988), ⁸Jacques et al. (2014), ⁹McMillan et al. (1989), ¹⁰Lucassen et al. (2004), ¹¹Pankhurst et al. (1999)

Depending on its origin environmental tracers can be subdivided into anthropogenic or natural tracers. Typical environmental tracers are listed in Figure 3.10. Tracers can also be classified by processes governing subsurface tracer concentration: (1) affected by decay or fractionation in subsurface (^{39}Ar , ^{14}C , ^{36}Cl , ^3H , ^{81}Kr , ^{85}Kr , ^2H , ^{18}O); (2) non-reactive in subsurface (CFC, SF_6 , pharmaceuticals); (3) accumulation during subsurface residence (^3He , ^4He , ^{36}Cl) (Turnadge & Smerdon, 2014). From tracer investigations groundwater flow and genesis can be determined in terms of: (1) infiltration age; (2) mixing of different water bodies; (3) fractionation processes; and (4) spatial origin of fluids.

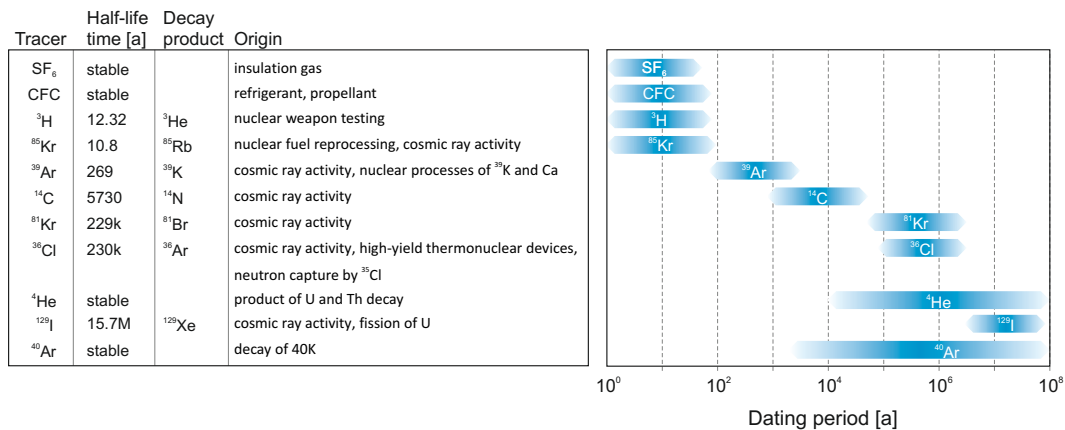


Figure 3.10.: Environmental tracers used for groundwater circulation analysis. References: Plummer & Busenberg (2006), Zhou & Ballentine (2006), Mazor & Bosch (1992), Torgersen & Clarke (1985), Loosli (1983), Fabryka-Martin et al. (1987), Collon et al. (2000), Lehmann et al. (2003), Rozanski & Florkowski (1979)

Within the geochemical exploration at Villarrica geothermal systems (see chapter 8) dilution of deep geothermal fluids by shallow, fresh groundwater is investigated. Anthropogenic tracers are selected as degree of dilution of an old, tracer-free, geothermal fluid with shallow groundwater with tracer concentrations similar to recent atmospheric concentrations could be quantified. Atmospheric tritium concentration in the southern hemisphere is low and erratic, due to the limited number of nuclear weapon tests in the southern hemisphere, and

hence groundwater dating and dilution analysis produce ambiguous results. Consequently I select chlorofluorocarbons to calculate dilution during ascent of geothermal fluids into shallow groundwater. Chlorofluorocarbons are organic compounds of carbon, chlorine and fluorine. In earth science CFC-11, CFC-12 and CFC-113 are used as anthropogenic tracers (Figure 3.11).

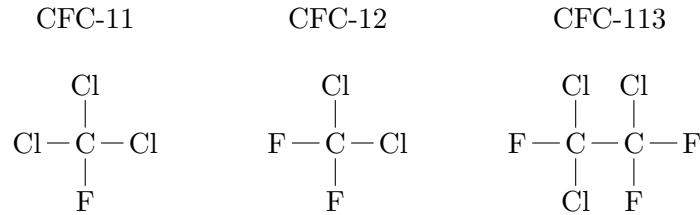


Figure 3.11.: Structural formula of chlorofluorocarbons used to investigate groundwater system

Emission of CFCs began in 1940's with the usage as refrigerants or propellants resulting in the growth of atmospheric and subsequently groundwater concentration. Pre-1940 infiltrated fluids are CFC-free. With the ban of CFCs in the 1990's atmospheric concentration starts to decline. Due to the atmospheric mean residence time between 44–180 a decline is ongoing. Because of the varying range of application each CFC species has a evolution of atmospheric concentration. Atmospheric concentrations in the southern hemisphere, averaged from Plummer & Busenberg (2006) and NOAA (2015) are presented in Figure 3.12.

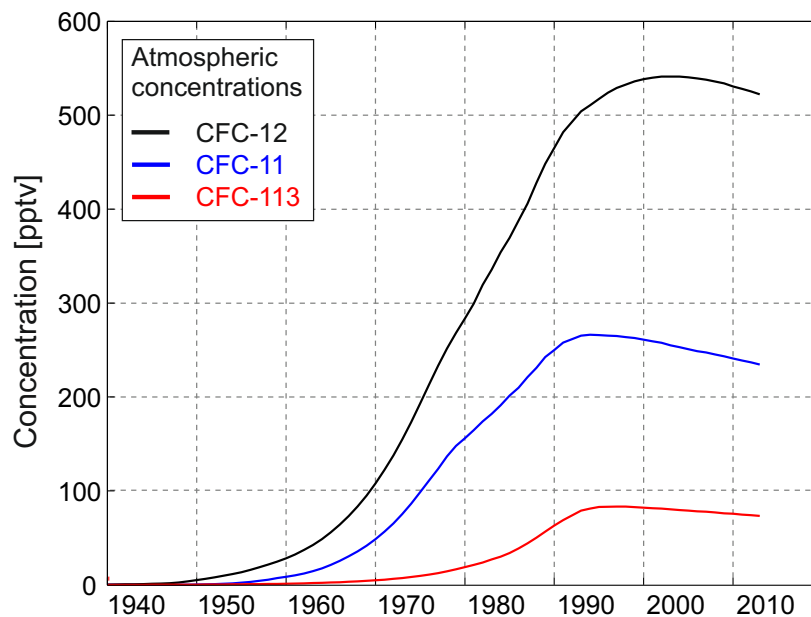


Figure 3.12.: Development of atmospheric concentration of CFC-11, CFC-12, CFC-113 in the southern hemisphere. Concentrations averaged from Plummer & Busenberg (2006) and NOAA (2015).

Age determination of geothermal fluids based on CFC concentration is a straightforward method assigning measured CFC concentrations in groundwater to atmospheric concentrations using equations given in Plummer & Busenberg (2006). The procedure assumes Piston-Flow no-mixing groundwater circulation. If estimated infiltration ages of different

CFCs vary or if dilution of the geothermal fluids is assumed, mixing of different water bodies has to be considered.

In geothermal springs measured anthropogenic tracers reflect a flux averaged mixture of different aged fluids or travel times (Gardner et al., 2011). Thus the analysis of different time-dependent CFC species enables determination of mixing ratios. Based on a known input function the concentration of time depended tracer in geothermal discharges can be calculated using equation 3.38 after Małozewski & Zuber (1982).

$$C(t_{obs}) = \int_{\infty}^0 C_{atmos}(t_{obs} - t) g(t) e^{-\lambda t} dt \quad (3.38)$$

where C_{atmos} is the atmospheric, time-dependent input function, λ the half-life of the tracers (in case of natural or radioactive decay in aqueous solution), t_{obs} the time of observation, t is the integration variable physically representing the infiltration age of each water portion and $g(t)$ is a weighting function depending on the selected mixing model. Different weighting functions, depending on selected mixing model are presented in Table 3.2

Table 3.2.: Weighting function $g(t)$ according to different mixing models (Gardner et al., 2011; Turnadge & Smerdon, 2014). τ is the mean residence time and ν is the fraction of total aquifer volume to the non-Piston Flow volume in the combined aquifer.

Mixing model	Abbreviation	Weighting function
Piston Flow	PFM	$\delta(t_{obs} - t)$
Exponential Mixing	EM	$\frac{1}{\tau} e^{-\frac{t}{\tau}}$
Linear Mixing	LM	$\frac{1}{2\tau}, t < 2\tau$ $0, t \geq 2\tau$
Exponential Piston Flow	EPM	$\frac{\eta}{\tau} e^{-\frac{\eta t}{\tau} + \eta^{-1}}, t > \tau(1 - \eta^{-1})$ $0, t \leq \tau(1 - \eta^{-1})$
Linear Piston Flow	LPM	$\frac{\eta}{2\tau}, \tau - \frac{\tau}{\eta} \leq t \leq \tau + \frac{\tau}{\eta}$ 0 for all other t

Selection of weighting function depends on assumed groundwater system. The Piston-Flow approach represents no-mixing subsurface circulation. Decline of the infiltrated CFC concentration C_{atmos} is limited to 1st order decay term. In case of CFCs decay is related to bacterial activity. Exponential mixing describes complete mixing of multiple water bodies of different travel times in a reservoir of constant thickness. The parameter mean transient time τ describes the average residence time of the different fluid bodies. The linear mixing model depicts complete mixing of multiple water bodies in a reservoir of linearly increasing thickness in the horizontal direction (Plummer & Busenberg, 2006). EPM and LPM are modification of standard cases, describing confined reservoirs. Alternatively to mixing models binary mixing (BM) between two water bodies can be used to describe geothermal groundwater flow system. BM (Eq. 3.39) is an end-member mixture between two differentially weighted water bodies (χ_1, χ_2) that possess different infiltration age and

hence different concentrations (c_{t1}, c_{t2}) resulting in observed concentration C_{obs} .

$$C_{obs} = C_{t1} \cdot \chi_1 + C_{t2} \cdot \chi_2 \quad (3.39)$$

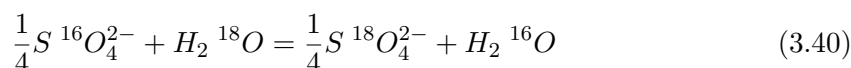
Once entered the liquid phase CFCs are temperature resistant (Tajima et al., 1996; Rittmeyer & Vehlow, 1993) and not effected by natural decay (Plummer & Busenberg, 2006) except for bacterial degradation in anoxic environment (Krone et al., 1989). Methanogenic and sulfate-reducing bacteria degrade different CFC species in anoxic environment (Lesage et al., 1992; Sonier et al., 1994) with observed half-life times in groundwater systems of <10 a (Hinsby et al., 2007). As a consequence infiltration ages are often overestimated through degraded CFC concentrations. Especially CFC-11 has increased degradation rates in anoxic environment compared to CFC-12 (Burton et al., 2002; Oster et al., 1996). In oxic environments degradation is not documented (Hinsby et al., 2007).

3.2.3. Geothermometry using the oxygen isotope fractionation of the sulfate-water system

Estimation of reservoir temperature is a crucial step during early exploration to evaluate the geothermal potential of a geothermal reservoir. Often calculated temperatures determine the continuation or abandonment of further exploration. A huge number of different geothermometer equations were developed in the last decades. Classical geothermometers calculate reservoir temperature from SiO₂ solubility (Fournier, 1977; Arnórsson, 1983; Verma, 2000), Na/K ratio (Giggenbach, 1988; Arnórsson, 2000), Mg/K ratio (Giggenbach, 1988; Fournier, 1991), Na/K/Ca (Fournier & Truesdell, 1973; Fournier, 1979) or Na/Li (Fouillac & Michard, 1981; Verma & Santoyo, 1997).

For a single geothermal spring a huge scattering in reservoir temperature can be calculated from the different classical geothermometers (Nitschke et al., 2017b). Often secondary processes such as dilution, precipitation during ascent, boiling due to pressure release or re-equilibration bias geochemical composition and thus inhibit adequate temperature estimation. Furthermore impacts of lithology on geothermometer application are not considered in geothermometer applications so far with first studies highlighting a strong impact of reservoir rock (Sanjuan et al., 2014; Nitschke et al., 2017b; Meller et al., 2017).

The oxygen exchange between sulfate species and H₂O is a temperature depended fractionation that can be used as a geothermometer (Hoering & Kennedy, 1957; Lloyd, 1968). Fractionation equilibrium for the H₂O - SO₄²⁻ system could be expressed according to equation 3.40.



Fractionation of $\delta^{18}O$ between water and sulfate is a very slow process at moderate temperatures. At earth surface conditions equilibrium is reached after 10⁵ a (Lloyd, 1968; Zhonghe, 2001). The kinetics of fractionation follow a first order process (Chiba & Sakai, 1985) and are accelerated by increased temperatures and decreases pH values (Hoering & Kennedy, 1957; Lloyd, 1968). At geothermal reservoir conditions (T>100 °C) and near neutral pH equilibrium is achieved rapidly, e.g. 99.9% isotopic exchange requires 18 a at 200 °C (McKenzie & Truesdell, 1977).

Chiba & Sakai (1985) recognize that the different sulfate species (SO₄²⁻, HSO₄⁻, H₂SO₄) affect the fractionation and thus the estimated reservoir temperatures. Dominant species depend on pH and redox conditions (Boschetti, 2013). In general for medium enthalpy

systems $<200^\circ\text{C}$ and $\text{pH}>5$ SO_4^{2-} is the dominant species, whereas in high enthalpy systems ($>250^\circ\text{C}$) in dependence of pH SO_4^{2-} ($\text{pH}>7$) or HSO_4^- ($\text{pH}<7$) prevail. As a consequence different geothermometer equations were established valid for different temperature ranges and sulfate species. Seal et al. (2000) combined existing data (Lloyd, 1968; Mizutani & Rafter, 1969) to create an equation for HSO_4^- at temperatures between $70\text{--}350^\circ\text{C}$. Halas & Pluta (2000) and Zeebe (2010) develop an equation to be used in medium enthalpy reservoirs considering SO_4^{2-} as dominate species. According to a recommendation of Sakai (1977) for evaluation of neutral to alkaline high-enthalpy geothermal systems the equation of Kusakabe & Robinson (1977) should be used.

Table 3.3.: Geothermometer equations for the oxygen isotope fractionation of the sulfate-water system

Author	Species	Temp. range	Equation
Seal et al. (2000)	HSO_4^-	$70\text{--}350^\circ\text{C}$	$10^3 \ln \alpha = \frac{3.26 \cdot 10^6}{T^2} - 5.81$
Halas & Pluta (2000)	SO_4^{2-}	$0\text{--}150^\circ\text{C}$	$10^3 \ln \alpha = \frac{2.41 \cdot 10^6}{T^2} - 5.77$
Zeebe (2010)	SO_4^{2-}	$0\text{--}150^\circ\text{C}$	$10^3 \ln \alpha = \frac{2.68 \cdot 10^6}{T^2} - 7.45$
Kusakabe & Robinson (1977)	BaSO_4	$110\text{--}350^\circ\text{C}$	$10^3 \ln \alpha = \frac{3.01 \cdot 10^6}{T^2} - 7.30$

Fractionation factor α can be calculated from equation 3.41. In the displayed case SO_4^{2-} is used.

$$\alpha(\text{SO}_4^{2-} - \text{H}_2\text{O}) = \frac{10^3 + \delta^{18}\text{O}(\text{SO}_4^{2-})}{10^3 + \delta^{18}\text{O}(\text{H}_2\text{O})} \quad (3.41)$$

Temperature-dependend kinetics are a strong advantage of this geothermometer as equilibrium is adjusted fast inside the reservoir whereas lower temperature during the ascent re-equilibration is hindered kinetically. The geothermometer works over wide temperature ranges (Table 3.3) and is less vulnerable to shallow dilution assuming low sulfate concentration of shallow groundwaters.

Limitations for the applications are given by the presence of sulfate bearing rocks (Cortecci, 1974), the oxidation of primary or secondary H_2S , or the modification of $\delta^{18}\text{O}$ by subsurface processes. Interaction with sulfate bearing rocks and, hence, dissolution of SO_4 modifies the $\delta^{18}\text{O}$ signature of the sulfate facies by adding a non temperature fractionated portion. The same accounts for the addition of SO_4 originating from the oxidation of H_2S , created through bacterial reduction of sulfate in anoxic environments (Lloyd, 1968). $\delta^{18}\text{O}$ signature of the H_2O can be affected by reservoir processes, modifying isotope signatures. E.g. the steam separation due to pressure release during ascent fractionates $\delta^{18}\text{O}$ and δD disguising also temperature fractionated $\delta^{18}\text{O}$ signature (McKenzie & Truesdell, 1977).

4. Geological and Tectonic Settings Preventing High-Temperature Geothermal Reservoir Development at Mt. Villarrica (Southern Volcanic Zone): Clay Mineralogy and Sulfate-Isotope Geothermometry

This manuscript has been published in *Proceedings World Geothermal Congress 2015*

SEBASTIAN HELD, EVA SCHILL, PABLO SÁNCHEZ, THOMAS NEUMANN, KATJA EMERICH, DIEGO MORATA and THOMAS KOHL [2015]: Geological and Tectonic Settings Preventing High-Temperature Geothermal Reservoir Development at Mt. Villarrica (Southern Volcanic Zone): Clay Mineralogy and Sulfate-Isotope Geothermometry; *Proceedings World Geothermal Congress 2015*, Melbourne, Australia, 19-25 April

Abstract

In the vicinity of the volcano Villarrica (South-Central Chile), geothermal manifestations at the surface are evident revealing low-enthalpy geothermal processes in the subsurface. The structural geology of the area, postulated by Sánchez et al. (2013), set up a first draft of a structural model but also naming the complexity of the structural geology in the area generated by the interaction of two major fault systems and a change in basement geology. In the first phase of the actual research project, geochemical methods are used to characterize the geothermal system. Besides standard geochemical techniques, clay mineralogy and $\delta^{18}\text{O}(\text{SO}_4)/\delta^{18}\text{O}(\text{H}_2\text{O})$ isotopes are used to determine the characteristics of the geothermal reservoir. The results of these techniques, pointing at a low-enthalpy reservoir in the vicinity of the active Villarrica volcano, are discussed in context of the special tectonic characteristics in the investigation area.

4.1. Introduction

Worldwide geothermal resources are classified according to their temperature into low temperature (100–150 °C) to ultra-high temperature (>300 °C) by [Sanyal \(2005\)](#). Volcanic regions are typically characterized by high temperature resources, where different volcanic rocks, such as rhyolitic and ignimbritic reservoir rocks in Taupo Volcanic Zone, New Zealand (e.g. [Graham, 1992](#); [Wood, 1992](#)) or volcanoclastic sediments in Miravalles Geothermal Field, Costa Rica ([Mainieri et al., 1985](#)), share high productivity originating from primary or secondary fluid permeability. Exploration of high-temperature systems focuses mainly on determining the cap rock, which seal the systems and prevents geothermal fluid from escaping ([Ussher et al., 2000](#)) to guarantee adequate mass flow ([Barbier, 2002](#)). Sufficient water recharge is essential for sustainable exploitation ([Barbier, 2002](#); [Ellis & Mahon, 1977](#)).

In Chile, the subduction of the Nazca Plate underneath the South American plate yields a volcanic arc ([Angermann et al., 1999](#); [Norabuena, 1998](#)) including more than 100 volcanos between 17°S and 54°S (e.g. [Stern, 2004](#)). This volcanic chain is interrupted by a volcanic gap between 28°S and 33°S, which is attributed to the Pampean Flat Slab Segment ([Barazangi & Isacks, 1976](#)). The Chilean chain can be subdivided into the Central (CVZ, 17-28°S), Southern (SVZ, 33-46°S), and the Austral Volcanic Zones (49-54°S) ([Stern, 2004](#)). To the north, the SVZ is limited by the flat slab and to the south it extends to the triple junction between the Nazca, South American, and the Antarctic plates. Recent subduction is slightly oblique to the trench with an angle of N78°E ([Somoza, 1998](#)) resulting in a NE-SW maximal horizontal stress in the main cordillera since the Pliocene ([Lavenu & Cembrano, 1999](#); [Nakamura, 1977](#)). The N-S to NNE-SSW aligned SVZ includes major stratovolcanoes and minor eruptive centers on top of a crust with decreasing thickness from north to south ([Hildreth & Moorbath, 1988](#); [Tassara & Yáñez, 2003](#)). The tectonic environment controls the localization of volcanic edifices to a large extent ([Cembrano & Lara, 2009](#)). Associated with this volcanism, high-temperature hot springs, fumaroles, and surface hydrothermal alteration products are often found in the vicinity of suspected or identified high-temperature geothermal reservoirs ([Hauser, 1997](#); [Tassi et al., 2010](#)). Examples for geothermal exploration in the SVZ are Planchón-Peteroa and Descabezado Grande ([Benavente & Gutierrez, 2011](#)), Sierra Nevada ([Muñoz et al., 2011](#)), Mariposa ([Hickson et al., 2011](#)) and Tinguiririca ([Clavero et al., 2011](#)). All these geothermal fields are located between 33°S and 39°S, where the Eocene-Miocene volcano-sedimentary Cura-Mallín Formation occurs underlying the recent volcanoes ([Charrier et al., 2007](#); [Jordan et al., 2001](#); [Radic, 2010](#)). The volcano-sedimentary Cura-Mallín Formation was deposited under non-marine conditions in basin environments ([Radic, 2010](#)). Two subunits are differentiated: (1) the Guapitrío Formation, a volcanic unit with minor sedimentary deposits, and (2) the Río Pedregoso Unit, a mainly sedimentary association with minor volcanic intercalations ([Suarez & Emparan, 1995](#)). Terrestrial sediments were deposited within extensional basins intercalated with lavas and volcanoclastic rocks ([Radic, 2010](#); [Suarez & Emparan, 1995](#)).

The first Chilean geothermal power plant in the SVZ is currently built in the vicinity of the Tolhuaca volcano¹ exploiting a high-enthalpy reservoir hosted in Cura-Mallín basement rocks and revealing the typical features such as fumaroles, steam-heated springs with temperatures between 20–60 °C and hydrothermal alteration products such as clay minerals and silica sinters ([Melosh et al., 2012](#)). About 200 km to the south of Tolhuaca, at Mt. Villarrica, the processes active in the subsurface do not favor the formation of such a

¹Status July 2017: Project abandoned

high-temperature reservoir even though a magma chamber is present at shallow depth (Hickey-Vargas et al., 1989).

Within this study, we will highlight the differences between high- and low-temperature reservoirs in Sierra Nevada (El Toro side) and Villarrica and discuss the tectonic situations that may be responsible for the absence of a high-enthalpy geothermal reservoir in the vicinity of one of the most active volcanoes of Chile (Ortiz, 2003). In this respect, we have analyzed clay minerals sampled from the surroundings of thermal springs in order to determine the formation of hydrothermal alteration products. We furthermore calculated reservoir temperatures from those springs to exclude the occurrence of hidden high-enthalpy reservoirs as far as possible

4.2. Geological setting

The geological setting of the Mt. Villarrica area is characterized by three major structural elements of regional significance, the Liquiñe-Ofqui Fault Zone (LOFZ), the Villarrica-Quetrupillán-Lanín lineament, and the change in basement rock (Figure 4.1). Starting in the vicinity of the triple junction, the LOFZ extends over 1200 km parallel to the volcanic arc (Adriasola et al., 2005; Rosenau et al., 2006) and is associated with dextral strike-slip/dip-slip structures (Cembrano et al., 1996). The LOFZ controls the Cenozoic emplacement of the North Patagonian Batholith (NPB) between 39°S and 47°S, which is interpreted as the root of the volcanic arc (Hervé, 1984; Munizaga et al., 1988; Pankhurst et al., 1999). Granodiorites and tonalites of Cretaceous to Miocene age dominate the complex lithology of the NPB (Hervé, 1994; Pankhurst et al., 1999). Besides N-S- to NNE-SSW-aligned faults belonging to LOFZ, subsidiary NE and NW faults are also common in the SVZ. NE aligned fault zones are considered as tension fractures often related to more mafic volcanism (Cembrano & Lara, 2009). NW-trending fault zones, such as the volcanic chain of Villarrica-Quetrupillán-Lanín, are interpreted as pre-Andean deep-seated fault zones created during Triassic-Jurassic break-up of Gondwana (Rapela & Pankhurst, 1992). Volcanism related to these show a great variety of locally more evolved magmas (Cembrano & Lara, 2009). The research area, located in the vicinity of the Villarrica volcano, is affected by the above described tectonic features. The LOFZ crosscut the area and is displaced by the NW-SE-aligned volcanic lineament (see Figure 4.1) probably running from Argentina to the Pacific coast (Lara et al., 2004). The NPB, occurring extensively south of the volcanic chain, crops out only occasionally as magmatic bodies intruded into or acting as basement of the Cura-Mallín Formation north of the Villarrica volcano. In Chile, the southern expansion of Cura-Mallín basins, characterized as intra-arc basins (Radic, 2010) and sometimes even as pull-apart basins (Hervé, 1994), is described only down to 39°S (Radic, 2010). The southern continuation is documented at the eastern slope of the Main Cordillera (Ramos et al., 2014) in Argentina. Gravity data published by Ramos et al. (2014) show an almost continuous gravity low between 37° and 41°S with a negative gravity signature between the Caburgua and Pucón lakes, indicating the occurrence of sedimentary basin structures. Cenozoic volcano-sedimentary Cura-Mallín units occur widespread north of the volcanic chain (see Figure 4.1) correlating with gravity anomalies but are almost completely abundant south of it.

In the vicinity of the Villarrica volcano, a limited number of thermal springs occur in direct association with fault zones (see Tab. 4.1). These are generally of low mineralization (Lara et al., 2004; Sánchez et al., 2013). To the south of the volcano, the hot springs trace the distinct run of the LOFZ. In contrast, thermal springs to the north of the Villarrica-Quetripillán-Lanín volcanic chain are distributed over an extended area. A high number of faults, with varying orientation, crosscut the northern part often with hot springs discharging at miscellaneous oriented faults mostly between batholithic rocks and Cenozoic basin deposits (Moreno & Lara, 2008). Studies of geothermal fluids from the Villarrica area indicate reservoir temperatures of 120–160 °C (Sánchez et al., 2013). Typical volcanic features, such as fumaroles and high-temperature springs, do not occur at the Villarrica volcano.

4.3. Methods and sampling procedure

10 fluid samples from single thermal springs were sampled to the north and south of the Villarrica-Quetripillán-Lanín lineament for chemical analysis. For comparison with a site characterized by high-enthalpy reservoir features, El Toro, a sub-boiling spring with steam-heated groundwater and fumarolic activity located on the flank of Sierra Nevada volcano was chosen (Figure 4.1). Sampling locations of the El Toro hot springs on the flank of Sierra Nevada is shown in Figure 4.2. It should be noted that the full fluid chemical analyses including major and trace elements, O/H isotopic, Strontium isotopic, and chlorofluorocarbon analyses will be presented in a forthcoming paper. Furthermore, clays occurring in the vicinity of two springs were analyzed for high-temperature alteration products linked to possible cap layer formation. We would like to point out that except from Coñaripe site (Figure 4.2), no clay minerals were found in the outcrops near to the springs in the Villarrica area. Locations of the sampled hot springs are shown in Figure 4.1. Most of the samples were collected from the Villarrica area.

Reservoir temperatures, inferred from cation geothermometers for Villarrica sources (Sánchez et al., 2013) are significantly lower than 200 °C. As cation geothermometers are vulnerable for dilution by meteoric water or kinematic effects during ascent, in this study, we applied sulfate-isotope geothermometry. The related temperature-dependent oxygen fractionation between water and sulfate species was first described by Hoering & Kennedy (1957), Mizutani & Rafter (1969), and Lloyd (1968). Besides the reduced vulnerability to dilution, its advantage over cation geothermometers is the slow reaction rate at lower temperatures, i.e. during ascent, resulting in fluids representing the fractionation in the deep reservoir (Chiba & Sakai, 1985). The dominant sulfate species at reservoir conditions is governing the fractionation (Sakai, 1977; Chiba & Sakai, 1985; Zeebe, 2010; Boschetti, 2013) and therefore, also the temperature estimate. After Boschetti (2013), at lower temperatures and near neutral pH, SO_4^{2-} is the dominate species resulting in the application of the formulas indicated below in Table 4.1. For the measurements sulfate was precipitated completely with stoichiometric abundant BaCl_2 . Measurements of $\delta^{18}\text{O}$ were done by isotope-ratio mass spectrometry (IRMS) using a GV Instruments IsoPrime combined with a HTO Pyrolysis from HEKAtech.

To determine the clay mineralogy, samples were grinded to grain size of up to 500 μm with an agate mill and subsequently homogenized. Simultaneous Thermal Analysis (STA) was conducted using a STA 449 C Jupiter from Netzsch connected to a quadrupole mass spectrometer (QMS 403 C, Aeolos, Netzsch). The STA was run between 35 and 1100 °C with a heating

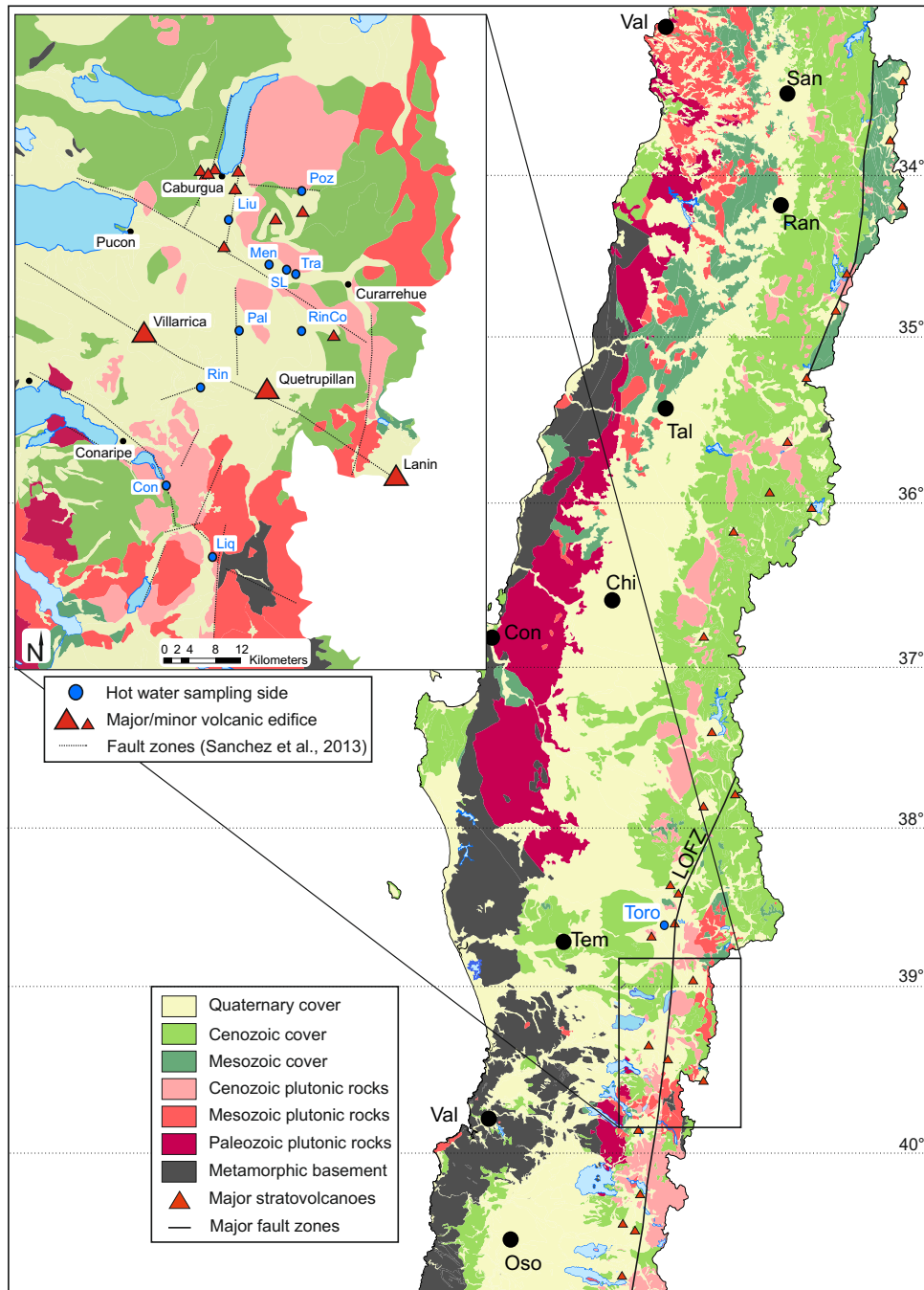


Figure 4.1.: Locations of fluid and clay sampling in the Villarrica and the Sierra Nevada area. The map is modified after Sánchez et al. (2013), Cembrano & Lara (2009), and 1:1'000'000 scale map of Servicio Nacional de Geología y Minería (SERNAGEOMIN) of Chile

rate of per – mode = symbol10 K min⁻¹. 50 mg sample material were used in a Pt/Rh crucible under a synthetic air/nitrogen atmosphere (50 + per – mode = symbol20 mL min⁻¹). Powder X-Ray Diffraction (XRD) measurements were done using a Siemens D5000 diffractometer with CuK α radiation. For bulk powder samples the diffractometer varied the 2θ angle between 5 and 80° with a step size of 0.02° and a step time of 3 s, whereas the texture samples are measured with an angle between 2 and 35°. Oriented samples were prepared by mixing the sample material with deionized water and pipetted onto a glass slide after ultrasonic treatment. After drying the textured sample were measured starting

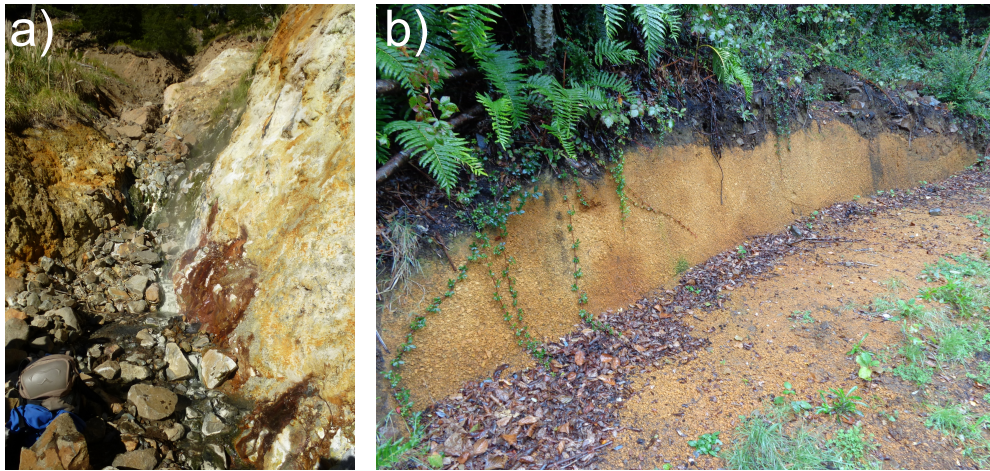


Figure 4.2.: a) Sampling location at the El Toro side (Sierra Nevada). In the red and grey parts are sub-boiling springs with 95 °C and fumarolic activity. b) Clay mineral outcrop in the vicinity of the Coñaripe hot spring. The spring is located four meters to the left of the outcrop, with the outcrop continuing until the spring.

with an untreated texture sample. Afterwards measurements were continued firstly adding ethylene glycol and afterwards heated up to 375° and 550°C. Settings at the Siemens D5000 diffractometer do not change. Additional Cation Exchange Capacity (CEC) and X-ray Fluorescence (XRF) measurements were conducted to evaluate XRD and STA-MS results but are not presented here. This will be included in a forthcoming paper.

4.4. Results

Results of STA-MS (Figure 4.3) show significant difference between the clays sampled near the El Toro and Coñaripe hot springs. High amounts of swelling 3-layer clay minerals indicated by an endothermic peak in DSC between 123–157 °C and the appearance of sulfides, probably pyrite, indicated by an exothermic peak in DSC at 441° and 476 °C with corresponding SO₂ peaks in the mass spectrometry, underline the secondary hydrothermal alteration at a high-enthalpy reservoir at El Toro. Further sulfate phases are also detected in the SO₂-MS curve for the El Toro sample. In contrast, Coñaripe samples reveal no indication for hydrothermal alteration minerals. Endothermic peaks in DSC and mass spectrometry rather indicate crystal water. These observations are confirmed by powder XRD analysis (Figure 4.4a). The sample only consists of silica and feldspars. The high noise ration points at amorphous material. In contrast, the powder XRD analysis of El Toro sample (Figure 4.4b) reveals a much more differentiated mineralogy of the sample. High amount of clay fraction ($d(001) > 10 \text{ \AA}$) accompanied by feldspars, quartz, sulfides, Gypsum, and probably talc and/or a second sulfate (e.g. Basaluminite) are evident. XRD-texture analyses indicate smectite as the major clay mineral fraction by $d(001) = 15.4 \text{ \AA}$ in the untreated sample (black curve, Figure 4.4c) shifted to 17 Å in sample treated with ethylene glycol (red curve, Figure 4.4c). Texture preparation confirms the appearance of minor amount of sulfides and sulfates. In conclusion, clay mineralogical analyses indicate secondary hydrothermally formed clay minerals at El Toro hinting at high-temperature processes, whereas the samples from the Coñaripe hot springs where probably formed by low-temperature weathering.

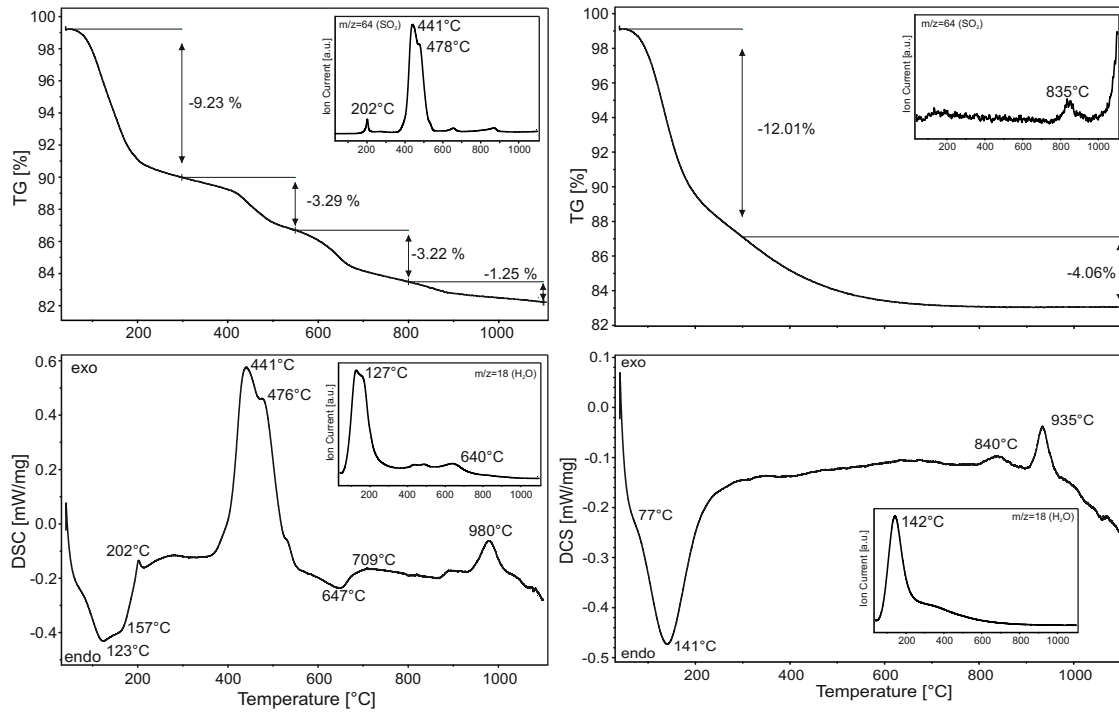


Figure 4.3.: Results from STA-MS analyses of El Toro sample (left) and Coñaripe sample (right). TG = Thermo Gravimetry, DSC= Differential Scanning Calorimetry

Since clay mineralogy points to high-temperature alteration typical for a cap layer at El Toro site and respective reservoir conditions are exploited there, it is considered as a representative example for high-enthalpy conditions in our study. Sulfate isotope geothermometer for the El Toro site reveals reservoir temperatures of $>300^{\circ}\text{C}$. It should be noted that in contrast to Villarrica area, at El Toro H_2SO_4 acts as the dominant species. Therefore, calculations after Seal et al. (2000) or Mizutani & Rafter (1969) have to be used, assuming that the origin of the hot fluid is the reservoir and not steam-heated groundwater. Sulfate-isotope geothermometry of the sampled springs in the Villarrica area reveals temperatures ranging from 83°C in Liquiñe to 134°C in Coñaripe (see Table 4.1). While cation geothermometers reveal a significantly higher reservoir temperature of $110\text{--}150^{\circ}\text{C}$ for Liquiñe, the reservoir temperature of Coñaripe is within the range of the cation thermometers (see Sánchez et al., 2013, for cation geothermometer data). It should be mentioned here, that we were not allowed to sample the Geometricas springs, which has the highest cation temperatures of $140\text{--}180^{\circ}\text{C}$ (Sánchez et al., 2013). In terms of reservoir temperature no significant differences can be observed between the area north and south of the Villarrica-Quetrupillán-Lanín volcanic chain (different grey shading in Table 4.1). The mean temperature obtained from sulfate-isotope geothermometry in the Villarrica area differs strongly from the high reservoir temperature at the El Toro side.

4.5. Discussion

Based on the presented clay mineralogy at Coñaripe, n.b. the spring with the highest reservoir temperature in the Villarrica area (except from Geometricas), the results do not indicate an outcropping cap layer, formed by hydrothermal alteration trough ascending thermal fluids, as often found in high-enthalpy geothermal fields. In addition, there are no hidden high-enthalpy reservoirs indicated by the sulfate-isotope geothermometry in the Villarrica area. In contrast geothermometry at El Toro combined with the appearing cap

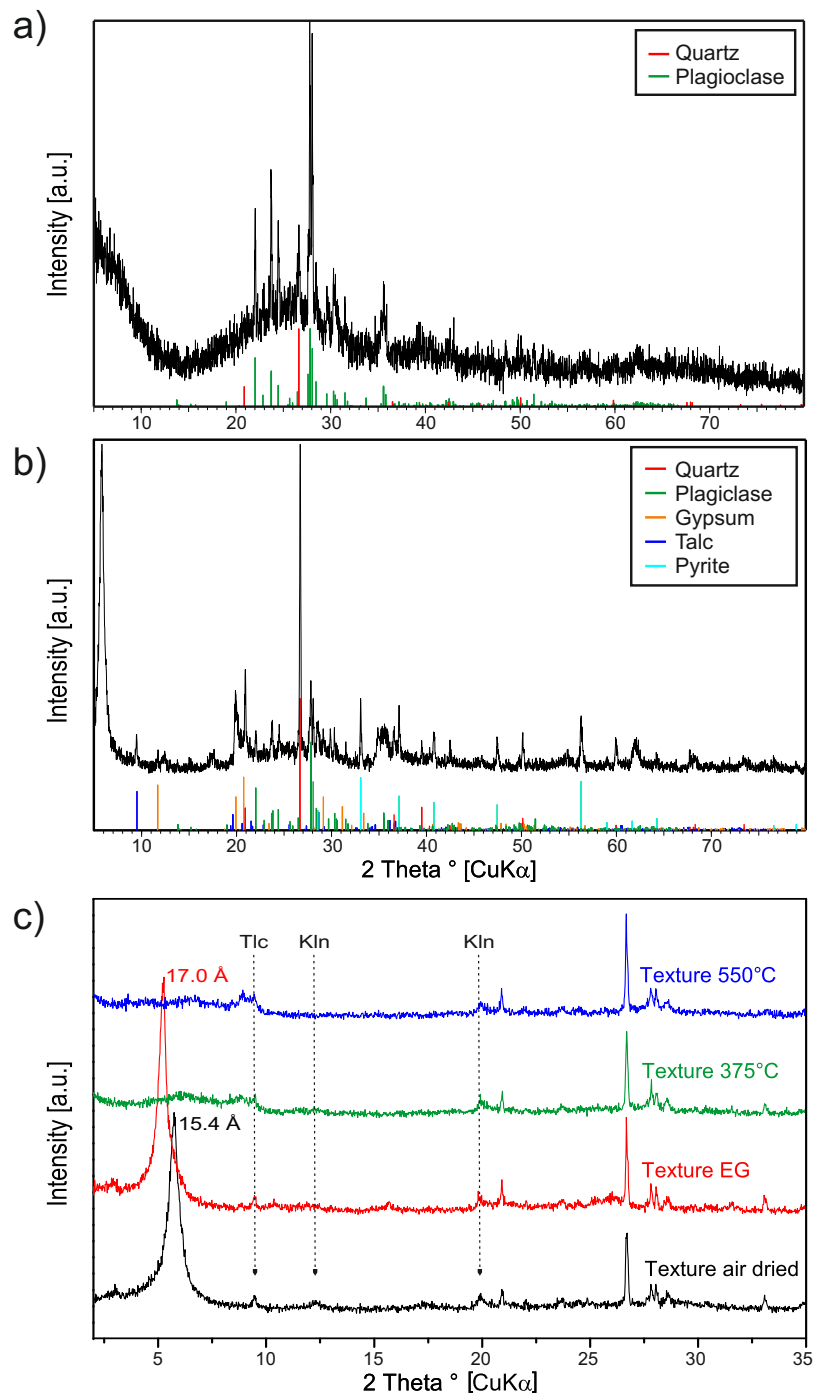


Figure 4.4.: XRD analyses on powder of Coñaripe (top), on powder of El Toro (middle), and texture analysis of El Toro (bottom). Abbreviations: Pyp = Pyrophyllite, Kln = Kaolinite

layer, formed by hydrothermal alteration products, points at an existing high-enthalpy reservoir feeding the hot springs.

Although all sampled springs are located in the vicinity of active volcanoes, it's obvious, that the results indicate different reservoir conditions, over both Villarrica and Sierra Nevada (El Toro) sites. At Mt. Villarrica, even though Hickey-Vargas et al. (1989) has proved the evidence of a shallow magmatic chamber, our results clearly indicate a more Alpine-type, low temperature geothermal system in contrast to the system at Sierra Nevada. Both

Table 4.1.: Results from geothermometry using $\delta^{18}\text{O}$ isotopes at SO_4 and H_2O of the Villarrica area. Light grey shaded area indicates springs located to the south of the Villarrica-Quetrupillán-Lanín volcanic chain; dark grey shaded indicates springs located north of this chain. Equations used are described in Halas & Pluta (2000) and Zeebe (2010)

Sample	$\delta^{18}\text{O} [\text{SO}_4]$ [‰]	$\delta^{18}\text{O} [\text{H}_2\text{O}]$ [‰]	Calc. Temperatures	Calc. Temperatures
			after Halas & Pluta (2000)	after Zeebe (2010)
			[°C]	[°C]
Rincon	0.33	-9.74	116	117
Liquine	3.78	-9.41	83	87
Coñaripe	0.63	-8.09	134	134
Trancura	0.14	-9.24	125	125
San Luis	0.04	-9.28	126	126
Palguin	0.74	-9.83	110	112
Los Pozones	0.68	-10.2	123	123
Liucura	2.55	-9.07	99	101
Rinconanda	0.56	-11.1	98	101
Menetue	1.55	-9.04	110	112
El Toro	-3.78	-7.14	322*	347**

* calculated after Seal et al. (2000), ** calculated after Mizutani & Rafter (1969)

systems share similar tectonic characteristics (see Table 4.2), which, nevertheless, provoke completely different settings from a geothermal point of view. Structural parameters, which govern the development of geothermal reservoirs in the SVZ, and their impact to the reservoir evolution, have to be investigated systematically using a wide range of different techniques.

In the following section, we will review the geological and structural characteristics of the two areas with respect to the observed geothermal features that affect the reservoir development. As mentioned above, the important tectonic features are:

- LOFZ: The N-S- to NNE-SSW-aligned intra-arc fault zone is the dominant feature in the southern SVZ. The locations of the large number of monogenetic cones and even stratovolcanoes are controlled by this dextral strike-slip fault zone. Interaction with the pre-Andean basement faults can result in horizontal displacement (Hackney et al., 2006) with implications for fluid-flow, sedimentary deposition, and fault behavior. Further north in the vicinity of Sierra Nevada and Tolhuaca volcanoes, the LOFZ bends to a NE-trending lineament, splits in several separate faults and finally fans out next to the Copahue-Callaqui ENE-aligned lineament continuing in the Antinir-Copahue fault zone (Folguera et al., 2004; Potent, 2003).
- NW-SE- or NE-SW-aligned faults: Appearance of the pre-Andean (Triassic-Jurassic) NW-aligned basement fault zones and NE-aligned extensional faults is linked strongly to the evolution of major stratovolcanoes, tectonically affecting magma chemistry due to the orientation of these fault zones (Cembrano & Lara, 2009). Fast magma ascent is simplified on NE-trending extensional fault zones, also favoring vertical fluid flow in extensional fault zones. However, NW-aligned fault zones under compressional/transpressional tectonic stress hinder direct magma ascent often resulting in formation of more evolved magmas (Cembrano & Lara, 2009). Vertical fluid flow is also prevented on NW-oriented faults.
- Basement: Basement rocks consist of granitoids of the NPB or the volcano-sedimentary Cura-Mallín Formation, which is deposited in extensional Eocene-Miocene basins.

Basin evolution is probably limited by pre-Andean fault zones acting as margin faults (Folguera et al., 2004; Jordan et al., 2001) with effects on sedimentary development in the direct vicinity of these basement faults. Furthermore, LOFZ lineament has been affected by basement geology with a more distinct run, where it passes the NPB and diversification of the alignment, as it enters areas affected by basin sedimentation. Finally, facial differentiation of the Cura-Mallín Formation (see Geological Setting section) into a more volcanic (Guapitrío Formation) and sedimentary (Río Pedregoso) subunit can also affect the evolution of geothermal reservoirs

Analyzing the appearance of these features in selected geothermal exploration areas (see Table 4.2), no tectonic feature by itself is responsible for the formation of high-enthalpy reservoirs in the SVZ. Also, combination of different tectonic features cannot explain the appearance of an exploitable resource, because every location is characterized by a variety of significantly different features. For example, basement rocks of Cura-Mallín Formation and granitoids of NPB are present at all locations. A direct link between one basement rock and the formation of high-enthalpy reservoirs cannot be established. The other features show similar ambiguity highlighting the complexity of the geothermal systems in the SVZ. As a result it becomes obvious that the explanation of the evolution of a high-enthalpy reservoir has to be made on a more local level considering the regional distribution of the tectonic features.

Table 4.2.: Tectonic features of the geothermal exploration areas

	LOFZ	NW / NE aligned secondary faults	Basement
Villarrica	N-S aligned, displaced by NW-aligned pre-Andean fault zone	NW-aligned pre-Andean fault zone with sinistral transpression + NE-aligned fault vents on Villarrica NE-shoulder	NPB, Cura-Mallín starting to the north
Sierra Nevada	NNE-NE-aligned	ENE-aligned fault with sinistral strike-slip movement	NPB, Cura-Mallín probably Guapitrío unit
Tolhuaca	NNE between Tolhuaca and Lonquimay volcano	Lonquimay and Tolhuaca volcanoes as well as fumaroles and hot springs on NW shoulder of Tolhuaca volcano aligned on NW lineament	Cura-Mallín probably Guapitrío unit, partly NPB
Mariposa	Not present	ENE-aligned fault zones in the transition from NSVZ to TSVZ interpreted sometimes as part of a graben system	Cura-Mallín and Granitoids

4.6. Outlook

On-going geochemical and geophysical measurements will be used to better constrain the reservoir conditions at Mt. Villarrica. Preliminary results from Strontium isotopes indicate two different geothermal systems to the north and south of the Villarrica-Quetripillán-Lanín volcanic chain. To exclude the dilution as process causing the low estimates of geothermometry, chlorofluorocarbon (CFC) analyses were conducted to determine the amount of dilution of the reservoir fluid by meteoric water. Finally, geochemical alteration experiments, matching the sampled thermal fluids with artificially altered water in equilibrium with possible reservoir rocks, should finally evaluate the hypothesis.

Besides, geochemical investigations extensive geophysical surveys were/will be conducted. Gravimetric measurements should determine the extent and thickness of the volcano-sedimentary basin, whereas magnetotelluric investigations should detect fluid flow paths in the subsurface. The local investigations should allow the characterization of the geothermal evolution at Villarrica. Tectonic features hindering the formation of a high-enthalpy reservoir should be determined after intense investigations. Following these, results will be compared to other geothermal exploration areas to validate the hypothesis.

Acknowledgements

The work presented was funded by the German Federal Ministry of Education and Research (BMBF) under the funding number 01DN12126 and is a contribution to the CONICYT-International Relationships Department-Scientific International Cooperation Program-Exchange Project #PCCI130025. This publication benefits from the HGF portfolio project “Geoenergy”. We like to thank Annett Steudel (KIT) for support with clay minerals identification measurements.

5. Resistivity distribution from mid-crustal conductor to near-surface across the 1200 km long Liquiñe-Ofqui Fault System, Southern Chile

This manuscript has been published in *Geophysical Journal International*

SEBASTIAN HELD, EVA SCHILL, MAXIMILIANO PAVEZ, DANIEL DÍAZ, GERARD MUÑOZ, DIEGO MORATA and THOMAS KOHL [2016]: Resistivity distribution from mid-crustal conductor to near-surface across the 1200 km long Liquiñe-Ofqui Fault System, Southern Chile; *Geophysical Journal International* (2017), 1387-1400

Abstract

Mid-crustal conductors are a common phenomenon in magnetotelluric studies. In the Andean Cordillera of southern Chile, they appear to concentrate along major fault zones. A high resolution, broad-band magnetotelluric survey including 31 stations has been carried out along two profiles perpendicular to (1) the Liquiñe-Ofqui Fault Systems (LOFS) and (2) the Villarrica-Quetrupillán-Lanín volcanic lineament running parallel to the Mocha-Villarrica Fault Zone (MVFZ). The survey aimed at tracing one of the known conductors from mid-crustal depth to near-surface along these faults. Directionality and dimensionality were analysed using tensor decomposition. Phase tensors and induction arrows reveal two major geoelectric strike directions following the strike of LOFS and MVFZ. 2-D inversion shows low resistivity zones along both fault systems down to a depth of >10 km, where the brittle-ductile transition is expected. Along the LOFS, the two anomalies are linked to (1) Lake Caburgua, where the LOFS broadens to about 2 km of lateral extension and seems to represent a pull-apart structure, and (2) the intersection with the Villarrica-Quetrupillán-Lanín volcanic lineament, where seismic activity was observed during the latest eruption in March 2015. A connection of the mid-crustal conductor to the ESE-WNW-striking fault zones is indicated from the presented data.

5.1. Introduction

Geodynamic processes on different scales such as deformation along major fault zones, formation of major geothermal fields or deposition of ore minerals in faults are connected to thermal fluids in the Earth's crust and often characterized by high electrical conductivity zones. While thermal conductivity structures revealed by abnormal heat flow pattern are limited to small variations (e.g. Kohl & Rybach, 1996), the dynamics of electric resistivity, covering several orders of magnitudes compared to typical crustal rock, characterize mid-crustal conductors (e.g. Unsworth, 2004; Hill et al., 2009; Wannamaker et al., 2014). The origin of these electric conductors has early been attributed to graphite (Frost et al., 1989; Jödicke, 1992). More recently, links to aqueous fluids and secondary minerals in fault zones (Korja et al., 2008; Brasse et al., 2009; Weckmann et al., 2012), to partial melt (Unsworth et al., 2005; Hill et al., 2009), and to metamorphic processes (Wannamaker et al., 2014; Zhang et al., 2015) have been discussed.

Worldwide, it is observed that these conductors have an upper depth limit near the brittle-ductile transition (Jones, 1992; Jiracek, 1995). The North and East Anatolian Fault Systems, for example, are both characterized by a broad low resistivity zone at mid-crustal depth that extends into the lower crust to depths below 10 km (Türkoğlu et al., 2015). At the San Andreas Fault lateral variation in resistivity seems to be related to active deformation mechanisms. At Parkfield, where a transition of the fault from a creeping to a locked section occurs, a superficial conductor to a depth of 2–3 km is observed (Unsworth et al., 1997). A connection between this zone and a mid-crustal conductor is proposed by Becken et al. (2008). A small fault-zone conductor was observed on the locked Carrizo segment (Mackie et al., 1997; Unsworth et al., 1999). The conductor extends to mid-crustal depths at Hollister where creeping movement on the faults are observed (Bedrosian, 2002).

In the compressional tectonic setting of the Southern Alps, a crustal conductor at 30–40 km depth has been attributed to fluids from prograde metamorphism within a thickening crust (Wannamaker et al., 2002). Interestingly, the conductor rises northwest toward the trace of the Alpine Fault and continues to vertical orientation near surface. This is attributed to fluids ascending across the brittle-ductile transition approaching the surface through induced hydro-fractures. Shallow extensions of the deep highly conductive features are coincident with modern, hydrothermal veining and gold mineralization interpreted to originate from the deep crust.

Although mid-crustal conductors in southern Chile occur close to deep-rooted major fault zones (Brasse et al., 2002; Kapinos et al., 2016), a prolongation through the brittle-ductile transition is not evident from long-period magnetotelluric (MT) data (Brasse et al., 2009). Broad-band MT survey including period ranges down to 1000 s in geothermal fields however, often show also a link between high conductivities and major fault zones down to about 7–8 km depth (e.g. Rowland & Sibson, 2004; Geiermann & Schill, 2010; Spichak et al., 2015). The relevance of fluid pathways from mid-crustal electric and thermal anomalies along fault zones is most evident in the Himalayan arc and the Tibetan plateau, where large-scale strike-slip fault pattern (e.g. Schill et al., 2004) allow for regionally significant advective heat transport (Hochstein & Regenauer-Lieb, 1998).

In the framework of a joint German-Chilean geothermal research project, the electric resistivity of the Villarrica area, located in the volcanic arc of Southern Chile, was investigated on reservoir scale. Low interstation-distance, broad-band MT measurements were closely linked to the existing long-period data along an E-W profile across the Liquiñe-Ofqui Fault

System (LOFS). LOFS is intersected by a secondary major fault zone striking ESE-WNW and offsetting the LOFS by a few kilometres in the study area (Rosenau et al., 2006). Therefore, a second profile has been acquired sub-perpendicular to this structure.

5.2. Geological setting

Villarrica Volcano (39°25'S, 71°56'W) and its two neighbouring volcanoes Quetrupillán and Lanín, are major Holocene stratovolcanoes formed by the subduction of the Nazca below the South America Plate. The Nazca Plate converges with a velocity of 7–9 cm a⁻¹ (Norabuena, 1998; Angermann et al., 1999), at an oblique direction of approx. N78°E (Somoza, 1998) and with a dip of 25–30° (Barazangi & Isacks, 1976) against the South America Plate forming the Andean Cordillera on the western margin of South America. Initiated in Jurassic times, subduction occurred mainly under a compressional tectonic regime with an extensional interval between Eocene and Miocene times (Pardo-Casas & Molnar, 1987; Melnick et al., 2006). The recent stress pattern is characterized by maximal horizontal stress trending N60°E and subhorizontal minimal stress (Lavenu & Cembrano, 1999; Rosenau et al., 2006). The trench is located 260 km west of the study area, whereas the subducted Nazca Plate lies at a depth of about 120 km below Mt. Villarrica (Krawczyk et al., 2006).

In south-central Chile, the Andean Cordillera overlies a thinned crust (Hildreth & Moorbath, 1988). Between the subduction of the Juan Fernandez Ridge (33°S) and the Chile Triple Junction (46°S) major stratovolcanoes occur along the so-called Southern Volcanic Zone in the Andean Cordillera (Stern, 2004). Volcanic centres are often located along the 1200 km long, N-S trending, intra-arc LOFS (Cembrano et al., 1996). Transpressional recent tectonics cause dextral strike-slip movement on that fault zone. In the study area the LOFS runs along the N-S oriented Lake Caburgua and continues to the south in the Valley Palguin (between Villarrica Volcano and Quetrupillán Volcano). Near Liquiñe (southern margin of research area) a maximum width of 2 km is documented for the LOFS (Hervé, 1976).

Additionally, NW-WNW and NE aligned fault zones are observed in the study area. The latter are considered as tension fractures related to the oblique maximum stress direction. NE trending fault zones occur in the investigation area on the NE flank of Villarrica Volcano (Cembrano & Lara, 2009). NW aligned fault zones are common in the south Andean Cordillera (Bohm et al., 2002; Melnick et al., 2006). Oriented parallel to minimal horizontal stress, they undergo active compression. In the vicinity of Villarrica Volcano, the ESE-WNW-aligned Mocha-Villarrica fault zone (MVFZ Rapela & Pankhurst, 1992; Hackney et al., 2006; Zaffarana et al., 2010) crosscuts and offsets the LOFS (Figure 5.1). The fault zone is accompanied by the lineament of the volcanic chain Villarrica-Quetrupillán-Lanín. It offsets the LOFS by a few km to the west indicating sinistral movement (Lange et al., 2008).

The volcanic rocks from Villarrica-Quetrupillán-Lanín stratovolcanoes show a variable basaltic-dacitic (sometimes rhyolitic) geochemical composition (Moreno et al., 1994; Lara et al., 2004) whereas minor eruptive centres, located to the north near the Caburgua lake and the Valley Liucura (Figure 5.2), show a less fractionated, mainly basaltic, composition. From isotopic studies magma chambers below the stratovolcanoes are assumed in shallow depth (Hickey-Vargas et al., 1989), neglecting in contrast the presence of major chambers below the small eruptive centres. Unlike Quetrupillán and Lanín, Villarrica Volcano reveals

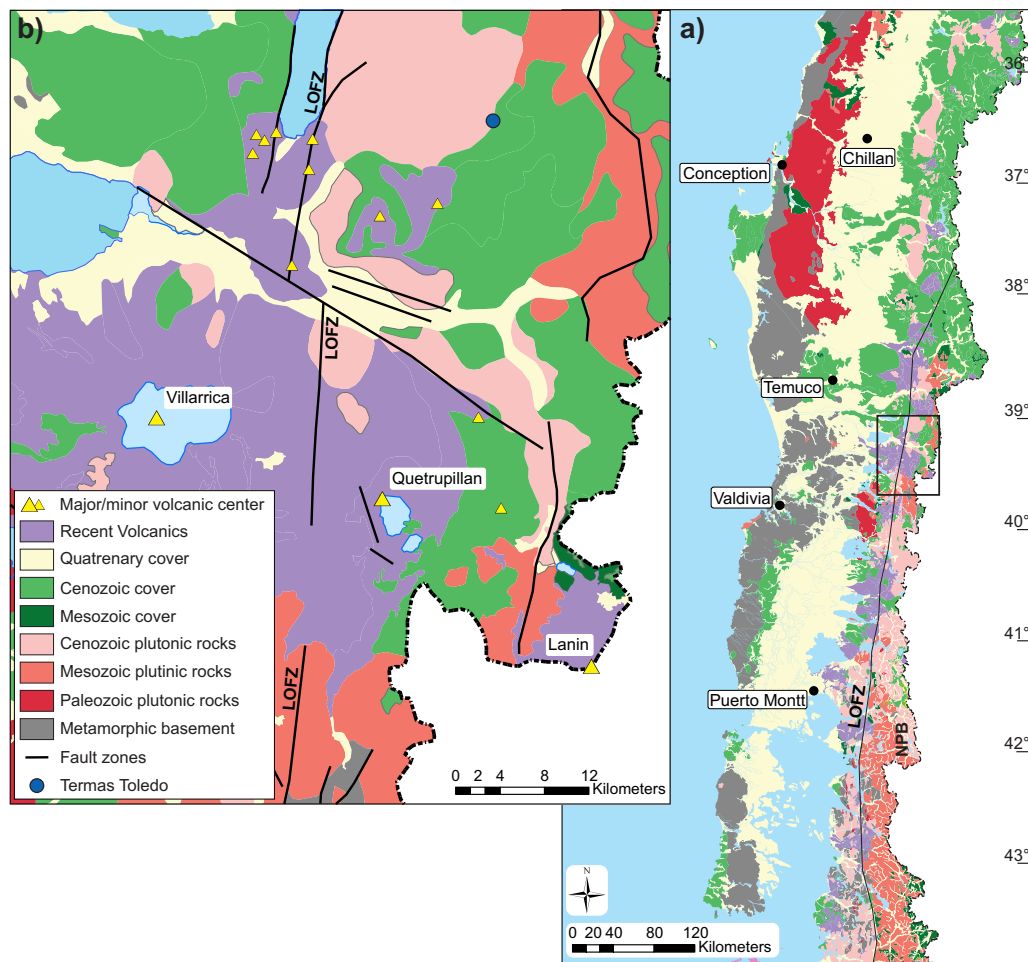


Figure 5.1.: (a) Geological map of southern Chile across the Cretaceous-Mesozoic North Patagonian Batholith (NPB) at the southern rim of the study area to Meso-Cenozoic volcano-sedimentary basin fillings and the dextral intra-arc Liquiñe Ofqui Fault System (LOFS) crosscutting the NPB and continuing to the N in the sedimentary sequence. (b) Geological and structural map of the study area. Both modified after 1:1'000'000 scale map, Servicio Nacional de Geología y Minería, Chile by including interpretations from Moreno & Lara (2008); Cembrano & Lara (2009); Sánchez et al. (2013); Lara & Moreno (2004).

a strong recent mostly strombolian activity of basaltic-andesitic composition (Ortiz, 2003; Hickey-Vargas et al., 2016)).

These Holocene volcanic rocks overlie granitic and volcanosedimentary formations (Figure 5.1). The granitoids belong to the North Patagonian Batholith (Hervé, 1984; Munizaga et al., 1988). This plutonic belt was emplaced between 39°-47°S during two phases in Late Cretaceous and Miocene times mainly along the trace of LOFS (Pankhurst et al., 1999). North of the volcanic chain the batholith is slowly replaced by Eocene-Miocene volcano-sedimentary units known as the Cura-Mallín formation (Jordan et al., 2001). In this time period extensional tectonics caused the formation of a sequence of sub-basins in south central Chile between 33°-39°S. Sedimentary thickness of up to 3000 m is documented (Radic, 2010), filled with non-marine sediments intercalated with pyroclastic rocks and lava flows mainly of andesitic composition (Niemeyer & Muñoz, 1983; Suarez & Empanan, 1995).

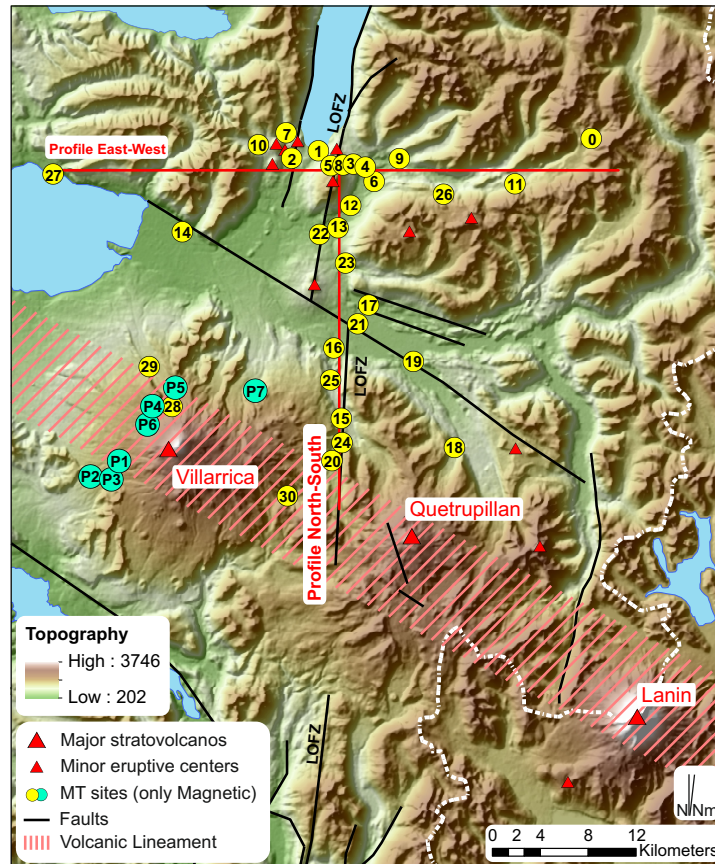


Figure 5.2.: Shaded relief topographic map of the study area next to the Villarrica Volcano. Topography is based on SRTM data from NASA. Local fault zones according to Lara & Moreno (2004); Moreno & Lara (2008); Sánchez et al. (2013). Numbered yellow dots: MT stations; numbered cyan dots: magnetic field stations; Station 0 represents the remote reference station; LOFS: Liquiñe Ofqui Fault System; N and nN: direction of geographic and magnetic north with a declination of 6.5°

5.3. Data acquisition

MT data were acquired mainly along two approximately E-W (25 km) and N-S (45 km) oriented profiles at the southern shore of Caburgua Lake and W of Villarrica volcano, respectively, including 31 MT stations (Figure 5.2). These measurements were conducted between November and December 2013. Due to insufficient connection of the electrodes to the massive rock at seven stations on the western flank of the volcano, only the magnetic field was measured in March 2014. The orientation of the E-W MT profile was selected assuming that the major tectonic elements, the N-S striking LOFS and Andean subduction zone determine the geoelectric strike direction (Muñoz et al., 1990; Brasse & Soyer, 2001). However, given the shallow target depth including major secondary fault orientations and considering the complex analysis of geoelectric strike by Brasse & Soyer (2001), we must also consider a potentially deviating geoelectric strike. Therefore, a second profile has been chosen sub-perpendicular to the lineament of the volcanic chain Villarrica-Quetrupillán-Lanín and MVFZ. Although both structures strike approximately $N120^\circ E$, the natural relief implied a 30° angle to the lot, that is, an N-S orientation of the profile.

In order to obtain high resolution at comparably shallow depth, that is, in the first

kilometres of the crust, and to connect to its deeper parts (see Brasse et al., 2009), a period band of 10^{-3} to 512 s was chosen for data acquisition. The E-W profile was measured with an average spacing of 1–2 km in the central parts and up to 6 km in the outer part, while the N-S profile spans a total of 45 km with an average station distance of 2 km. A remote station was operated quasi-continuously for 26 d, with an interruption of 4 d due to animal activity, during the entire MT campaign. The station is situated at the eastern rim of the E-W profile (station 0 in Figure 5.2).

Data were acquired over 1–3 d allowing for robust data processing. Measurements were carried out using four MT stations with an ADU-07e data logger, three MSF-07e coil magnetometers and four EFP-06 electrodes (Metronix Inc.). Magnetometers and electrodes were oriented N-S, E-W and vertical. All horizontal magnetic and electric sensors were buried at about 20 cm depth. The vertical magnetic sensor was buried completely. Cables were fixed to the surface and partly buried to reduce the influence of motion (e.g. by wind).

5.4. Data processing and results

Time series data were processed to determine the impedance tensor using mutual remote reference processing in order to reduce local electromagnetic noise (Gamble et al., 1979). The improvements of different processing steps and further optimization are shown for a representative example (site 5) in Figure 5.3. Two different processing codes were applied: The © WinGLink code (Schlumberger, version 2.21) including a 50 Hz and harmonics notch filter yields high quality transfer function data at short periods ($T < 1$ s), but shows low-quality processing results at $T > 1$ s with out-of-quadrant phase data at all stations (e.g. Figure 5.3 a-c). Therefore, at $T > 1$ s robust data processing techniques after Egbert & Booker (1986) were applied. The application of the notch filter improves data quality at higher frequencies significantly (e.g. Figure 5.3 b). Mutual remote referencing technique enhance data quality mainly at intermediate periods $T = 0.1$ –10 s (Figure 5.3 c). Acceptable quality of the transfer function is reached after merging the differently processed two period ranges, $T < 1$ s and $T > 1$ s (Figure 5.3 d).

Off-diagonal components of transfer functions Z of all MT stations are presented in the Supplementary Material. Note that although for six stations (12-17) remote processing is not applicable, rather smooth transfer function with equally small errors compared to remote processed sites are obtained in most cases.

Data quality has been assessed using the following criteria. Poor data quality is characterized by a change of apparent resistivity or phase between two periods by >1 order of magnitude or $>15^\circ$. For inversion, individual data points were discarded, if of poor quality or if error bars exceed one order of magnitude (apparent resistivity) or more than 20° (phase angle). Finally, <10 per cent of individual outliers were excluded from inversion (transparent in Supplementary Material). Only station 22 was excluded completely from inversion.

5.4.1. Directionality and dimensionality analysis

In order to verify the validity of the initial assumption of 2-D distribution of subsurface structures as well as the potential geoelectric strikes, dimensionality and directionality have to be investigated. Generally, Swift skew values < 0.1 (Swift, 1967) allow for 1- or 2-D interpretation of the geoelectric structure of the subsurface for $T < 1$ s (Supplementary Material), but do not exclude 3-D conductivity distribution. Increasing Skew values at

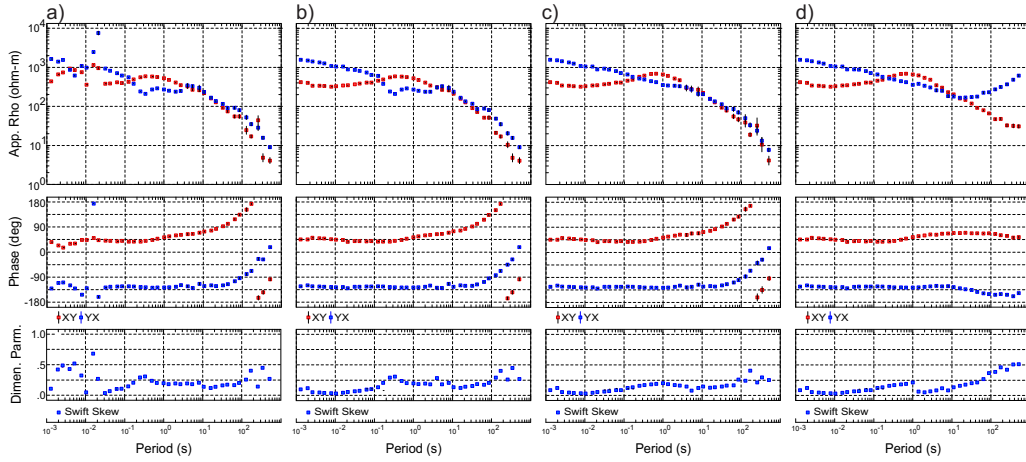


Figure 5.3.: Representative transfer functions (site 5, Figure 5.2) with successively enhanced processing steps from (a) single site processing, (b) single site processing including a 50 Hz and harmonics notch filter to (c) and (d) mutual remote reference techniques combined with notch filtering. Processing was carried out using © WinGLink software (Schlumberger, version 2.21) for all frequency ranges except in (d), when frequencies >1 s were processed using the [Egbert & Booker \(1986\)](#) algorithm due to out-of-quadrant behavior of the phase in (a)-(c).

longer periods and particular stations with higher values at distinct frequencies suggest significant 3-D behaviour (Supplementary Material). Neglecting galvanic distortion using impedance tensor decomposition after [Bahr \(1991\)](#) (Eq. 5.1),

$$\eta = \frac{\sqrt{|[Z_{xx}x - Z_{yy}y, Z_{xy}y + Z_{yx}x] - [Z_{xx}x + Z_{yy}y, Z_{xy}y - Z_{yx}x]|}}{|Z_{xy}y - Z_{yx}x|} \quad (5.1)$$

hereafter called Bahr skew, most of the sites show values $\eta < 0.3$ for $T < 8$ s allowing for both, 2-D and 3-D interpretation (Figure 5.4). At larger periods $T > 20$ s these low η -values are also prevailing. For $8 \text{ s} \leq T \leq 20 \text{ s}$, values are significantly higher indicating dominant 3-D resistivity distribution. Note that high Bahr skew values coincide with large errors in the transfer functions at higher periods (e.g. stations 3, 7 and 13 at $T = 8$ s, Supplementary Material). To address the geoelectric strike direction, a decomposition analysis was carried out after [Becken & Burkhardt \(2004\)](#) analysing the ellipticity of electric and magnetic field polarization (Figure 5.5). Strike direction was determined using single-site, multi-frequency analysis for each MT station individually. Reduction of cumulative minimum ellipticity was achieved by splitting the total period range into three intervals (Figure 5.5). Although high variation of strike direction is observed for $T < 0.1$ s, a principal strike direction of approximately N350°E to N7.5°E occurs at eleven of 31 stations. A secondary direction of approximately N120°E is observed at five sites. The latter is found to be the dominant direction in the period band $T = 0.1\text{--}10$ s occurring at eleven of 31 stations, whereas the roughly N-S direction is found at four sites, only. For $T > 10$ s, scattering is reduced and the dominant direction is found to be approximately N-S again. It can be summarized that both assumptions, the 2-D distribution of structures in the subsurface and the two geoelectric strike directions, approximate natural subsurface conditions to a large extent.

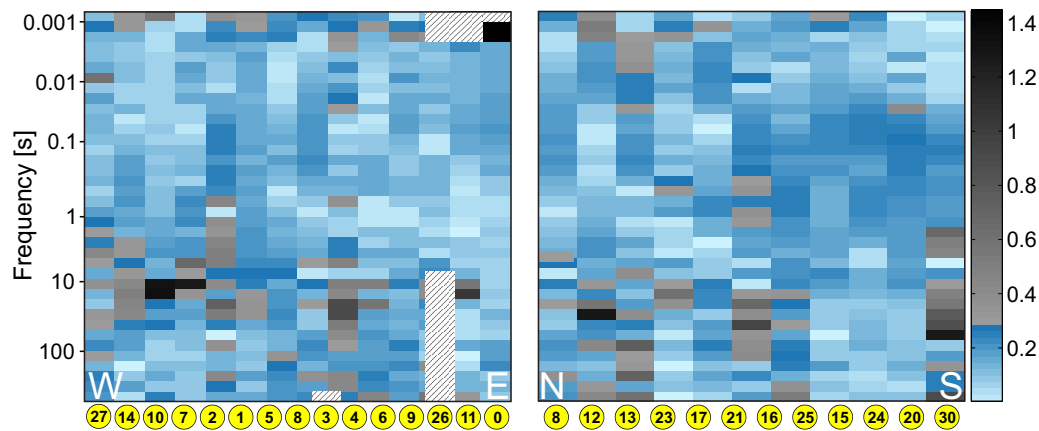


Figure 5.4.: Evaluation of dimensionality using phase sensitive skew of impedance tensor after (Bahr, 1991) on the E-W profile (left) and N-S profile (right). Impedance tensors with skew values below 0.3 (indicated by blue colours) are valid for 2-D interpretation. Hatched areas: no data available.

5.4.2. Vertical magnetic field data

Induction arrows representing the real part of the magnetic field component are presented for different frequencies in Figure 5.6 using Wiese convention (Wiese, 1962), that is, induction arrows point away from relatively high conductive features. In agreement with skew analysis, for $T < 0.02$ s, they show strong scattering in direction and intensity (representative results at $T = 1/128$ s in Figure 5.6). For 0.02 s $< T < 0.5$ s ($T = 0.125$ s in Figure 5.6), induction arrows east of the LOFS point towards E, whereas stations west of the fault point towards W. Supported by a small vertical magnetic field component at the fault zone (station 8 and 30), the presence of a conductor coinciding with the LOFS is indicated.

Stations located at the western flank of the volcano deviate from this pattern as they point away from the centre of the volcano. Although topographic effects cannot be ruled out completely, the arrow pattern does not display the topography of the Villarrica Volcano. With increasing distance to the Villarrica-Quetrupillán-Lanín lineament, the vertical magnetic component increases and is oriented perpendicular to this lineament. Thus, a conductor parallel to the lineament can be assumed. In contrast, at $T = 0.5$ – 6 s ($T = 1.39$ s in Figure 5.6) the possible dominance of the LOFS on inductions arrows decreases, as they experience a general northeastward rotation and a reduction in intensity E of the LOFS. Induction arrows at stations possibly linked to the Villarrica-Quetrupillán-Lanín lineament remain unchanged with respect to smaller periods. Moreover more stations, also in greater distance to volcanic lineament, possess NE direction perpendicular to the volcanic chain.

At increasing depths ($T = 10$ – 50 s), induction arrows show a smaller vertical magnetic field component, indicating a homogenous electromagnetic interval ($T=11.1$ s in Figure 5.6). With increasing depth the induction vectors rotate to NNW-NNE directions ($T = 512$ s in Figure 5.6) described by (Brasse et al., 2009) and interpreted as an anisotropy caused by a tensile fracture regime parallel to maximum horizontal stress.

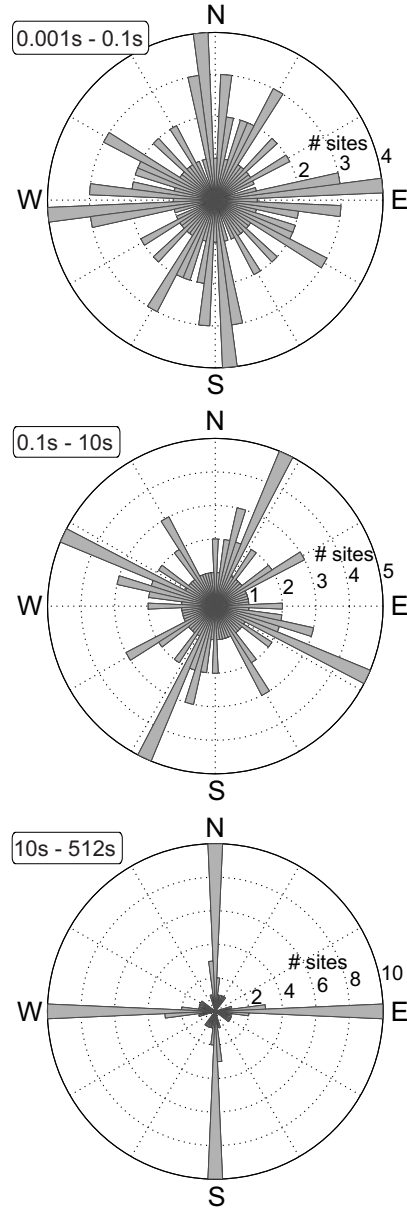


Figure 5.5.: Directionality analysis after [Becken & Burkhardt \(2004\)](#) using regional strike mode determining a single strike at each station. With exception of the period range of 10–512s, for which data availability and quality reduces the stations to 21, all 31 stations were analysed. Results were divided in period ranges manually yielding intervals of different prevailing strike regimes.

5.4.3. Phase tensor

Phase tensor analysis after [Caldwell et al. \(2004\)](#) is used to determine the directional behaviour of the regional conductivity structures in the study area. The galvanic distortion independent phase tensor Φ can be written as

$$\begin{bmatrix} \phi_{11} & \phi_{12} \\ \phi_{21} & \phi_{22} \end{bmatrix} = \frac{1}{\det(X)} \begin{bmatrix} X_{22}Y_{11} - X_{12}Y_{21} & X_{22}Y_{12} - X_{12}Y_{22} \\ X_{11}Y_{21} - X_{21}Y_{11} & X_{11}Y_{22} - X_{21}Y_{12} \end{bmatrix} \quad (5.2)$$

with X and Y being real and imaginary part of the impedance tensor. The phase tensor can be visualized by an ellipse with the principle axes φ_{Max} , φ_{Min} representing the eigenvectors of the tensor. In this analysis, the angle $\alpha - \beta$ of φ_{Max} to the observer's coordinate system

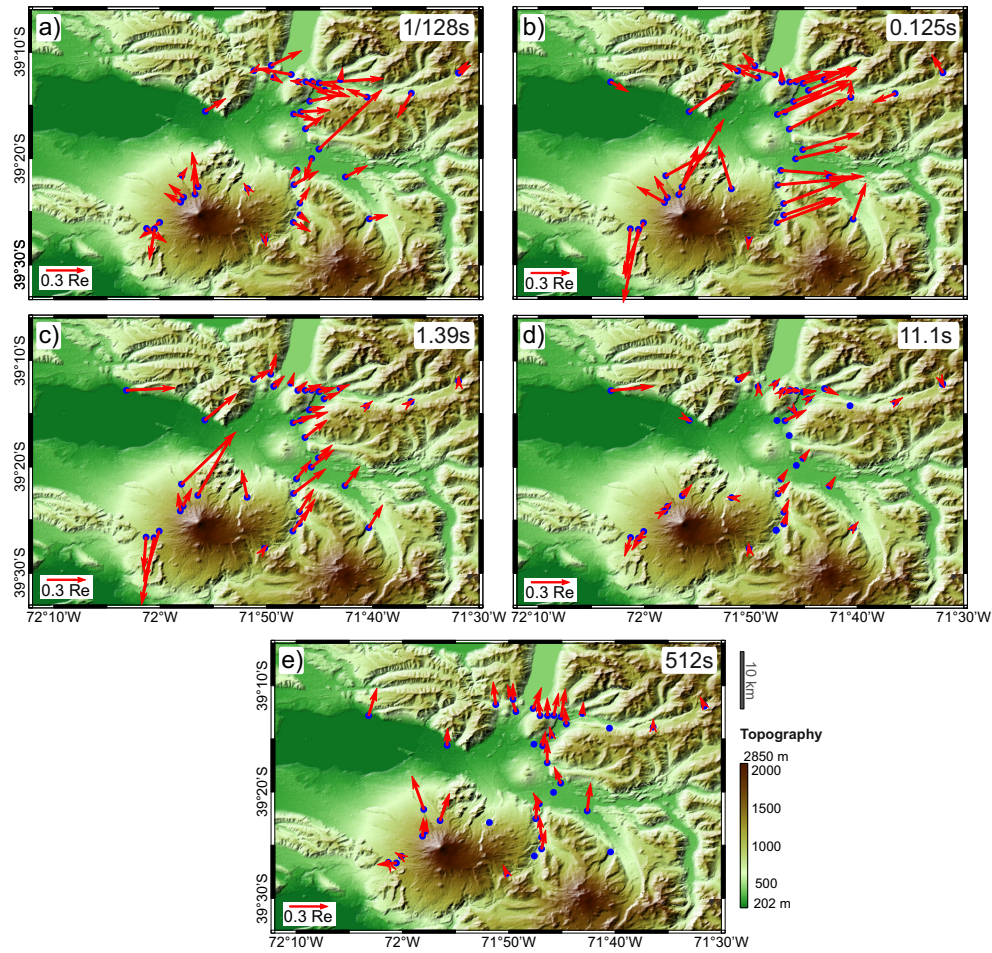


Figure 5.6.: Induction arrows of representative frequencies (Wiese convention (Wiese, 1962)). Selected periods show effects of local, shallow fault zones (1/128 s, 0.125 s, 1.39 s), an electromagnetically homogenous depth interval (11 s) and a strong southward directed electromagnetic signal caused by an unknown conductor/mechanism first described by Brasse et al. (2009).

indicates preferred flow direction of regional induction currents. The phase tensor skew angle β completes the full description of the tensor. It is a measure of asymmetry in the regional MT response. While, comparable to Bahr and Swift skew, low values of the phase tensor skew are inconclusive, persistent directions of principal axes of the phase tensor with period and location along strike seem to provide good indication for approximation of 2-D subsurface conditions. φ_{Max} indicates conductivity gradients, in a 2-D case parallel or perpendicular to the regional geoelectric strike (Caldwell et al., 2004).

Figure 5.7 displays the phase tensors at different periods. Although β values are significantly different from zero, indication for 2-D behaviour is indicated by rather consistent orientation of φ_{Max} . In general, a comparably high $\varphi_{Max}:\varphi_{Min}$ ratio is observed for $T > 20$ s coinciding with a rather consistent orientation of φ_{Max} in N-S direction across the study area (Figure 5.7d). Although absolute values of φ_{Max} and φ_{Min} increase in the interval $0.05 < T < 20$ s, a comparably low $\varphi_{Max}:\varphi_{Min}$ ratio and a preferential φ_{Max} orientation of approximately N30°E is persistent throughout this period range (representative results at $T = 0.125$ s and 1.39 s in Figs. 5.7b and c). At smallest periods, comparably low φ_{Max} and φ_{Min} are observed along with high directional scattering. In summary, the phase tensor analyses are

consistent with observations from induction arrows and dimensionality analyses. All three allow for relating geoelectric data to tectonic structures in the study area.

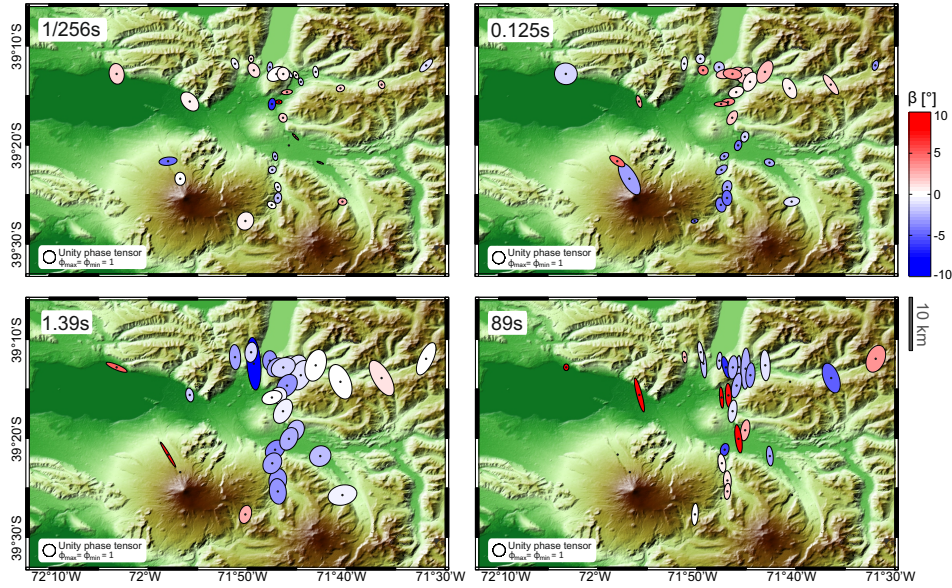


Figure 5.7.: Phase tensor ellipses at different periods (after Caldwell et al., 2004). Lengths of the axes are proportional to principle values (φ_{Max} , φ_{Min}) of the phase tensor. Major axis rotated from E-W direction by angle $\alpha - \beta$, (see description of α and β in the text). Colour code of ellipses display the skew angle β , describing the phase tensor asymmetry.

5.5. Inversion of MT and vertical magnetic field data

Since dimensionality analyses do not exclude a 2-D subsurface structure to a large extent, but a change from N-S to N120°E in geoelectric strike is observed at intermediate periods, 2-D inversion was carried out on the two profiles (E-W and N-S in Figure 5.2). Respecting the geoelectric strike, the measurements acquired at stations along the N-S profile have been rotated by 120°. Inversion of MT data was carried out employing TE, TM modes and the vertical magnetic field transfer function individually or in different combinations on rectangular meshes with a size of 1075 x 480 km and 165 x 100 cells for the E-W profile and 1058 x 480 km and 140 x 90 cells on the N-S profile including topography. The 2-D nonlinear conjugate gradients algorithm (Rodi & Mackie, 2001) minimizes the misfit between modelled and observed data with a regularization term related to the spatial smoothness of the modelled resistivity distribution. Smoothing parameter τ describes the ratio between roughness and data misfit. The trade-off between data fit and model smoothness is analysed in Figure 5.8 after Hansen & O'Leary (1993). Using a reduced mesh size of 65 horizontal x 36 vertical elements inversion results are obtained for $\tau = 0.3$ to $\tau = 300$. Based on the L-curve smoothing parameters $\tau = 7.5$ was selected for further inversion. It should be noted that main features are persistent through the variations of τ hinting on robust features (Figure 5.8).

Since our inversion concept is based on 2-D subsurface structures for distinct depth ranges and TE modus is more sensitive to 3-D effects, a parameter set A with a higher error floor of

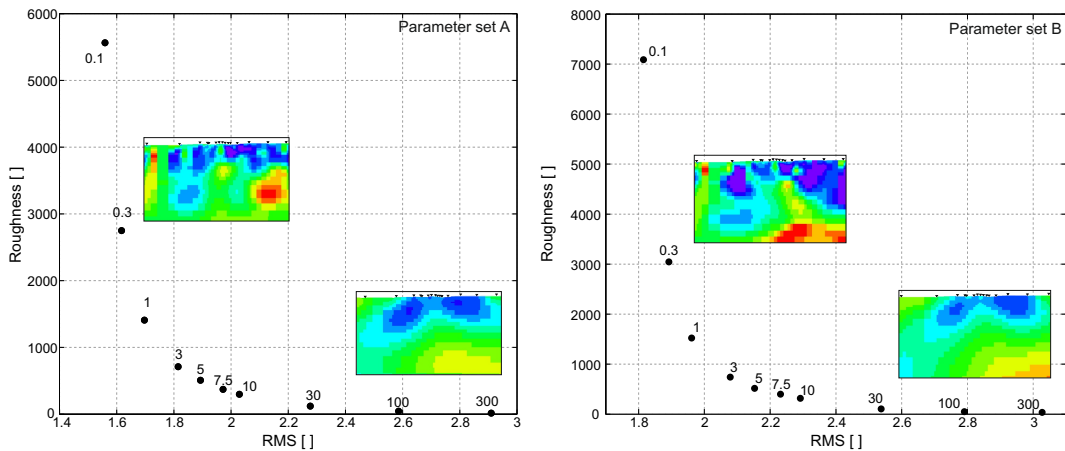


Figure 5.8.: Model roughness versus root mean square (RMS) data misfit for smoothing parameter values τ between 0.3 and 300 for parameter set A ($\rho(\text{TE}) = 70$ per cent, $\rho(\text{TM}) = 15$ per cent, $\phi(\text{TM}, \text{TE}) = 5$ per cent, $T_x = 0.065$) and B ($\rho(\text{TE}) = 20$ per cent, $\rho(\text{TM}) = 20$ per cent, $\phi(\text{TM}, \text{TE}) = 5$ per cent, $T_x = 0.1$). Pictures presenting modelling results of the E-W profile smoothing parameters $\tau = 0.3$ and $\tau = 300$. Resistivity colour scale as in Figure 5.9.

70 per cent for TE apparent resistivity compared to 15 per cent for TM mode after Becken et al. (2008) is applied. Compared to phase error floor of 5 per cent, the error floors of apparent resistivity are higher to reduce static shift. For the vertical field data an absolute error floor of 0.065 was used. Since we aim at linking near-surface structures to deep MT soundings, a second set of inversion parameters approximating Brasse et al. (2009) has been used. This dataset B weights TE and TM modes equally analysing effects of 3-D resistivity distribution with error floors of 20 per cent for apparent resistivity, 5 per cent for phases and 0.1 for vertical field data. To constrain the electromagnetic features manual sensitivity tests were performed by fixing resistivities to replace conductive/resistive features and the omission of single sites. All features discussed in the following show robust behaviour. Inversions were started from 100 m uniform half space. Additional test inversions starting from a 500 m uniform half space yield similar results. Inversion results after 150 iterations with an average RMS misfit of 1.86 (set A) and 2.14 (set B) for the E-W and 2.14 (set A) and 2.32 (set B) for the N-S profiles, respectively, are shown in Figure 5.9a. Note that errors of set B exceed errors of set A significantly near the deep conductor (Con2). Inversion results are presented for inversion parameter sets A (Figure 5.8b) and B (Figure 5.8c) for both profiles, E-W and N-S to a depth of 32.65 and 26.00 km, respectively. From 2-D inversion of the two profiles four major features can be identified:

- (1) In the E-W profile, E of station 27, a high resistivity layer with ρ up to $>5000 \Omega\text{m}$ is observed at near-surface to a depth of about 7.5 to 12 km. Such a high resistive layer can also be observed in the central part of the N-S profile below stations 13 to 25. Station 27 is located at the transition from the volcanic chain to the longitudinal valley to the W, which is filled up with 5 km thick sediments.
- (2) In the E-W profile, a narrow rather vertical structure of moderate conductivity (Con1) with $\rho = 100 \Omega\text{m}$ intersects this high resistivity structure below stations 5 and 8 to a depth of approximately 10 km. This anomaly continues about 5 km to the S as shown in the N-S profile underneath stations 8 and 12. Using parameter set B, in the N-S profile it appears more conductive. We consider this to be a boundary effect. Tests using fixed resistivity inversion exclude Lake Caburgua as a possible origin of this anomaly.

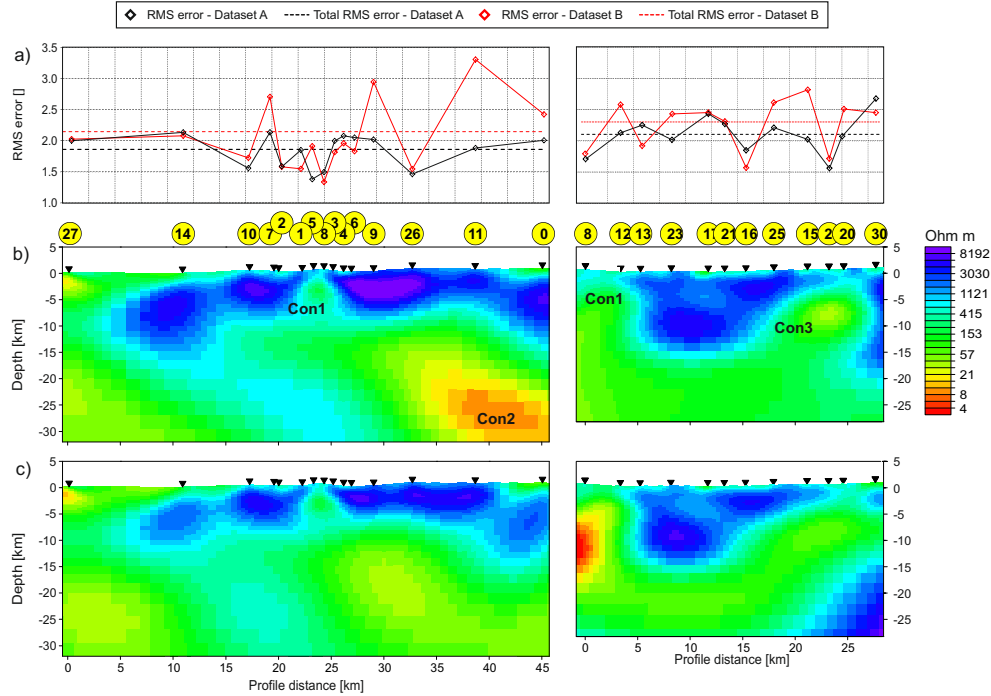


Figure 5.9.: Inversion of MT data along the E-W (left) and N30°E profile (right) for parameter sets A (error floors 70 per cent for TE apparent resistivity, 15 per cent for TM apparent resistivity, 5 per cent for the phases, 0.065 for the vertical field) and B (error floors 20 per cent for apparent resistivity, 5 per cent for the phases, 0.1 for the vertical field). (a) Individual MT station RMS (dots) and average RMS across the profile (dashed lines) for parameter sets A and B after 150 iterations. (b) Results of inversion of MT data using parameter set A. (c) Results of inversion of MT data using parameter set B.

(3) At a depth of about 20 km, a deep conductor Con2 with ρ up to 10 Ωm appears at the eastern part of the E-W profile in inversion parameter set A extending to the lower boundary of the section. In parameter set B, this Con2 is characterized by a resistivity of up to $\approx 30 \Omega\text{m}$ and a slight offset to the W. Corresponding RMS is significantly higher compared to parameter set A. These resistivities and the lateral location are consistent with the anomaly C in [Brasse & Soyer \(2001\)](#) and B in [Kapinos et al. \(2016\)](#).

(4) Along the N-S profile, a second moderate conductor (Con3) with $\rho = 20 \Omega\text{m}$ is indicated in the southern part below stations 24 and 20. Con3 seems to be part of a larger structure with an apparent northward dip. It is located below the volcanic lineament.

Since this study aims at a possible connection of mid-crustal conductors to major fault zones, we first investigate the origin of Con1 coinciding with the LOFS near Lake Caburgua using simple forward modelling of end member scenarios (Figure 5.10). Two scenarios have been tested based on geological and resistivity observations. Scenario 1 (Figure 5.10a) assumes the width of LOFS bound by the faults E and W of Lake Carburgua (Figure 5.2) resulting in a width of 2 km. Scenario 2 (Figure 5.10b) starts from a width of 0.25 km based on Con1 at near-surface (see station 8 in Figure 5.9). Following minimum resistivity of Con1 gained from inversion, for the forward modelling the start value was set to 100 Ωm for scenario 1 and 30 Ωm for scenario 2. Synthetic MT data were generated by forward modelling adding a 5 per cent Gaussian noise. Parameter set A was used for the inversion, which was terminated after 150 iterations allowing for a comparison between synthetic

and measured data. Both scenarios trace equally well the high resistivity contrast from up to $>5000 \Omega\text{m}$ to about $100\text{--}200 \Omega\text{m}$ at about 10 km depth and are able to reproduce Con1. The shape of the Con1 is well traced by forward modelling results of scenario 2, whereas the width of Con1 at a depth of about 5 km seems to be related to a broader structure such as assumed in scenario 1. We would like to point out here that although not matching Con1 at near-surface, a combination of the two scenarios, that is, a so-called flower structure, possibly reproduces best Con1.

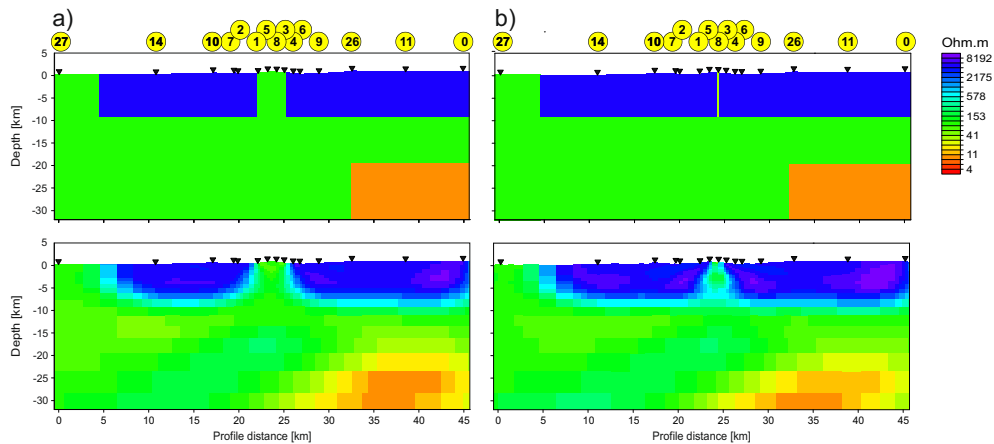


Figure 5.10.: Forward modelling of end member scenarios for the width of LOFS (5 per cent Gaussian noise). (a) Following the width of the LOFS at Lake Caburgua (most likely representing a pull-apart structure), an upper limit of 2 km has been used for scenario 1. (b) Following the width of the low resistivity at the surface (Figure 5.9), a lower limit of 0.25 km has been used for scenario 2.

5.6. Discussion

Generally, the results from MT measurements in the Villarrica area are subdivided in three depth sections that are characterized by differences in dimensionality, resistivity and directional behaviour. The three period ranges, near-surface (about 10^{-3} to 10^{-1} s), intermediate (about 10^{-1} to 10^1 s) and long-period ranges, represent depth section of about <10 km, $10\text{--}20$ km and >20 km, respectively. The near surface is characterized by N-S/E-W geoelectric strike directions prevailing over scattering. A link to the LOFS and thus an N-S preferential strike direction can be concluded from induction arrows. Coinciding with relatively low phase angles in the period range of $T < 5 \times 10^{-2}$ s, this period range is characterized by ρ up to $>5000 \Omega\text{m}$, except from the LOFS, where moderate conductivity (Con1) with $\rho = 100 \Omega\text{m}$ intersects this high resistivity layer. The vertical transition to intermediate resistivity of about $100\text{--}200 \Omega\text{m}$ occurs in a narrow depth range of about <2 km. The change from high to intermediate background resistivity points to the brittle-ductile transition. Bailey (1990) predicted a conductive lower crust, where fault zones are not able to penetrate into the ductile zone, as enhanced vertical permeability will empty the saturated lower crust rapidly reducing conductivity. Ivanov & Ivanov (1994) observed this phenomenon for fault zones worldwide. Below, geoelectric strike direction changes in the intermediate section to ESE-WNW, indicated in both the directionality and induction arrow analyses. In agreement with the observation of Brasse et al. (2009), the geoelectric strike at long periods is clearly N-S/E-W oriented. At this depth, our results connect to the low resistivity anomalies observed during long-period MT measurements.

In order to further characterize these high conducting structures their possible origin is discussed subsequently. The brittle-ductile transition is generally observed at a depth of 10–15 km coinciding with a temperature range of 250–500 °C (Sibson, 1977; Ivanov & Ivanov, 1994). Taking into account the local heat flow density of 130–170 mW/m² (Hamza & Muñoz, 1996), assuming an average thermal conductivity of 2.8 W m⁻¹ K⁻¹ and a radioactive heat production of 5 μW m⁻³, we may estimate that the temperature at 10 km depth exceeds the critical temperature for the brittle-ductile transition. This hypothesis is supported by the coincidence of crustal conductance and a seismically quiet zone below 10 km depth, observed N of the study area (Bohm et al., 2002; Lange et al., 2008).

In summary, the intermediate resistivity anomalies Con1 and Con3 indicate fault controlled systems that can form a connection from mid-crustal depth (Con2) to near surface. Comparably high conductivity in faults zones has been attributed to clay alteration or saline fluids. In the following, bulk resistivity of about 30 Ωm of the fault zone related to Con1, obtained from forward modelling is investigated for clay content, porosity and cementation factor for fluid filled pores after Archie (1942) assuming that the tortuosity factor $a = 1$ (Eq. 5.3) and for coupled fluid and clay filled pores after Waxman & Smits (1968) (Eq. 5.4).

$$\sigma_B = \sigma_f \cdot \theta^m \quad (5.3)$$

$$\sigma_B = \theta^m (B \cdot Q_V + \sigma_f) \quad (5.4)$$

where σ_B and σ_f are the specific electric conductivities of saturated bulk rock and the fluid phase, θ the porosity, m the cementation factor, Q_V the concentration of sodium exchange cations in clay minerals and B represents an empirical equivalent conductance of the counterions as a function of σ_f . For determination of σ_f , 10 per cent dilution, indicated by chlorofluorocarbon analysis, has been considered to the maximum $\sigma_f = 1340 \mu\text{S cm}^{-1}$ measured at Termas Toledo (Figure 5.1). Conductivity correction to reservoir temperature has been carried out after Dakhnov (1962). Maximum reservoir temperature of 140 °C has been estimated from sulfate geothermometry for the low mineralized geothermal fluids in the study area (Held et al., 2015). Following Eq. 5.3 with a generally accepted cementation factor of $m = 2$ for highly consolidated rocks, high values of about 26 per cent of fracture porosity are obtained (column 2 of Table 5.1). We may either assume that the cementation factor in the fault zone is reduced by mechanical damage or that the high conductivity is related to considerable clay content for which Eq. 5.3 is not valid. For the latter calculations were performed using Eq. 5.4 assuming that matrix resistivity exceeds by far the clay or fluid resistivity, and a cation exchange capacity (CEC) of non-swelling clay minerals CEC = 20 meq per 100 g. In Eq. 5.4 CEC is incorporated in Q_V (see Waxman & Smits, 1968). For both effects, we reduce the percentage of fracture porosity (Table 5.1).

The origin of enhanced conductivity at Con2 is assumed to be caused by partial melting. The melt fraction of Con2 can be roughly estimated after Glover et al. (2000) (Eq. 5.5).

$$\sigma_B = \sigma_m (1 - \chi_m)^p + \sigma_f (1 - \chi_f)^m \quad (5.5)$$

where σ_B , σ_m and σ_f are the conductivities of bulk rock, melt fraction and fluid phase,

Table 5.1.: Calculations of required porosities assuming a plausible range of clay content (columns) and cementation factors (rows). n/a: determined resistivity (= 30 Ωm) cannot be achieved using this porosity/clay content composition

m	Archie 1942		Wayman & Smits 1968			
	% Clay					
	0	1	5	10	15	25
1	6.9	4.1	n/a	n/a	n/a	n/a
1.5	16.9	15.2	9.3	4.5	2.3	0.9
2	26.3	25.1	21.1	16.7	13.3	9.1

χ_m and χ_f the volume fraction of melt and fluids and p and m the cementation factors of each phase. Cementation factor for melt is best represented by $p = 1.3$ (ten Grotenhuis et al., 2005). Electrical conductivity of molten rock was estimated to range between 1 and 30 S m^{-1} (Lebedev & Khitarov, 1964; Tyburczy & Waff, 1983). Bulk rock resistivity of $<10 \Omega \text{ m}$ was achieved by adding 1.1 per cent melt with melt conductivity of 30 S m^{-1} or 2.7 per cent with melt conductivity of 10 S m^{-1} . Note that in the vicinity of stations 26 and 11 young volcanic edifices (Cerro Redondo and Relicura) are observed (Moreno & Lara, 2008) supporting the hypothesis of partial melt generating Con2.

The penetration of a fault into the ductile zone may result in a listric fault geometry (e.g. Brun & Wenzel, 1991). In the case of the Villarrica area, Con2 and other mid-crustal conductors coincide with deep rooted, regional fault zones (Kapinos et al., 2016). The inversion and end-member case forward modelling results of the broad-band MT data indicate that the connection between Con2 and the near surface Con1 is possibly masked by the decrease of the resistivity contrast below the brittle ductile transition.

Con3 reaches shallow subsurface level at the eastern flank of the Villarrica volcano. This part of the volcano revealed seismic activity at shallow depth during the last eruption in March 2015 OVDAS (2015). With depth the Con3 structure shows an apparent northward dip down to about 20 km depth where it disappears in the general intermediate crustal conductive layer. Connecting the two profiles, even a dip towards NNE can be imagined for this anomaly. This would follow the directions of the major tectonic structures such as the volcanic chain lineament and the MVFZ. Induction arrows at intermediate to large depth support the occurrence of a conductive structure running parallel to the volcanic chain as well. This hints at a possible connection between Con2 and Con3.

5.7. Conclusions

High-resolution and broad-band MT measurements of the Villarrica Volcano area contribute to the understanding of the geothermal and tectonic setting of the area by indicating the geometry of the major structural elements. They provide additional support on the hypothesis of a connection between mid-crustal conductors and regional fault zones. The following observations are the most significant:

- (1) Generally, high resistivities are observed in the upper 10–15 km followed by intermediate resistivities below. They are separated by a rather sharp contrast, which is likely to represent the brittle-ductile transition.
- (2) In the upper crust the LOFS is characterized by a subvertical conductor (30 Ωm) down to a depth of about 10 km with enhanced conductivities, which may be attributed to partly interconnected, most likely fracture porosity and/or clay fillings.

(3) In the lower crust a high conductivity anomaly ($5\ \Omega\text{m}$) reveals a tendency to connect to near-surface anomalies. This is however probably masked by low resistivity contrast between LOFS and the ductile crust.

Our results show that mid-crustal conductors in southern Chile might be connected to major fault zones. In line with indication from 3-D inversion of long-period MT data, they are most likely connected to the WNW-ESE striking features such as the volcanic lineament or the MVFZ. The variability in geoelectric strike in the short to long period MT data suggests the application of full 3-D inversion, which will be published in a forthcoming paper. Further key questions concern the relation between the amount of fluid and type of deformation in strike-slip faults. The study area around Villarrica offers the exceptional opportunity to analyse the fluid composition of thermal springs and their relation to the regional tectonic features.

Acknowledgements

The study is part of a collaborative research project between Karlsruhe Institute of Technology (KIT) and the Andean Geothermal Center of Excellence (CEGA, Fondap-Conicyt 15090013). The authors appreciate the support from the BMBF-CONICYT International Scientific Collaborative Research Program (FKZ 01DN14033/ PCCII30025). Additional support from the Helmholtz portfolio project “Geoenergy” in the topic “Geothermal Energy Systems” and EnBW Energie Baden-Württemberg AG is gratefully acknowledged. Special thanks to the highly motivated team of students from University of Chile for the field measurements is expressed. We are grateful to Bernhard Friedrichs (Metronix Inc) fruitful remarks during pre-processing, to Michael Becken’s provision of his Matlab tool for the dimensionality analysis and to Adele Manzella and Cristina Pomposiello for their constructive review of the manuscript.

Supplementary Material Magnetotellurics

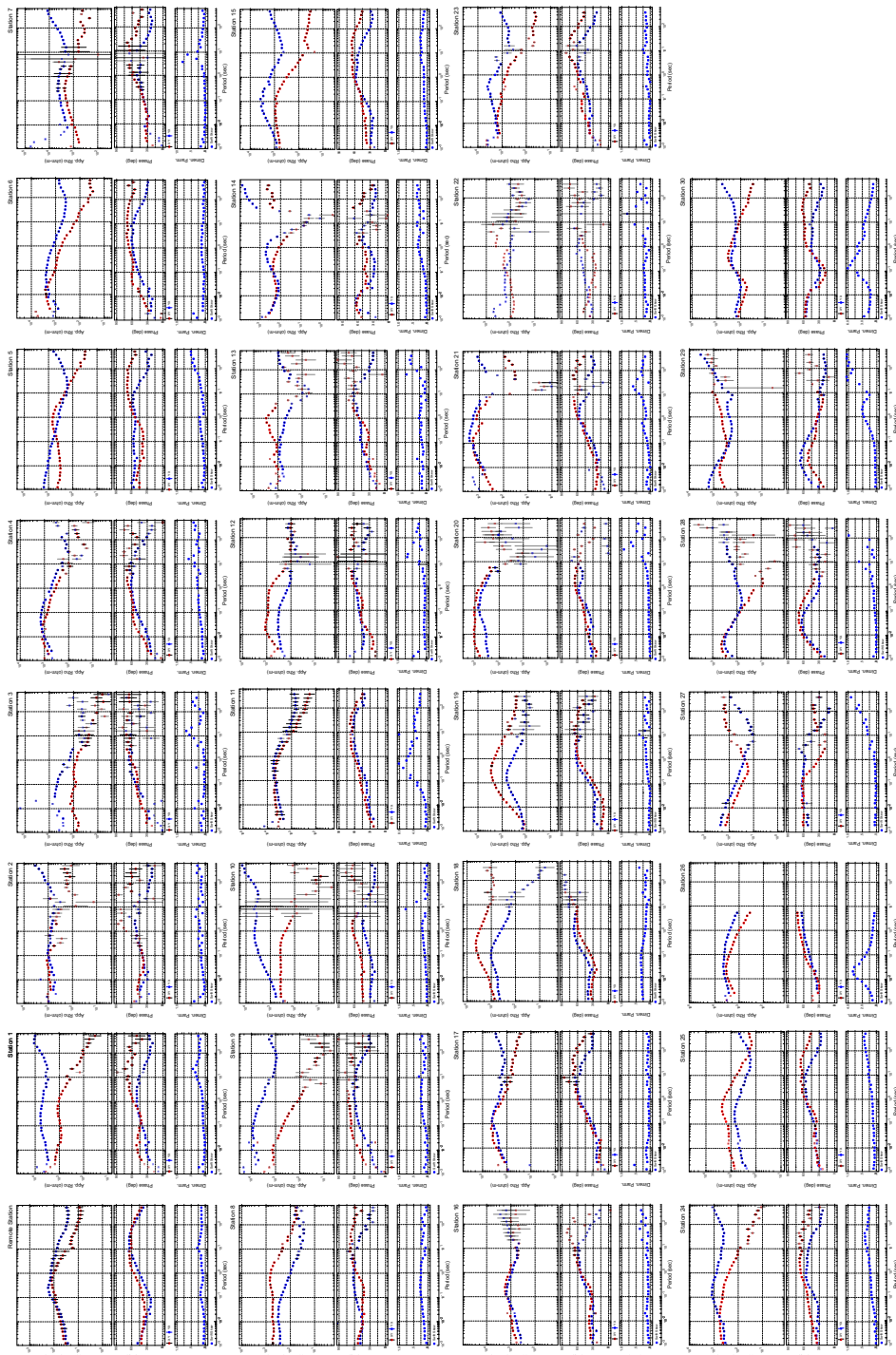


Figure 5.11.: Apparent resistivity, phase and Swift skew values of MT transfer functions of all acquired MT station. Data from stations 12 to 17 were processed without remote reference. Results from frequencies marked by transparent dots have been excluded from inversion due to large errors. Station 22 excluded completely from inversion.

6. Fault zone characterization using gravimetric techniques

6.1. Introduction

Geothermal resource exploitation targeting fault zones have a high potential for sufficient mass flow. Given the relation between permeability and porosity, explorations techniques are needed revealing fault zone porosity especially in depth. EM methods allow an indirect determination of fault zone porosity via the enhanced conductivity of fluid filled pore space (e.g. [Türkoğlu et al., 2015](#); [Held et al., 2016](#)). However, the occurrence of secondary conductive phases (clay minerals, ore minerals, graphite) produces ambiguous results complicating electromagnetic estimation of fault porosity.

Negative gravity anomaly are often detected related to fault zones, e.g. shown for San Andreas fault zone ([Wang et al., 1986](#)). [Guglielmetti et al. \(2013\)](#) in their study of the Maritime Alps, document negative Bouguer anomalies coinciding with local faults, where geothermal fluids discharge. Negative density contrast are also observed for faults inside the Soultz geothermal reservoir ([Schill et al., 2010](#)). In all these studies the negative anomalies are related to enhanced porosities caused by a combination of shearing and hydrothermal alteration modifying initial rock composition by recrystallisation and dissolution. [Altwegg et al. \(2015\)](#) present a method to analyze fault zone porosities from their impact on gravity data. For the geothermal prospect in St. Gallen, Switzerland the gravity signal of the target fault zone was identified and used to predict the enhanced porosity inside the fault zone compared to the intact bulk rock.

In this study I will combine electromagnetic and gravimetric methods to constrain fault zone porosity and clay content in the Villarrica geothermal system. The geothermal system, located at the Villarrica-Quetrupillán-Lanín volcanic chain in southern Chile (Figure 6.1), is selected as investigation area because of the presence of major fault zones and the availability of high-resolution magnetotelluric data ([Held et al., 2016](#)). The intra-arc, N-S aligned Liquiñe-Ofqui Fault system (LOFS) is intersected by oblique-to-the-arc, WNW-ESE oriented Mocha-Villarrica-fault zone (MVFS). The geology of Southern Chile as well as structural and regional geology of the research area are presented in chapter 2. The neotectonic development of Southern Chile, discussing the occurrence and characteristics of the intersecting fault zone systems, is highlighted in chapter 2.4.

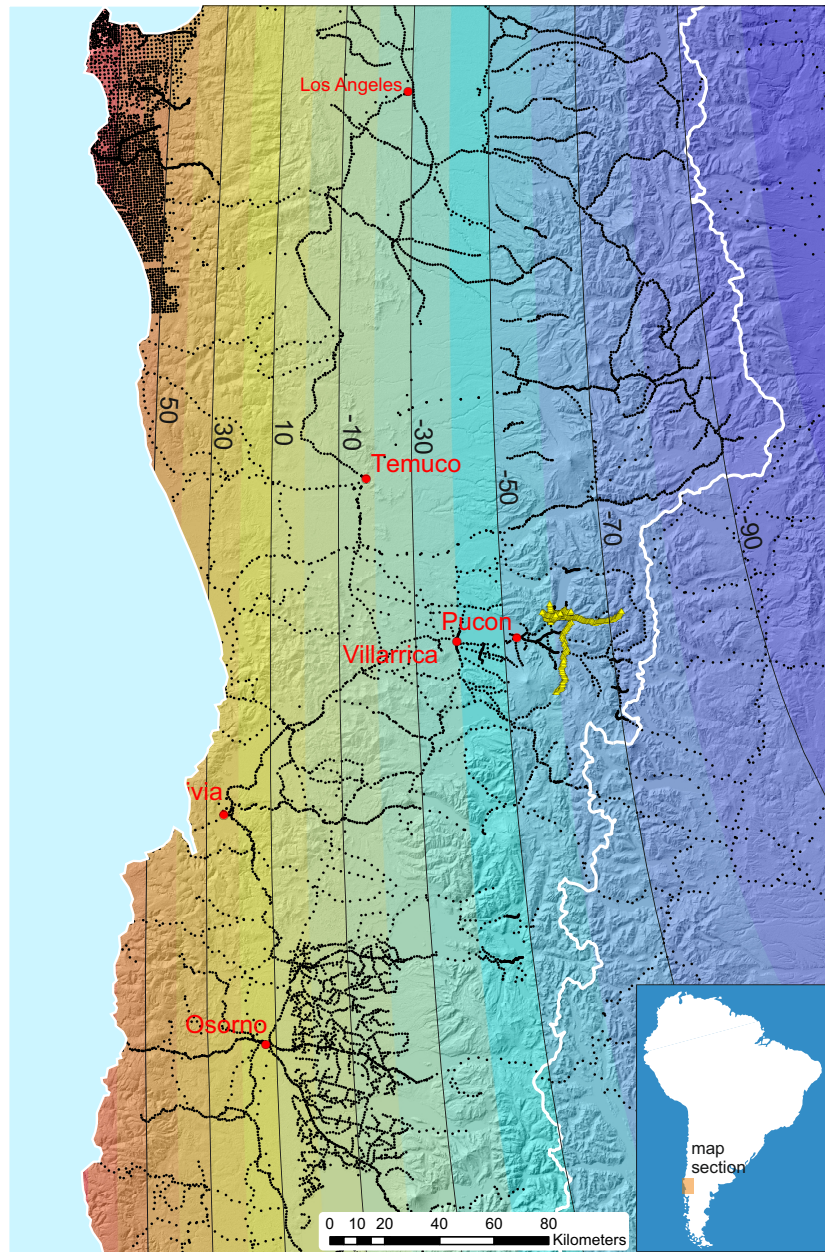


Figure 6.1.: Location of gravity measurement locations in southern Chile recorded by SFB267 (black dots) including the here presented measurements (yellow triangles) in the Villarrica area. Regional trend derived from Bouguer Anomaly by second order polynomial function.

Gravity data of Chile are recorded during multi-disciplinary program SFB 267 “Deformation Processes in the Andes” (Schmidt & Götze, 2006). The huge gravity dataset covers whole Chile north of 43°S with a minor gap in the Andean Cordillera between 30° and 37°S . The location of data points for southern Chile are depicted in Figure 6.1. Unfortunately the measurements do not possess the accuracy and resolution required for the investigation of spatially limited gravity signals of fault zones (compare chapter 6.2.2).

Magnetotelluric surveys recorded in Southern Chile (Brasse & Soyer, 2001; Kapinos et al., 2016) reveal effects of fault zone to subsurface conductivity distribution. The selected low frequency recordings do not have the capacity to resolve fault zone structure in general and especially in shallow depth. Held et al. (2016) investigate the fault zone structure in

detailed using a high-resolution magnetotelluric survey. Fault zone porosity was estimated from conductivity signatures alone yet limited in distinction between different conductivity increasing phases (fluids, clay minerals, etc.). This study benefits from the combination of the determined conductivity distribution with gravity signals, recorded in this study, to analyze the porosity and clay content of fault zones.

222 gravity data points are measured predominantly on two profiles following the MT profiles. Gravity data are processed yielding Bouguer Anomaly. Using Butterworth filtering techniques (Abdelfettah et al., 2014; Baillieux et al., 2014) the gravity signal wavelengths are analyzed revealing information about signal depth and extension. The density contrast of LOFS is quantified by gravity forward modeling. Finally gravity results are combined with magnetotelluric results in order to characterize the LOFS in terms of porosity and clay content. Identification of fault zone properties enable an estimation of hydraulic permeability and, hence, geothermal exploitability.

6.2. Methods

6.2.1. Acquisition of gravity and GPS data

A total of 222 gravity stations, following the perpendicular magnetotelluric profiles (Held et al., 2016), with an inter-station distance of 200–500 m were measured in October 2015. Measurements were conducted using a Scintrex®CG-5 Autograv gravimeter. The resolution of the gravimeter is $1 \mu\text{Gal}$. In case of local temporal disturbance gravity measurements were repeated until variance was $<0.01 \text{ mGal}$. Daily instrumental drift was determined by a looping procedure as base camp measurement site was recorded repeatedly each day. Instrumental drift correction and tide correction were applied to all gravity stations. Accurate positioning of gravity stations was ensured using two TRIMBLE R8 GNSS receiver. Elevation of each gravity station was determined using differential GPS between movable GNSS rover and stationary, continuously-running GNSS unit at base camp (-39.163577°S , -71.581492°W). GPS base station absolute coordinates were calculated using online GPS processing services (Auspos, GAPS, CSRS). At each gravity station further GPS measurements were conducted to determine the topography around the gravity measurement site as no detailed (digital) elevation model with a resolution $<30 \text{ m}$ is available. In total 817 GPS points were determined. Differential post processing, relying on determined absolute coordinates of base station, was done using Trimble Business Center (version 2.97) software improving horizontal and vertical precision significantly. GPS measurements with vertical precision $> 3 \text{ m}$ are discarded resulting in 798 GPS measurement with a mean vertical precision of 0.378 m . As a consequence two gravity stations have to be discarded (see gap between N-S and E-W profile, Figure 6.2).

The outcrops, sampled during geochemical survey, are used to estimate the densities of rock formations occurring in the research area. For sampling locations and details about the sampled outcrops compare chapter 8. Density is determined using Archimedes' principle. Rock formations are classified into plutonic, volcanic and volcano-sedimentary rocks as discussed in chapter 2. Plutonic and volcanic rocks have average densities of 2.71 and 2.69 g cm^{-3} respectively, with overlapping and moderate scattering (Figure 6.3). Rocks of volcano-sedimentary units have higher variations of density owed the different rock types accumulating in the Cura-Mallín formation (Suarez & Emparan, 1995). Generally lower densities are measured with an average value of 2.49 g cm^{-3} . Fluids of Liquiñe hot spring discharge out of a N-S aligned fault zone associated with LOFS. Two rock samples

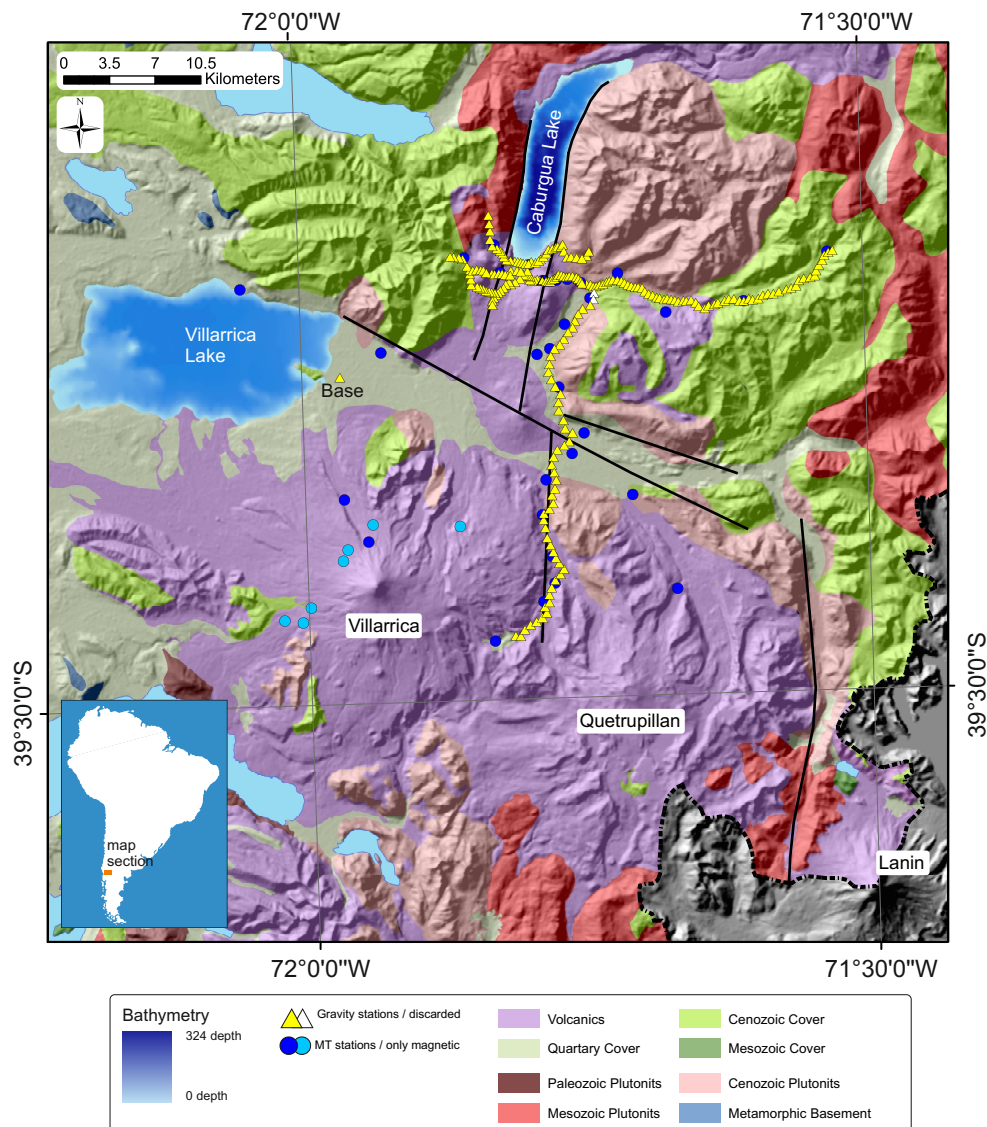


Figure 6.2.: Map of the research area around Villarrica-Quetrupillán-Lanín volcanic chain including geologic and topographic information. Detailed description of the regional geology is given in chapter 2. Gravity measurement locations marked by yellow triangles. For comparison, location of MT measuring sites are displayed by blue circles. Bathymetry of Caburgua and Villarrica Lake digitalized from maps of Servicio Hidrográfico y Oceanográfico de La Armada de Chile (Shoa). Shaded relief map derived from CGIAR-CSI version of SRTM data. Geological map modified after 1:1'000'000 scale map, Servicio Nacional de Geología y Minería, Chile by including interpretations from Cembrano & Lara (2009); Sánchez et al. (2013); Moreno & Lara (2008); Lara et al. (2004)

out of the fault zone were collected. The samples consist at least in part of fine grained hydrothermal alteration products. Densities are determined to 1.96 and 2.29 g cm⁻³.

6.2.2. Data processing

Prior to gravity processing topographic data have to be prepared. Digital elevation data is deduced from Shuttle Radar Topographic Mission (SRTM) with a resolution of 30 m (data provided by CGIAR-CSI). Bathymetry of Caburgua and Villarrica Lakes are digitalized from maps of Servicio Hidrográfico y Oceanográfico de La Armada de Chile (Shoa). From

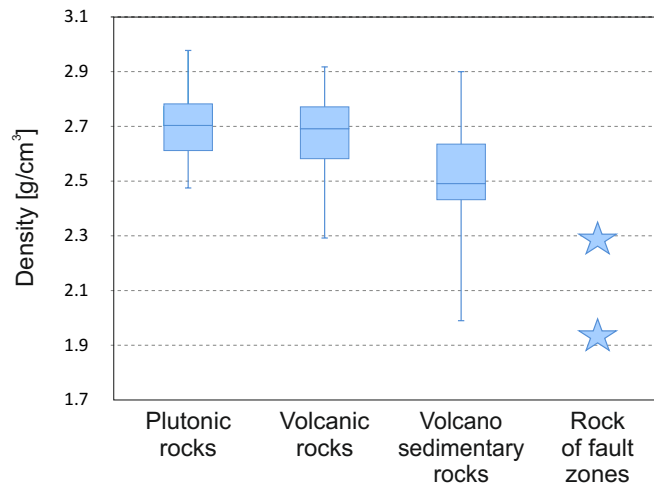


Figure 6.3.: Statistical density evaluation of rock formations occurring in the research area. GPS measurements a 5 m resolution digital elevation model (DEM) is generated for a radius of 45 m around the gravity stations.

The 220 gravity stations have been processed using the code GraviFor3D (Abdelfettah & Schill, 2011). The code computes gravimetric corrections simultaneously. Topographic data are discretized into rectangular prisms calculating the effect of each prism to each gravity station. Terrain correction considers topography up to a maximum distance of 167 km, with the higher resolution DEM for the inner zone (45 m radius) generated from GPS data.

Regional gravity trend is obtained from gravity survey of multi-disciplinary program SFB 267 “Deformation Processes in the Andes” (Schmidt & Götze, 2006). The regional trend is deviated from Bouguer anomaly (provided by Schmidt & Götze (2006) calculated with 2.67 g cm^{-3} Bouguer plate density) using second order polynomial function. The calculated regional trend is depicted (Figure 6.1) showing a strong decrease of Bouguer Anomaly from Pacific ocean towards the Andes, due to continuous increase of continental crust thickness (Krawczyk et al., 2006). The regional trend was subtracted from each Bouguer Anomaly of each gravity measurement of the local dataset. Data from SFB 267 were not re-processed and combined to the here measured dataset, as station locations were not determined by GPS. Thus vertical uncertainties can only be specified to $<20 \text{ m}$ increasing Bouguer uncertainty tremendously.

Unprocessed gravity measurements are displayed in Figure 6.4 by evaluation against station elevation. Gravity measurements situated inside the Villarrica-Quetrupillán-Lanín volcanic chain deviate by a flatter slope = -0.1715 (purple circles) from measurements north of the chain (slope = -0.2089). Neglecting terrain correction, from the slope of gravity-elevation relation a first estimate of Bouguer Plate density can be derived (Eq. 3.37). Inside the volcanic chain an average density of 3.277 g cm^{-3} is estimated, while for the northern sector densities of 2.38 g cm^{-3} are calculated. Those values contrast the density determination from outcrops. Nonetheless a density contrast between the volcanic chain and the sector north of it can be stated. Gravity stations presumably affected by higher bulk density are marked in displayed Bouguer anomaly (Figure 6.5).

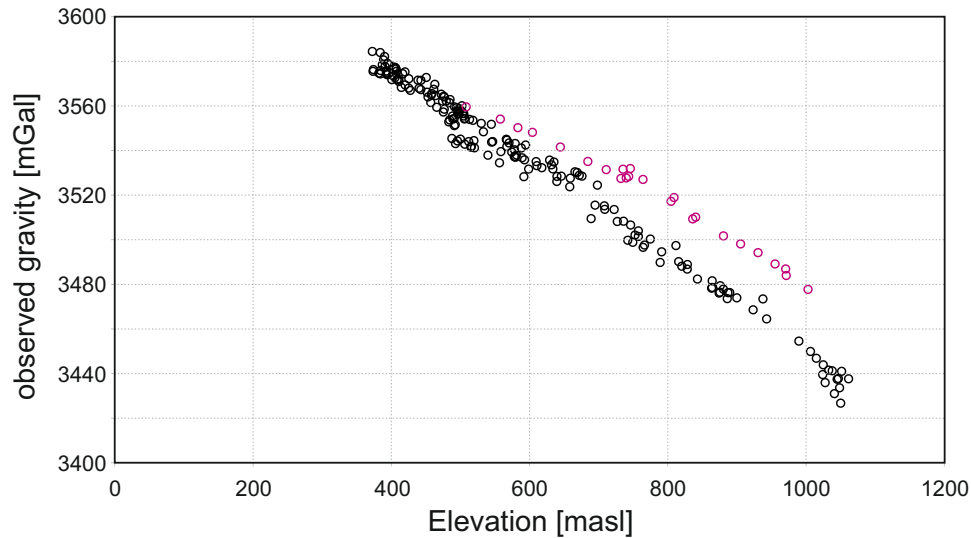


Figure 6.4.: Binary diagram of observed gravity vs. measured station elevation. Measurements inside the volcanic chain (purple) deviate significantly from measurements north of the chain.

6.2.3. Butterworth filtering

Gravity data, since being a potential field, presents the superposition of various signals of different size and depth resulting in the Bouguer Anomaly. Differentiation and localization of gravity anomalies, hence formations of diverging density, is substantial for identification of subsurface density distribution. [Abdelfettah et al. \(2014\)](#) introduce a method to localize Permo-Carboniferous graben structures in Northern Switzerland, which are target areas for geothermal energy production or shale gas exploitation. Their exploration concept based on the Butterworth filtering ([Butterworth, 1930](#)) technique applied on gravimetric datasets, which allow them to investigate the geometry and thickness of Permo-Carboniferous grabens. Previous to application on the Swiss dataset the authors demonstrate the performance of the technique by differentiating density anomalies in a synthetic model.

Different high-pass and bandpass Butterworth filters of varying wavelength are applied on the measured Bouguer anomaly. Investigated wavelengths are controlled by selected lower and upper cut-off frequencies. Short wavelengths, analyzed by application of high-pass filters, highlight gravity signals from shallow depth suppressing signals from large-scale, deep structures. Selection of bandpass filters suppress shallow, near surface density contrasts generated e.g. by Quaternary deposits and investigate density contrasts of long wavelength. [Guglielmetti et al. \(2013\)](#) use the technique in their geothermal prospection of Maritime Alps. The reduction of regional trends by application of high-pass filters enable the evaluation of the shallow gravity pattern highlighting geothermal zones by negative gravity anomalies related to regional fault zones. Within this study we apply the technique to investigate the gravimetric signal of the major fault zones to derive fault depths and geometry. Furthermore the prominent change in basement geology (see chapter 2 and chapter 8) and its effect on Bouguer Anomaly shall be investigated.

6.2.4. Gravity modeling

Subsurface density distribution is investigated by using gravity forward modeling. Based on the subsurface model from magnetotelluric investigations ([Held et al., 2016](#)) subsurface gravity distributions are generated in order to fit the measured Bouguer Anomaly. Forward

models are calculated using the Code g2D, developed by Yassine Abdelfettah. The code bases on concepts of Parasnis (1986) and Blackely (1995) computing the gravity response of 2D subsurface density distributions incorporating topography. Target of the forward models is the characterization of the fault zones. Therefore subsurface geometry and densities of the geologic features were modified iteratively. Starting from predicted density values and geometries, the contribution of the geological structures to the gravity response is determined by reduction of the misfit between modeled and measured gravity. The adjustment is performed for each structure individually.

6.3. Results

6.3.1. Processing of gravity data

Computed Bouguer Anomaly for E-W and N-S profiles are presented in Figure 6.5. As indications for different reference densities exist, Bouguer Anomalies are computed for different Bouguer Plate densities. Due to the quasi 2D distribution of the stations a spatial interpolation and presentation of Bouguer Anomaly is refrained. Uncertainties of gravity recording and elevation determination are calculated for each side presented in Figure 6.5. Uncertainties range between 0.33–1.14 mGal and the median is 0.45 mGal. For the E-W profile relative Bouguer Anomalies have a spread of 12.5 mGal ($\rho_{BP} = 2.3 \text{ g cm}^{-3}$) or 21 mGal ($\rho_{BP} = 3.3 \text{ g cm}^{-3}$) respectively. Bouguer anomaly for the N-S profile has the highest spread (21.7 mGal) for plate density of 2.3 g cm^{-3} and 16.7 mGal for a Plate density of 3.3 g cm^{-3} . As the regional trend was removed from the data (Figure 6.1) the apparent anomalies are related to local density contrasts.

First approximation of reference densities for the northern sector indicate on lower densities of 2.38 g cm^{-3} (Chapter 6.2.2). However plutonic and volcano-sedimentary rocks prevail along the E-W profile having mean densities of 2.71 g cm^{-3} and 2.49 g cm^{-3} respectively. Comparison of shape of Bouguer Anomaly and relief, so-called Nettleton's method (Figure 6.5), discards high reference densities ($\rho_{BP} \geq 3.0 \text{ g cm}^{-3}$) by a negative correlation between topography and Bouguer Anomaly and low reference densities ($\rho_{BP} = 2.3 \text{ g cm}^{-3}$) by a positive correlation. By visual inspection 2.45 g cm^{-3} is identified to be the density least affected by topographic effects. Nevertheless, as uncertainties remain in the following Bouguer Anomalies computed by reference densities of 2.45 and 2.7 g cm^{-3} are considered for interpretation of the E-W profile.

For both reference densities two negative Bouguer anomalies in the western part of the profile are recognizable. The eastern negative anomaly corresponds with a topographic height related to Caburgua scoria cone, while the western anomaly is located below Caburgua Valley. Both anomalies are situated along fault zone branches of LOFS running along east and west shores of Caburgua Lake. At both reference densities the eastern anomaly has a more negative signature. The negative anomalies are separated by a constrained, positive anomaly of steep gradients particular towards its eastern side. Besides these small-scale anomalies the Bouguer Anomaly for both reference densities increases to higher values towards the west. Towards the east the Bouguer anomaly computed with $\rho_{BP} = 2.7 \text{ g cm}^{-3}$ shows a constant plateau with minor, small-scale variations, while the Bouguer anomaly of $\rho_{BP} = 2.45 \text{ g cm}^{-3}$ trend towards positive values, decreasing again at the end of the profile. For the Bouguer anomaly of $\rho_{BP} = 2.45 \text{ g cm}^{-3}$ a negative anomaly with a long wavelength, spanning the whole profile, could be assumed generating the positive anomalies towards the profiles margins superimposing fault zone signatures.

For the N-S profile a general density contrast is indicated (see chapter 6.2.1). The locations of stations, influence by higher densities, are marked by a grey shading. For the northern sector Bouguer plate densities between 2.45 and 2.7 g cm^{-3} , selected for processing of E-W profile, are plausible, while at the volcanic chain higher reference densities are assumed. This is supported by the positive correlation between topography and Bouguer Anomaly if calculated with ρ_{BP} between 2.3 and 2.7 g cm^{-3} . Independent from reference density beginning at the northern margin the Bouguer Anomaly decreases towards a minimum in the central part of the profile still outside the volcanic domain. This gravity anomaly is located at Trancura Valley, where Quaternary sediments are deposited at least superficially (Moreno & Lara, 2008). Furthermore a WNW-ESE aligned fault zone is assumed to be located in that Valley (Figure 6.2). The volcanic chain is characterized by a higher Bouguer Anomaly with a constrained maxima between UTM = $5\,630\,000$ - $5\,635\,000 \text{ mS}$.

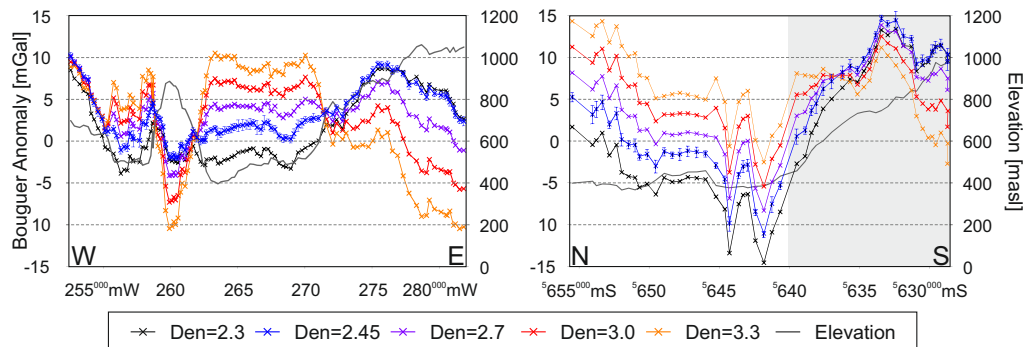


Figure 6.5.: Computed Bouguer Anomaly along a) E-W profile and b) N-S profile using varying densities in order to determine appropriate bulk densities (Nettleton method). By eye a density of 2.45 g cm^{-3} is determined least affected by topography for the E-W profile. Due to obtain a better visibility measurement uncertainties are shown just for 2.45 g cm^{-3} reference density.

6.3.2. Results from Butterworth filtering

Butterworth filtering is applied to reveal the geometry and depth of gravity signal origin. Therefore several high-pass filter of differing cutoff wavelengths (10, 20, 60 km) are used to highlight signals from shallow depth. Additionally bandpass filter of constant lower cutoff wavelength of 60 km and variable upper cutoff wavelength of 10, 20 and 30 km are selected to mask the impact of shallow structures. For both profiles Butterworth filtering is applied on the two datasets processed with different Bouguer Plate densities (2.45 and 2.7 g cm^{-3}).

For the E-W profile (Figure 6.6), the selected bandpass filters cannot reproduce the shape of the processed Bouguer Anomaly. Whether the 10/60 km bandpass filter partially indicates positive gravity anomalies to the west and east (Figure 6.6a) no significant gravity anomalies are identified by filters of increasing upper cutoff wavelength. On the contrary the anomalies associated with the LOFS are traced by the high-pass filters. The positive anomaly, separating the local negative anomalies, is marked by an overlap of all high-pass filters. Increasing cutoff wavelength does not change the gravity signal of that local positive anomaly indicating a very shallow depth of origin. The local negative gravity anomalies associated with the two fault zone branches, are reproduced by all selected high-pass filters. Yet the adjustment between Bouguer Anomaly and filtering response improves with increasing cutoff wavelength. Hence, the structures can be interpreted to occur in shallow depth reaching until intermediate depth. The positive gravity anomalies to the

profile' margins can be best matched by the 60 km high-pass filter. Also the 10/60 km bandpass filter reveals part of the signal. The inducing structures have shallow components yet reaching also greater depth. Note that the eastern maximum of Bouguer Anomaly computed with 2.45 g cm^{-3} plate density cannot be traced by any Butterworth filter exactly.

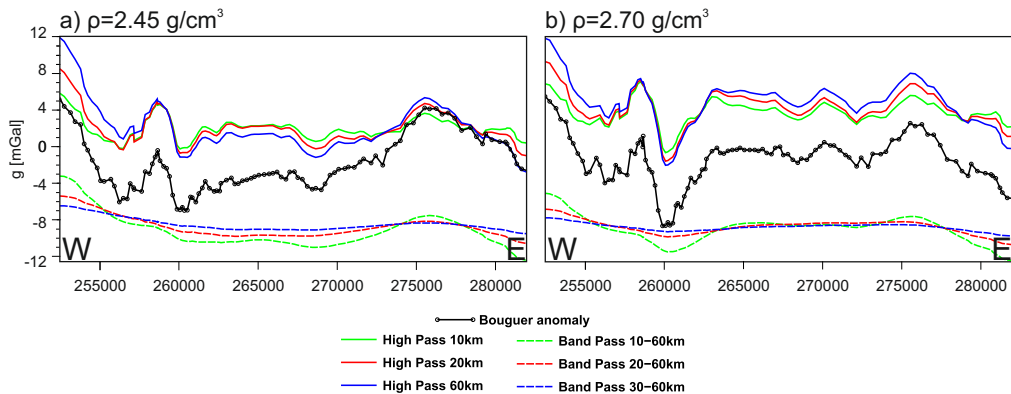


Figure 6.6.: Residual anomalies of E-W profile, calculated with a) 2.45 g cm^{-3} and b) 2.70 g cm^{-3} reference density, computed by application of high-pass and band-pass Butterworth filters.

In contrast to the situation of the E-W profile, for the N-S profile the Bouguer Anomaly can be appropriately matched by the 10/60 km bandpass filter (Figure 6.7). Considering the characteristics of the method it's obvious that the high-pass 60 km filter matches the Bouguer Anomaly as well. Yet high-pass filters of smaller cutoff wavelengths cannot display the shape of Bouguer Anomaly, especially with respect to positive maxima towards the north and inside the volcanic chain. Thus the prominent density contrasts are related to structures of higher wavelength, thus generated in greater depth or by greater lateral expansion. The local minimum in the center of the profile is reproduced by all high-pass filters indicating small-scale, shallow origin.

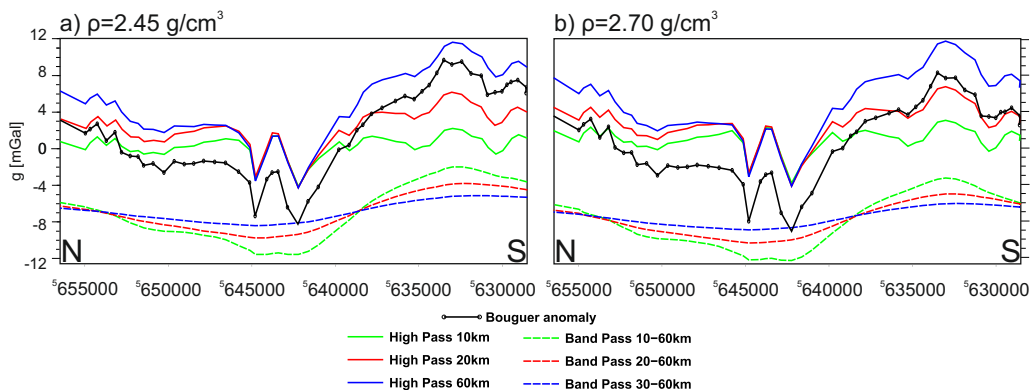


Figure 6.7.: Residual anomalies of N-S profile, calculated with a) 2.45 g cm^{-3} and b) 2.70 g cm^{-3} reference density, computed by application of high-pass and band-pass Butterworth filters.

6.3.3. Gravity forward modelling

In the following the density decrease due to faulting of LOFS is quantified. Therefore forward models on E-W profile of different fault geometries and densities are computed to

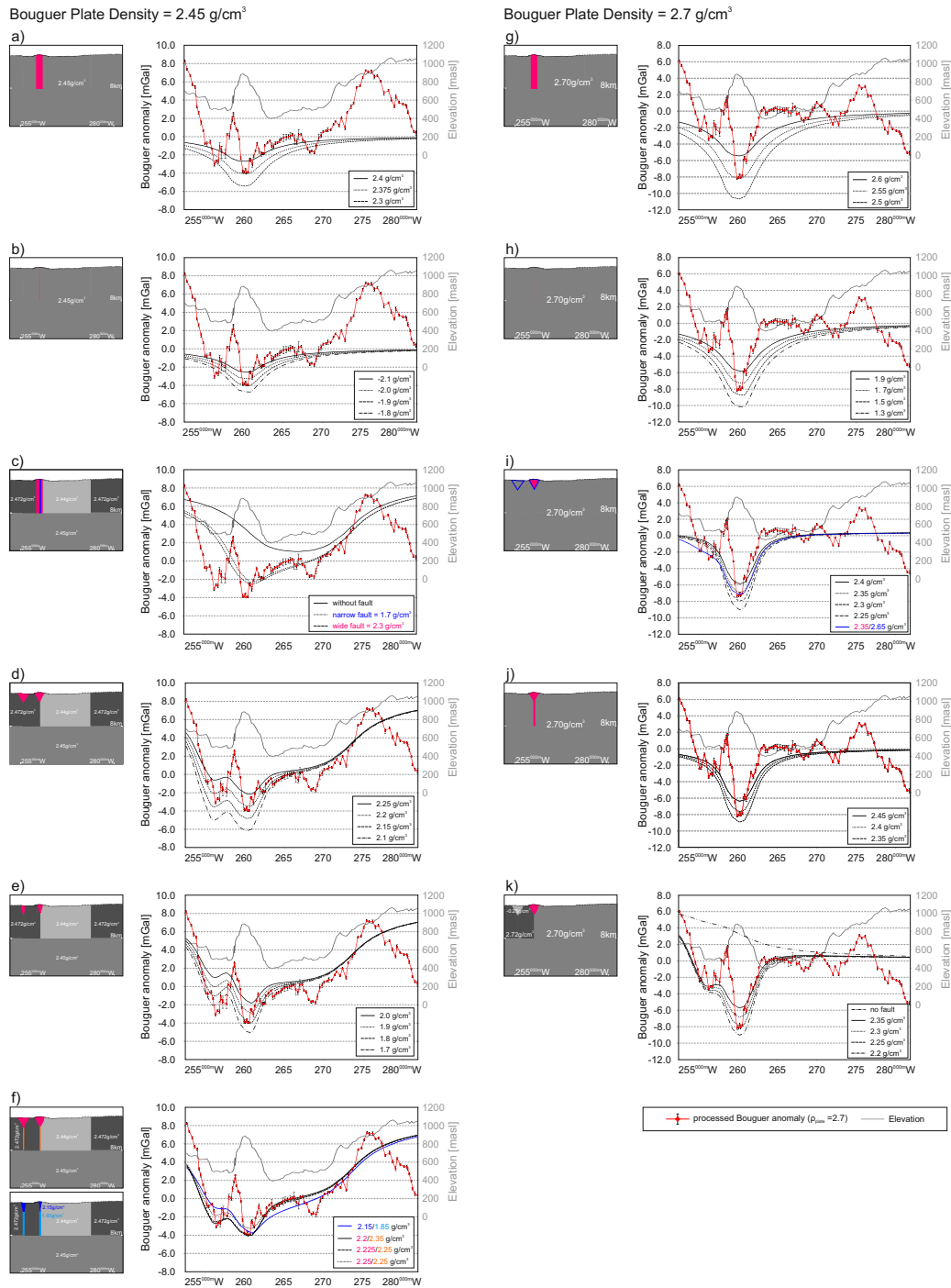


Figure 6.8.: Results of 2D gravity forward modeling along E-W profile using reference density of 2.45 g/cm^3 (left) and 2.70 g/cm^3 (right). The six respectively five different plots display results of varying geometries, which are presented in the scheme to the left of each plot. Each curve represent density variations for the colored features of the subsurface model.

match the measured Bouguer Anomaly. As the modeling targets LOFS, a minimization of misfit between modeled and measured gravity is focused on central parts of E-W model intersecting LOFS. As uncertainties concerning reference density remain, forward models are computed for both selected densities: 2.45 g cm^{-3} (Figure 6.8a-f) and 2.70 g cm^{-3} (Figure

6.8g-k). Starting geometries are derived from results of magnetotelluric measurements (Chapter 5) by incorporation of (1) a 2 km wide (Figure 6.8a and g) and (2) a narrow 250 m wide, both vertical fault zone (Figure 6.8b and h) reaching a depth of 8 km. Examining the shape of model response it's getting obvious that Bouguer Anomaly cannot be reproduced using that simplified model. Consequently adjustment of model response is done by the application of more complex models, still keeping the geometries simple. The overall shape of Bouguer Anomaly, calculated with 2.45 g cm^{-3} reference density, possess a minimum of long wavelength situated in the center of the profile. Two reproduce that gravity signal, theoretically two scenarios are worth considering: 1) a low density structure in greater depth centered below the minimum or 2) density contrast in shallow to intermediate depth with higher densities at both profiles margins. With respect to results of Butterworth filtering option two was preferred (Figure 6.8c).

MT publication suspected that the LOFS forms a flower structure along the Caburgua Lake. Thus, different simplifications adapting flower structure geometry are tested (Figure 6.8d-f and i-k). The shape of the gravity anomalies of both reference densities differs significantly in the LOFS affected part of the profile. Whether the positive anomaly remains unchanged, the negative anomalies differ noticeable from each other concerning amplitude and geometry. [Moreno & Lara \(2008\)](#) assume that the LOFS has two branches running on both shores of the Caburgua Lake (Figure 6.2). The gravity anomaly computed with 2.45 g cm^{-3} reference density shows two negative anomalies of comparable amplitude located on the continuation of both shores of Caburgua Lake. The 2.70 g cm^{-3} Bouguer Anomaly has an sole minimum at the eastern branch of the LOFS and merely a local, limited minimum at the western branch.

Best adjustment results regarding the central parts are obtained for geometries and densities presented in Figure 6.8f and Figure 6.8k. The density contrasts between bulk rock and fault zone affected areas are quantified to 0.225 g cm^{-3} , computed with 2.45 g cm^{-3} reference density, and 0.45 g cm^{-3} , assuming 2.70 g cm^{-3} reference density. Those values have to be interpreted as reflecting average densities of a wider fault zone body, that certainly possess internal density contrasts. The positive anomaly, separating the two minima, cannot be reproduced with any 2D modeling approach. We deduce strong but local impacts of 3D subsurface structure. The steep gradients of Bouguer Anomaly combined with the short wavelength hint on small-scale bodies of elevated density.

6.4. Discussion

The LOFS is an active, major fault zone associated with location of several stratovolcanoes in the SVZ ([Cembrano & Lara, 2009](#)). The fault system has a significant electromagnetic signal identified by magnetotelluric measurements ([Brasse & Soyer, 2001](#); [Kapinos et al., 2016](#); [Held et al., 2016](#)). The here presented gravity dataset documents a strong effect of the LOFS to subsurface density distribution. Low gravity values are associated with the run of LOFS indicating low densities in the subsurface. Two gravity minima are depicted. The eastern minimum corresponds to the predicted eastern branch of LOFS (e.g. [Moreno & Lara, 2008](#)). Along this fault branch Quaternary volcanic activity is documented in form of small eruptive centers ([Hickey-Vargas et al., 2002](#)). The eastern branch has the more negative gravity response. High frequency MT data locate the center of an area of decreased resistivities $30 \Omega\text{m}$ at the eastern branch ([Held et al., 2016](#)). The western, less intense gravity anomaly coincides with the western branch of LOFS, which has no

significant electromagnetic signal. Nevertheless, the contribution of alluvial sediments in the Caburgua Valley decreasing gravity cannot be excluded.

Butterworth filtering reveal a shallow to intermediate depth of the fault zone, matching with magnetotelluric results displaying a vertical conductor up to depth of 8–10 km. Gravity forward modeling generates a best-fit between the modeled gravity response and Bouguer Anomaly by broader areas of decreased density in shallow depth narrowing with increasing depth. The selected geometry assumes a flower structure type fault zone. Maximum gravity contrast of -0.235 g cm^{-3} and -0.45 g cm^{-3} were determined considering the modeling results of the different reference densities.

Decrease of rock density by fracturing is a well-known phenomenon (Telford et al., 2012). It is assumed that density reduction results from hydrothermal alteration and dissolution as stress-induced cracks are not supposed to decrease the porosity and, hence, density to that extent (Wang et al., 1986). Density contrasts associated to faults and fractures are documented based on gravimetric investigations. Guglielmetti et al. (2013) studied geothermal hot springs in the Maritime Alps and computed density contrasts of -0.15 g cm^{-3} for local fault zones associated with fluid ascent. Schill et al. (2010) determined density contrasts of -0.2 g cm^{-3} for fault zones inside the Soultz geothermal reservoir. For the San Andreas fault near Bear Valley a density contrast of -0.25 g cm^{-3} is computed (Wang et al., 1986). For those studies porosities between 10–12 % are calculated. In case of Soultz the computed porosity values (Baillieux et al., 2014) fall within the porosity range measured at cores from the geothermal reservoir (Géraud et al., 2010).

In the following fault zone characteristics are studied by evaluation of porosity, cementation factor and clay filling. Therefore results of gravity and magnetotellurics are combined decreasing the number of variables in the procedure. Gravity results, hence modelled density contrast ρ_{mod} are coupled to fault zone characteristics using equation 6.1:

$$\rho_{mod} = \rho_f * \phi + ((1 - \phi)\chi_{clay})\rho_{clay} + (1 - \phi - ((1 - \phi)\chi_{clay}))\rho_s \quad (6.1)$$

where ρ_f is the density of fluid at reservoir conditions, ϕ the porosity, χ_{clay} the proportion of clay in the rock matrix and ρ_s and ρ_{clay} the bulk rock respectively clay mineral density. Combination of gravity and magnetotelluric (fault zone resistivity of $30 \Omega\text{m}$) results is conducted in a first step following Archie's law (Archie, 1942) determining porosity and cementation factor, while in the second step clay content is additionally considered using calculations after Waxman & Smits (1968). Basic principles and equations (Eq. 5.3 and 5.4) are presented in Chapter 5. Parameters needed are summarized in Table 6.1. Average densities of clays are taken from Kaden (2012). Average values of cation exchange capacity (CEC) of illite are extracted from Kaden (2012) and Schnetzer (2017) and for smectite from Wolters et al. (2009) and Schnetzer et al. (2016). Investigation of meteoric dilution yield minimum degrees of dilution of a few percent (Chapter 8). For determination of fluid conductivity σ_f at reservoir conditions, maximum fluid density of $1340 \mu\text{S/cm}$, measured in Termas Toledo, is corrected for dilution and temperature (Dakhnov, 1962) estimating 140°C maximum reservoir temperature (Chapter 4).

Determination of fault zone fillings neglecting clay content (Archie approach) by combination of equations 5.3 and 6.1) yield unique solutions as number of equations are equal to number of unknowns (ϕ , cementation factor m). Density contrasts and fault zone resistivity can be reproduced by a porosity of 14.9 % and a cementation factor $m = 1.37$ considering the model based on a reference density of 2.45 g cm^{-3} . In terms of porosity the calculated

Table 6.1.: Parameters used in fault zone characterization using the equations of Archie (1942) and Waxman & Smits (1968).

		Archie	Waxman & Smits
Resistivity bulk rock	Ωm	10 000	10 000
Conductivity fluid [at discharge conditions]	S m	7.46	7.46
Fluid dilution	%	5	5
Conductivity meteoric fluid	S m	0.004	0.004
Bulk rock density ρ_s	g cm^{-3}	2.45	2.45
Density fluid ρ_f [at reservoir condition]	g cm^{-3}	0.926	0.926
Estimated reservoir temperature	$^{\circ}\text{C}$	140	140
Density Illite ρ_{clay}	g cm^{-3}		2.73
CEC Illite	$\text{meq}/100\text{g}$		22
Density Smectite ρ_{clay}	g cm^{-3}		2.67
CEC Smectite	$\text{meq}/100\text{g}$		80

values matches computations of other studies (Baillieux et al., 2014; Wang et al., 1986; Guglielmetti et al., 2013). Cementation factor m is measure for the connectivity of pore space. For consolidated sandstone cementation factors between 1.8–2.0 are commonly used (Archie, 1942). For permeable fault zones low cementation factors of 1.0 - 1.6 are expected (Türkoğlu et al., 2015; Bertrand et al., 2012). The here calculated value matches the expected range. Density contrast of gravity modeling with reference density of 2.70 g cm^{-3} yield a porosity of 25.4% and a cementation factor of 1.91. The results are doubtful as a high connectivity, thus a low cementation factor could be assumed by that high porosities. Furthermore the computed values contradict the above mentioned observations for fault zones.

Clay minerals are formed by hydrothermal alteration (Browne, 1978; Velde, 1995), which have a strong impact on rock conductivity due to their ability to carry charges in their interlayers. Clay minerals abundance, affecting the resistivity and density of LOFS, is evaluated using the equations after Waxman & Smits (1968) (Equations 5.4 and 6.1). In geothermal reservoirs the occurrence of illite and smectite is often observed affecting rock resistivity strongly. Smectite has due to high cation exchange capacity (Wolters et al., 2009) a high conductivity while the conductivity of illite is, in general, lower (Emerson & Yang, 1997; Ussher et al., 2000). The abundance of clay minerals by considering the differences on resistivity of both illite and smectite is evaluated. As the equation system is underdetermined, for each porosity and cementation factor clay content is calculated minimizing above mentioned equations. Values are discarded if tolerance of $\pm 5 \Omega\text{m}$ and $\pm 0.05 \text{ g cm}^{-3}$ is exceeded. Mathematically valid results considering again both reference densities are presented in Figure 6.9. For comparison results of Archie approach are included, possessing, as expected, a calculated clay content of 0%. For reference density of 2.45 g cm^{-3} (Figure 6.9 a and b) mathematical solutions are achieved for a porosity range between 11–21% depending on cementation factor and clay content. Higher cementation factors require enhanced proportions of clay to reduce fault zone resistivity to the observed values. Increasing porosity entails decreasing clay contents to balance the contribution to fault zone conductivity. For lower cementations factors $m = 1.0 - 1.6$, presumably valid for permeable fault zones, low percentages of clay minerals in order of $\leq 2\%$ (smectite) or $\leq 5\%$ (illite) are computed. The presence of smectite in the fault zone naturally yields lower clay proportions compared to the presence of illite due to its higher CEC and, thus, conductivity. The determination of a small amount of clay minerals in the fault

zones confirms the observations of chapter 4, where no clay mineral outcrops or zones of hydrothermal alteration were found in the Villarrica area.

For a reference density of 2.70 g cm^{-3} only porosities above 22% and high cementation factors yield mathematically valid results (Figure 6.9 c and s) confirming computations by Archie approach. Considering also findings obtained during gravity processing (Chapter 6.2.2 and 6.3.1) the results indicate that 2.45 g cm^{-3} might be the valid reference Bouguer Plate density along the E-W profile.

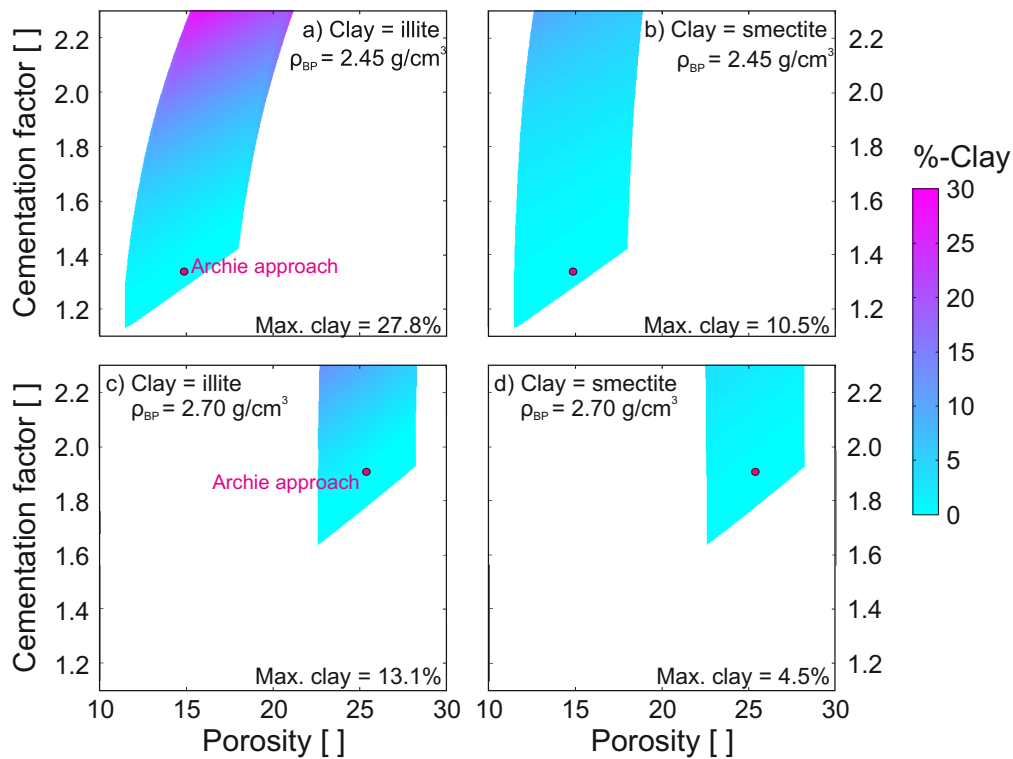


Figure 6.9.: Evaluation of fault zone characteristics by investigation of porosity, clay content and cementation factor according to Waxman & Smits (1968) equations. Results from Archie approach incorporated yielding an explicit solution neglecting clay content. Results based on reference density of 2.45 g cm^{-3} are presented in a) and b), while results from reference density of 2.70 g cm^{-3} are shown in c) and d). Clay content computed assuming the occurrence of illite displayed in a) and c) and smectite presented in b) and d)

6.5. Conclusion

High-resolution gravity measurements accompanying the magnetotelluric survey complement investigations of the tectonic and geothermal setting of the Villarrica geothermal system by disclosure of the characteristics of major fault zones. N-S striking, intra-arc LOFS crosscutting the geothermal systems is target of the investigations studying the fault zone composition in terms of porosity and clay content. Major observations are summarized:

1. The location of LOFS coincide with a significant negative Bouguer Anomaly that could be related to low density fault zone

2. Butterworth filtering assigns the gravity signal to originate from shallow to intermediate depth confirming magnetotelluric results detecting reduced resistivities until 8–10 km depth
3. Forward modeling quantifies gravity contrast of LOFS in comparison to undisturbed bulk rock to 0.225 g cm^{-3}
4. Combination with fault zone resistivity, fault zone porosity can be constraint to $\approx 11\text{--}20\%$. Clay mineral content is determined to be $<5\%$ depending on clay mineral type.

The investigations of fault zone composition show that the LOFS possesses an elevated porosity and low amount of clay minerals. Consequently a high permeability is assumed confirmed by the occurrence of hot springs discharging along the run of LOFS (compare chapter 7: Palguín, Liucura, Liquiñe, Carranco, Chihuío hot springs).

7. Hydrochemistry of the hot spring fluids of Villarrica geothermal system in the Andes of Southern Chile

This manuscript has been published in *Geothermal Research Council Transactions*

SEBASTIAN HELD, FABIAN NITSCHKE, EVA SCHILL, DIEGO MORATA, ELISABETH EICHE and THOMAS KOHL [2017]: Hydrochemistry of the hot spring fluids of Villarrica geothermal system in the Andes of Southern Chile; *Geothermal Research Council Transactions* (41)

Abstract

The Villarrica-Quetrapillán-Lanín volcanic chain is surrounded by >20 hot springs, located on the flanks and in the valleys around the volcanos. The hot springs that are extensively used for spa purpose discharge thermal water of intermediate temperatures (27° - 81 °C), mostly alkaline pH and low mineralization. To investigate fluid origin and genesis of Villarrica geothermal system the thermal waters are analyzed for hydrochemical composition, $\delta^{18}\text{O}/\delta\text{D}$ isotopes and $^{87}\text{Sr}/^{86}\text{Sr}$ isotope ratios. They are Na dominated indicating strong water-rock interaction. Anion composition varies significantly, without any clear spatial relationship. The majority of springs have similar concentrations of major anions spreading between the SO_4 , bicarbonate- and Cl-endmembers. Magmatic degassing can be traced solely by slightly elevated B concentrations in springs around the volcanic chain. Conformity with other species that might originate from magmatic degassing (e.g. Cl, SO_4 , bicarbonate, F) is not observed. Apart from a few springs located on the flanks of the volcano, full equilibrium is reached. The $\delta^{18}\text{O}/\delta\text{D}$ isotope signatures reveal a meteoric origin of thermal waters. $^{87}\text{Sr}/^{86}\text{Sr}$ ratios enable a tentative allocation to plutonic and volcanic host rocks south and north of the volcanic chain. In conclusion, the thermal waters can be described as originating from water-rock interaction between igneous rocks and meteoric waters reaching full equilibrium with minor impact of magmatic degassing at the volcanic chain.

7.1. Introduction

The hot springs of the Villarrica geothermal system are located in the surroundings of the Villarrica volcano (-39.4205°S, -71.9397°W), which is part of the WNW-ESE aligned Villarrica-Quetripillán-Lanín volcanic chain. Among those, frequent activity occurs only at Villarrica (Petit-Breuilh & Lobato, 1994). Geologically, the system is characterized by intersecting fault zones and a prominent lithology change between the North Patagonian Batholith (NPB) in the south and the Cura-Mallín Formation in the north. The spatial distribution of hot springs shows significant differences on both sides of the volcanic chain (Figure 7.1). South of the chain, the number of springs is limited to a few that are located along major fault zones, while north of it, a larger number of springs are distributed over an extended area often related to secondary faults and fractures or boundaries between different rock types.

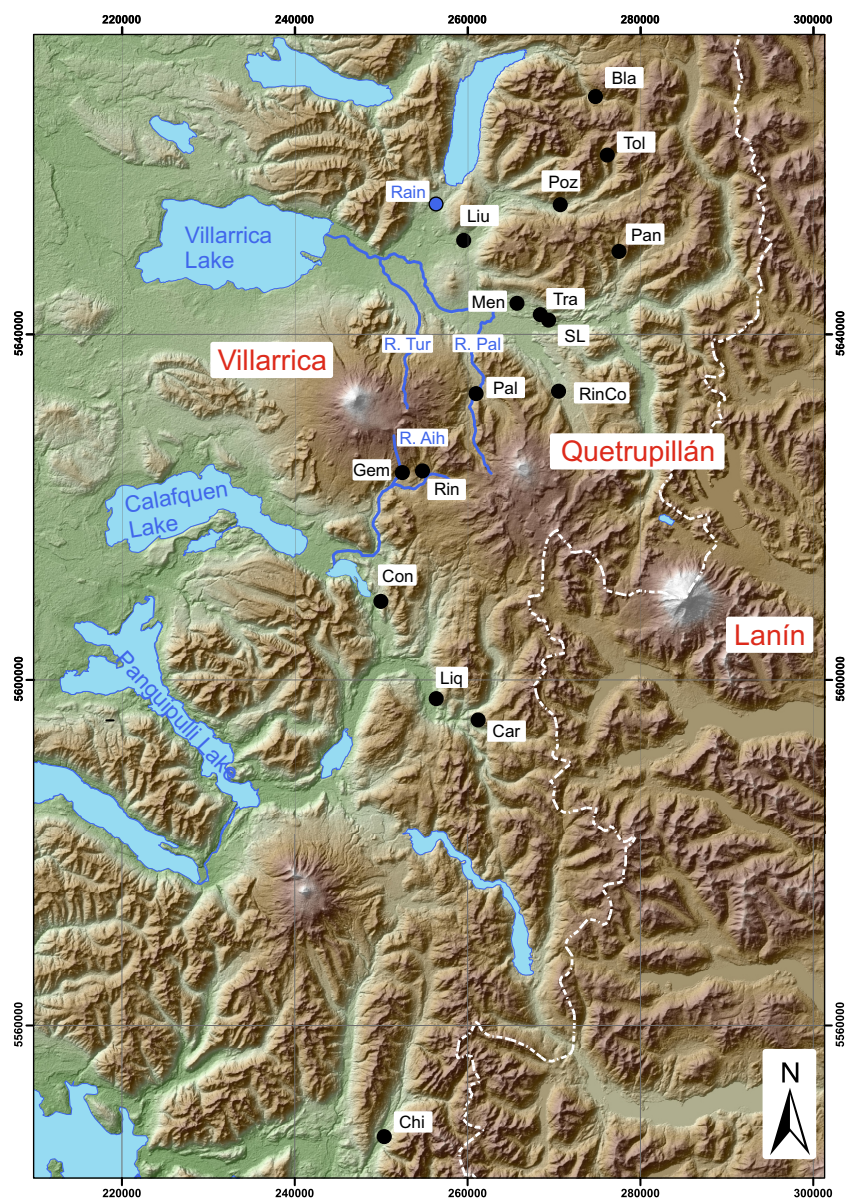


Figure 7.1.: Relief map of research area including the location of hot springs (black circles) and meteoric water (blue: lakes, rivers, rainfall). Shaded relief map derived from CGIAR-CSI version of SRTM data

The springs reveal intermediate outflow temperatures of 27–80 °C (Hauser, 1997), slightly acidic to mostly alkaline pH values of 6.1–9.3 and low total dissolved solids (TDS) $<900 \text{ mg L}^{-1}$. At most locations, springs discharge in different outflows with discharges of around 1 L s^{-1} (Pérez, 1999). The springs are investigated geochemically in a regional study on the Villarrica and Mocho-Choshuenco volcanic systems by Sánchez et al. (2013), who suggests a distinction between geothermal discharges affected by the different regional fault systems with reservoir temperatures $<180 \text{ °C}$. This coincides with the documented absence of a high-enthalpy geothermal system (Held et al., 2015, 2016).

With the overall aim to understand the complex flow system, in this first study we investigate the origin and genesis of the thermal waters based on chemical and isotope fluid composition. Identification of equilibrium state is the key target, as further fluid evaluation (e.g. geothermometry, dilution analysis, etc.) requires the assumption of water-rock equilibrium. As direct interaction between host rocks and thermal waters on basis of hydrochemical compounds is masked by temperature controlled processes (e.g. cation exchange in feldspars) and secondary alteration processes, we use Sr isotopes to identify the host rock.

7.2. Geological setting

The geological and tectonic setting of the Chilean Andes is a result of the oblique subduction of the Nazca Plate beneath the South American Plate, generating active volcanism along the SVZ (Stern, 2004). Volcanic centers and also their characteristics are spatially related to prominent structural weak zones (Lara et al., 2006; Cembrano & Lara, 2009).

Structurally, the southern SVZ is dominated by the Liquiñe-Ofqui fault system (LOFS), a N-S to N10°E aligned, major intra-arc fault zone at 37°S - 48°S (Cembrano et al., 1996). In the study area, the LOFS crosses the volcanic chain between Villarrica and Quetrupillán volcanos (Moreno & Lara, 2008). The LOFS is accompanied by NE and NW faults. The latter are deeply rooted and so-called Andean Transverse Fault (ATF) zones (Pérez-Flores et al., 2016) that are interpreted as pre-Andean (Rapela & Pankhurst, 1992). They are unfavorably oriented for reactivation in the current stress field (Cembrano & Moreno, 1994). North of Villarrica, LOFS is intersected and offset by such an ATF, the WNW-ESE striking Mocha-Villarrica fault zone (MVFZ). The Villarrica-Quetrupillán-Lanín volcanic chain follows the orientation of MVFZ.

At the Villarrica-Quetrupillán-Lanín volcanic chain, the geology is marked by the above mentioned lithology transition (Figure 7.9). Volcano-sedimentary rocks of the Cura-Mallín formation gradually replace the plutonic rocks of the NPB (Hervé, 1984; Munizaga et al., 1988). The batholith complex was emplaced during episodic magmatic events between Late Jurassic to Pleistocene age (Pankhurst et al., 1999). Plutonic rocks of Cretaceous and Miocene age prevail possessing dioritic to tonalitic composition (Adriasola et al., 2005). Rocks of the Cura-Mallín formation are deposited between Eocene and Miocene age in a sequence of intra-arc basins under extensional tectonics (Jordan et al., 2001; Charrier et al., 2007). The formation shows a high variety of deposited rocks ranging from lacustrine, deltaic and fluvial sediments to a volcanic facies of pyroclastic deposits and lava flows (Radic, 2010; Suarez & Emparan, 1995).

7.3. Materials and Methods

A number of 15 hot springs in the study area were sampled, analyzed (Figure 7.1) and completed by data of [Sánchez et al. \(2013\)](#) for Termas Geométricas, where the access was denied. Chihuío hot spring further south along the continuation of LOFS was additionally selected (Figure 7.1) to increase the number of springs along the LOFS. To assess the signature of meteoric water additional sampling of rainfall, lake and river water was completed from literature ([Risacher et al., 2011](#); [Pérez, 1999](#)) (Table 7.1, Figure 7.1)

During fluid sampling, temperature, pH-value (SenTix 41), specific electrical conductivity (TetraCon325), dissolved oxygen content (CellOx325) were (all measured with a WTW Multi 340i) and pKS_{4.3} and pKS_{8.2} (both acidimetric titration with 0.01 M HCl), were measured on site. At each spring, the discharge with maximum temperature was selected for sampling. Water samples were prepared for laboratory analysis by filtering (cellulose acetate, pore size <0.45 µm) and acidified with nitric acid (sub-boiled) for cation analysis immediately after sampling. Samples for isotope measurements ($\delta^{18}\text{O}$, δD , $^{87}\text{Sr}/^{86}\text{Sr}$) were collected without further treatment. Fluids were stored in polyethylene vessels avoiding any head space.

If not mentioned otherwise, fluid analyses were made at the Karlsruhe Institute of Technology, Germany. Samples were analyzed for cations by inductively coupled plasma mass spectrometry (ICP-MS: Thermo Fisher, X-Series2) and anions by ion chromatography (IC: Dionex, ICS-1000). Quality assurance was done by including certified water into the measuring procedure (ICP-MS: CRMTMDW-A; High Purity Standards, USA; IC: River Water CRM-LGC6020). Aqueous SiO₂ was determined photometrically based on silicomolybdenum-complexes with a Perkin Elmer Lambda 2S. Stable water isotope analysis (expressed as $\delta^{18}\text{O}$ and δD ‰V-SMOW, respectively) was conducted using cavity-ring-down spectroscopy with a Liquid-Water Isotope Analyzer 24d (Los Gatos Research). Sr isotope ratio measurements of thermal waters were performed using thermal ionization mass spectrometry at IsoAnalysis UG, Berlin (TIMS: Micromass Sector 54). Reproducibility for each parameter, determined by repeated measurements of samples or standards is given in Table 7.1.

Table 7.1.: Outlet temperatures (in °C), pH, chemical composition, $\delta^{18}\text{O}/\delta\text{D}$ and $^{87}\text{Sr}/^{86}\text{Sr}$ values of the thermal discharges from Villarrica geothermal system, southern Chile; n.a.: not available, n.m.: not measured, bdl.: below detection limit; Data source a) this work, b) Sánchez et al. (2013), c) Risacher et al. (2011), d) Pérez (1999)

Sample Units	Sample label	Latitude [°S]	Longitude [°W]	Altitude [masl]	Temp. [°C]	Cond [$\mu\text{S}/\text{cm}$]	pH	TDS [mg/L]	O ₂ [mg/L]
Carranco	Car	-39.7654	-71.7922	450	82.0	560	8.9	375	n.m.
Chihuido	Chi	-40.1939	-71.9345	312	85.0	780	8.9	485	n.m.
Coñaripe	Con	-39.6349	-71.9239	260	71.7	780	7.8	524	n.m.
Liquine	LiQ	-39.7394	-71.8429	328	71.0	540	9.1	338	n.m.
Liucura	Liu	-39.2595	-71.7926	618	29.5	400	7.9	304	n.m.
Los Pozones	Poz	-39.2263	-71.6513	736	53.1	500	9.1	295	n.m.
Menetue	Men	-39.3291	-71.7193	336	50.5	400	9.3	312	0.17
Palguin	Pal	-39.4197	-71.7830	477	47.5	400	8.7	292	0.17
Panqui	Pan	-39.2534	-71.5306	926	50.8	580	8.0	390	n.m.
Rincon	Rin	-39.5077	-71.8543	939	37.5	420	7.6	375	0.18
Rinconada	RinCo	-39.4215	-71.6696	605	27.6	940	6.1	788	n.m.
Rio Blanco	Bla	-39.1086	-71.6136	733	54.1	580	7.7	400	n.m.
San Luis	SL	-39.3400	-71.6906	429	41.0	530	9.1	236	0.11
Toledo	Tol	-39.1802	-71.5849	920	42.5	1340	7.8	871	n.m.
Trancura	Tra	-39.3402	-71.6946	372	36.0	300	9.0	229	0.12
Geometricas	Gem	-39.5003	-71.8778	888	72.4	n.m.	8.4	720	n.m.
Lago Villarrica	Lake Vill	-39.2723	-71.9800	240	15.5	40	7.9	75	5.2
Rain Caburgua	Rain	-39.2199	-71.8153	420	n.m.	40	7.6	37	n.m.
Lago Calafquen	Lake Call	-39.4906	-72.1635	200	13.6	n.m.	7.6	75	n.m.
Lago Panguipulli	Lake Pan	-39.7132	-72.3471	130	11.0	n.m.	7.0	54	n.m.
Rio Palguin	R. Pal	n.a.	n.a.	n.a.	n.a.	n.m.	7.3	53	n.m.
Rio Turbio	R. Tur	n.a.	n.a.	n.a.	n.a.	n.m.	6.1	33	n.m.
Rio Aihue	R. Aih	n.a.	n.a.	n.a.	n.a.	n.m.	7.3	64	n.m.
Lago Calafquen	Lake Cal2	n.a.	n.a.	n.a.	n.a.	n.m.	6.5	25	n.m.
Lago Villarrica	Lake Vil2	n.a.	n.a.	n.a.	n.a.	n.m.	6.4	51	n.m.

Sample Units	Na [mg/L]	K [mg/L]	Ca [mg/L]	Mg [mg/L]	SiO ₂ [mg/L]	Rb [$\mu\text{g}/\text{L}$]	Cs [$\mu\text{g}/\text{L}$]	Sr [$\mu\text{g}/\text{L}$]	$\delta^{18}\text{O}$ ‰SMOW	δD ‰SMOW
Carranco	90.3	2.54	4.42	0.025	84.0	23.5	30.6	74.0	-9.92	-66.5
Chihuido	110	4.17	12.97	0.034	102	15.8	5.8	331	-10.25	-69.2
Coñaripe	126	3.93	7.25	0.566	93.9	23.9	24.5	60.4	-8.10	-56.1
Liquine	68.9	2.22	4.40	0.037	107	23.8	20.8	65.9	-9.45	-63.9
Liucura	65.6	3.47	11.0	1.57	51.0	6.81	0.91	83.9	-9.07	-61.4
Los Pozones	71.7	1.57	11.6	0.144	50.4	12.9	19.1	168	-10.24	-67.2
Menetue	73.6	1.27	6.74	0.393	82.1	14.0	22.0	58.6	-9.04	-62.2
Palguin	67.2	1.82	5.61	0.481	67.9	9.39	9.52	27.2	-9.87	-69.8
Panqui	63.9	2.20	42.9	0.396	46.1	13.6	29.0	313	-10.38	-71.4
Rincon	68.1	4.57	12.0	1.91	83.9	21.1	5.05	35.9	-9.74	-69.1
Rinconada	113	16.5	27.0	22.9	118	28.3	1.49	105	-11.08	-73.3
Rio Blanco	87.4	2.49	14.1	0.589	64.9	9.3	7.67	339	-10.13	-68.0
San Luis	50.4	1.05	6.64	0.416	59.4	6.67	5.69	72.6	-9.25	-63.4
Toledo	181	5.99	81.4	0.260	69.4	51.9	100	1100	-10.41	-71.4
Trancura	50.4	1.12	7.86	0.418	57.1	5.49	3.76	70.0	-9.21	-62.6
Geometricas	160	9.63	46.5	0.129	83.0	n.m.	n.m.	433	-10.10	-70.0
Lago Villarrica	4.75	1.40	5.43	1.83	17.5	2.7	0.2	24.6	-8.57	-59.2
Rain Caburgua	0.66	0.528	9.11	0.164	0.02	0.4	0.0	4.5	-7.79	-55.8
Lago Calafquen	4.39	0.938	5.25	1.87	16.2	n.m.	n.m.	n.m.	n.m.	n.m.
Lago Panguipulli	2.85	0.665	4.25	1.12	12.2	n.m.	n.m.	n.m.	n.m.	n.m.
Rio Palguin	4.10	1.10	4.00	1.50	24.0	bdl.	bdl.	18.0	n.m.	n.m.
Rio Turbio	2.50	0.500	2.80	1.10	12.0	n.m.	n.m.	n.m.	n.m.	n.m.
Rio Aihue	6.20	0.900	4.40	1.20	25.0	bdl.	bdl.	35.0	n.m.	n.m.
Lago Calafquen	4.40	1.00	5.60	2.00	19.0	n.m.	n.m.	n.m.	n.m.	n.m.
Lago Villarrica	3.80	0.900	4.90	1.80	19.0	n.m.	n.m.	n.m.	n.m.	n.m.

Sample Units	B [mg/L]	Cl [mg/L]	F [mg/L]	SO ₄ [mg/L]	HCO ₃ [mg/L]	CO ₃ [mg/L]	$^{87}\text{Sr}/^{86}\text{Sr}$ <0.000012	Ion balance error	Data source
Carranco	0.390	34.1	2.70	59.1	65.5	30.5	0.71124	-2.2	a
Chihuido	0.072	13.9	0.63	190	23.8	25.0	0.70425	-0.7	a
Coñaripe	3.68	82.9	1.30	103	101	n.a.	0.70410	-1.5	a
Liquine	0.193	17.4	1.15	80.3	24.4	31.5	0.70620	-5.5	a
Liucura	0.531	35.3	0.85	76.3	58.0	n.a.	0.70419	-0.6	a
Los Pozones	0.634	46.2	1.16	79.1	15.3	16.5	0.70413	-0.6	a
Menetue	0.354	26.2	3.98	65.9	18.3	33.0	0.70411	-1.3	a
Palguin	0.617	21.1	1.87	79.4	24.4	21.0	0.70452	-2.1	a
Panqui	0.551	25.5	0.21	164	42.7	n.a.	0.70408	1.9	a
Rincon	0.830	20.9	0.77	115	67.1	n.a.	0.70413	-3.3	a
Rinconada	1.59	40.6	0.31	151	296	n.a.	0.70406	-3.2	a
Rio Blanco	0.133	21.8	1.10	103	104	n.a.	0.70442	1.4	a
San Luis	0.110	7.86	1.61	72.4	18.3	18.0	0.70400	-2.3	a
Toledo	1.11	109	1.18	382	36.6	n.a.	0.70407	2	a
Trancura	0.117	8.08	1.49	68.8	1.5	31.5	0.70413	-2.9	a
Geometricas	5.02	48.7	1.20	421	29.0	n.a.	n.m.	-5.6	b
Lago Villarrica	0.010	2.26	0.040	2.26	39.7	n.a.	0.70417	-6.9	a
Rain Caburgua	0.002	1.48	bdl.	0.28	24.4	n.a.	0.70632	6.6	a
Lago Calafquen	bdl.	1.60	n.m.	2.21	32.5	n.a.	n.m.	0.6	c
Lago Panguipulli	bdl.	1.28	n.m.	1.83	22.1	n.a.	n.m.	0.9	c
Rio Palguin	bdl	1.80	0.100	3.00	27.0	n.a.	n.m.	-2.5	d
Rio Turbio	bdl.	5.00	0.180	1.90	12.0	n.a.	n.m.	-4.7	d
Rio Aihue	0.100	2.90	0.200	14.0	18.0	n.a.	n.m.	-5	d
Lago Calafquen	0.200	4.20	0.050	2.70	31.0	n.a.	n.m.	-1.8	d
Lago Villarrica	0.200	4.10	0.160	2.30	28.0	n.a.	n.m.	-2.1	d

7.4. Hydrochemistry of geothermal springs

The physicochemical composition of the thermal waters is analyzed with particular focus on the origin and the equilibrium state of the fluids, and is summarized in Table 7.1. Outflow temperatures of thermal waters range from 27.6 (Rinconada) to 80.7 °C (Chihuío), while pH values indicate slightly acidic (6.1, Rinconada) to alkaline (9.3, Menetué) conditions. Total dissolved solids vary between 229 and 871 mg L⁻¹ with elevated values at the following springs: Toledo (871 mg L⁻¹), Rinconada (788 mg L⁻¹), Geometricas (721 mg L⁻¹), and Coñaripe (524 mg L⁻¹)

7.4.1. Main components

Thermal fluids of the study area are clearly Na-dominated (Figure 7.2). It is well-known that leaching of igneous host rocks (e.g. Ellis & Mahon, 1977; Giggenbach et al., 1983; Smellie et al., 1995; Stober & Bucher, 1999) results in Na-dominated fluids with alkaline pH and low TDS. Compared to local meteoric waters, thermal waters are depleted in Mg by its incorporation into hydrothermal alteration products (e.g. clay minerals, mica, etc.) (Giggenbach, 1988). The Rinconada thermal spring discharging at the foot of Quetrupillán volcano deviates slightly by an elevated magnesium concentration, enriched in absolute concentrations also in comparison to local meteoric waters.

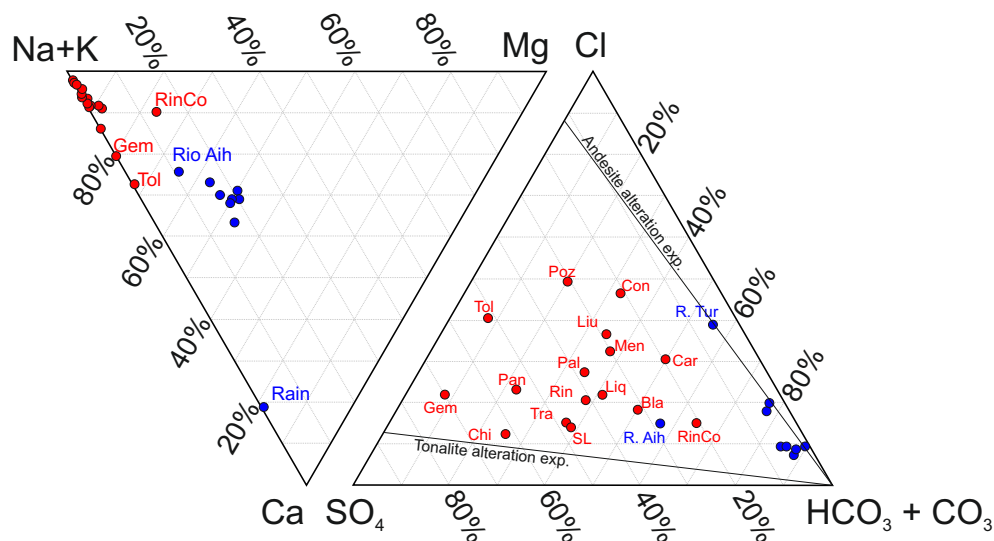


Figure 7.2.: Ternary diagrams of Na+K-Mg-Ca (left) and Cl-SO₄-HCO₃+CO₃ (right) in mmol/kg for thermal (red circles) and meteoric (blue circles) waters of Villarrica area. Additionally SO₄/Cl ratios from alteration batch experiments (Nitschke et al., 2017a) of possible reservoir rocks of the area are incorporated in anion ternary.

The Cl-SO₄-HCO₃+CO₃ ternary diagram (Figure 7.2) reveals scattering anion concentrations between the SO₄-rich hot springs of Geometricas, the Cl-rich of Coñaripe and Los Pozones and bicarbonate-rich of Rinconada. A slight tendency towards SO₄-rich hot springs however is indicated. The meteoric waters, with absolute Cl and SO₄ far below the concentration of thermal waters, have high bicarbonate concentrations typical for fluids interacting with atmospheric CO₂. Deviation of Rio Aihue sample, observed also for cations, is likely to be caused by infiltration of thermal water, as the small creek flows through the valley, where Geometricas thermal spring discharges.

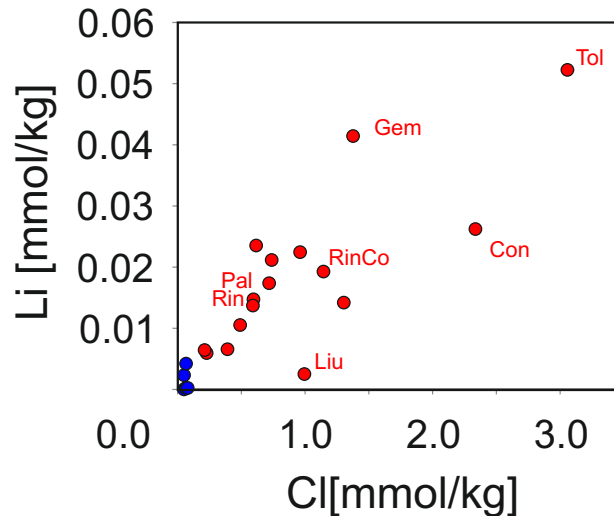


Figure 7.3.: Binary diagram of the Cl-Li system for thermal and meteoric waters of Villarrica area. Symbols as in Figure 7.2.

In the following, we analyzed additional indicators with respect to the origin of this diverse pattern. In a geothermal context, Cl dominated, mature waters are indicative of deep reservoir origin (e.g. Giggenbach, 1991; Tassi et al., 2010) with high Cl concentrations attributed to volatile input of magmatic HCl degassing or from intense leaching of host rocks (Ellis & Mahon, 1977). The origin of Cl is first inferred from the comparison with Li concentration, the latter being a conservative fluid constituent originating from rock leaching. Both conservative constituents of the fluid show linear correlation even when including springs close to the volcano (Figure 7.3). This hints to a similar origin/mobilization process, i.e. rock leaching in a deep reservoir. The fact that the Cl concentrations of thermal waters near the volcano do not exceed the concentrations of springs in greater distance (Figure 4b) confirms the exclusion of a magmatic origin of Cl.

Comparison of Cl and B concentrations reveals a spatial relationship for thermal springs near the volcanic chain (Rin, RinCo, Gem, Pal, Con) (Figure 7.4). In context of geothermal system boron is considered to originate from magmatic degassing or rock leaching and enters the fluid phase as H_3BO_3 (Arnórsson & Andrésdóttir, 1995). The B/Cl ratio shows a spatial relationship with the distance to the volcanic chain (Rin, RinCo, Gem, Pal, Con in Figure 7.4). B concentrations are elevated in thermal springs near the volcano (Figure 7.4a) leading to B/Cl ratios between 0.09 and 0.3. At larger distance, a uniform B/Cl ratio <0.05 indicates no enrichment of B through magmatic degassing processes (Figure 7.4b). The B/Cl ratio of 0.05-0.3 is generally low compared to conventional volcanic systems, where ratios of up to 1 are reported (e.g. Tassi et al., 2010; Arnórsson & Andrésdóttir, 1995). Yet the values exceed ratios from pure leaching of basaltic rocks (e.g. Arnórsson & Andrésdóttir, 1995; Taylor, 1964).

SO_4 dominated waters in geothermal systems are often related to steam-heated, acidic groundwater occurring in shallower levels above the deep reservoir. Besides oxidation of H_2S or SO_2 volatiles originating from redox depending magmatic degassing, elevated SO_4 concentrations can be generated by interaction with evaporites or igneous host rock, enriched in sulfide or sulfate-bearing minerals. A correlation between B and SO_4 is not observed (Figure 7.4c). Considering also the non-acidic character, also of the SO_4 -rich thermal waters, “steam heating” by sulfur-rich volatiles is not assumed. The deviation of

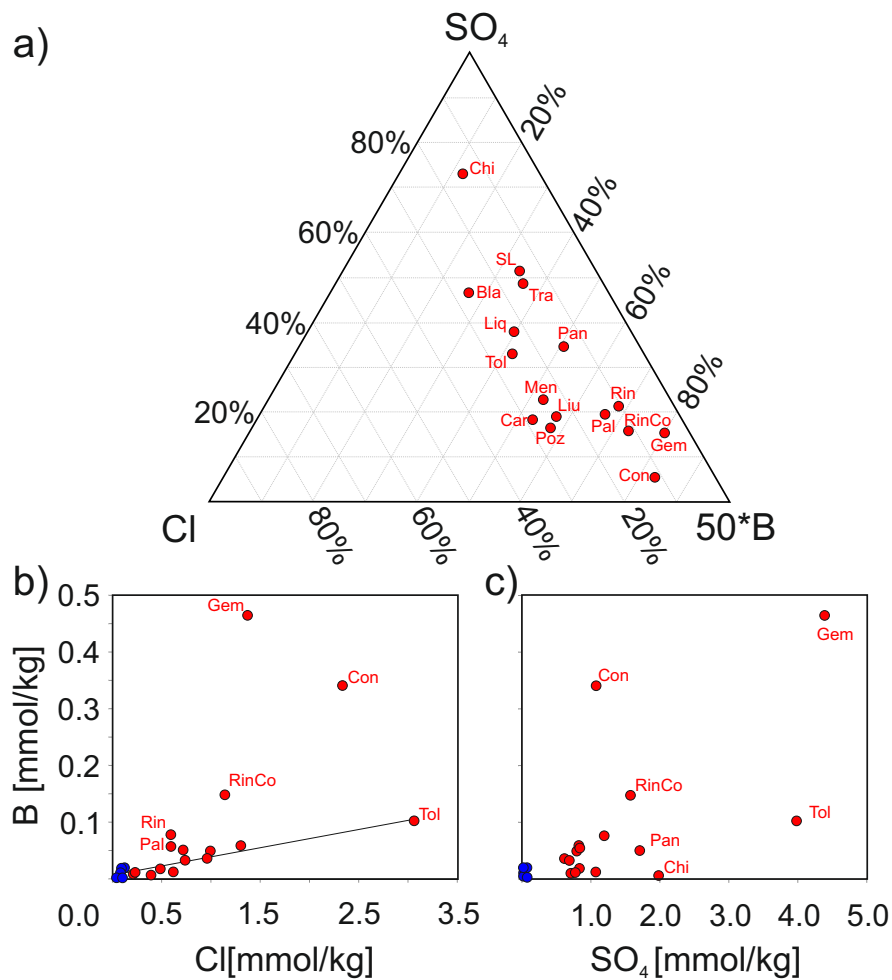


Figure 7.4.: Evaluation of Cl-SO₄-B ratios in a) ternary diagram b) Cl vs. B ratio and c) SO₄ vs. B ratio for thermal waters of Villarrica area. Symbols as in Figure 7.2.

Ca/SO₄ from the stoichiometric ratio (Figure 7.5) and the absence of evaporitic outcrops in the research area discharge evaporitic origin of SO₄. Consequently, sulfate in the thermal springs may originate from leaching of host rocks that might be enriched in sulfate or sulfide minerals due to paleo-magmatic volatile sulfur input. In this respect, leaching experiments of two main two rock types present in the study area, i.e. tonalite of the NPB, and andesite of the Cura-Mallín formation, were performed resulting in elevated concentrations of SO₄ and Cl >1 mmol in the fluid (see results in Figure 7.2) (Nitschke et al., 2017a).

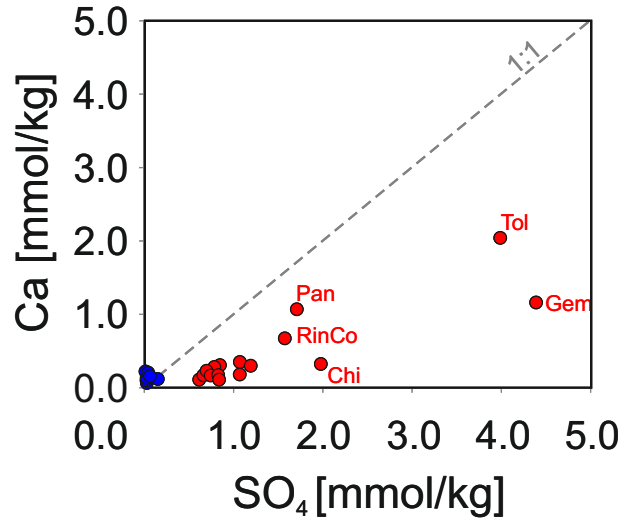


Figure 7.5.: Ca^{2+} vs. SO_4^{2-} binary diagram. Symbols as in Figure 7.2.

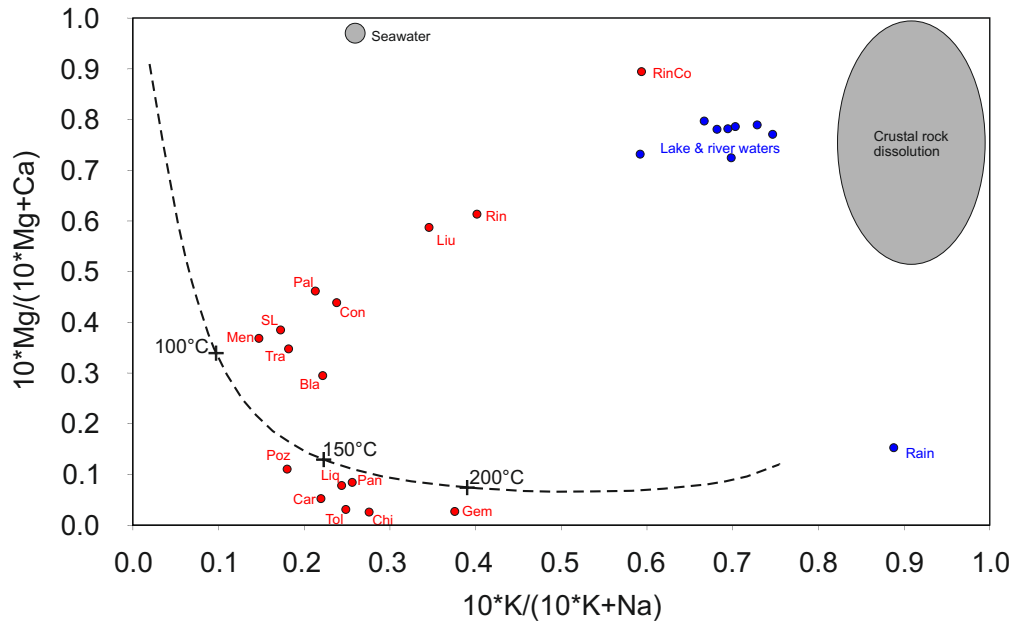


Figure 7.6.: Evaluation of equilibrium state using $10 \text{ Mg}^{2+}/(10 \text{ Mg}^{2+} + \text{Ca}^{2+})$ vs. $10 \text{ K}^{+}/(10 \text{ K}^{+} + \text{Na}^{+})$ binary diagram in mmol/kg. The equilibrium composition of waters interacting with an average crustal rock and the field characterized by fluids in the stage of initial rock dissolution after Giggenbach (1988). Symbols as in Figure 7.2.

7.4.2. Equilibrium state

Evaluation of the equilibrium state of thermal waters is first carried out by comparison of its hydrochemical composition with theoretical compositions of thermal waters from a) isochemical dissolution of crustal rock and (e.g. Taylor, 1964) b) full equilibrium with recrystallized, thermodynamically stable crustal rock (Giggenbach, 1984, 1988) (Figure 7.6). The hydrochemical signatures of the samples follow a well-documented path from the field of initial dissolution of crustal rocks over the lake and river waters and springs

located near the volcano (RinCo, Rin and to a minor extend Palguin and Coñaripe) and Liucura hot spring to the majority of thermal springs that achieve equilibrium conditions at temperatures $>100^{\circ}\text{C}$. The position of the mentioned springs suggests a transition between initial rock dissolution towards approaching equilibrium reflecting limited water-rock interaction. Note that such a path may also be caused by dilution with Mg-rich superficial water.

For further investigation of equilibrium state, the Rb-Li-Cs ternary is used (Giggenbach, 1991) (Figure 7.7a). Water compositions resulting from initial rock dissolution are characterized by high Rb concentrations lowering its concentration by continuous water-rock interaction by uptake in secondary alteration products. The thermal waters have adjusted Rb concentrations while approaching equilibrium. In agreement with the evaluation of cation composition (Figure 7.6), near volcano springs show highest Rb concentrations and thus lowest degree of equilibrium but far from the state of initial rock dissolution. The deviation of the samples (Liu, RinCo, Rin) from equilibrium (Figure 7.6, Figure 7.7) can be attributed either to a) a state of still approaching equilibrium or b) dilution with Mg-rich groundwater. Thus, a quantitative determination of meteoric dilution is mandatory for trustworthy temperature estimation and will be investigated in a forthcoming publication.

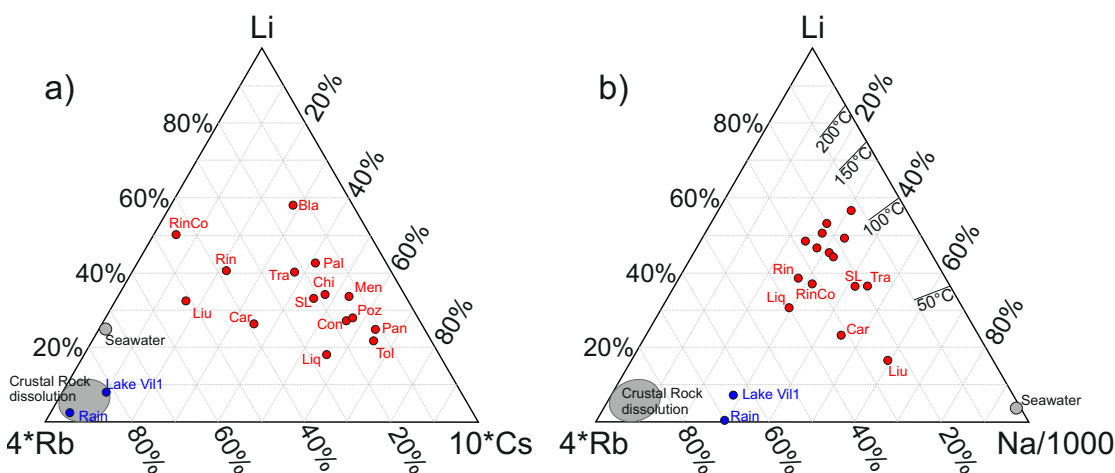


Figure 7.7.: a) 4Rb-Li-10 Cs and b) 4Rb-Li-Na/1000 ternary diagrams in mmol/kg for thermal (red circles) and meteoric (blue circles) waters of Villarrica area emulating the original plot by Giggenbach (1991). Constant Na/Li ratios are incorporated by black lines representing reservoir temperature estimates using equation of Fouillac & Michard (1981). Thermal water of Geometricas hot spring are not shown, as data from Sánchez et al. (2013) do not contain Rb and Cs measurements.

The temperature dependence of Li concentration in thermal fluids is used in the Na/Li geothermometer (e.g. Fouillac & Michard, 1981). In this respect, the Rb-Li-Na ternary diagram (Figure 7.7b) enables the evaluation of the equilibrium state by distance from the initial rock dissolution field combined with a first estimation of reservoir temperature by Na/Li ratios. Hydrochemical composition of thermal waters, resulting from initial dissolution of crustal rock, is generated according to the procedure of Giggenbach (1988, 1991). Compared to the equilibrium temperatures estimated in Figure 7.6, Na/Li temperatures ranging between 20°C and 120°C are significantly lower. Note that in Liucura and Carranco Na/Li temperatures appear to be even lower than the discharge temperatures of

the springs.

7.4.3. Stable isotopes

With the aim to identify the origin of the thermal water, the isotopic compositions are displayed in Figure 7.8. The $\delta^{18}\text{O}$ and δD values of geothermal discharges vary between -7.8 and -11.1 ‰V-SMOW and -55.8 and -73.3 ‰V-SMOW, respectively. Conformity with the global and Chilean meteoric water lines indicates the meteoric origin of the fluids. This observation is in agreement with investigations of Sánchez et al. (2013) and Tardani et al. (2016).

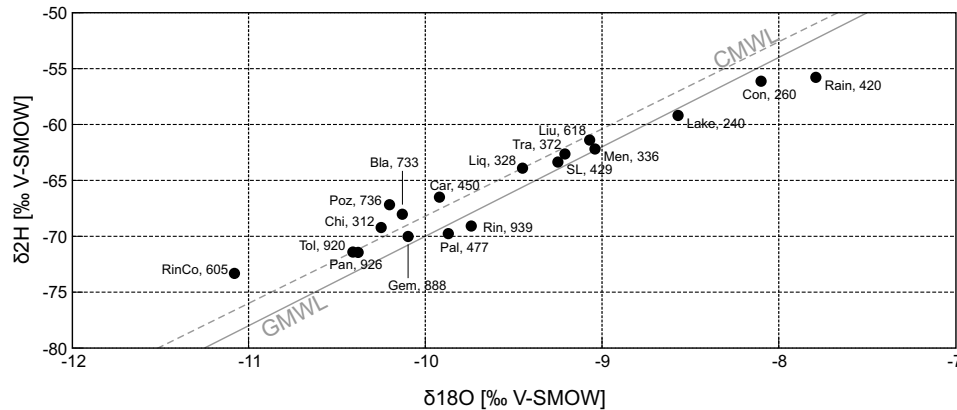


Figure 7.8.: $\delta^{18}\text{O}/\delta\text{D}$ plot for the sampled geothermal fluids and meteoric waters. Numbers given after the labels represent outflow altitude in meters above sea level. GMWL = global meteoric water line (Craig, 1961), CMWL = Chilean meteoric water line (Spangenberg et al., 2007).

Sr isotope ratios of thermal waters enable an allocation of possible host rocks, as the $^{87}\text{Sr}/^{86}\text{Sr}$ ratios of different rock classes vary significantly. As a consequence of water-rock interaction the fluid adapts $^{87}\text{Sr}/^{86}\text{Sr}$ ratios from the host rock. The $^{87}\text{Sr}/^{86}\text{Sr}$ ratios of Villarrica thermal waters range between 0.7040 (San Luis) to 0.7112 (Carranco), while a majority of springs have a uniform distribution between 0.7040-0.7042 (Figure 9). The local rainwater has a ratio of 0.7063. Strontium isotope signatures of volcanic rocks from nearby stratovolcanoes (Llaima, Villarrica, Quetrupillán, Lanín, Mocho-Choshuenco) have a uniform distribution of $^{87}\text{Sr}/^{86}\text{Sr} < 0.7041$ (Déruelle et al., 1983; Jacques et al., 2014; McMillan et al., 1989; Hickey-Vargas et al., 1989). $^{87}\text{Sr}/^{86}\text{Sr}$ ratios of plutonic rocks of NPB possess a wider range between 0.7045-0.707 (Lucassen et al., 2004; Pankhurst et al., 1999, 1992; Munizaga et al., 1988) Isotope ratios for Cura-Mallín formation are not measured. Here, a similarity to source rock of the volcano-sedimentary deposits is assumed.

Comparing the Sr isotopes of thermal waters with rocks, similar isotope ratios are observed for thermal waters:

- of uniform values < 0.7042 and volcanic rocks north of the Villarrica-Quetrupillán-Lanín volcanic chain, and
- of higher isotope signature and plutonic rocks south of the Villarrica-Quetrupillán-Lanín volcanic chain.

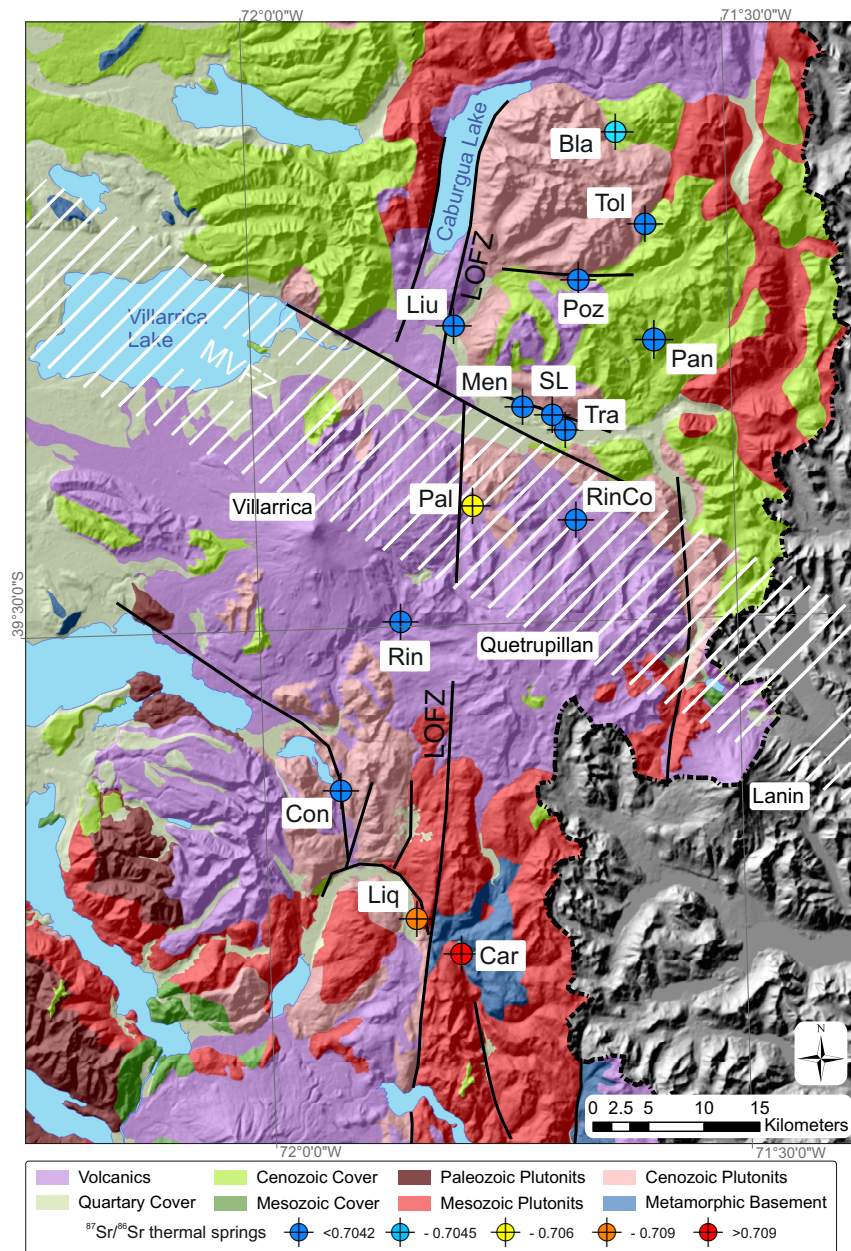


Figure 7.9.: Spatial distribution of $^{87}\text{Sr}/^{86}\text{Sr}$ ratios of hot springs with the color code representing Sr isotope ratios. Geological map modified after 1:1'000'000 scale map, Servicio Nacional de Geología y Minería, Chile by including interpretations from Cembrano & Lara (2009); Sánchez et al. (2013); Moreno & Lara (2008); Lara et al. (2004). Shaded relief map derived from CGIAR-CSI version of SRTM data.

7.5. Conclusion and outlook

Based on the analysis of hydrochemical composition of the thermal waters, the following conclusions can be derived:

- The meteoric origin of the thermal waters is revealed by meteoric $\delta^{18}\text{O}/\delta\text{D}$ signatures, excluding strong impact of magmatic fluids.
- Na-dominated, alkaline thermal waters indicate water-rock interaction with igneous

rocks.

- The anion compositions of thermal springs show some variations. Elevated Cl and SO₄ concentrations can be attributed to rock leaching.
- The slightly increased B/Cl ratios at the volcanic chain, without significant increase of other volatiles of magmatic origin, indicates limited occurrence of magmatic degassing. As the Cl concentrations of thermal waters near the volcano do not exceed the concentrations of springs in greater distance, a magmatic origin of Cl is doubtful.
- The majority of waters have reached equilibrium with host rocks. From ⁸⁷Sr/⁸⁶Sr ratios, water-rock interaction with plutonic host rocks south of the volcanic chain and volcanic host rocks to the north of it can be derived.

This study presents a characterization of thermal water, which is based solely on hydrochemical evaluation. To improve the geochemical exploration of the Villarrica geothermal system additional work is required, such as: the quantification of meteoric dilution, the evaluation of uncertainties of reservoir temperature estimation and an improvement of these methods and the precise tracing of the lithological contrast occurring in the study area.

Acknowledgements

The study is part of a collaborative research project between Karlsruhe Institute of Technology (KIT) and the Andean Geothermal Center of Excellence (CEGA, Fondap-Conicyt 15090013). The authors appreciate the support under the BMBF- CONICYT International Scientific Collaborative Research Program (FKZ 01DN14033/ PCCI130025). Additional support under the topic “Geothermal Energy Systems” of the Helmholtz portfolio project “Geoenergy” and by EnBW Energie Baden-Württemberg AG is gratefully acknowledged. Special thanks go to our colleagues Gabriel Perez and Pablo Sánchez for the support during fluid sampling and the many fruitful discussions. The authors would like to thank Ilka Kleinhanns from the University of Tübingen and Jochen Schneider from Hydrosion GmbH for help during strontium isotope analytics and interpretation.

8. Geochemical characterization of the geothermal system at Villarrica volcano, Southern Chile; Part 1: Impacts of lithology on the geothermal reservoir

This manuscript has been published in *Geothermics*

SEBASTIAN HELD, EVA SCHILL, JOCHEN SCHNEIDER, FABIAN NITSCHKE, DIEGO MORATA, THOMAS NEUMANN and THOMAS KOHL [2018]: Geochemical characterization of the geothermal system at Villarrica volcano, Southern Chile; Part 1: Impacts of lithology on the geothermal reservoir; *Geothermics* (74), 226-239

Abstract

Besides temperature, mineralogy, residence time and dilution are crucial for assessing water-rock interaction intensity. The geothermal system at the Villarrica-Quetrupillán-Lanín volcanic chain, Southern Chile, is located across a prominent lithological transition from plutonic rocks of the North Patagonian Batholith (NPB) to volcano-sedimentary units. With the goal to investigate the impact of lithology on medium-enthalpy geothermal fluids, 15 hot spring discharges were sampled and analyzed for anthropogenic tracers and isotopic composition and compared to the analyses of 31 reservoir rock analogues. Comparison of strontium isotope signatures between rock analogues and hot spring discharges allow an allocation of associated reservoir rocks. Chlorofluorocarbons quantify the dilution of the geothermal springs by shallow groundwater, ranging from almost CFC-free samples to dilution with modern meteoric water by up to 50 %. Fluids discharging from plutonic rocks have low proportions of dilution with modern waters, while hot springs discharging from the volcano-sedimentary rocks have a higher and variable dilution with modern waters. The fractionation of oxygen isotopes of the $\text{SO}_4\text{-H}_2\text{O}$ system reveals reservoir temperature estimates of 80–100 °C in the plutonic sequence matching discharge temperatures. For the springs discharging from volcano-sedimentary units higher reservoir temperatures of 100–140 °C are calculated. On basis of the analysis, a conceptual reservoir model can be derived. Fast fluid ascent is indicated along Liquiñe-Ofqui fault system in the NPB

by similar discharge and reservoir temperatures and low surficial dilution rates. Large differences in discharge and reservoir temperatures in the Cura-Mallín formation along with a high influx of surficial water may be attributed to a more branched pathway pattern. In conclusion lithology maybe an important factor when coming to the utilisation of geothermal resources.

8.1. Introduction

Hydraulic, thermal and geochemical characteristics of a geothermal system are intrinsically related to the local permeability distribution. Natural permeability in geothermal systems is controlled by critically oriented faults or fractures in the ambient stress field directing fluid movement (e.g. Rowland & Sibson, 2004; Zoback, 2010). In a given regional stress pattern mechanical strength contrasts, caused by varying lithologies, may individually affect fracture mechanics resulting in different characteristics of fault or fracture zones (e.g. Meixner et al., 2014). A well-studied example in this context is the Armutlu peninsula in NW-Turkey (Eisenlohr, 1997), where the assembly of crystalline basement rocks, marble, and evaporites causes individual, lithological dependent circulation systems resulting in different hydrochemical compositions and reservoir temperatures. However, also in the case of a pure crystalline setting, such as the well investigated areas of the Black Forest region, SW-Germany, Stober & Bucher (1999) identified the coexistence of two flow systems with different hydraulic properties that can be related to lithological changes between granite and gneiss. Herein, the change in lithology is accompanied by a permeability contrast that limits the occurrence of thermal springs to granitic formations being generated by a deep circulation system extending down to a depth of 4 km. The gneiss complexes host low-temperature mineral springs only. The flow is concentrated on sparse, high-permeability conduits without great penetration depth. In both studies the lithological control on geothermal circulation was identified by strong variations in hydrochemical fluid composition.

In case of the geothermal system at the Villarrica volcano the lithology contrast between plutonic units of the North Patagonian Batholith and volcano-sedimentary rocks of the Cura-Mallín formation, cannot be recognized in the main fluid composition (Held et al., 2017). Investigating the interplay between tectonics and fluid composition in a regional study, the system was found to be partitioned, which was attributed exclusively to the location and orientation of major fault zones neglecting the lithological contrast (Sánchez et al., 2013). The formation of the hot spring fluids was investigated by interpretation of their composition (Held et al., 2017) identifying water-rock interaction as being the process governing the fluid composition of the hot springs. Magmatic processes affect the geothermal springs only to a minor extent revealed e.g. by results of the analysis of oxygen and hydrogen isotope signatures (Sánchez et al., 2013; Held et al., 2017). The absence of typical indications for a high-enthalpy geothermal reservoir (Held et al., 2015, 2016) supports the image of a medium-enthalpy geothermal systems with limited magmatic input.

Within this study comprehensive, geochemical fluid and rock sampling and analysis were conducted on 31 potential reservoir rock analogues and 15 hot spring samples of the Villarrica geothermal system to trace the lithological transition in the fluids and determine its impact on the thermal fluids. Complementary to the previous studies the fluids are analyzed for Sr isotopes, chlorofluorocarbon (CFC) concentrations and $\delta^{18}\text{O}$ values of sulfate, while the rocks are analyzed for geochemical composition and Sr isotope signatures.

The investigations are part of a large geoscientific research project including hydrochemical, geophysical and structural measurements. An estimation of reservoir temperatures including a site-specific re-evaluation of solute geothermometry is conducted in the second part of a joint hydrochemical investigation of the Villarrica geothermal system (Nitschke et al., 2018).

8.2. Geological setting

The lithological transition between the Cura-Mallín formation and the North Patagonian Batholith is located in the Southern Volcanic Zone (SVZ) of Southern Chile. Volcanism in SVZ is related to the subduction of the Nazca Plate beneath the South American Plate. Structural geology of the central and southern SVZ is dominated by the Liquiñe-Ofqui fault system (LOFS), a N-S to N10°E oriented fault system running along the volcanic arc (Cembrano et al., 1996). The stress pattern causes a dextral strike-slip movement on the LOFS. The fault system is accompanied by WNW-ESE oriented Andean Transverse Fault zones (ATF) (Pérez-Flores et al., 2016). These ATFs are disoriented with respect to the prevailing stress field and undergo sinistral strike-slip movement (Cembrano & Moreno, 1994). Between 37°-39°S, the Bío-Bío-Aluminé fault system (BAFS) and the Mocha-Villarrica fault zone (MVFZ) are prominent structures in WNW-ESE direction (Figure 8.1a).

The research area around the WNW-ESE aligned Villarrica-Quetrupillán-Lanín volcanic chain (Figure 8.1b) is characterized by a complex tectonic pattern of intersecting fault zones. The LOFS, oriented N-S to NNE-SSW in the Villarrica area, passes the volcanic chain between Villarrica and Quetrupillán volcanos (Figure 8.1) (Moreno & Lara, 2008). The LOFS is offset by the MVFZ by a few kilometers (López Escobar et al., 1995), then splits into two legs and continues on both shores of the N-S oriented Lake Caburgua. A detailed depth study of the LOFS along the southern shore of Lake Caburgua using a magnetotelluric survey revealed a sub-vertical orientation in upper crustal levels (Held et al., 2016). A fault system width of <3 km is modeled for the Caburgua segment in agreement with the determined values of 2 km near the Liquiñe village (Hervé, 1976). The >300 km long MVFZ runs transverse to the Andean volcanic arc (e.g. Bohm et al., 2002). Detailed magnetotelluric investigations reveal a broad, northward dipping fault zone (Held et al., 2016). Pérez-Flores et al. (2016) expect reservoirs of magma or fluid associated with ATF as the misorientation regarding the regional stress field impede vertical permeability (Tardani et al., 2016).

South of the Villarrica-Quetrupillán-Lanín volcanic chain plutonic rocks of the North Patagonian Batholith prevails (Hervé, 1984; Munizaga et al., 1988) (Figure 8.1). The pluton was emplaced between 39°-47°S during episodic magmatic events between Late Jurassic and Pleistocene (Pankhurst et al., 1999). Two phases of intensive plutonism are dated to be of Cretaceous and Miocene age. The batholith complex consists of plutonic rocks of dioritic to tonalitic composition (Adriasola et al., 2005). North of the volcanic chain, the plutonic basement occurs subordinately only, being replaced by the volcano-sedimentary Cura-Mallín formation of Eocene to Miocene age (Jordan et al., 2001) (Figure 8.1). The formation was deposited in a sequence of intra-arc basins in south central Chile (33°-39°S), which had developed under extensional tectonics between Eocene and Miocene (Charrier et al., 2007). The formation of up to 3000 m in thickness consists of two facies (Radic, 2010). The Rio Pedregoso facies is composed of lacustrine, deltaic and fluvial

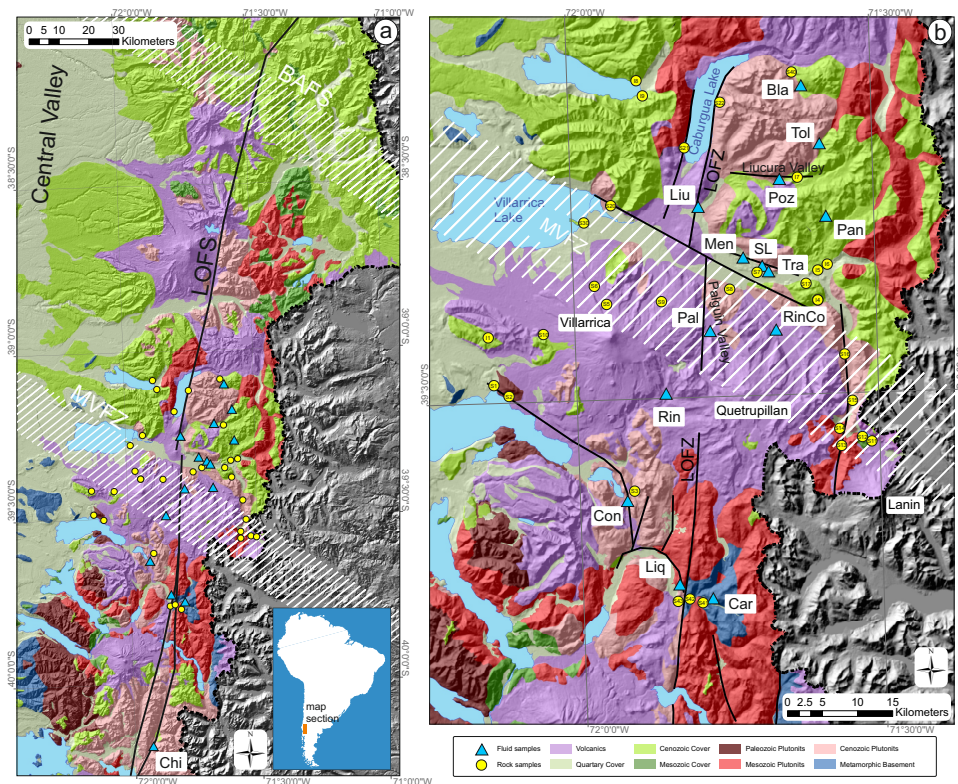


Figure 8.1.: a) Geological map of the volcanic arc of Southern Chile between 38.0°S - 40.4°S displaying outcrops of the NPB (reddish colors) in the south of the Villarica-Quetrupillán-Lanín volcanic chain and volcano-sedimentary basin fillings (bright green color) of the Cura-Mallín formation north of it. Intra-arc LOFS (simplified in Figure a) crosscuts the NPB and continues to the N in the volcano-sedimentary sequence, intersected by Andean Transfer faults in the form of the BAFS and MVFZ. b) Research area showing rock (yellow circles) and fluid (blue triangles) sampling locations. Hot spring abbreviations are listed in Table 8.2. The location of Chi, which was additionally analyzed to increase sample number along LOFS, is depicted in Figure a. Faults in Figure b are taken from geological maps of the study area (Lara et al., 2004; Moreno & Lara, 2008). A shaded relief map derived from CGIAR-CSI version of SRTM data. Geological map modified after 1:1'000'000 scale map, Servicio Nacional de Geología y Minería, Chile by including interpretations from Cembrano & Lara (2009), Sánchez et al. (2013), Moreno & Lara (2008), and Lara et al. (2004).

sediments, and is intercalated with the Guapitrío facies, a volcanic facies of pyroclastic deposits and lava flows (Suarez & Emparan, 1995). In the study area north of the volcanic chain, the Guapitrío facies dominates (Villalón, 2015). It is assumed that the Cura-Mallín formation hosts geothermal reservoirs in Southern Chile, e.g. the Tolhuaca geothermal system (Sánchez-Alfaro et al., 2016).

Subduction generates more than 60 Holocene stratovolcanoes in the SVZ, accompanied by a high number of minor eruptive complexes (Stern, 2004). Volcanic centers are spatially related to prominent structural weak zones (Lara et al., 2006). The active Villarica volcano belongs to the WNW-ESE oriented volcanic chain, following the lineament of the MVFZ. Magma chambers are assumed to be located at upper and lower crustal depths

below Villarrica Volcano (Hickey-Vargas et al., 1989). Unlike Quetrupillán and Lanín, Villarrica exhibits a strong, frequent activity of basaltic-andesitic composition with >20 major eruptions per century (Petit-Breuilh & Lobato, 1994).

8.3. Materials and methods

In the surroundings of the Villarrica-Quetrupillán-Lanín volcanic chain, more than 20 hot springs discharge with temperatures of up to 80 °C (Hauser, 1997). Outflow conditions of the springs are described in detail by Pérez (1999). Often, at each location there are several springs with volume flow of around 1 L/s discharge varying slightly in terms of temperature and hydrochemical composition. The full hydrochemical dataset of the 15 sampled springs is presented in (Held et al., 2017). Hence, we describe merely the complementary materials and methods required for the additional investigations. If not mentioned otherwise measurements are conducted at the Institute of Applied Geosciences at the Karlsruhe Institute of Technology (Germany). The thermal springs were sampled additionally to investigate chlorofluorocarbons and oxygen isotopes of sulfate species. Samples for CFC determination were collected in 1 L glass bottles with metal lined caps. To protect the samples from atmospheric contamination, the bottles were enclosed by tight copper tins, also filled with sampling water. During sampling, copper tins and enclosed bottles were set on the base of a vessel (≈ 10 L) and were filled with a tube from inside the glass bottle. A minimum of three bottle volumes were pumped through a tube from the bottom of the bottle before capping bottle and copper tin underwater. Three samples (Con, Tol and Bla, Figure 1) were discarded, as in these cases contamination with atmospheric CFCs could not be excluded due to the outflow conditions (unknown equilibration state as discharging in hot pools). CFC analysis was performed at the Spurenstofflabor Dr. Harald Oster, Wachenheim, Germany, using purge and trap gas chromatography with an electron capture detector (GC-ECD).

In order to provide a sufficient amount of sulfate for the determination of $\delta^{18}\text{O}$ isotopes, 1L fluid samples were collected without further treatment stored in polyethylene vessels avoiding any head space. Total sulfate was precipitated as BaSO_4 by adding a stoichiometric excess of BaCl_2 before measuring oxygen isotope ratios of precipitates by isotope-ratio mass spectrometry (IRMS: GV Instruments IsoPrime combined with HTO Pyrolysis by HEKAtech measured at 1350 °C using the following standards NBS127, N3, V-SMOW, GISP, LK2, LK3).

31 rock samples were collected in the vicinity of the volcanic chain. Sampling locations were chosen to a) obtain a comprehensive collection of possible reservoir rock analogues of the research area and b) establish spatial relationships between thermal springs and nearby rocks. These circumstances result in the selection of outcrops (Figure 1). Prior to analysis, the rock samples were ground-up using an agate disk mill. Main element concentrations were determined using wavelength-dispersive X-ray spectroscopy (Bruker AXS, S4 Explorer). Ground-up rock samples were analyzed for Rb and Sr concentrations by energy-dispersive X-ray fluorescence (Panalytical, Epsilon 5). Sr isotope ratios of rock samples were measured by the University of Tübingen, Isotope Geochemistry Group using thermal ionization mass spectrometry (TIMS: FinniganMAT 262).

Table 8.1.: Major element composition, concentrations of Rb and Sr, and $^{87}\text{Sr}/^{86}\text{Sr}$ isotope ratio of rock samples from Villarrica area. Classification according to rock type and age (VV, VL, VQ: Volcanic rock Villarrica/Lanín/Quetrupillán; PP: Paleozoic; plutonic rocks of NPB = MP: Mesozoic plutonic rock and CP: Cenozoic plutonic rock; MB: Metamorphic basement; MC: Mesozoic cover; CC: Cenozoic cover = Cura-Mallín formation). Age classification according to Moreno & Lara (2008) and Lara et al. (2004). n.m. = not measured

Sample point	Lat. [°W]	Long. [°S]	Na ₂ O [%]	MgO [%]	Al ₂ O ₃ [%]	SiO ₂ [%]	K ₂ O [%]	CaO [%]	TiO ₂ [%]	MnO [%]	Fe ₂ O ₃ [%]	LoI [%]	Σ [%]
S1	72.13	39.48	2.31	4.54	17.6	49.0	0.474	8.90	1.15	0.168	11.4	2.11	97.6
S2	72.13	39.49	3.31	1.80	14.7	61.0	0.547	4.77	0.56	0.040	7.07	3.92	97.8
S3	71.92	39.63	3.13	0.627	13.6	71.9	4.09	2.04	0.328	0.042	2.20	0.380	98.3
S5	71.95	39.38	3.04	5.13	17.5	51.4	0.692	9.72	1.19	0.144	9.70	0.019	98.7
S6	71.97	39.35	2.86	6.40	16.6	51.2	0.640	9.63	1.12	0.152	9.94	0.118	98.9
S7	71.69	39.34	4.15	0.489	14.2	71.6	3.04	2.07	0.256	0.049	2.19	0.712	98.9
S8	71.74	39.36	3.71	1.26	13.4	71.4	1.98	1.50	0.348	0.056	3.10	1.68	98.5
S9	71.86	39.38	3.48	3.38	17.3	55.2	0.825	7.86	1.03	0.152	9.05	0.143	98.6
S10	72.05	39.41	3.30	2.88	17.0	57.2	0.849	6.48	0.710	0.152	6.79	2.81	98.4
S11	71.51	39.56	3.13	5.154	17.5	50.0	1.21	8.45	1.25	0.171	10.8	0.338	98.3
S12	71.53	39.56	3.56	0.71	13.6	70.1	3.32	1.94	0.252	0.054	2.68	2.08	98.4
S13	71.56	39.56	3.56	3.70	17.7	54.5	1.03	7.36	0.960	0.128	7.39	1.46	98.0
S14	71.57	39.54	3.17	3.57	16.6	56.2	2.24	6.34	0.774	0.118	6.96	2.00	98.2
S15	71.54	39.51	3.60	3.57	16.9	56.9	1.35	6.43	0.946	0.200	6.23	2.08	98.4
S16	71.55	39.45	4.54	2.55	16.8	56.6	1.67	5.90	1.21	0.170	7.92	0.663	98.5
S17	71.62	39.35	3.50	0.425	13.2	73.2	3.78	1.35	0.242	0.047	1.76	1.05	98.5
S20	71.93	39.25	2.73	2.02	13.7	65.8	1.77	5.03	0.521	0.092	5.40	1.16	98.3
S21	71.81	39.18	2.20	0.089	11.7	74.0	4.11	2.58	0.129	0.044	1.50	1.77	98.1
S22	71.75	39.12	3.81	2.62	17.0	57.9	1.63	6.13	0.876	0.110	6.46	0.930	97.8
S30	71.98	39.27	1.66	4.29	19.4	44.6	0.158	10.0	0.479	0.129	7.39	9.20	97.3
S40	71.63	39.08	3.96	0.201	12.3	76.5	3.76	0.384	0.151	0.021	0.740	0.655	98.6
S41	71.82	39.76	3.00	1.90	13.9	66.6	2.21	2.52	0.646	0.071	4.90	1.87	97.8
S42	71.83	39.76	2.86	1.33	12.5	73.1	2.00	1.85	0.537	0.056	3.62	0.942	98.9
S43	71.84	39.76	3.09	0.468	13.0	74.9	4.34	1.61	0.199	0.048	1.47	0.470	99.6
I1	72.13	39.40	2.84	2.65	16.5	55.8	0.826	6.23	0.891	0.068	7.22	6.18	99.4
I4	71.60	39.39	2.51	4.68	17.3	54.9	1.51	8.15	0.967	0.139	7.88	2.24	100.5
I5	71.58	39.34	2.99	4.28	17.8	52.2	1.18	8.26	1.24	0.168	9.49	2.30	100.3
I6	71.60	39.35	3.70	0.949	14.2	72.3	4.13	1.96	0.406	0.072	2.52	1.03	101.4
I7	71.64	39.22	3.23	1.56	14.3	66.0	1.92	4.12	0.612	0.101	4.34	4.90	101.3
I8	71.90	39.09	3.87	5.02	19.0	49.7	0.777	6.38	1.32	0.111	9.49	3.98	100.0
I9	71.88	39.11	4.65	0.930	14.2	62.7	0.734	3.59	0.568	0.208	7.13	2.10	97.0

Sample point	Rock class	c(Rb) [ppm]	c(Sr) [ppm]	Rb/Sr	$^{87}\text{Sr}/^{86}\text{Sr}$	σ $^{87}\text{Sr}/^{86}\text{Sr}$
S1	VV	n.m.	n.m.	n.m.	n.m.	n.m.
S2	PP	15.0	162	0.093	0.7072	± 0.000009
S3	CP	149	214	0.695	0.7044	± 0.000010
S5	VV	n.m.	n.m.	n.m.	n.m.	n.m.
S6	VV	15.8	416	0.038	0.7040	± 0.000008
S7	CP	75.6	210	0.361	0.7043	± 0.000010
S8	MP	75.0	291	0.258	0.7047	± 0.000010
S9	VV	18.9	422	0.045	0.7041	± 0.000010
S10	CC	36.3	549	0.066	0.7044	± 0.000008
S11	VL	33.7	665	0.051	0.7040	± 0.000010
S12	MC	125	152	0.820	0.7065	± 0.000010
S13	CP	27.6	501	0.055	0.7045	± 0.000009
S14	MP	88.5	374	0.237	0.7051	± 0.000010
S15	CP	n.m.	n.m.	n.m.	n.m.	n.m.
S16	VQ	35.6	550	0.065	0.7040	± 0.000090
S17	CC	119	191	0.621	0.7041	± 0.000011
S20	CP	54.8	202	0.271	0.7041	± 0.000009
S21	MP	138	265	0.520	0.7060	± 0.000010
S22	CP	55.7	576	0.097	0.7040	± 0.000008
S30	CC	16.5	384	0.043	0.7042	± 0.000009
S40	CP	n.m.	n.m.	n.m.	n.m.	n.m.
S41	MP	72.0	291	0.248	0.7130	± 0.000009
S42	MB	75.5	165	0.458	0.7174	± 0.000010
S43	CP	156	166	0.940	0.7085	± 0.000009
I1	CC	23.5	417	0.056	0.7041	± 0.000011
I4	CC	n.m.	n.m.	n.m.	n.m.	n.m.
I5	CC	35.8	598	0.060	0.7040	± 0.000009
I6	CC	137	221	0.618	0.7040	± 0.000009
I7	CC	71.4	176	0.406	0.7041	± 0.000010
I8	CC	14.7	548	0.027	0.7044	± 0.000007
I9	CC	18.3	352	0.052	0.7042	± 0.000009

8.4. Results and discussion

8.4.1. Analysis of reservoir rock analogues: Potential host rocks of the geothermal system

The geochemistry of sampled rocks is analyzed to characterize the host rock interacting with the geothermal fluids. The analysis of reservoir rock analogues should identify geochemical variations between the different, igneous rock types that might be traced within the fluid signature. Element concentrations of the sampled reservoir rock analogues are summarized in Table 8.1. In the research area mainly three distinct rock types outcrop (Moreno & Lara, 2008): 1) plutonic rocks of dioritic to granitic composition belonging to NPB, 2) fresh volcanic rocks of rather uniform basaltic to andesitic composition 3) volcano-sedimentary units of the Cura-Mallín formation possessing highly variable SiO_2 concentrations, thus overlapping both, volcanic and plutonic rock facies (Figure 8.2). In the study area the volcano-sedimentary unit is dominated by the volcanic Guapitrío facies, as the samples range from pure andesitic lava flows to volcanoclastic conglomerates and lahar deposits (Villalón, 2015).

The spatial distribution of collected rocks marks the gradual transition from pure occurrence of batholithic rocks south of the volcanic chain to volcano-sedimentary units of the Cura-Mallín formation alternating with plutonic outcrops north of the chain (Figure 8.1). The occurrence of plutonic rocks does not cease north of the volcanic chain but is limited in size and incidence. North of the volcanic chain thermal springs often discharge at boundaries between plutonic and volcano-sedimentary rocks (Figure 8.1). The fresh volcanic rocks cover plutonic or volcano-sedimentary rocks in the vicinity of volcanic edifices.

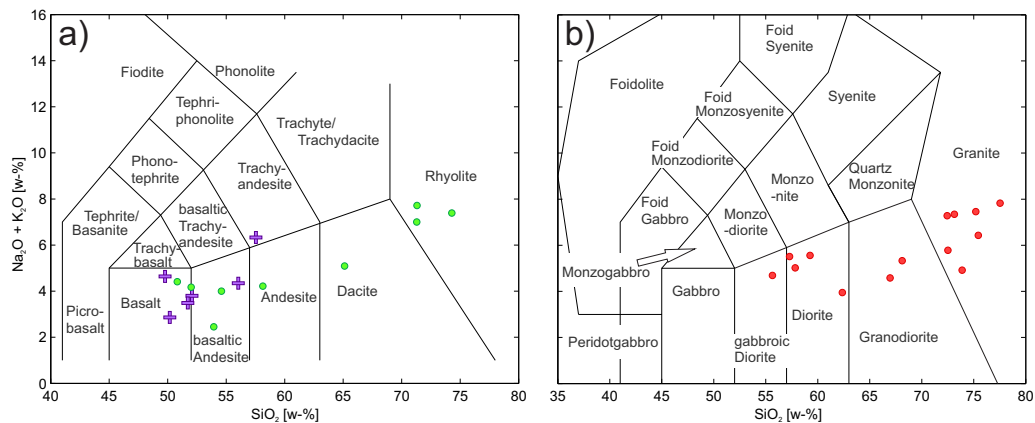


Figure 8.2.: Classification of sampled rocks using the TAS diagram for a) volcanic rocks (Le Maitre, 2005) and b) plutonic rocks (Middlemost, 1994). Volcanic rock samples are subdivided into volcanic rocks of recent activity (purple crosses) and volcano-sedimentary units (green circles).

The elemental composition and its statistical variance of different rock classes is shown in Figure 8.3 revealing the geochemical similarity between rocks of plutonic and volcano-sedimentary origin. Boxplots for SiO_2 , Al_2O_3 , Na_2O , MgO and CaO overlap extensively, significant differences occur only in terms of K_2O content. Yet it can be noted that recent volcanic rocks differ from plutonic or and volcano-sedimentary rocks, particularly MgO , CaO and Al_2O_3 concentrations. Despite this, allocation between geothermal fluid composition and related host rock geochemistry is masked, especially in this case of similar geochemical

composition, by secondary processes (different solubilities of primary minerals, precipitation of alteration products, temperature-dependent cation exchange e.g. in feldspars) and thus deceptive.

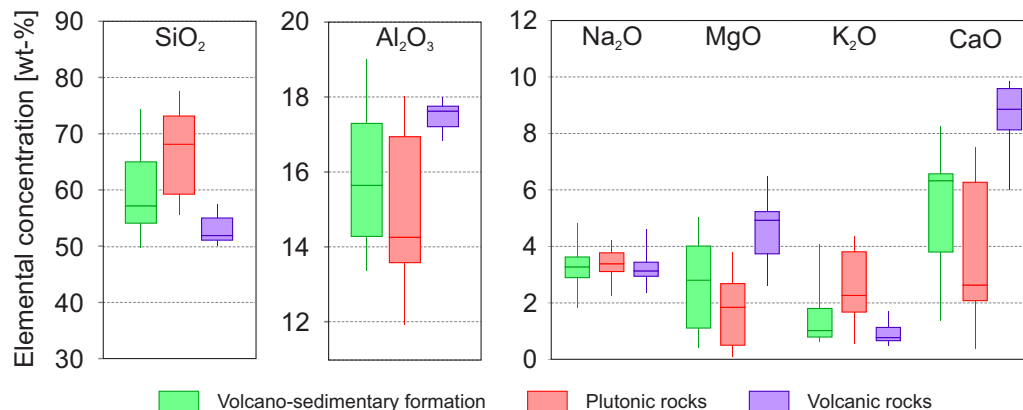


Figure 8.3.: Main elemental composition of reservoir rock analogues in boxplot display. Volcano-sedimentary and plutonic rocks have similar element distribution considering the variance in concentrations.

As a consequence Rb and Sr are used for comparison between fluid and rock signature (see the following chapter). Rb and Sr can substitute for K and Ca in the rock matrix due to their similar atomic radius and charge (Faure & Powell, 1986). Rb and Sr concentrations of the reservoir rock analogues as well as ⁸⁷Sr/⁸⁶Sr ratios, which are used in a combined approach, are listed in Table 8.1. Rb concentrations of the rock samples vary between 14.7 and 156 ppm with a positive correlation of Rb and K concentrations (Figure 8.4b). Sr rock concentrations range between 152 and 664 ppm, with an apparent but less clear correlation of Sr and Ca (Figure 8.4a). Plutonic rocks and K-rich volcano-sedimentary rocks (S12, S17, I6, I7) possess high Rb concentrations, while fresh volcanic rocks and the majority of the volcano-sedimentary rocks have low Rb concentrations. The opposite is observed for Sr and Ca concentrations: plutonic rocks and volcano-sedimentary rocks with low Ca-concentrations have comparably low Sr concentrations while volcanic and Ca-rich volcano-sedimentary rocks possess higher Sr concentrations.

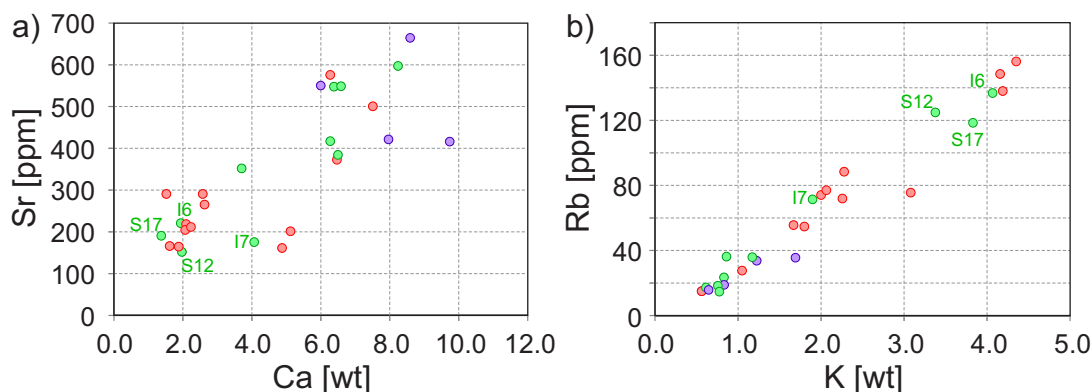


Figure 8.4.: a) Sr vs. Ca and b) Rb vs. K binary diagrams presenting the correlation between those elements in the rock samples (color code according to Figure FluidFig3)

Table 8.2.: Sampling locations, physico-chemical parameters, chemical composition, stable isotopes ($\delta^{18}\text{O}$ from H_2O and SO_4) and Sr isotope ratios from thermal springs around Villarrica volcano. Concentrations of solutes are given in mg/L, isotope ratios in ‰V-SMOW; n.m. = not measured, n.a. = not available, bdl.= below detection limit. Data for cation composition, Rb and Sr concentrations as well as $^{87}\text{Sr}/^{86}\text{Sr}$ and $\delta^{18}\text{O}(\text{H}_2\text{O})$ are taken from Held et al. (2017) and listed for completeness. For the complete dataset see 7

Sample	Label	Latitude [°S]	Longitude [°W]	Altitude [masl]	T [°C]	pH	TDS [mg/L]
Carranco	Car	39.7654	71.7922	450	82.0	8.9	375
Chihuito	Chi	40.1939	71.9345	312	85.0	8.9	485
Coñaripe	Con	39.6349	71.9239	260	71.7	7.8	524
Liquine	Liq	39.7394	71.8429	328	71.0	9.1	338
Liucura	Liu	39.2595	71.7926	618	29.5	7.9	304
Los Pozones	Poz	39.2263	71.6513	736	53.1	9.1	295
Menetue	Men	39.3291	71.7193	336	50.5	9.3	312
Palguin	Pal	39.4197	71.783	477	47.5	8.7	292
Panqui	Pan	39.2534	71.5306	926	50.8	8.0	390
Rincon	Rin	39.5077	71.8543	939	37.5	7.6	375
Rinconada	RinCo	39.4215	71.6696	605	27.6	6.1	788
Rio Blanco	Bla	39.1086	71.6136	733	54.1	7.7	400
San Luis	SL	39.34	71.6906	429	41.0	9.1	236
Toledo	Tol	39.1802	71.5849	920	42.5	7.8	871
Trancura Lake	Tra	39.3402	71.6946	372	36.0	9.0	229
Villarrica Rainwater	Lake	39.2723	71.9800	240	15.5	7.9	75
Caburgua	Rain	39.2199	71.8153	420	n.m.	7.6	37

Sample	Cl [mg/L]	Rb [$\mu\text{g}/\text{L}$]	Sr [$\mu\text{g}/\text{L}$]	Rb/Sr	$^{87}\text{Sr}/^{86}\text{Sr}$	$2\sigma^{87}\text{Sr}/^{86}\text{Sr}$	$\delta^{18}\text{O}(\text{H}_2\text{O})$ ‰ V-SMOW	$2\sigma\delta^{18}\text{O}(\text{H}_2\text{O})$
Carranco	34.1	23.5	74.0	0.318	0.71124	± 0.000009	-9.92	± 0.06
Chihuito	13.9	15.8	331	0.048	0.70425	± 0.000009	-10.25	± 0.03
Coñaripe	82.9	23.9	60.4	0.396	0.70410	± 0.000012	-8.10	± 0.02
Liquine	17.4	23.8	65.9	0.361	0.70620	± 0.000013	-9.45	± 0.04
Liucura	35.3	6.81	83.9	0.081	0.70419	± 0.000008	-9.07	± 0.03
Los Pozones	46.2	12.9	168	0.077	0.70413	± 0.000008	-10.24	± 0.03
Menetue	26.2	14.0	58.6	0.239	0.70411	± 0.000013	-9.04	± 0.00
Palguin	21.1	9.39	27.2	0.345	0.70452	± 0.000013	-9.87	± 0.06
Panqui	25.5	13.6	313	0.043	0.70408	± 0.000010	-10.38	± 0.00
Rincon	20.9	21.1	35.9	0.588	0.70413	± 0.000013	-9.74	± 0.04
Rinconada	40.6	28.3	105	0.270	0.70406	± 0.000008	-11.08	± 0.14
Rio Blanco	21.8	9.26	339	0.027	0.70442	± 0.000010	-10.13	± 0.05
San Luis	7.86	6.67	72.6	0.092	0.70400	± 0.000012	-9.25	± 0.04
Toledo	109	51.9	1100	0.047	0.70407	± 0.000010	-10.41	± 0.02
Trancura Lake	8.08	5.49	70.0	0.078	0.70413	± 0.000012	-9.21	± 0.04
Villarrica Rainwater	2.26	2.70	24.6	0.110	0.70417	± 0.000013	-8.57	± 0.05
Caburgua	1.48	0.352	4.47	0.079	0.70632	± 0.000009	-7.79	± 0.06

Sample	$\delta^{18}\text{O}(\text{SO}_4)$ ‰V-SMOW	$2\sigma\delta^{18}\text{O}(\text{SO}_4)$	CFC-11 [pmol/L]	Error-11 [pmol/L]	CFC-12 [pmol/L]	Error-12 [pmol/L]	CFC-113 [pmol/L]	Error-113 [pmol/L]
Carranco	3.19	± 0.05	0.43	± 0.05	0.34	± 0.05	0.05	± 0.05
Chihuito	2.11	± 0.1	0.22	± 0.05	0.14	± 0.05	0.03	± 0.05
Coñaripe	0.63	± 0.14	n.m.	n.m.	n.m.	n.m.	n.m.	n.m.
Liquine	3.78	± 0.1	0.32	± 0.05	0.2	± 0.05	0.04	± 0.05
Liucura	2.55	± 0.23	2.2	± 0.3	1.3	± 0.1	0.2	± 0.05
Los Pozones	-0.68	± 0.19	0.6	± 0.1	0.37	± 0.05	0.06	± 0.05
Menetue	1.55	± 0.04	0.5	± 0.1	0.36	± 0.05	0.05	± 0.05
Palguin	0.74	± 0.16	0.8	± 0.1	0.52	± 0.05	0.07	± 0.05
Panqui	-1.99	± 0.34	0.7	± 0.1	0.49	± 0.05	0.06	± 0.05
Rincon	0.33	± 0.19	1.6	± 0.2	0.88	± 0.05	0.13	± 0.05
Rinconada	0.56	± 0.15	1.7	± 0.2	1	± 0.1	0.15	± 0.05
Rio Blanco	0.85	± 0.28	n.m.	n.m.	n.m.	n.m.	n.m.	n.m.
San Luis	0.04	± 0.21	1.2	± 0.2	0.72	± 0.05	0.1	± 0.05
Toledo	-1.95	± 0.09	n.m.	n.m.	n.m.	n.m.	n.m.	n.m.
Trancura Lake	0.14	± 0.17	1.1	± 0.2	0.73	± 0.05	0.09	± 0.05
Villarrica Rainwater	n.a.	n.a.	3.5	± 0.4	2.1	± 0.2	0.32	± 0.05
Caburgua	n.a.	n.a.	n.m.	n.m.	n.m.	n.m.	n.m.	n.m.

8.4.2. Deduction of reservoir rock type using Rb/Sr and $^{87}\text{Sr}/^{86}\text{Sr}$ isotope ratios

Allocation between host rock and geothermal fluids can be derived from Sr isotope ratios in combination with Rb/Sr ratios (Graham, 1992; Cortecchi et al., 2005), as the fluid adapts the Rb and Sr concentrations as well as $^{87}\text{Sr}/^{86}\text{Sr}$ ratios from the host rock. $^{87}\text{Sr}/^{86}\text{Sr}$, based on the radioactive β -decay of ^{87}Rb to ^{87}Sr , depends on decay time, hence rock ages, and initial Rb concentration. Rb concentration correlates often with K concentration as Rb substitutes

K in a rock matrix due to similar atomic ratios and charge. $^{87}\text{Sr}/^{86}\text{Sr}$ isotope ratios are not affected by fractionation within the liquid phase (Stettler, 1977) thus preserving the rock signature. In geothermal fluids Rb behaves nearly conservatively (Graham, 1992), as shown by the near constant Rb/Cl ratios (Table 8.2), affected only within early stages of water-rock interaction by the uptake in illite before reaching full equilibrium (Giggenbach, 1991). Sr concentrations in geothermal fluids can, after equilibration and adaption of rock signature, be decreased by Sr incorporation in Ca-rich precipitates (e.g. calcite).

To differentiate between plutonic and basaltic host rocks, $^{87}\text{Sr}/^{86}\text{Sr}$ is often sufficient due to clearly separated isotope ratios. Presumably due to short decay times the Cenozoic rocks of NPB can possess low $^{87}\text{Sr}/^{86}\text{Sr}$ isotope ratios (generally not as low as volcanic rocks of basaltic origin but similar). The sampled Cenozoic plutonic rocks (S3, S7, S13, S20, S22) have low $^{87}\text{Sr}/^{86}\text{Sr}$ values between 0.7040–0.7045 (Table 8.1) overlapping in its minimum values volcanic signatures. To assure the distinction between plutonic and volcanic rocks Rb/Sr ratios are incorporated resulting in the Rb/Sr vs. $^{87}\text{Sr}/^{86}\text{Sr}$ diagram (Figure 8.5).

Statistical evaluation of Rb/Sr and $^{87}\text{Sr}/^{86}\text{Sr}$ values for plutonic and volcanic rocks is conducted using relevant datasets for NPB (N=212) (Munizaga et al., 1988; McMillan et al., 1989; Pankhurst et al., 1992, 1999) and volcanic rocks of major stratovolcanoes between 38.6°S and 40°S (N=79) (Hickey-Vargas et al., 1989; McMillan et al., 1989; Jacques et al., 2014). 2-D Boxplots are constructed reflecting areas of higher probability concerning Rb/Sr and $^{87}\text{Sr}/^{86}\text{Sr}$ ratios for each rock type. A significant differentiation between volcanic and plutonic rocks becomes obvious, as volcanic rocks have low Rb/Sr ratios (<0.075) and narrow $^{87}\text{Sr}/^{86}\text{Sr}$ range while plutonic rocks generally have higher Rb/Sr ratios (>0.21) and $^{87}\text{Sr}/^{86}\text{Sr}$ >0.7045 showing also a greater scattering. Nevertheless, overlaps of both probability fields exist documented by the whiskers. Literature data for the Cura-Mallín formation is not available.

The reservoir rock analogues of our survey at Villarrica-Quetrupillán-Lanín volcanic chain coincide with regional datasets (Figure 8.5): volcanic rocks plot within a narrow volcanic box, while plutonic rocks have a higher scattering still coinciding with the plutonic probability field. The majority of the Cura-Mallín samples have low Rb/Sr ratios comparable to volcanic rocks with similar or slightly elevated $^{87}\text{Sr}/^{86}\text{Sr}$ ratios (0.7040–0.7045). Volcano-sedimentary rocks of elevated K and Rb concentrations (Figure 8.4) have Rb/Sr ratios similar to plutonic rocks yet maintaining a low Sr isotope signature (I6, I7, S17 = 0.7040 - 0.7041).

Rb concentrations of spring discharges range from 5.5 to 51.9 $\mu\text{g}/\text{L}$, whereas Sr concentrations differ between 27.2 and 1099.7 $\mu\text{g}/\text{L}$. Sr isotope ratios of thermal spring waters exhibit variations between 0.7040 (SL) and 0.7112 (Car), whereas the local rain water has a ratio of 0.7063. The springs can be subdivided: 1) springs located within the plutonic field or exceeding it (Liq, Car) clearly related to water-rock interaction with plutonic rocks; 2) fluids of low Rb/Sr and $^{87}\text{Sr}/^{86}\text{Sr}$ ratios matching the signatures of volcanic or volcano-sedimentary rocks (Tol, Pan, Bla, Liu, Poz, Tra, SL); 3) hot spring fluids of elevated Rb/Sr ratios (0.2–0.6) but lowered $^{87}\text{Sr}/^{86}\text{Sr}$ ratios (Men, Rin, RinCo, Con, Pal). Whether the first two assignments are clear, the origin of the springs of lowered $^{87}\text{Sr}/^{86}\text{Sr}$ and elevated Rb/Sr ratios have to be discussed further. Possible origins are: a) interaction with plutonic rock of a low $^{87}\text{Sr}/^{86}\text{Sr}$ ratio; b) interaction with rocks of the Cura-Mallín formation possessing high Rb/Sr ratios; c) interaction with volcanic rocks in the state towards approaching full equilibrium and hence not depleted in terms of Rb; d) a mixture

of fluids interacting with volcanic and plutonic rocks. Although the origin of these springs could not be finally assigned, the lithology transition at the volcanic chain can be clearly traced. Springs south of the volcanic chain (Liq, Car) have Rb/Sr and $^{87}\text{Sr}/^{86}\text{Sr}$ signatures of fluids interacting with plutonic rocks, while the springs north of the chain (Tol, Pan, Liu, Poz, SL, Tra, Bla) have volcanic or volcano-sedimentary signatures. Considering the distribution of geological formations and the discharge location of the hot springs (Figure 8.1), an interaction between those fluids and the volcano-sedimentary Cura-Mallín formation is indicated. The documented intermediate signatures of springs in the volcanic chain might indicate an interaction with both plutonic and volcanic or volcano-sedimentary rocks (option d) coinciding with the lithology transition.

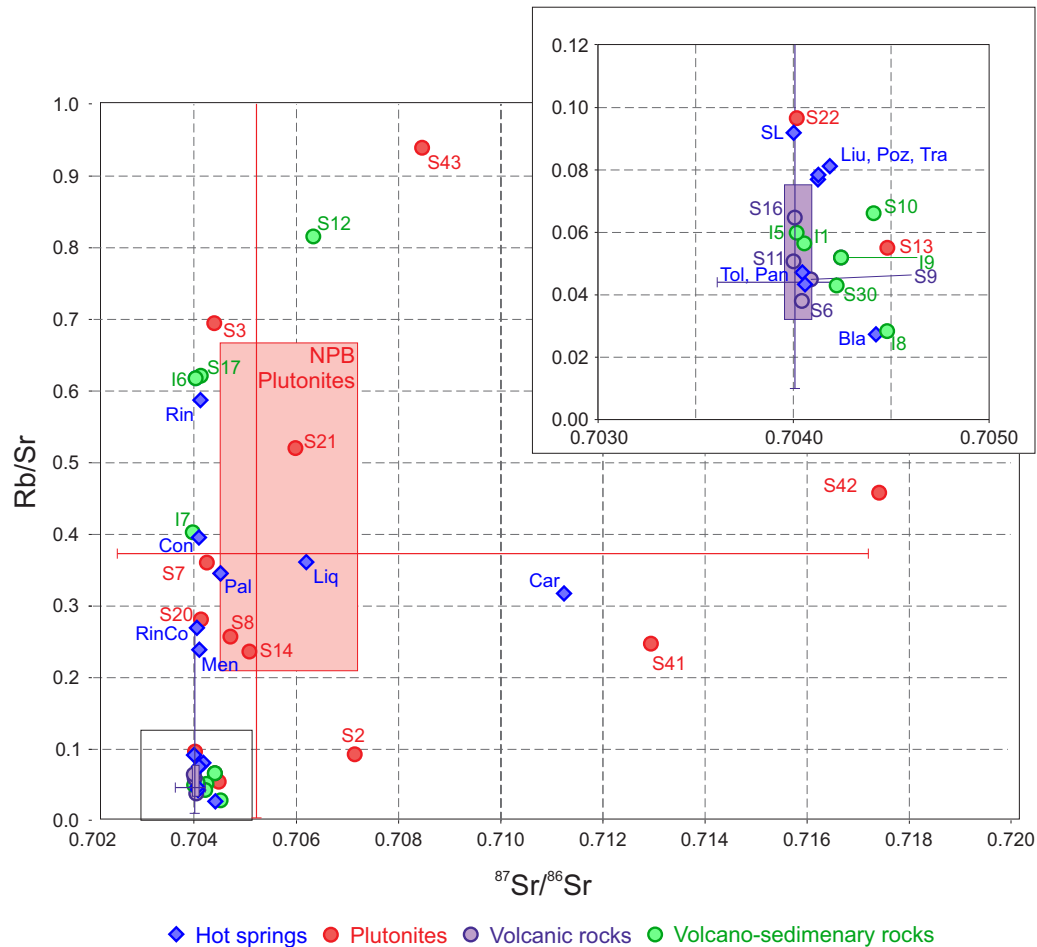


Figure 8.5.: Rb/Sr vs. $^{87}\text{Sr}/^{86}\text{Sr}$ plot for hot spring discharges (blue diamonds) and rock samples (circles, colorcode according to Figure 8.3) from the Villarrica area. Additionally statistical relevant datasets for Rb/Sr and $^{87}\text{Sr}/^{86}\text{Sr}$ ratios are incorporated for NPB (N=212) (Munizaga et al., 1988; McMillan et al., 1989; Pankhurst et al., 1992, 1999) and volcanic rocks of major stratovolcanoes between -38.6°S and -40°S (N=79) (Hickey-Vargas et al., 1989; McMillan et al., 1989; Jacques et al., 2014). The data is presented in 2-D boxplots for NPB (red) and volcanic rocks (purple). Chihuío hot spring not included as no outcrops of nearby rocks were collected. Signature of S12 has to be considered carefully as Mesozoic sedimentary rocks occur only sparsely in a restricted area near the Lanín volcano without clear relation to geothermal fluids.

8.4.3. Temperature dependent oxygen isotope fractionation of the SO₄-H₂O system

The oxygen isotope fractionation between H₂O and SO₄, due to its temperature dependence, is used as a tool to determine reservoir temperature (Hoering & Kennedy, 1957). The results of the method will be compared to the reservoir temperatures calculated after re-evaluation of geothermometric techniques carried out by Nitschke et al. (2018).

Fractionation of ¹⁸O in the SO₄-water system as a geothermometric tool was chosen, as it is lithology independent in igneous systems. Hydrothermal alteration processes in such systems, usually in form of well-documented clay mineral precipitation or cation exchange reactions of the feldspars, do not affect the oxygen fractionation. SO₄ assimilation through leaching of evaporitic rocks or SO₄-rich groundwater would adversely affect temperature estimation (e.g. Cortecchi, 1974), which can be neglected considering the absence of evaporitic rocks (Moreno & Lara, 2008). Modification of the oxygen isotope composition of SO₄ by dilution with shallow SO₄-rich groundwater is also negligible due to a low SO₄ concentration (<5% of thermal waters) of the local groundwater (Held et al., 2017). Reservoir processes affecting the oxygen isotope signatures, especially phase separation through boiling during decompression results in incorrect temperature estimations. Yet ¹⁸O(H₂O) evaluation (see $\delta^{18}\text{O}/\delta^2\text{D}$ diagram in (Held et al., 2017)) indicates the absence of boiling in the Villarrica geothermal fluids, neglecting temperature estimation distortion. Impacts on oxygen isotope composition of H₂O by dilution with shallow groundwater cannot be excluded. Even with the quantification of dilution (see next chapter) its correction is not feasible due to the unknown oxygen isotope composition of the infiltrating fluid, which is difficult to determine in areas of pronounced relief. Equilibration kinetics of oxygen fractionation is rather fast under conditions of a medium- and high-temperature geothermal reservoir (Hoering & Kennedy, 1957) decreasing strongly at low ambient temperatures (Lloyd, 1968; Zhonghe, 2001)). For geothermal applications the kinetics implicate that temperature estimation of low-enthalpy reservoirs will fail but for medium- and high-temperature reservoirs the temperature estimation will not be masked by re-equilibration in shallow reservoirs, being known e.g. from the Mg/K geothermometer (Giggenbach, 1991).

Oxygen isotope ratios of fluids range between -8.1 and -11.1 ‰ V – SMOW and for SO₄ vary between 3.78 and -1.99 ‰ V – SMOW (Table 8.2). The fractionation factor α can be calculated as:

$$\alpha = \frac{10^3 + \delta^{18}\text{O}(\text{SO}_4^{2-})}{10^3 + \delta^{18}\text{O}(\text{H}_2\text{O})} \quad (8.1)$$

Geothermometer equations and, hence, equilibrium conditions have to be selected according to the sulfate species (SO₄²⁻, HSO₄⁻, H₂SO₄) and physicochemical parameters prevailing in the reservoir (Boschetti, 2013). For the expected medium-enthalpy system <200 °C (Sánchez et al., 2013; Held et al., 2015) and pH > 5, SO₄²⁻ is the dominant species, resulting in the selection of equations according to Zeebe (2010) and Halas & Pluta (2000).

Oxygen fractionation of the SO₄²⁻-H₂O system is evaluated using the method firstly described by Boschetti (2013) and applied by e.g. in Awaleh et al. (2015, 2017) with the fractionation coefficient being plotted versus discharge temperature (Figure 8.6). The distribution of our data suggests two clusters. Samples Liq, Car and Chi plot close to the equilibrium line, indicating similarity between reservoir and discharge temperatures.

Temperature estimations from oxygen isotope fractionation are in accordance with re-evaluated temperature estimations from SiO_2 and Na/K geothermometers in the range of 83–94 °C (Table 8.3) (Nitschke et al., 2018). These springs are located south of the volcanic chain along the LOFS in the plutonic sequence. It seems that the fluids are not affected by cooling during ascent.

The majority of springs display a shift from equilibrium pointing to a significantly higher equilibration temperature compared to the discharge temperature. These springs are located in the volcanic chain or north of it. The reservoir temperatures, calculated by oxygen isotope fractionation are significantly higher (100–140 °C) than for springs in the plutonic sequence. Conformity between temperature estimates from oxygen isotope fractionation and re-evaluated solute geothermometer is obtained, the few outliers are discussed in Nitschke et al. (2018).

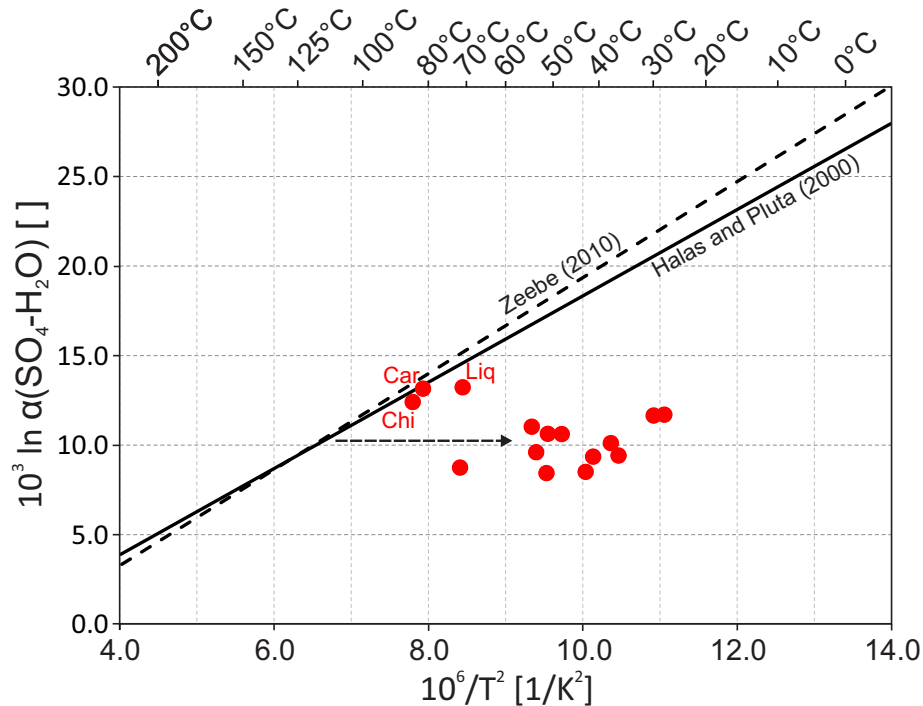


Figure 8.6.: Evaluation of oxygen isotope fractionation by depicting the fractionation factor α over discharge temperature. Reservoir temperature can be estimated by horizontal projection to geothermometer equations after Halas and Halas & Pluta (2000) or Zeebe (2010). As a consequence, the depicted dashed, horizontal arrow represents conductive cooling.

8.4.4. Estimating Surficial Dilution using chlorofluorocarbons (CFCs)

Anthropogenic tracers with evolving atmospheric concentrations can be used to estimate subsurface residence times and the mixing of different fluid bodies. Usually tritium is the method of choice, but as tritium input into the southern hemisphere is low due to the limited number of nuclear tests there and, hence, produces ambiguous results, we selected chlorofluorocarbons as anthropogenic tracers. Emission of CFCs began in the 1940s with the usage as refrigerants or propellants resulting in an increase of atmospheric and subsequently groundwater concentration. After the Montreal protocol, CFCs were replaced resulting in a decrease of atmospheric concentrations (Figure 8.7).

Table 8.3.: Reservoir temperature estimations calculated using the geothermometer based on oxygen isotope fractionation of the SO_4 -water system. Calculations of fractionation factor α and temperatures after the formulas of Halas & Pluta (2000) and Zeebe (2010).

Sample	α	Zeebe (2010) T [°C]	Halas & Pluta (2000) T [°C]
Carranco	1.0132	88	84
Chihuahua	1.0125	94	91
Conaripe	1.0088	134	134
Liquine	1.0133	87	83
Liucura	1.0117	101	99
Loz Pozones	1.0097	123	123
Menetue	1.0107	112	110
Palguin	1.0107	112	110
Panqui	1.0085	138	139
Rincon	1.0102	117	116
Rinconanda	1.0118	101	98
Rio Blanco	1.0111	108	106
San Luis	1.0094	126	126
Toldeo	1.0085	137	138
Trancura	1.0095	125	125

CFC concentrations in the geothermal spring discharges are reported in Table 8.2. All samples of thermal springs and meteoric waters contain CFCs. As expected, high concentrations are observed in meteoric samples (Lake Pucón: e.g. $\text{CFC}_{11} = 3.5 \text{ pmol L}^{-1}$) due to a continuous exchange with the atmosphere. Geothermal springs have lower values (e.g. $\text{CFC}_{11} = 0.22\text{--}2.2 \text{ pmol L}^{-1}$). Particularly low values of $\text{CFC}_{11} < 0.5 \text{ pmol L}^{-1}$ are observed for springs south of the volcanic chain (Liq, Car, Chi). For comparison to atmospheric concentrations aqueous concentrations [pmol L^{-1}] of fluids determined are converted into atmospheric concentrations [pptv] using eq. 8.2 (Plummer & Busenberg, 2006).

$$C_i = K_{H,i} \chi_i (P - p_{\text{H}_2\text{O}}) \quad (8.2)$$

where C_i is the aqueous concentration of each CFC, $K_{H,i}$ is the CFC specific Henry's law constant dependent upon TDS and temperature, χ_i the dry air mole fraction of each CFC, P the elevation-dependent total atmospheric pressure and $p_{\text{H}_2\text{O}}$ the temperature-dependent water vapor pressure. Results of the conversion are shown in Table 8.4. The results of selected springs are presented in comparison to atmospheric concentration evolution in the southern hemisphere in Figure 8.7. Direct age determination (simple matching of fluid and atmospheric concentrations as presented by (Plummer & Busenberg, 2006)) yields non-modern infiltration. Consistently CFC_{11} and CFC_{12} values for thermal springs yield similar age estimations (e.g. Pan: $\text{age}(\text{CFC}_{11}) = 1967.5$; $\text{age}(\text{CFC}_{12}) = 1969$), with younger infiltration ages being obtained from CFC_{113} (Pan: $\text{age}(\text{CFC}_{11}) = 1975$). This discrepancy is, according to Plummer & Busenberg (2006), an indication of subsurface mixing processes. Thus, in the following section subsurface flow is investigated with respect to mixing processes comparing observed CFC concentrations of hot springs with theoretical groundwater concentrations of different subsurface mixing models.

Anthropogenic tracers determined in thermal springs reflect a flux-averaged mixture of differently aged fluids (Gardner et al., 2011). The mixing of groundwater depends on the mixing processes (Turnadge & Smerdon, 2014). We compare no-mixing, piston flow to binary mixing and exponential mixing. Binary mixing (Eq. 8.3) is an end-member mixture of two differentially weighted (χ) water bodies of different infiltrations ages and, hence, different input concentrations (C_1, C_2) resulting in the observed concentration C_{obs} .

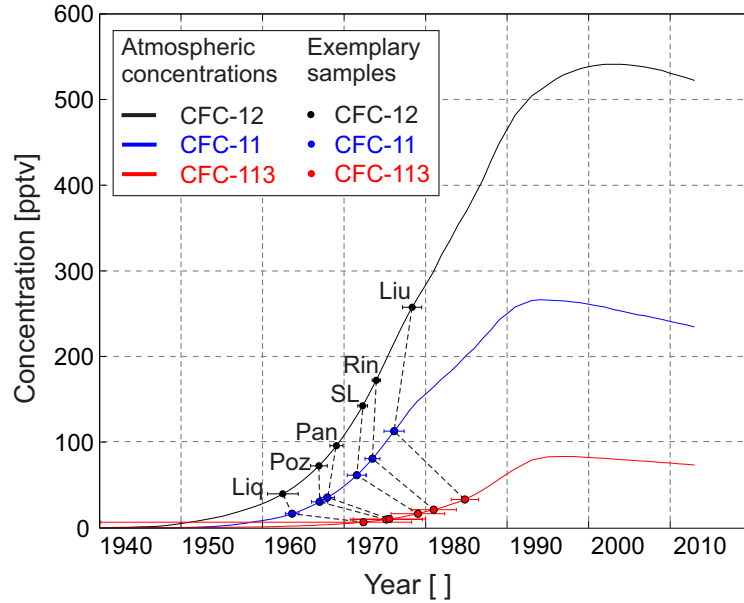


Figure 8.7.: Evolution of atmospheric concentrations of CFCs (CFC-11, CFC12, CFC-113) in the southern hemisphere. Data averaged from [Plummer & Busenberg \(2006\)](#) and [NOAA \(2015\)](#). Results for selected springs (Liq, Liu, Pan, Poz, Rin, SL) are converted into atmospheric concentrations [pptv] (see text).

$$C_{obs} = C_1\chi + C_2(1 - \chi) \quad (8.3)$$

In the geothermal context, binary mixing reflects the mixing of old and hence CFC-free reservoir fluid with CFC bearing meteoric groundwater. This approach represents the mixing of the thermal fluid crossing shallow groundwater during ascent. Exponential mixing (Eq. 8.4) describes complete mixing of multiple water bodies with different infiltration ages and hence CFC content. In the geothermal context, it displays a flow system of variable flow paths and/or the progressive addition of meteoric water to the geothermal reservoir. The observed CFC concentration $C(t_{obs})$ represents the average concentrations with a mean subsurface transient time τ ([Małoszewski & Zuber, 1982](#)).

$$C(t_{obs}) = \int_0^{\infty} C_{atmos}(t_{obs} - t') e^{-\lambda t'} \frac{1}{\tau} e^{-\frac{t'}{\tau}} dt' \quad (8.4)$$

, where C_{atmos} is the date-specific infiltrated CFC concentration, t_{obs} the time of observation, t' is the integration variable representing the infiltration age of each water portion and the exponential term accounts for first-order decay with half-life λ (included when appropriate e.g. in terms of intense bacterial reduction).

In the first step, it is tested whether subsurface mixing can be described by the binary mixing approach (Figure 8.8), while in a second step exponential mixing is evaluated (Figure 8.9). In Figure 8.8 analyzed CFC concentrations of hot spring waters are compared with theoretical fluid concentrations of (1) no-mixing fluid flow (piston-Flow) or (2) binary mixing. The binary mixing line (Eq. 8.3) is constructed by the connection of CFC-free fluid ($c(\text{CFC}) = 0$) with the CFC signature of recently infiltrated groundwater (assumed infiltration age = 2013) (Figure 8.8). For the CFC-11/CFC-12 system (Figure 8.8a) CFC concentrations of thermal discharges match the Piston-Flow and partially also the

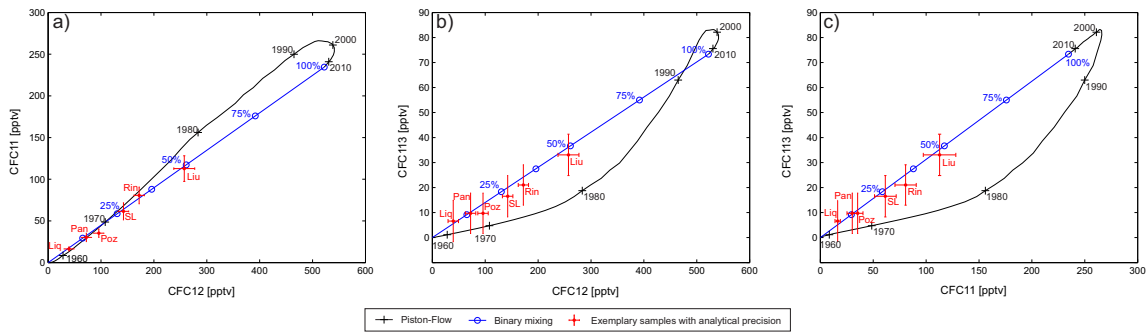


Figure 8.8.: Tracer plots comparing a) CFC-11 vs. CFC-12, b) CFC-12 vs. CFC-113, and c) CFC-11 vs. CFC-113 for southern hemisphere atmospheric input concentrations. Black lines represent the Piston-Flow approach with selected infiltration ages (+). The blue lines depict binary mixing of modern water, infiltrated 2013 with pre-modern, CFC-free water. Blue circles representing different mixing ratios. Red dots show analyzed CFC concentrations of selected thermal fluids. For legibility, only selected springs are displayed, full results in Table 8.4.

binary mixing approach. However, when considering the remaining concentration plots, a discrepancy becomes obvious (Figure 8.8b and c). Here the binary mixing and the measured CFC concentrations show a significant coincidence, whereas the Piston-Flow fluid movement is not the process generating hot spring waters of the Villarrica system. All thermal springs (also those not presented) match the constructed binary mixing curve within the range of the errors. Mixing ratios of old, CFC-free and meteoric fluids in exchange with recent atmospheric CFC concentrations can be derived from the positions along the binary mixing curve. Proportions from 50–96 % of old fluid are determined for the analyzed samples (Table 8.4). Higher degrees (>90 %) of an old, CFC-free fraction are determined for springs along the LOFS in the plutonic sequence (Chi, Liq, Car).

Table 8.4.: Results of subsurface mixing analysis. Binary mixing determines proportions of old, CFC-free fluid, while exponential mixing displays the mixing by mean transit time averaging residence times of different fluid bodies. Not shown are analyses of Coñaripe, Rio Blanco and Toledo hot springs as contamination with atmospheric CFCs could not be excluded.

Hot spring	CFC-11 [pptv]	σ -11 [pptv]	CFC-12 [pptv]	σ -12 [pptv]	CFC-113 [pptv]	σ -113 [pptv]	Binary mixing [% old CFC-free]	Mean transit time [a]
Carranco	21.7	2.5	66.5	9.8	8.1	8.1	90±0.5	300-400
Chihuio	11.1	2.5	27.4	9.8	4.9	8.1	96±0.5	>500
Lake Pucon	179.4	20.5	415.9	39.6	52.9	8.3		
Liquine	16.4	2.6	39.6	9.9	6.6	8.3	93±0.5	450-550
Liucura	112.7	15.4	257.4	19.8	33.1	8.3	51±4	50-60
Los Pozones	30.2	5.0	72.3	9.8	9.7	8.1	86.5±1.5	200-300
Menetue	25.6	5.1	71.3	9.9	8.3	8.3	88±1.5	300-400
Palguin	40.3	5.0	101.6	9.8	11.3	8.1	82±2	170-190
Panqui	35.3	5.0	95.9	9.8	9.7	8.1	83±0.5	180-210
Rincon	80.6	10.1	172.1	9.8	21.0	8.1	67±2	80-100
Rinconada	84.4	9.9	193.8	19.4	23.8	7.9	63±4	80-90
San Luis	61.5	10.2	142.5	9.9	16.5	8.3	73±2.5	110-120
Trancura	56.2	10.2	144.2	9.9	14.8	8.2	72.5±3	120-140

Exponential mixing curves, additionally displaying exemplary mean transient times, are plotted in Figure 8.9. Fluids, resulting from a mixing process based on an exponential mixing model, can be characterized by the mean transient time τ , averaging the ages of mixed water bodies. The CFC concentrations of thermal spring waters match the exponential mixing curve within the range of errors. Mean transient times of 50–500 a are

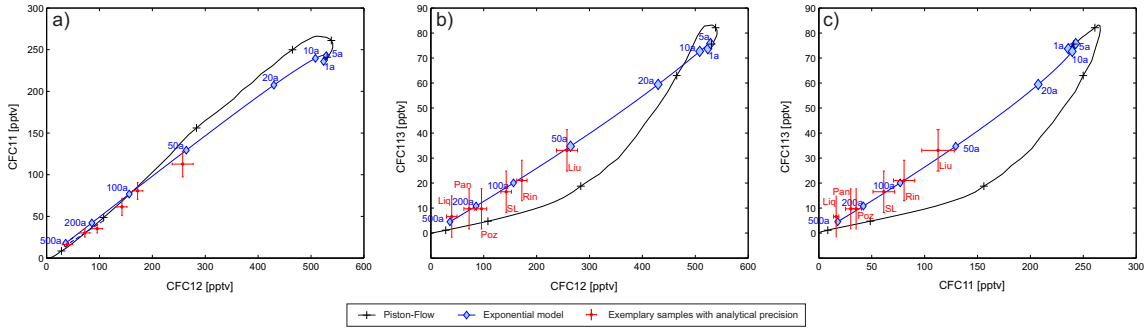


Figure 8.9.: Tracer plots comparing a) CFC-11 vs. CFC-12, b) CFC-12 vs. CFC-113, and c) CFC-11 vs. CFC-113 for southern hemisphere atmospheric input concentrations. Black lines represent the Piston-Flow approach with selected infiltration ages (+) for orientation. Blue lines depict exponential mixing with varying mean transient times (diamonds). Red dots show CFC concentrations of selected thermal fluids. Full results can be taken from Table 8.4.

determined (Table 8.4). As expected and in coincidence with results from binary mixing high mean transit times are calculated for springs along the LOFS (Liq, Car, Chi).

8.4.5. Comprehensive discussion and conceptual model

The results of analysis of CFC concentrations reveals that subsurface mixing strongly affects the circulation system. It becomes obvious that the mixing process (binary end-member mixing or continuous exponential mixing) cannot be resolved as the two theoretical mixing lines have only minor deviations and, hence, CFC signatures of the hot springs match both mixing lines. Considering the measured local heat flow density of $q_0 = 132\text{--}168 \text{ mW m}^{-2}$ (Hamza & Muñoz, 1996) and assuming a thermal conductivity range of $\lambda = 2.0\text{--}3.0 \text{ W m}^{-1} \text{ K}^{-1}$ (e.g. Eppelbaum et al., 2014) and a radioactive heat production range of $A = 0.5\text{--}3 \mu\text{W/m}^3$ (e.g. Jaupart et al., 2016; Rybach, 1976) for crustal rocks, the reservoir depth can be constrained to $z = 1600\text{--}3100 \text{ m}$ considering the estimated maximum reservoir temperatures of $140 \text{ }^\circ\text{C}$. For geothermal fluids of comparable reservoirs, infiltration ages typically $>1000 \text{ a}$ are determined, often even exceeding $10\,000 \text{ a}$ (e.g. Pearson Jr. et al., 1991; Morikawa et al., 2005; Yokochi et al., 2013; Waber et al., 2017). Mean transient time of $50\text{--}500 \text{ a}$, as required to fulfil the CFC signatures of the fluids in terms of exponential mixing, conflicts with observations for geothermal circulation systems worldwide. As a consequence we believe that binary mixing between a deep CFC-free geothermal fluid and shallow groundwater with a modern CFC signature is most likely to reflect the subsurface mixing process. This mixing takes place during ascent of the geothermal fluid to the surface.

The lithology transition affects the geothermal circulation systems. In the plutonic sequence south of the volcanic chain, hot springs (Chi, Liq, Car) occur along the distinct run of the LOFS master fault. The highest percentages of the old fluid fraction are observed from results of CFC analysis. In combination with the (quasi) equality between reservoir and discharge temperature we conclude a highly channeled fluid ascent, presumably taking place on distinct, permeable fault zones. At the volcanic chain and to the north of it, the hot springs, discharging from volcanic or volcano-sedimentary formations, have higher and more variable proportions of mixing with meteoric waters. The hot springs have a more disperse spatial distribution often associated with secondary faults or

lithology boundaries. In combination with the discrepancy between reservoir and discharge temperatures a branched, less focused fluid circuit is indicated. The differences in fluid pathways may be related to the different responses of the lithologies to the regional stress field. For instance, a similar behavior is inferred for the differences between gneisses and granites in the Black Forest by [Stober & Bucher \(1999\)](#), where the development of deep conduits is limited to granitic bodies.

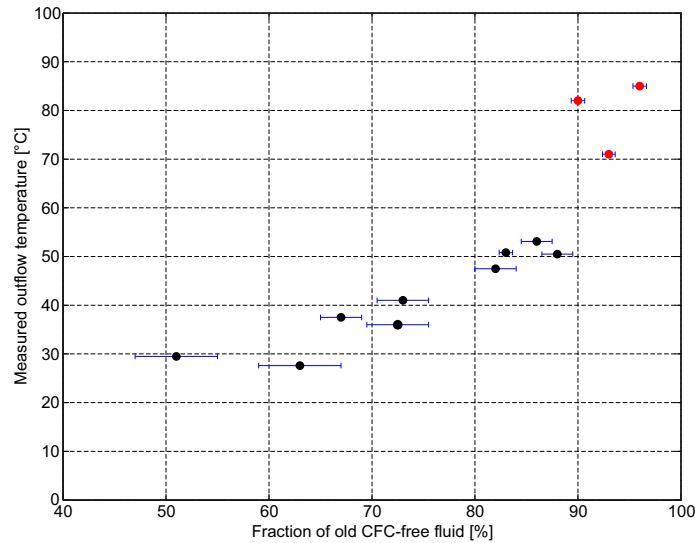


Figure 8.10.: Evaluation of subsurface cooling presented by plotting the ratio of old fluid, determined from CFC investigations vs. discharge temperature. Red circles: Springs south of the volcanic chain along the LOFS; black circles: Springs north of or along the volcanic chain; blue: Error bars of fraction estimation.

Reservoir temperature estimations from oxygen fractionation of the $\text{H}_2\text{O}-\text{SO}_4$ system are in good agreement with refined solute ([Nitschke et al., 2018](#)) and multi-component ([Nitschke et al., 2017a](#)) geothermometric methods. In these studies, on selected springs in the volcanic chain (RinCo, Rin) higher temperatures (up to 180°C) are estimated in agreement with maximum temperature estimations for the Geometricas hot spring ([Sánchez et al., 2013](#)). From all methods used, the following reservoir temperatures can be derived: a) $80\text{--}100^\circ\text{C}$ for springs along the LOFS in plutonic rocks, b) $100\text{--}140^\circ\text{C}$ for springs north of the volcanic chain and c) elevated temperatures (up to 180°C) for some springs in the volcanic chain. The low discharge temperatures in group b) cannot be explained by higher dilution rates with shallow, cold groundwater alone, since linear temperature extrapolation towards 100% CFC-free fluid does not yield the determined reservoir temperatures (Figure 8.10). Hence, a combination of conductive cooling and cooling by mixing with meteoric groundwater causes the decrease in the outflow temperature.

The origin of the different reservoir temperatures in plutonic and volcano-sedimentary formations might be related to: A) different basal heat flow q_0 ; B) variations in circulation depth of the geothermal fluids or C) different heat conductivities λ of the two lithologies. Whether the two first options are possible, option C is doubtful, as higher reservoir temperatures in the volcano-sedimentary formations would require higher heat conductivities of these rocks keeping the remaining parameters (A, q_0 , z) constant. Yet in general plutonic rocks have heat conductivities exceeding that of volcanic rocks (e.g. [Eppelbaum et al., 2014](#)). The elevated temperatures in the volcanic chain might result from a limited, local intrusion of volcanic volatiles generated by magmatic degassing ([Held et al., 2017](#)) or a

locally enhanced geothermal gradient both possibly related to the volcanic activity of the Villarrica volcano.

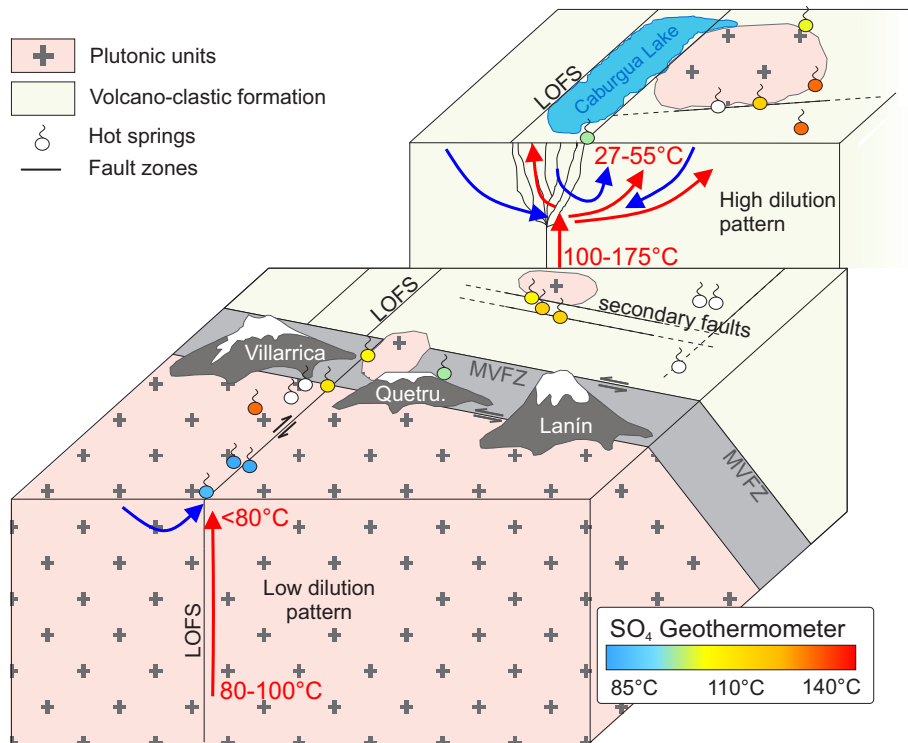


Figure 8.11.: Conceptual model illustrating the lithology-controlled fluid circulation proposed for the Villarrica geothermal system. Hot spring locations are marked by circular springs symbols with color code representing estimated reservoir temperature from oxygen isotope fractionation of the $\text{SO}_4\text{-H}_2\text{O}$ system (white symbols = springs not sampled). Blue and red arrows represent the movement of meteoric and deep geothermal fluids respectively.

In the following a conceptual model summarizing all studies of the Villarrica geothermal system (Sánchez et al., 2013; Held et al., 2015, 2016, 2017; Nitschke et al., 2017a, 2018) (Figure 8.11). The geothermal system is located at the intersection of LOFS with WNW-ESE oriented Andean Transfer faults (MVFZ and secondary faults). For the Caburgua segment a sub-vertical LOFS, <3 km in width, is revealed by magnetotellurics presumably forming a flower structure. For the MVFZ a north dipping structure below the volcanic chain is detected by MT measurements. The medium enthalpy geothermal system is recharged by meteoric water. Fluid composition is controlled by water-rock interaction with igneous rock. Indications for a major magmatic contribution are lacking. Elevated B/Cl ratios observed for springs at the volcanic chain indicate a minor contribution of magmatic vapor addition. This observation is in accordance with the findings of Wrage et al. (2017), which are able to relate higher B/Cl ratios in SVZ to ATF faults misoriented to the regional stress field. The gradual transition from plutonic rocks of NPB to volcano-sedimentary rocks of the Cura-Mallín formation can be located in the volcanic chain by Sr isotopes and Rb/Sr ratios in the geothermal fluids. The geothermal circulation pattern appears to be lithology-controlled and therefore showing formation-specific differences. In the plutonic sequence along the LOFS a channeled fluid flow on discrete, permeable conduits is suggested. In the Cura-Mallín formation, ramified fluid movement appears to be distributed over a wide spread fracture and fault network. Similar fluid movement conditions are

suggested by [Sánchez-Alfaro et al. \(2016\)](#) for the Tolhuaca geothermal reservoir, also present inside the Cura-Mallín formation. The findings support the concept of [Wrage et al. \(2017\)](#) proposing subhorizontal flow in volcano-sedimentary units of the Cura-Mallín formation and vertical flow prevailing in plutonic units. Reservoir temperatures of 100–140 °C in the volcano-sedimentary units exceed the maximum temperatures of 80–100 °C determined for hot springs discharging from plutonic rocks. Maximum in-situ temperatures of up to 180 °C are estimated for individual hot springs on the flanks of the Villarrica volcano.

8.5. Conclusion

The principal goal of geothermal exploration methods is the identification of hydraulic and thermal reservoir properties. Very often, in early stages of geothermal exploration hot spring fluids are the only, yet indirect access to the subsurface allowing forecasts on geothermal reservoir conditions. The specific situation at the Villarrica-Quetrupillán-Lanín volcanic chain with numerous hot springs discharging could be used to test different geochemical methodologies. The combination of different geochemical methods (CFC, Sr isotopes, geothermometry, etc.) enables a detailed investigation on subsurface conditions regarding subsurface mixing, identification of reservoir rocks and reservoir temperatures.

Since only minor geochemical variations of rock composition are exposed, Sr isotope signatures in combination with Rb and Sr concentrations turned out to be a most sensitive lithology tracer. The lithology transition can be traced in the fluid signature and situated in the volcanic chain. Therewith the methodology can be used to exhibit the contrast between the plutonic formations south of the volcanic chain towards the volcano-sedimentary units in the north. CFC species in combination with the fractionation of oxygen isotopes quantify the fluid systems in terms of subsurface mixing processes and reservoir temperatures. The results provide key information for a geochemically-based conceptual model hinting at a disperse, rather slow circulation along a branched fault and fracture network at higher subsurface temperatures in the volcano-sedimentary sequence. In the plutonic formations, a channeled, faster flow along distinct fault zones of the LOFS at lower subsurface temperatures is derived. Thus, lithological control of the circulation pattern is indicated. Additional hydrogeological or geophysical information would be required to support the identification of optimum geothermal reservoir conditions linked to the Cura-Mallín formation.

The application of CFC analysis offers important perspectives for future geothermal resource analysis. Since effects from dilution can be quantified and eliminated, it allows for a reconstruction of the true reservoir fluid composition. Only then, trustful estimations of reservoir temperatures can be conducted minimizing the large spread of temperature estimations from classical geothermometer approaches. For the Villarrica system the re-evaluation of different solute geothermometers, conducted in the second part of the combined study ([Nitschke et al., 2018](#)), generates concordant and plausible subsurface temperatures disclosing mid-enthalpy conditions. Besides enhancement of geothermometry the true reservoir fluid composition also enables a reliable prediction of scaling and corrosion.

Acknowledgements

The study is part of a collaborative research project between Karlsruhe Institute of Technology (KIT) and the Andean Geothermal Center of Excellence (CEGA, Fondap-Conicyt 15090013). The authors appreciate the support under the BMBF- CONICYT

International Scientific Collaborative Research Program (FKZ 01DN14033/ PCCI130025). Additional support under the topic “Geothermal Energy Systems” of the Helmholtz portfolio project “Geoenergy” and by EnBW Energie Baden-Württemberg AG is gratefully acknowledged. Special thanks go to our colleagues Diego Aravena, Daniele Tardani, Gabriel Perez, Elisabeth Eiche, Ignacio Villalón, and especially to Pablo Sánchez for the support during fluid sampling and many fruitful discussions. The authors would like to thank Ilka Kleinhanns from the University of Tübingen for help in the strontium isotope measurements of the rock samples. We thank Tiziano Boschetti and an anonymous reviewer for their fruitful comments that helped a lot to improve the manuscript.

9. Comprehensive discussion and outlook

Increasing demand of geothermal energy for future global energy mix requires accelerated exploitation of geothermal resources. To realize the IEA guidelines initially the exploitation of conventional resources is envisaged followed by the expansion of EGS resources in a second phase (IEA, 2011). Conventional systems are associated to areas of enhanced geothermal gradients originating from anomalous heat sources like active volcanism, magmatic intrusions, active rifting, mantle upwelling, etc. (Harvey et al., 2016). A majority of conventional resources is associated with active plate margins characterized by volcanism or magmatism. Development of conventional systems has advanced for some countries, e.g. Iceland, USA, Philippines, Indonesia, Mexico, New Zealand (Bertani, 2016), yet South American countries are lacking substantial amounts of geothermal energy production so far. Chile, with its more >4000 km long, active plate boundary, has an substantial geothermal potential (e.g. Lahsen et al., 2010; Procesi, 2014; Aravena & Lahsen, 2012), but so far only minor geothermal production as infrastructural and legislative barriers impeding geothermal development in the past (compare Chapter 1.2). The change of legislation (IRENA, 2015), the foundation of scientific geothermal research, e.g. CONICYT funded Centro de Excelencia en Geotermia de los Andes (CEGA) and the launch of national and global geothermal development funds (e.g. World Bank: Clean Technology Fund, Government of Chile/Inter-American Development Bank: Geothermal Risk Mitigation Program (MiRiG), KfW/EU: Geothermal Development Facility) boosts geothermal development in Chile. As initial results a first geothermal power plant - Cerro Pabellon - with an installed capacity of 48 MW_{el} could be installed. The project, as a majority of high-enthalpy geothermal resources in Chile, is located in the Andean Cordillera remote from potential energy consumers.

Within this thesis we focus on the exploration of a low/medium enthalpy resources in Chile, which occur also in the proximity of potential energy consumers. These resources are often related to major fault zones or particular geologic formations. In Germany these resources are in focus of geothermal exploitation. For the Munich area heat supply for district heating is successfully realized by geothermal energy (e.g. Dorsch & Pletl, 2012). Electricity generation using binary power plants is realized in the Upper Rhine Valley, SW Germany/NE France (e.g. Baujard et al., 2017). In the framework of this work we want to draw attention to these resources in Chile as realization and exploitation benefits from

accessibility, consumer proximity and thermal water conditions (limited scaling due to small degree of oversaturation, small corrosion potential due to usually high pH and limited TDS, sustainable reservoir fluid management (no steam loss)). Yet the low/medium enthalpy geothermal systems require an adaptation of exploration strategy, which are adjusted for the exploration of high-enthalpy resources. The BMBF funded ExCapp¹ project as well as the follow-up, CONICY-BMBF funded MultiGeoEx² project support the development of an adjusted exploration strategy. The research team from KIT and CEGA scientists selected the Villarrica geothermal system to develop and demonstrate the selected and adjusted methods.

Major findings: Geophysical exploration

The selected approach, the combination of magnetotelluric (Chapter 5) and gravimetric (Chapter 6) methods, has proven its potential to disclose fault zone properties. In terms of low/medium enthalpy systems fault zones are of substantial importance as: (1) fault zones, if permeable, allow fluid convection that transports fluids of elevated temperatures to exploitable depth. Consequently, the geothermal gradient is locally increased generating temperature anomalies, e.g. observed for the Soultz-sous-Forêts or Landau geothermal systems (Baillieux et al., 2013). (2) permeable fault zones, if spudded by a well, allow sufficient fluid flow for geothermal exploitation. Permeability depends on shearing activity and hydrothermal alteration and can be described in terms of porosity and precipitation of hydrothermal alteration products. Especially clay minerals are of major importance due to their ability to decrease permeability of a fault zone.

The design of the measurement network with small inter-station distances provide high-resolution subsurface investigation as even small lateral discrepancies are recorded. That procedure turned out to be mandatory to reveal fault zone geometry, compared for instance to the MT data of Brasse & Soyer (2001), which were able to record fault zone signal without determining its extension and geometry. For MT the recording of broad-band frequency range entails the tracing of the fault zone from shallow to mid-crustal depth revealing its run from surface outcrop to greater depth and identify a possible connection to mid-crustal conductors (e.g. Jones, 1992; Unsworth, 2004; Hill et al., 2009; Wannamaker et al., 2014). The magnetotelluric survey reveals the geometry and the depth of the major fault zones. Liquiñe-Ofqui fault system is characterized by a sub-vertical, <3 km wide fault zone reaching to brittle-ductile transition in a depth of 8–10 km. Further extension towards a existing mid-crustal conductor is masked by a low resistive ductile crust. Mocha-Villarrica fault zone is described as a northward dipping fault zone reaching below brittle-ductile transition connecting to a mid-crustal conductor.

Gravity results confirm the location of LOFS by identification of negative gravity anomalies while the MVFZ does not possess a negative gravity anomaly at the location identified by increased conductivity in MT results. The absence of gravity anomaly might be related to the tectonic regime affecting the two fault zones. While for the LOFS transpressional/transensional regime prevail (Lavenu & Cembrano, 1999; Rosenau et al., 2006), the perpendicular orientation of MVFZ to maximum horizontal pressure σ_1 causes compressional tectonics on the fault preventing porosity generation (Cembrano & Lara, 2009). The combination of gravity and magnetotellurics allows a investigation of LOFS fault zone properties in terms of porosity and clay mineral fillings. Higher porosities (11–20%) and

¹Exploration and Characterization of High-Enthalpy Reservoirs for Geothermal Power Production in Chile

²Multidisciplinary geothermal Exploration in the Southern Volcanic Zone of Chile

low clay mineral contents (<2–5%) are determined indicating elevated permeabilities. Consequently, from geophysical measurements a geothermal potential of the LOFS in terms of volume flow \dot{m} (Eq. 9.1) is derived. Future research would benefit from a 3-D interpretation of the magnetotelluric data. Shallow galvanic distortion could be identified and eliminated from the data and 3-D subsurface resistivity distribution could be investigated. Fault zone geometry, especially strike direction and horizontal prolongation, could be traced from shallow to greater depth. A detailed 3-D investigation of the volcanic chain would analyze its relation to MVFZ and investigate the characteristics of the magma chamber of Villarrica volcano. In general, as the two fault zones have different orientations with respect to the regional stress field, the discrepancies in their response to the tectonic stress field in terms of fault zone geometry and resistivity signal contributes to the understanding of faulting mechanism.

Major findings: Geochemical exploration

Hydrochemical fluid composition is used to study the THC conditions and processes in the Villarrica geothermal system. The discharging hot springs are thereby used as a window to the subsurface. In the complex geology the impacts of major geologic structures are investigated: (1) the major fault zones and their contribution to the fluid circulation; (2) the lithology contrast between North Patagonian Batholith and Cura-Mallín formation and its significance for fluid flow on faults and fractures and finally (3) a contribution of the active Villarrica volcano in terms of the impact of the magma chamber (heat source, magmatic volatiles, etc.). The pure analysis of fluid composition (Chapter 7) reveals a meteoric fluid origin and no input of magmatic fluids or degassed volatiles. The fluid chemistry originates from water-rock interaction of different equilibrium stages between the fluids and crystalline rocks. Additional hydrochemical techniques and analysis of reservoir rock analogues were used to investigate the lithological impact especially on the hydraulic circulation. Strontium isotope ratios ($^{87}\text{Sr}/^{86}\text{Sr}$) are able to trace the lithology contrasts in the fluids comparing $^{87}\text{Sr}/^{86}\text{Sr}$ and $\text{Rb}^+/\text{Sr}^{2+}$ ratios of fluids and rocks. The fractionation of ^{18}O of the $\text{H}_2\text{O}-\text{SO}_4$ system reveals reservoir temperatures of 80–100 °C for the NPB and 100–140 °C for Cura-Mallín formation. Furthermore the analysis reveals effects of lithology on fluid flow. Those lithological impacts on fluid movement are additionally studied by CFC analysis quantifying the amount of shallow dilution and the subsurface mixing process. Low proportions of shallow meteoric fluids are documented for springs in NPB, while the springs in volcanic or volcano-sedimentary environment possess higher amounts of meteoric dilution. Consequently the circulation system inside the NPB is characterized as channeled fluid flow along major fault zones, while a more dispersed flow on a branched fracture network in the volcano-sedimentary units is derived. Geothermal potential evaluation (Eq. 9.1) depends also on reservoir temperatures. As the results of reservoir temperature evaluation from ^{18}O fractionation mismatch the findings from earlier studies (Sánchez et al., 2013) a re-evaluation of existing solute geothermometers was developed and conducted. I contributed to the geothermometric re-evaluation of the Villarrica geothermal system that is primary part of a second PhD thesis by Fabian Nitschke. Based on above mentioned findings a concept was developed enhancing classical solute geothermometers by incorporation of meteoric dilution, lithological impacts and in-situ pH adaption (Nitschke et al., 2018). Furthermore reservoir temperature estimations are conducted adapting and modifying the statistical multicomponent approach (Nitschke et al., 2017a). Results of re-evaluated solute geothermometers and multicomponent geothermometry yield consistent temperature estimations. Initially high temperature uncertainties $\gg 100$ K are lowered

to ≤ 10 K. Reservoir temperatures, for the majority of springs between 100° to 130°C , of selected springs exceed 140°C reaching a maximum of 180°C . Thus also in terms of thermal conditions the Villarrica geothermal systems possess sufficient potential.

Outlook: Anthropogenic tracers

Finally I want to expand on the importance of anthropogenic tracers for geothermal exploration. The combination of different tracers enables an identification and quantification of subsurface mixing processes, which is of essential significance to determine reservoir fluid composition. Correct reservoir temperature forecast is only feasible using correct brine composition and also a proper forecast of scaling and corrosion potential depends on real fluid chemistry. Both factors affect economics of future design of a geothermal project and thus are essential during geochemical exploration. To improve the method additionally tracers could be included complementing the dating period of CFCs. Additional measurements of sulfur hexafluoride (SF_6) can analyze the young fluid component. SF_6 is a colorless gas used as an electrical insulator. As atmospheric concentration evolution differs from that of chlorofluorocarbons the ambiguity of mixing processes (binary v. exponential mixing, Chapter 8) can be overcome by a combination of SF_6 and CFC species resulting in significant discrepancies between BM and EM mixing lines (Figure 9.1) (also e.g. Koh et al., 2007). Additionally the old fluid component should be dated to evaluate the circulation time of the geothermal system. Therefore different tracers can be used presented in Chapter 3.2.2. Dating of old fluid component enables a characterization of fluid circulation that, in combination with geophysical measurements, identifies geothermal properties of the reservoir.

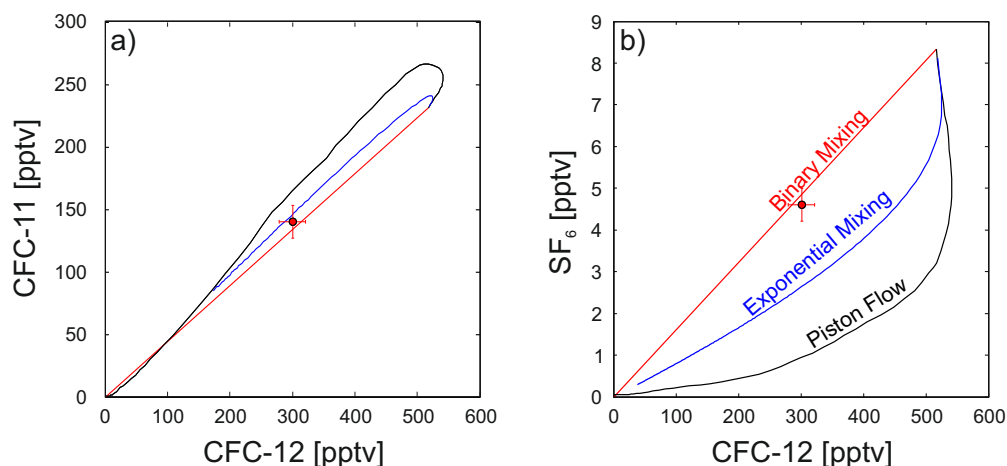


Figure 9.1.: Visualization of the characterization of young fluid proportion in terms of mixing process by a) exclusive application of CFCs or b) addition of SF_6 . Sampling point displayed presenting the effect of average uncertainties.

Outlook: Development of the Villarrica geothermal system

For the future development of the Villarrica geothermal system some preliminary steps shall guarantee the an ideal usage of the underground resource also considering the numerous geothermal spas and their role for Pucón as a touristic hot spot. Therefore, the results of geochemical and geophysical exploration shall be merged in a numerical 3-D THC model of the research area, similar to the complexe THC reservoir models of New Zealand geothermal

systems (Clearwater et al., 2012; Pearson & Prieto, 2012). The numerical model will deepen the understanding of the Villarrica geothermal reservoir by examination of the following issues: (1) verification of geothermal gradient, which was roughly estimated on limited data base (Chapter 5.6), (2) simulation of geothermal circulation to confirm subsurface residence time and geometry, (3) analyzes of water-rock interaction including equilibration time of fluids and (4) the impact of Villarrica magma chamber to the Villarrica geothermal system. Therefore, the relevant major geologic features (lithology contrast, major fault zones) and the topography have to be integrated in the model. Boundary conditions have to simulate natural conditions, incorporating the hot springs (T , \dot{m}) conditions including the fluid composition and hydraulical constraints (precipitation, river runoff). The numerical model can quantify the geothermal potential and support to solve the resource conflict between geothermal and balneological utilization (see next paragraph).

After simulation the geothermal potential could be quantitatively evaluated using the results of the numerical model. Yet, a first qualitative estimation is possible taking the exploration results as a basis. According to equation 9.1 the geothermal energy output is controlled by the temperature of the produced fluids T_{prod} , thus reservoir temperature, and the fluid flux \dot{m} , while the density ρ , the fluid capacity c_p are unchangeable fluid parameter and injection temperature T_{inj} is consumption controlled.

$$E = \rho c_p \dot{m} (T_{prod} - T_{inj}) \quad (9.1)$$

The LOFS has a proven elevated porosity and low clay mineral content. Consequently, considering also the hot springs discharging from the fault zone, a permeable fault zone can be assumed. From elevated fault zone width and depth extension sufficient fluid flux can be expected, when exploiting the fault zone. Reservoir temperatures for the Cura-Mallín formation are in the range of 100–130 °C sometimes exceeding 150 °C (Nitschke, 2017), while inside the NBP lower reservoir temperatures of 80–100 °C are expected. Temperatures, especially those estimated for Cura-Mallín formation, are sufficient for geothermal energetic utilization. In the framework of MultiGeoEx project Geothermie Neubrandenburg GmbH (GTN) develop a design for the geothermal heating of a hotel complex associated to a thermal spa (Termas Menetúe). Enlarging this concept one can discuss a district heating for the city of Pucón using geothermal energy. This concept considers also the low efficiency of energy conversion of a binary power plants, which have to be used at this geothermal environment, at lower production temperatures. During the cold season the inhabitants of Pucón use firewood heating polluting the city strongly accepting health problems. Geothermal district heating would definitely reduce anthropogenic pollution and increase the standard of living. Nevertheless the conflict of use between geothermal and balneological utilization has to be considered, especially as thermal spa tourism ensures monthly income of many employees. Pucón is one of the touristic hot spots of Chile, thus a profound feasibility study is required evaluating also the public acceptance of geothermal energy in Pucón. For this purpose the detailed numerical reservoir model has to simulate a possible geothermal utilization in order to analyze the effect on the fluid circulation controlling hot spring discharge used for balneology. Also a location of possible wells has to be identified that minimize the potential risk of draining thermal springs.

Assuming reservoir temperatures of 120 °C, injection temperature of 60 °C, that are often found in pure geothermal district heating projects (Schulz et al., 2013), and anticipate intermediate flow rates, installed thermal capacities between 5–15 MW could be expected.

Comparable realized geothermal district heating systems in the Munich area, Germany, could connect >5000 households that would cover, for the Pucón case, large proportions of the local population. As for Pucón the geothermal utilization of low/medium enthalpy systems needs a benefit-risk assessment other small cities in rural Southern Chile will benefit strongly from individual district heating concept reducing air pollution. Besides building heating geothermal heat can be used for process energy supply providing low-cost energy for industrial purposes. Low-cost energy supply might favor the foundation of decentralized, small-scale industries diversifying local labor market. Meanwhile the low/medium enthalpy reservoirs are in the focus of Chilean geothermal development documented by first exploration activities for the Lonquimay (Pedroza et al., 2017) and Aysén (Aravena et al., 2016a) areas.

References

- Abdelfettah, Y. & Schill, E. (2011). Accurate gravity data correction and 3-D gravity forward modeling. *Proceedings Swiss Geoscience Meeting*.
- Abdelfettah, Y., Schill, E., & Kuhn, P. (2014). Characterization of geothermally relevant structures at the top of crystalline basement in Switzerland by filters and gravity forward modelling. *Geophysical Journal International*, 199, 226–241.
- Adriasola, A. C., Thomson, S. N., Brix, M. R., Hervé, F., & Stöckhert, B. (2005). Post-magmatic cooling and late Cenozoic denudation of the North Patagonian Batholith in the Los Lagos region of Chile, 41°S–42°15'S. *International Journal of Earth Sciences*, 95(3), 504–528.
- Allmendinger, R. W., Jordan, T. E., Kay, S. M., & Isacks, B. L. (1997). The evolution of the Altiplano-Puna plateau of the central Andes. *Annual Review of Earth and Planetary Sciences*, 25(1), 139–174.
- Altwegg, P. (2015). *Gravimetry for geothermal exploration*. PhD thesis, University of Neuchâtel.
- Altwegg, P., Schill, E., Abdelfettah, Y., Radogna, P.-V., & Mauri, G. (2015). Toward fracture porosity assessment by gravity forward modeling for geothermal exploration (Sankt Gallen, Switzerland). *Geothermics*, 57, 26–38.
- Angermann, D., Klotz, J., & Reigber, C. (1999). Space-geodetic estimation of the Nazca-South America Euler vector. *Earth and Planetary Science Letters*, 171, 329–334.
- Aravena, D., Estay, N., Otero, S., Muñoz, M., García, K., Maripangui, R., Valdes, A., & Morata, D. (2016a). Geothermal exploration in the Aysén region, Chilean Patagonia. *Proceedings New Zealand Geothermal Workshop*.
- Aravena, D. & Lahsen, A. (2012). Assessment of exploitable geothermal resources using magmatic heat transfer method, Maule Region, Southern Volcanic Zone, Chile. *GRC Transactions*, 36, 1307–1314.
- Aravena, D., Muñoz, M., Morata, D., Lahsen, A., Parada, M. Á., & Dobson, P. (2016b). Assessment of high enthalpy geothermal resources and promising areas of Chile. *Geothermics*, 59, 1–13.
- Archie, G. E. (1942). The electrical resistivity log as an aid in determining some reservoir characteristics. *Trans. AIME*, 146, 54–62.
- Arnórsson, S. (1983). Chemical equilibria in Icelandic geothermal systems - Implications for chemical geothermometry investigations. *Geothermics*, 12, 119–128.
- Arnórsson, S. (2000). *Isotopic and chemical techniques in geothermal exploration, development and use*. International Atomic Energy Agency.

- Arnórsson, S. & Andrésdóttir, A. (1995). Processes controlling the distribution of boron and chlorine in natural waters in Iceland. *Geochemica et Cosmochemica Acta*, 20, 4125–4146.
- Aron, F., Allmendinger, R. W., Cembrano, J., González, G., & Yáñez, G. (2013). Permanent fore-arc extension and seismic segmentation: Insights from the 2010 Maule earthquake, Chile. *Journal of Geophysical Research: Solid Earth*, 118(2), 724–739.
- Asch, G., Schurr, B., Bohm, M., Yuan, X., Haberland, C., Heit, B., Kind, R., Woelbern, I., Bataille, K., Comte, D., Pardo, M., Viramonte, J., Rietbrock, A., & Giese, P. (2006). Seismological Studies of the Central and Southern Andes. In: Oncken, O., Chong, G., Franz, G., Giese, P., Götze, H.-J., Ramos, V.A., Strecker, M.R. & Wigger, P. (eds): *The Andes—Active Subduction Orogeny*; Springer-Verlag, (pp. 443–457).
- Awaleh, M. O., Boschetti, T., Soubaneh, Y. D., Baudron, P., Kawalieh, A. D., Dabar, Omar Assowe abd Ahmed, M. M., Amhmed, S. I., Daoud, M. A., Egueh, N. M., & Mohamed, J. (2017). Geochemical study of the Sakalol-Harralol geothermal field (Republic of Djibouti): Evidenced of a low enthalpy aquifer between Manda-Inakir and Asal rift settings. *Journal of Volcanology and Geothermal Research*, 331, 26–52.
- Awaleh, M. O., Hoch, F. B., Kadieh, I. H., Soubaneh, Y. D., Egueh, N. M., Jalludin, M., & Boschetti, T. (2015). The geothermal resources of the Republic of Djibouti - I: Hydrochemistry of the Obock coastal hot springs. *Journal of Geochemical Exploration*, 152, 54–66.
- Bahr, K. (1988). Interpretation of the magnetotelluric impedance tensor: regional induction and local telluric distortion. *Journal of Geophysics*, 62, 119–127.
- Bahr, K. (1991). Geological noise in magnetotelluric data: a classification of distortion types. *Physics of the Earth and Planetary Interiors*, 66(1-2), 24–38.
- Bailey, R. C. (1990). Trapping of aqueous fluids in the deep crust. *Geophysical Research Letters*, 17(8), 1129–1132.
- Baillieux, P., Schill, E., Abdelfettah, Y., & Dezayes, C. (2014). Possible natural fluid pathways from gravity pseudo-tomography in the geothermal fields of Northern Alsace (Upper Rhine Graben). *Geothermal Energy*, 2(16), 1–14.
- Baillieux, P., Schill, E., Edel, J.-B., & Mauri, G. (2013). Localization of temperature anomalies in the Upper Rhine Graben: insights from geophysics and neotectonic activity. *International Geology Review*, 55(14), 1744–1762.
- Bangs, N. L. & Cande, S. C. (1997). Episodic development of a convergent margin inferred from structures and processes along the Southern Chile margin. *Tectonics*, 16(3), 489–503.
- Barazangi, M. & Isacks, B. L. (1976). Spatial distribution of earthquakes and subduction of the Nazca plate beneath South America. *Geology*, 4, 686–692.
- Barbier, E. (2002). Geothermal energy technology and current status: an overview. *Renewable and Sustainable Energy Reviews*, 6(1-2), 3–65.
- Baria, R., Baumgärtner, J., Glassm, H., Bennett, T., Teza, D., & Jupe, A. (2017). Unconventional geothermal technology to help the climate change issue in the densely populated areas of the world with a demand for higher energy. *Proceedings Workshop on Geothermal Reservoir Engineering, Stanford University*, (pp. 1–11).
- Bartels, J., Heck, N. H., & Johnston, H. F. (1939). The three-hour-range index measuring geomagnetic activity. *Terrestrial Magnetism and Atmospheric Electricity*, 44(4), 411–454.

- Baujard, C., Genter, A., Dalmais, E., Maurer, V., Hehn, R., Rosillette, R., & Vidal, J. (2017). Geothermics Hydrothermal characterization of wells GRT-1 and GRT-2 in Rittershoffen, France: Implications on the understanding of natural flow systems in the Rhine Graben. *Geothermics*, 65, 255–268.
- Beck, S., Zandt, G., Myers, S., Wallace, T., Silver, P., & Drake, L. (1996). Crustal-thickness variations in the Central Andes. *Geology*, 24(5), 407.
- Beck Jr., M. E., Rojas, C., & Cembrano, J. (1993). On the nature of buttressing in margin-parallel strike-slip fault systems. *Geology*, 21(8), 755.
- Becken, M. & Burkhardt, H. (2004). An ellipticity criterion in magnetotelluric tensor analysis. *Geophysical Journal International*, 159(1), 69–82.
- Becken, M., Ritter, O., & Burkhardt, H. (2008). Mode separation of magnetotelluric responses in three-dimensional environments. *Geophysical Journal International*, 172, 67–86.
- Bedrosian, P. A. (2002). Magnetotelluric imaging of the creeping segment of the San Andreas Fault near Hollister. *Geophysical Research Letters*, 29(11).
- Benavente, O. & Gutierrez, F. (2011). Magmatic-Hydrothermal Systems Associated to Planchón-Peteroa and Descabezado Grande-Quizapu-Cerro Azul Volcanic Complexes, VII Region, Chile. *GRC Trans*, 35, 699–702.
- Bertani, R. (2016). Geothermal power generation in the world 2010–2014 update report. *Geothermics*, 60, 31–43.
- Bertrand, E. a., Unsworth, M. J., Chiang, C.-W., Chen, C.-S., Chen, C.-C., Wu, F. T., Türkoğlu, E., Hsu, H.-L., & Hill, G. J. (2012). Magnetotelluric imaging beneath the Taiwan orogen: An arc-continent collision. *Journal of Geophysical Research*, 117(B1), 1–15.
- Bibby, H. M. (1986). Analysis of multiple-source bipole-dipole resistivity surveys using the apparent resistivity tensor. *Geophysics*, 51, 972–983.
- Blackely, R. (1995). *Potential theory in gravity and magnetic applications*. Cambridge University Press.
- Blackwell, D., Wisian, K., Benoit, D., & Gollan, B. (1999). Structure of The Dixie Valley Geothermal System, a "Typical" Basin and Range Geothermal System, From Thermal and Gravity Data. *GRC Transactions*, 23(23), 525–531.
- Bohm, M., Lüth, S., Echtler, H., Asch, G., Bataille, K., Bruhn, C., Rietbrock, A., & Wigger, P. (2002). The Southern Andes between 36°S and 40°S latitude: seismicity and average seismic velocities. *Tectonophysics*, 356(4), 275–289.
- Boschetti, T. (2013). Oxygen isotope equilibrium in sulfate–water systems: A revision of geothermometric applications in low-enthalpy systems. *Journal of Geochemical Exploration*, 124, 92–100.
- Brass, G. W. (1976). The variation of marine $^{87}\text{Sr}/^{86}\text{Sr}$ ratio during Phanerozoic time: interpretation using a flux model. *Geochimica et Cosmochimica Acta*, 40, 721–730.
- Brasse, H. (2002). The Bolivian Altiplano conductivity anomaly. *Journal of Geophysical Research*, 107(B5).

- Brasse, H., Kapinos, G., Li, Y., Mütschard, L., Soyer, W., & Eydam, D. (2009). Structural electrical anisotropy in the crust at the South-Central Chilean continental margin as inferred from geomagnetic transfer functions. *Physics of the Earth and Planetary Interiors*, 173(1-2), 7–16.
- Brasse, H., Pamela, L., Rath, V., Schwalenberg, K., Soyer, W., & Haak, V. (2002). The Bolivian Altiplano conductivity anomaly. *Journal of Geophysical Research*, 107(B5).
- Brasse, H. & Soyer, W. (2001). A magnetotelluric study in the Southern Chilean Andes. *Geophysical Research Letters*, 28(19), 3757–3760.
- Brown, M., Díaz, F., & Grocott, J. (1993). Displacement history of the Atacama fault system 25°00'S-27°00'S, Northern Chile. *GSA Bulletin*, 105(9), 1165–1174.
- Browne, P. (1978). Hydrothermal alteration in active geothermal field. *Annual Review of Earth and Planetary Sciences*, 6, 229–250.
- Brun, J. P. & Wenzel, F. (1991). Crustal-scale structure of the southern Rhinegraben from ECORS-DEKORP seismic reflection data. *Geology*, 19(7), 758.
- Burton, W. C., Plummer, L. N., Busenberg, E., Lindsey, B. D., & Gburek, W. J. (2002). Influence of Fracture Anisotropy on Ground Water Ages and Chemistry, Valley and Ridge Province, Pennsylvania. *Ground Water*, 40(3), 242–257.
- Butterworth, S. (1930). On the Theory of Filter Amplifiers. *Wireless Engineer*, 7, 536–541.
- Cahill, T. & Isacks, B. L. (1992). Seismicity and shape of the subducted nazca plate. *Journal of Geophysical Research*, 97(B12), 17503.
- Caldwell, T. G., Bibby, H. M., & Brown, C. (2004). The magnetotelluric phase tensor. *Geophysical Journal International*, 158(2), 457–469.
- Cande, S. C. & Leslie, R. B. (1986). Late cenozoic tectonics of the southern chile trench. *Journal of Geophysical Research*, 91(B1), 471.
- Cembrano, J. & Herve, F. (1993). The Liquiñe Ofqui Fault Zone: A major Cenozoic strike slip duplex in the Southern Andes. *Proceedings 2nd ISAG; Oxford (UK)*, (pp. 175–178).
- Cembrano, J., Hervé, F., & Lavenu, A. (1996). The Liquiñe Ofqui fault zone: a long-lived intra-arc fault system in Southern Chile. *Tectonophysics*, 259, 55–66.
- Cembrano, J. & Lara, L. E. (2009). The link between volcanism and tectonics in the Southern Volcanic Zone of the Chilean Andes: A review. *Tectonophysics*, 471(1–2), 96–113.
- Cembrano, J., Lavenu, A., Reynolds, P., Arancibia, G., López, G., & Sanhueza, A. (2002). Late Cenozoic transpressional ductile deformation north of the Nazca-South America-Antarctica triple junction. *Tectonophysics*, 354(3-4), 289–314.
- Cembrano, J., Lavenu, A., Yañez, G., Riquelme, R., García, M., Gonzáles, G., & Hérail, G. (2007). Neotectonics. In: Moreno, T. & Gibbons, W (eds.): *The Geology of Chile*; The Geological Society of London.
- Cembrano, J. & Moreno, H. (1994). Geometria y naturaleza contrastante del volcanismo cuaternario entre los 38°y 46°S: Dominios compresionales y tensionales en un régimen transcurrente? *Proceedings Congreso Geológico Chileno*, (pp. 240–244).

- Charrier, R., Pinto, L., & Rodríguez, M. P. (2007). Tectonostratigraphic evolution of the Andean orogen in Chile. In: Moreno, T. & Gibbons, W (eds.): *The Geology of Chile*; The Geological Society of London, (pp. 21–1186).
- Chiba, H. & Sakai, H. (1985). Oxygen Isotope Exchange Rate between Dissolved Sulfate and Water at Hydrothermal Temperatures. *Geochimica et Cosmochimica Acta*, 49, 993–1000.
- Chinn, D. S. & Isacks, B. L. (1983). Accurate source depths and focal mechanisms of shallow earthquakes in western South America and in the New Hebrides Island Arc. *Tectonics*, 2(6), 529–563.
- Cifuentes, I. L. (1989). The 1960 Chilean earthquakes. *Journal of Geophysical Research*, 94(B1), 665.
- Clauser, C. (2004). *Einführung in die Geophysik*. Springer Verlag Berlin Heidelberg.
- Clavero, J. & Moreno, H. (2004). Evolution of Villarrica Volcano, southern Andes. in: Lara, L. & Clavero, J.E. (eds): *Villarrica Volcano, southern Andes; SERNAGEOMIN*, Bol. 61, 17–27.
- Clavero, J., Pineda, G., Mayorga, C., Giavelli, A., Aguirre, I., Simmons, S., Martini, S., Soffia, J., Arriaza, R., Polanco, E., & Achurra, L. (2011). Geological, geochemical, geophysical and first drilling data from Tinguiririca geothermal area, Central Chile. *GRC Transactions*, 35, 731–734.
- Clearwater, E., O’Sullivan, M., Brockbank, K., & Mannington, W. (2012). Modelling the Ohaaki geothermal system. *Proceedings TOUGH Symposium, Lawrence Berkeley National Laboratory Berkeley, California*, (pp. 215–222).
- Coira, B., Davidson, J., Mpodozis, C., & Ramos, V. (1982). Tectonic and magmatic evolution of the Andes of Northern Argentina and Chile. *Earth-Science Reviews*, 18(3-4), 303–332.
- Collon, P., Kutschera, W., Loosli, H., Lehmann, B., Purtschert, R., Love, A., Sampson, L., Anthony, D., Cole, D., Davids, B., Morrissey, D., Sherrill, B., Steiner, M., Pardo, R., & Paul, M. (2000). ^{81}Kr in the Great Artesian Basin, Australia: a new method for dating very old groundwater. *Earth and Planetary Science Letters*, 182(1), 103–113.
- Cornejo, P., Matthews, S., & Pérez de Arce, C. (2003). The K-T compressive deformation event in northern Chile (24–27°S). *Proceedings of the 10th Congreso Geológico Chileno, Concepcion*.
- Cortecci, G. (1974). Oxygen isotopic ratios of sulfate ions-water pairs as a possible geothermometer. *Geothermics*, 3, 60–64.
- Cortecci, G., Boschetti, T., Mussi, M., Lameli, C. H., Mucchino, C., & Barbieri, M. (2005). New chemical and original isotopic data on waters from El Tatio geothermal field, Northern Chile. *Geochemical Journal*, 39(6), 547–571.
- Craig, H. (1961). Isotopic variations in meteoric waters. *Science*, 133, 1702–1703.
- Cumming, W., Vieytes, H., Ramírez, C., & Sussman, D. (2002). Exploration of the La Torta geothermal prospect, Northern Chile. *GRC Transactions*, 26, 3–7.
- Cusicanqui, H., Mahon, W., & Ellis, A. J. (1975). The Geochemistry of the El Tatio Geothermal Field, Northern Chile. *Proceedings 2nd United Nations Symposium on the Development and Use of Geothermal Resources*, (pp. 703–711).

- Dakhnov, V. N. (1962). *Geophysical well logging*. Q. Colorado Sch. Mines.
- Davidson (1988). The origin and evolution of magmas from the San Pedro-Pellado Volcanic Complex, S. Chile: multicomponent sources and open system evolution. *Contrib. Mineral. Petrol.*, 100, 429–445.
- Davidson, J., Harmon, R. S., & Wörner, G. (1991). The source of central andean magmas: some considerations. in: Harmon, R.S. & Rapela, C.W. (eds): *Andean Magmatism and its tectonic setting*; Geological Society of America, Special Publications, (pp. 233–243).
- Davies, J. H. (1999). The role of hydraulic fractures and intermediate-depth earthquakes in generating subduction-zone magmatism. *Nature*, 398(6723), 142–145.
- DeMets, C., Gordon, R. G., Argus, D. F., & Stein, S. (1990). Current plate motions. *Geophysical Journal International*, 101(2), 425–478.
- Déruelle, B., Harmon, R. S., & Moorbath, S. (1983). Combined Sr-O isotope relationships and petrogenesis of Andean Volcanics of South America. *Nature*, 302(28), 814–816.
- Dewey, J. & Lamb, S. (1992). Active tectonics of the Andes. *Tectonophysics*, 205(1-3), 79–95.
- Diraison, M., Cobbold, P. R., Gapais, D., & Rossello, E. A. (1997). Magellan Strait: Part of a Neogene rift system. *Geology*, 25(8), 703–706.
- Dorbath, C. & Paul, A. (1996). Tomography of the Andean crust and mantle at 20°S: first results of the Lithoscope experiment. *Physics of the Earth and Planetary Interiors*, 97(1-4), 133–144.
- Dorsch, K. & Pletl, C. (2012). Bayerisches Molassebecken - Erfolgsregion der Tiefengeothermie in Mitteleuropa. *Geothermische Energie*, 73(2), 14–18.
- Duba, A., Heikamp, S., Meurer, W., Nover, G., & Will, G. (1994). Evidence from borehole samples for the role of accessory minerals in lower-crustal conductivity. *Nature*, 367, 59–61.
- Duba, A. G. & Shankland, T. J. (1982). Free carbon and electrical conductivity in the earth's mantle. *Geophysical Research Letters*, 9(11), 1271–1274.
- Duchi, V., Minissale, A. A., & Rossi, R. (1986). Chemistry of thermal springs in the Larderello-Travale geothermal region, Southern Tuscany, Italy. *Applied Geochemistry*, 1, 659–667.
- Echternacht, F., Tauber, S., Eisel, M., Brasse, H., Schwarz, G., & Haak, V. (1997). Electromagnetic study of the active continental margin in Northern Chile. *Physics of the Earth and Planetary Interiors*, 102(1-2), 69–87.
- Egbert, G. & Booker (1986). Robust estimation of geomagnetic transfer functions. *Geophysical Journal International*, 87, 173–194.
- Eisenlohr, T. (1997). The thermal springs of the Armutlu peninsula (NW Turkey) and their relationship to geology and tectonics. In: *Active Tectonics of Northwestern Anatolia - The Marmara Poly-Project*, (pp. 197–228).
- Elderfield, H. (1986). Strontium Isotope Stratigraphy. *Palaeogeography, Palaeoclimatology, Palaeoecology*, 57, 71–90.
- Ellis, A. J. & Mahon, W. (1977). *Chemistry and Geothermal Systems*. Academic Press.

- Emerson, D. & Yang, Y. (1997). Effects of water salinity and saturation on the electrical resistivity of clays. *Preview*, 68, 19–24.
- Eppelbaum, L., Kutasov, I., & Pilchin, A. (2014). *Applied Geothermics*. Springer-Verlag.
- Fabryka-Martin, J., Davis, S., & Elmore, D. (1987). Applications of ^{129}I and ^{36}Cl in hydrology. *Nuclear Instruments and Methods in Physics Research*, 29, 361–371.
- Faure, G. & Powell, J. L. (1972). *Strontium isotope geology*. Springer Verlag.
- Faure, G. & Powell, J. L. (1986). *Principles of isotope geology*. New York: Wiley.
- Folguera, A., Ramos, V. A., Hermanns, R. L., & Naranjo, J. (2004). Neotectonics in the foothills of the southernmost Central Andes (37° – 38°S): Evidence of strike-slip displacement along the Antiñir-Copahue fault zone. *Tectonics*, 23(5), 1–23.
- Fontes, S., Harinarayana, T., Dawes, G., & Hutton, V. (1988). Processing of noisy magnetotelluric data using digital filters and additional data selection criteria. *Physics of the Earth and Planetary Interiors*, 52(1-2), 30–40.
- Forsythe, R. & Nelson, E. (1985). Geological manifestations of ridge collision: Evidence from the Golfo de Penas-Taitao Basin, Southern Chile. *Tectonics*, 4(5), 477–495.
- Fouillac, C. & Michard, G. (1981). Sodium/Lithium ratio in water applied to geothermometry of geothermal reservoirs. *Geothermics*, 10(1), 55–70.
- Fournier, R. (1991). Water geothermometers applied to geothermal energy. In: D'Amore, F. (ed.): *Applications of Geochemistry in Geothermal Reservoir Development*; UNITAR.
- Fournier, R. O. (1977). Chemical geothermometers and mixing models for geothermal systems. *Geothermics*, 5, 41–50.
- Fournier, R. O. (1979). A revised equation for the Na/K Geothermometer. *GRC Transactions*, 3, 221–224.
- Fournier, R. O. & Truesdell, A. H. (1973). An empirical Na-K-Ca geothermometer for natural waters. *Geochimica et Cosmochimica Acta*, 37, 1255–1275.
- Francis, P. & Hawkesworth, C. (1994). Late Cenozoic rates of magmatic activity in the Central Andes and their relationship to continental crust formation. *Journal of the Geological Society of London*, 151, 845–854.
- Frost, B. R., Fyfe, W. S., Tazaki, K., & Chan, T. (1989). Grain boundary graphite in rocks and implications for high electrical conductivity. *Nature*, 340, 134–136.
- Futa, K. & Stern, C. R. (1988). Sr and Nd isotopic and trace element compositions of Quaternary volcanic centers of the Southern Andes. *Earth and Planetary Science Letters*, 88, 253–262.
- Gamble, T. D., Goubau, W. M., & Clarke, J. (1979). Magnetotellurics with a remote magnetic reference. *Geophysics*, 44(1), 53–68.
- Gardner, W. P., Susong, D. D., Solomon, D. K., & Heasler, H. P. (2011). A multitracer approach for characterizing interactions between shallow groundwater and the hydrothermal system in the Norris Geyser Basin area, Yellowstone National Park. *Geochemistry, Geophysics, Geosystems*, 12(8), 1–17.

- Geiermann, J. & Schill, E. (2010). 2-D magnetotellurics at the geothermal site at Soultz-sous-Forêts: Resistivity distribution to about 3000 m depth. *Comptes Rendus Geoscience*, 342(7-8), 587–599.
- Genter, A., Evans, K., Cuenot, N., Fritsch, D., & Sanjuan, B. (2010). Contribution of the exploration of deep crystalline fractured reservoir of Soultz to the knowledge of enhanced geothermal systems (EGS). *Comptes Rendus Geoscience*, 342(7-8), 502–516.
- Géraud, Y., Rosener, M., Surma, F., Place, J., Le Garzic, É., & Diraison, M. (2010). Physical properties of fault zones within a granite body: Example of the Soultz-sous-Forêts geothermal site. *Comptes Rendus Geoscience*, 342(7-8), 566–574.
- Giese, P., Scheuber, E., Schilling, F., Schmitz, M., & Wigger, P. (1999). Crustal thickening processes in the Central Andes and the different natures of the Moho-discontinuity. *Journal of South American Earth Sciences*, 12(2), 201–220.
- Giggenbach, W. F. (1984). Mass transfer in hydrothermal alteration systems - A conceptual approach. *Geochimica et Cosmochimica Acta*, 48, 2693–2711.
- Giggenbach, W. F. (1988). Geothermal solute equilibria. Derivation of Na-K-Mg-Ca geothermometers. *Geochimica et Cosmochimica Acta*, 52, 2749–2765.
- Giggenbach, W. F. (1991). Chemical techniques in geothermal exploration. In: D'Amore, F. (ed.): *Applications of Geochemistry in Geothermal Reservoir Development*; UNITAR, (pp. 118–144).
- Giggenbach, W. F., Gonfiantini, R., Jangi, B. L., & Truesdell, A. H. (1983). Isotopic and chemical composition of Parbati Valley geothermal discharges, North-West Himalays, India. *Geothermics*, 12(2), 199–222.
- Gough, D. I. (1986). Seismic reflectors, conductivity, water and stress in the continental crust. *Nature*, 323(11), 143–144.
- Graham, I. J. (1992). Strontium isotope composition of Rotorua geothermal waters. *Geothermics*, 21, 165–180.
- Groom, R. & Bailey, R. (1989). Decomposition of magnetotelluric impedance tensors in the presence of local three-dimensional galvanic distortion. *Journal of Geophysical Research*, 94, 1913–1925.
- Guglielmetti, L., Negro, F., Mauri, G., Vuataz, F., Abdelfettah, Y., Clerc, N., Giroud, N., Marguet, L., & Schill, E. (2013). GeoNE: An integrated project for the exploration of low enthalpy deep aquifers in the canton of Neuchatel, Western Switzerland. *Proceedings European Geothermal Congress*.
- Gutscher, M.-A. (2002). Andean subduction styles and their effect on thermal structure and interplate coupling. *Journal of South American Earth Sciences*, 15(1), 3–10.
- Haak, V. & Hutton, R. (1986). Electrical resistivity in continental lower crust. *Geological Society, London, Special Publications*, 24(1), 35–49.
- Haak, V., Stoll, J., & Winter, H. (1991). Why is the electrical resistivity around KTB hole so low? *Physics of the Earth and Planetary Interiors*, 66, 12–23.
- Haberland, C., Rietbrock, A., Lange, D., Bataille, K., & Hofmann, S. (2006). Interaction between forearc and oceanic plate at the south-central Chilean margin as seen in local seismic data. *Geophysical Research Letters*, 33(23), 1–5.

- Hackney, R. I., Echtler, H. P., Franz, G., Friedrich, H.-j. G., Dmitriy, L., Melnick, D., Meyer, U., Schmidt, S., Tašárová, Z., Tassara, A., & Wienecke, S. (2006). The Segmented Overriding Plate and Coupling at the South-Central Chilean Margin (36–42°S). In: Oncken, O., Chong, G., Franz, G., Giese, P., Götze, H.-J., Ramos, V.A., Strecker, M.R. & Wigger, P. (eds): *The Andes—Active Subduction Orogeny*; Springer-Verlag, (pp. 355–374).
- Halas, S. & Pluta, I. (2000). Empirical calibration of isotope thermometer $\delta^{18}\text{O}$ (SO_4^{2-}) $\delta^{18}\text{O}$ (H_2O) for low temperature brines. *Proceedings Isotope Workshop, European Society for Isotope Research, Kraków, Poland*, (pp. 68–71).
- Hampel, A., Kukowski, N., Bialas, J., Huebscher, C., & Heinbockel, R. (2004). Ridge subduction at an erosive margin: The collision zone of the Nazca Ridge in southern Peru. *Journal of Geophysical Research: Solid Earth*, 109(B2), 1–19.
- Hamza, V. M. & Muñoz, M. (1996). Heat flow map of South America. *Geothermics*, 25(6), 599–646.
- Hansen, P. C. & O’Leary, D. P. (1993). The use of the L-Curve in the regularization of discrete ill-posed problems. *SIAM Journal on Scientific Computing*, 14(6), 1487–1503.
- Harvey, C. B., Beardsmore, G., Moeck, I., & Rüter, H. (2016). *Geothermal exploration: Global strategies and applications*. IGA Academy Books.
- Haschke, M., Günther, A., Melnick, D., Echtler, H., Reutter, K.-J., Scheuber, E., & Oncken, O. (2006). Central and southern andean tectonic evolution inferred from arc magmatism. In: Oncken, O., Chong, G., Franz, G., Giese, P., Götze, H.-J., Ramos, V.A., Strecker, M.R. & Wigger, P. (eds): *The Andes—Active Subduction Orogeny*; Springer-Verlag.
- Hauser, A. (1997). Catastro y caracterizacion de las fuentes de aguas minerales y termals de Chile. *SERNAGEOMIN*, Bol. 50, pp. 83.
- Heinson, G. & Lilley, F. (1993). An application of thin-sheet electromagnetic modelling to the Tasman Sea. *Physics of the Earth and Planetary Interiors*, 81(1), 231–251.
- Heiskanen, W. A. & Moritz, H. (1967). *Physical geodesy*. W. H. Freeman and Company.
- Held, S., Nitschke, F., Schill, E., Morata, D., Eiche, E., & Kohl, T. (2017). Hydrochemistry of the hot spring fluids of Villarrica geothermal system in the Andes of Southern Chile. *GRC Transactions*, 41.
- Held, S., Schill, E., Pavez, M., Díaz, D., Muñoz, G., Morata, D., & Kohl, T. (2016). Resistivity distribution from mid-crustal conductor to near-surface across the 1200 km long Liquiñe-Ofqui Fault System, Southern Chile. *Journal of Geophysical Research*, 207(3), 1387–1400.
- Held, S., Schill, E., Sánchez, P., Neumann, T., Emmerich, K., Morata, D., & Kohl, T. (2015). Geological and tectonic settings preventing high-temperature geothermal reservoir development at Mt. Villarrica (Southern Volcanic Zone): Clay mineralogy and sulfate-isotope geothermometry. *Proceedings World Geothermal Congress 2015*.
- Herron, E. M., Cande, S. C., & Hall, B. R. (1981). An active spreading center collides with a subduction zone: A geophysical survey of the Chile Margin triple junction. in: Kulm, L. D. (ed.): *Nazca Plate: Crustal Formation and Andean Convergence*; Geological Society of America, 154, 683–702.

- Hervé, F. (1994). The Southern Andes Between 39° and 44°S Latitude: The Geological Signature of a Transpressive Tectonic Regime Related to a Magmatic Arc. In: Reutter, K.J. and Scheuber, E. and Wigger P.J.(eds.): *Tectonics of the Southern Central Andes*; Springer-Verlag, (pp. 243–248).
- Hervé, F. (1976). Estudio geológico de la falla Liquiñe-Reloncaví en el área de Liquiñe; antecedentes de un movimiento transcurrente (Provincia de Valdivia). *Congr. Geol. Chil. Actas*, 1, B39–B56.
- Hervé, F. (1984). Rejuvenecimiento de edades radiométricas y el sistema de fallas Liquiñe-Ofqui. *Com. Dep. Geol. Univ. Chile*, 35, 107–116.
- Herve, F., Faundez, V., Calderón, M., Massonne, H.-J., & Willner, A. (2007). Metamorphic and plutonic basement complexes. In: Moreno, T. & Gibbons, W (eds.): *The Geology of Chile*; The Geological Society of London.
- Hickey-Vargas, R., Frey, F., Gerlach, D., & López-Escobar, L. (1986). Multiple sources for basaltic arc rocks from the Southern Volcanic Zone of the Andes (34°–41°S): Trace element and isotopic evidence for the contribution from subducted oceanic crust, mantle and continental crust. *Journal of Geophysical Research*, 91(6), 5963–5983.
- Hickey-Vargas, R., Holbik, S., Tormey, D., Frey, A., & Moreno-Roa, H. (2016). Basaltic rocks from the Andean Southern Volcanic Zone: Insights from the comparison of along-strike and small-scale geochemical variations and their sources. *Lithos*, 258–259(3), 115–132.
- Hickey-Vargas, R., Moreno-Roa, H., López-Escobar, L., & Frey, F. (1989). Geochemical variations in Andean basaltic and silicic lavas from the Villarrica-Lanín volcanic chain (39.5°S): an evaluation of source heterogeneity, fractional crystallization and crustal assimilation. *Contributions to Mineralogy and Petrology*, 103(3), 361–386.
- Hickey-Vargas, R., Sun, M., López-Escobar, L., Moreno-Roa, H., Reagan, M. K., Morris, J. D., & Ryan, J. G. (2002). Multiple subduction components in the mantle wedge: Evidence from eruptive centers in the Central Southern volcanic zone, Chile. *Geology*, 30(3), 199–202.
- Hickson, C. J., Ferraris, F., Rodríguez, C., Sielfeld, G., Henríquez, R., Gislason, T., Selters, J., Benoit, D., White, P., Southon, J., Ussher, G., Charroy, J., Smith, A., Lovelock, B., Lawless, J., Quinlivan, P., Smith, L., & Yehia, R. (2011). The Mariposa Geothermal System, Chile. *GRC Transactions*, 35.
- Hildreth, W. & Moorbath, S. (1988). Crustal contributions to arc magmatism in the Andes of Central Chile. *Contributions to Mineralogy and Petrology*, 98, 455–489.
- Hill, G. J., Caldwell, T. G., Heise, W., Chertkoff, D. G., Bibby, H. M., Burgess, M. K., Cull, J. P., & Cas, R. A. F. (2009). Distribution of melt beneath Mount St Helens and Mount Adams inferred from magnetotelluric data. *Nature Geoscience*, 2(11), 785–789.
- Hinsby, K., Højberg, A. L., Engesgaard, P., Jensen, K. H., Larsen, F., Plummer, L. N., & Busenberg, E. (2007). Transport and degradation of chlorofluorocarbons (CFCs) in the pyritic Rabis Creek aquifer, Denmark. *Water Resources Research*, 43(10).
- Hochstein, M. P. & Regenauer-Lieb, K. (1998). Heat generation associated with collision of two plates: The Himalayan geothermal belt. *Journal of Volcanology and Geothermal Research*, 83(1-2), 75–92.

- Hoering, T. C. & Kennedy, J. W. (1957). The exchange of oxygen between sulfuric acid and water. *Journal of American Chemical Society*, 79, 56–60.
- Hoffmann-Rothe, A. (2002). *Combined structural and magnetotelluric investigation across the West Fault Zone in northern Chile*. PhD thesis, Deutsches GeoForschungsZentrum GFZ.
- Hoffmann-Rothe, A., Kukowski, N., Dresen, G., Echtler, H., Oncken, O., Klotz, J., Scheuber, E., & Kellner, A. (2006). Oblique convergence along the Chilean margin: Partitioning, margin-parallel faulting and force interaction at the plate interface. In: Oncken, O., Chong, G., Franz, G., Giese, P., Götze, H.-J., Ramos, V.A., Strecker, M.R. & Wigger, P. (eds): *The Andes—Active Subduction Orogeny*; Springer-Verlag.
- Hofmann-Wellenhof, B. & Moritz, H. (2006). *Physical geodesy*. Springer-Verlag.
- Husen, S., Kissling, E., Flueh, E., & Asch, G. (1999). Accurate hypocentre determination in the seismogenic zone of the subducting Nazca Plate in northern Chile using a combined on-/offshore network. *Geophysical Journal International*, 138(3), 687–701.
- IEA (2011). *Technology roadmap: Geothermal heat and power*. International Energy Agency.
- Inoue, A., Utada, M., & Wakita, K. (1992). Smectite-to-illite conversion in natural hydrothermal systems. *Applied clay science*, 7, 131–145.
- IRENA (2015). *Renewable energy policy brief: Chile*. IRENA, Abu Dhabi.
- Isacks, B. L. (1988). Uplift of the Central Andean Plateau and bending of the Bolivian Orocline. *Journal of Geophysical Research*, 93(B4), 3211–3231.
- Ivanov, S. N. & Ivanov, K. S. (1994). Hydrodynamic zoning of the earth's crust and its significance. *Journal of Geodynamics*, 17(4), 155–180.
- Jacques, G., Hoernle, K., Gill, J., Wehrmann, H., Bindeman, I., & Lara, L. E. (2014). Geochemical variations in the Central Southern Volcanic Zone, Chile (38–43°S): The role of fluids in generating arc magmas. *Chemical Geology*, 371, 27–45.
- Jarrard, R. D. (1986). Relations among subduction parameters. *Reviews of Geophysics*, 24(2), 217–284.
- Jaupart, C., Mareschal, J.-C., & Iarotsky, L. (2016). Radiogenic heat production in the continental crust. *Lithos*, 262, 398–427.
- Jiracek, G. R. (1995). Geoelectromagnetics charges on. *Reviews of geophysics*.
- Jödicke, H. (1992). Water and graphite in the earth's crust - An approach to interpretations of conductivity models. *Surveys in Geophysics*, 13, 381–407.
- Jones, A. G. (1992). Electrical conductivity of the continental lower crust. In: Fountain, D. M., Arculus, R. J. & Kay, R. W. (eds.): *Continental Lower Crust*; Elsevier, (pp. 81–143).
- Jones, A. G. & Groom, R. W. (1993). Decomposition and modelling of the BC87 dataset. *Journal of Geomagnetism and Geoelectricity*, 45, 1127–1150.
- Jones, F. W. & Price, A. (1970). The perturbations of alternating geomagnetic fields by conductivity anomalies. *Geophysical Journal of the Royal Astronomical Society*, 20(3), 317–334.

- Jordan, T. E., Burns, W. M., Veiga, R., Pángaro, F., Copeland, P., Kelly, S., & Mpodozis, C. (2001). Extension and basin formation in the Southern Andes caused by increased convergence rate - A mid-Cenozoic trigger for the Andes. *Tectonics*, 20(3), 308–324.
- Kaden, H. (2012). *Determination of frequency dependent complex dielectric permittivity and modeling of dielectric properties of clay-water mixtures containing swellable and non-swellable clay minerals at low water contents*. PhD thesis, Karlsruhe Institute of Technology.
- Kapinos, G., Montahaei, M., Meqbel, N., & Brasse, H. (2016). Three-dimensional electrical resistivity image of the South-Central Chilean subduction zone. *Tectonophysics*, 666, 76–89.
- Karakuş, H. & Şimşek, Ş. (2013). Tracing deep thermal water circulation systems in the E-W trending Büyük Menderes Graben, Western Turkey. *Journal of Volcanology and Geothermal Research*, 252, 38–52.
- Kay, S., Ramos, V., & Gorring, M. (2002). Geochemistry of Eocene plateau basalts related to ridge collision in southern Patagonia. *Proceedings XV Congreso Geológico Argentino, El Calafate*.
- Kirby, S., Engdahl, R. E., & Denlinger, R. (1996). Intermediate-depth intraslab earthquakes and arc volcanism as physical expressions of crustal and uppermost mantle metamorphism in subducting slaby. in: Bebout, G.E., Scholl, D.W., Kirby, S.H. & Platt, J.P. (eds): *Subduction from top to bottom*; American Geophysical Union, 96, 195–215.
- Kley, J., Monaldi, C., & Salfity, J. (1999). Along-strike segmentation of the Andean foreland: causes and consequences. *Tectonophysics*, 301(1-2), 75–94.
- Klohn, C. (1960). Geología de la Cordillera de Los Andes de Chile Central, Provs. de Santiago, Colchagua y Curicó. *Instituto de Investigaciones Geológicas, Santiago*, Boletín 8.
- Koh, D. C., Plummer, L. N., Busenberg, E., & Kim, Y. (2007). Evidence for terrigenous SF₆ in groundwater from basaltic aquifers, Jeju Island, Korea: Implications for groundwater dating. *Journal of Hydrology*, 339(1-2), 93–104.
- Kohl, T. & Rybach, L. (1996). Thermal and hydraulic aspects of the KTB drill site. *Geophysical Journal International*, 124(3), 756–772.
- Kohn, S. B., Bonet, C., DiFrancesco, D., & Gibson, H. (2011). Geothermal exploration using gravity gradiometry - a Salton Sea example. *GRC Transactions*, 35.
- Korja, T., Smirnov, M., Pedersen, L. B., & Gharibi, M. (2008). Structure of the central Scandinavian Caledonides and the underlying Precambrian basement, new constraints from magnetotellurics. *Geophysical Journal International*, 175, 55–69.
- Krawczyk, C. M., Mechie, J., Lüth, S., Tasarová, Z., Wigger, P., Stiller, M., Brasse, H., Echtler, H. P., Araneda, M., & Bataille, K. (2006). Geophysical Signatures and Active Tectonics at the South-Central Chilean Margin. In: Oncken, O., Chong, G., Franz, G., Giese, P., Götze, H.-J., Ramos, V.A., Strecker, M.R. & Wigger, P. (eds): *The Andes—Active Subduction Orogeny*; Springer-Verlag, (pp. 172–192).
- Krone, U. E., Thauer, R. K., & Hogenkamp, H. P. C. (1989). Reductive dehalogenation of chlorinated C1-hydrocarbons mediated by corrinoids. *Biochemistry*, 28(11), 4908–4914.

- Kukowski, N. & Oncken, O. (2006). Subduction erosion - the "normal" mode of fore-arc material transfer along the Chilean margin? In: Oncken, O., Chong, G., Franz, G., Giese, P., Götze, H.-J., Ramos, V.A., Strecker, M.R. & Wigger, P. (eds): *The Andes—Active Subduction Orogeny*; Springer-Verlag.
- Kusakabe, M. & Robinson, B. W. (1977). Oxygen and sulfur isotope equilibria in the BaSO₄-HSO₄-H₂O system from 110 to 350°C and applications. *Geochimica et Cosmochimica Acta*, 41(8), 1033–1040.
- Lahsen, A. (1976). Geothermal exploration in Northern Chile - Summary. In: *Circum-Pacific Energy and Mineral Resources*; The American Association of petroleum Geologists, (pp. 169 – 175).
- Lahsen, A., Munoz, N., & Parada, M. A. (2010). Geothermal development in Chile. *Proceedings World Geothermal Congress 2010, Bali, Indonesia*.
- Lange, D., Cembrano, J., Rietbrock, A., Haberland, C., Dahm, T., & Bataille, K. (2008). First seismic record for intra-arc strike-slip tectonics along the Liquiñe-Ofqui fault zone at the obliquely convergent plate margin of the Southern Andes. *Tectonophysics*, 455(1-4), 14–24.
- Lara, L. E., Lavenu, A., Cembrano, J., & Rodríguez, C. (2006). Structural controls of volcanism in transversal chains: Resheared faults and neotectonics in the Cordón Caulle–Puyehue area (40.5°S), Southern Andes. *Journal of Volcanology and Geothermal Research*, 158(1-2), 70–86.
- Lara, L. E. & Moreno, H. (2004). Geología del área Liquiñe-Neltume, Carta Geológica de Chile, No. 83, Serie Geología Básica ,.
- Lara, L. E., Naranjo, J. A., & Moreno, H. (2004). Lanín volcano (39.5°S), Southern Andes: geology and morphostructural evolution. *Revista Geologica de Chile*.
- Larsen, J. C. (1975). Low Frequency (0.1–6.0 cpd) electromagnetic study of deep mantle electrical conductivity beneath the Hawaiian Islands. *Geophysical Journal of the Royal Astronomical Society*, 43(1), 17–46.
- Larson, R. L. (1991). Geological consequences of superplumes. *Geology*, 19(10), 963–966.
- Lavenu, A. & Cembrano, J. (1999). Compressional- and transpressional-stress pattern for Pliocene and Quaternary brittle deformation in fore arc and intra-arc zones (Andes of Central and Southern Chile). *Journal of Structural Geology*, 21, 1669–1691.
- Le Maitre (2005). *Igneous rocks: A classification and glossary of terms: Recommendation of the International Union of Geological Sciences, Subcommission on the Systematics of Igneous Rocks*. Cambridge Univ. Press, 2. ed. edition.
- Lebedev, E. B. & Khitarov, N. I. (1964). Dependence on the beginning of melting of granite and the electrical conductivity of its melt on highwater vapor pressure. *Geochemical International*, 1, 193–197.
- Lehmann, B., Love, A., Purtschert, R., Collon, P., Loosli, H., Kutschera, W., Beyerle, U., Aeschbach-Hertig, W., Kipfer, R., Frappe, S., Herczeg, A., Moran, J., Tolstikhin, I., & Gröning, M. (2003). A comparison of groundwater dating with ⁸¹Kr, ³⁶Cl and ⁴He in four wells of the Great Artesian Basin, Australia. *Earth and Planetary Science Letters*, 211(3-4), 237–250.
- Lesage, S., Brown, S., & Hosler, K. R. (1992). Degradation of chlorofluorocarbon-113 under anaerobic conditions. *Chemosphere*, 24(9), 1225–1243.

- Lindsay, D. D., Zentilli, M., & Rojas de la Rivera, J. (1995). Evolution of an active ductile to brittle shear system controlling mineralization at the Chuquicamata porphyry copper deposit, Northern Chile. *International Geology Review*, 37(11), 945–958.
- Lizarralde, D., Chave, A., Hirth, G., & Schultz, A. (1995). Northeastern Pacific mantle conductivity profile from long-period magnetotelluric sounding using Hawaii-to-California submarine cable data. *Journal of Geophysical Research: Solid Earth*, 100(B9), 17837–17854.
- Lloyd, R. M. (1968). Oxygen isotope behavior in the sulfate-water system. *Journal of Geochemical Exploration*, 73, 6099–6110.
- Loosli, H. (1983). A dating method with ^{39}Ar . *Earth and Planetary Science Letters*, 63, 51–62.
- Losito, G. & Muschietti, M. (1998). Is the illite group the cause of high electrical conductivity in certain lithospheric areas? *Annali Di Geofisica*, 41(3), 369–381.
- Lowrie, A. & Hey, R. (1981). Geological and geophysical variations along the western margin of Chile near Lat. 33° to 36°S and their relation to Nazca plate subduction. In: Kulm, La Verne D., Dymond, J., Dasch, E. J., Hussong, D. M. & Rederick, R. (eds.): *Nazca Plate: Crustal formation and Andean convergence*; Geological Society of America.
- Lowrie, W. (2007). *Fundamentals of geophysics*. Cambridge University Press.
- López Escobar, L., Cembrano, J., & Moreno, H. (1995). Geochemistry and tectonics of the Chilean Southern Andes basaltic Quaternary volcanism (37° - 46°S). *Revista Geologica de Chile*, 22, 219–234.
- López-Escobar, L., Kilian, R., Kempton, P. D., & Tagiri, M. (1993). Petrography and geochemistry of Quaternary rocks from the Southern Volcanic Zone of the Andes between $41^\circ30'\text{S}$ and $46^\circ00'\text{S}$, Chile. *Revista Geologica de Chile*, 20(1), 33–55.
- Lüth, S., Wigger, P., & ISSA Research Group (2003). A crustal model along 39°S from a seismic refraction profile-ISSA 2000. *Andean Geology*, 30(1), 83–101.
- Lucassen, F., Trumbull, R., Franz, G., Creixell, C., Vásquez, P., Romer, R. L., & Figueroa, O. (2004). Distinguishing crustal recycling and juvenile additions at active continental margins: the Paleozoic to recent compositional evolution of the Chilean Pacific margin (36° - 41°S). *Journal of South American Earth Sciences*, 17(2), 103–119.
- Lund, J. W. & Boyd, T. L. (2016). Direct utilization of geothermal energy 2015 - worldwide review. *Geothermics*, 60, 66–93.
- Mackie, R. L., Livelybrooks, D. W., Madden, T. R., & Larsen, J. C. (1997). A magnetotelluric investigation of the San Andreas Fault at Carrizo Plain, California. *Geophysical Research Letters*, 24(15), 1847–1850.
- Madden, T. & Nelson, P. (1986). A defense of Cagniard's magnetotelluric method. *Society of Exploration Geophysicists*, (pp. 89–102).
- Madden, T. & Thompson, W. (1965). Low-frequency electromagnetic oscillations of the Earth-ionosphere cavity. *Reviews of Geophysics*, 3(2), 211–254.
- Mainieri, A., Granados, E., Corrales, R., & Vaca, L. (1985). Miravalles Geothermal Field, Costa Rica, Technical Report. *GRC Transactions*.

- Maloszewski, P. & Zuber, A. (1982). Determining the turnover time of groundwater systems with the aid of environmental tracers. *Journal of Hydrology*, 57(3-4), 207–231.
- Mareschal, M., Kurtz, R. D., Chouteau, M., & Chakridi, R. (1991). A magnetotelluric survey on Manitoulin Island and Bruce Peninsula along GLIMPCE seismic line J: Black shales mask the Grenville Front. *Geophysical Journal International*, 105(1), 173–183.
- Mazor, E. & Bosch, A. (1992). Helium as a semi-quantitative tool for groundwater dating in the range of 10^4 - 10^8 years. In: *Isotopes of noble gases as tracers in environmental studies*; IAEA Vienna.
- McCracken, K., Oristabgli, M., & Hohmann, G. (1986). Minimization of noise in electromagnetic exploration systems. *Geophysics*, 51(3), 819–832.
- McKenzie, W. F. & Truesdell, A. H. (1977). Geothermal reservoir temperatures estimated from the oxygen isotope compositions of dissolved sulfate and water from hot springs and shallow drillholes. *Geothermics*, 5, 51–61.
- McMillan, N. J., Harmon, R. S., Moorbath, S., López-Escobar, L., & Strong, D. F. (1989). Geology crustal sources involved in continental arc magmatism: A case study of volcan crustal sources involved in continental arc magmatism : A case study of volcan Mocho-Choshuenco , southern Chile. *Geology*, 17, 1152–1156.
- Meixner, J., Schill, E., Gaucher, E., & Kohl, T. (2014). Inferring the in situ stress regime in deep sediments: an example from the Bruchsal geothermal site. *Geothermal Energy*, 2(1), 7.
- Meller, C., Bremer, J., Baur, S., Bergfeldt, T., Blum, P., Canic, T., Eiche, E., Gaucher, E., Hagenmeyer, V., Heberling, F., Held, S., Herfurth, S., Isele, J., Kling, T., Kuhn, D., Kumar, A., Mayer, D., Müller, B., Neumann, T., Nestler, B., Nitschke, F., Nothstein, A., Nusiaputra, Y., Orywall, P., Peters, M., Sahara, D., Schäfer, T., Schill, E., Schilling, F., Schröder, E., Selzer, M., Stoll, M., Wiemer, H.-J., Wolf, S., Zimmermann, M., & Kohl, T. (2017). Integrated research as key to the development of a sustainable geothermal energy technology. *Energy Technology*, 5(7), 965–1006.
- Melnick, D., Rosenau, M., Folguera, A., & Echtler, H. (2006). Neogene tectonic evolution of the Neuquén Andes western flank. In: Kay, S. & Ramos, V. (eds.): *Evolution of an Andean margin: A tectonic and magmatic view from the Andes to the Neuquén Basin (35°-39°S Lat)*; GSA Special Papers, (pp. 73–95).
- Melosh, G., Moore, J., & Stacey, R. (2012). Natural reservoir evolution in the Tolhuaca geothermal field, Southern Chile. *Proceedings Workshop on Geothermal Reservoir Engineering, Stanford, California*.
- Middlemost, E. A. (1994). Naming materials in the magma/igneous rock system. *Earth-Science Reviews*, 37(3-4), 215–224.
- Minierstio de Energía (2016). *Anuario estadístico de energía*. Comisión Nacional de Energía.
- Ministerio de Energía (2012). *National energy strategy 2012 - 2030*. Gobierno de Chile.
- Mizutani, Y. & Rafter, T. A. (1969). Oxygen isotopic composition of sulphates — Part 3. oxygen isotopic fractionation in the bisulphate ion–water system. *New Zealand Journal of Science*, 12, 54–59.

- Müller, R. D., Roest, W. R., Royer, J.-Y., Gahagan, L. M., & Sclater, J. G. (1997). Digital isochrons of the world's ocean floor. *Journal of Geophysical Research: Solid Earth*, 102(B2), 3211–3214.
- Moreno, H. & Clavero, J. (2006). Geología del área del Volcán Villarrica. Carta Geológica de Chile, No. 98, Serie Geología Básica.
- Moreno, H., Clavero, J., & Lara, L. E. (1994). Actividad explosiva postglacial del Volcan Villarrica, Andes del Sur (39°25'S). *Actas 7th Congreso Geologico Chileno*, (pp. 329–333).
- Moreno, H. & Lara, L. E. (2008). Geología de área Pucón-Curarrehue. Carta Geológica de Chile, No. 115, Serie Geología Básica.
- Morikawa, N., Kazahaya, K., Yasuhara, M., Inamura, A., Nagao, K., Sumino, H., & Ohwada, M. (2005). Estimation of groundwater residence time in a geologically active region by coupling ^4He concentration with helium isotopic ratios. *Geophysical Research Letters*, 32(2), 1–4.
- Moritz, H. (1980). Geodetic reference system 1980. *Journal of Geodesy*, 54, 395 – 405.
- Munizaga, F., Herve, F., Drake, R., Pankhurst, R. J., Brook, M., & Snelling, N. (1988). Geochronology of the Lake Region of south-central Chile (39°–42°S): Preliminary results. *Journal of South American Earth Sciences*, 1(3), 309–316.
- Muñoz, G. (2014). Exploring for geothermal resources with electromagnetic methods. *Surveys in Geophysics*, 35(1), 101–122.
- Muñoz, J. & Niemeyer, H. (1984). Laguna de Maule y del Bío Bío, Carta Geológica de Chile, No. 64, Serie Geología Básica.
- Muñoz, M., Alam, M. A., Parada, M. Á., & Lahsen, A. (2011). Geothermal system associated with the Sierra Nevada Volcano, Araucanía Region, Chile. *GRC Transactions*, 35, 935–942.
- Muñoz, M., Fournier, H., Mamani, M., Febrer, J., Borzotta, E., & Maidana, A. (1990). A comparative study of results obtained in magnetotelluric deep soundings in Villarrica active volcano zone (Chile) with gravity investigations, distribution of earthquake foci, heat flow empirical relationships, isotopic geochemistry $^{87}\text{Sr}/^{86}\text{Sr}$ and SB systematics. *Physics of the Earth and Planetary Interiors*, 60, 195–211.
- Nakamura, K. (1977). Volcanoes as possible indicators of tectonic stress orientation - principle and proposal. *Journal of Volcanology and Geothermal Research*, 2, 1–16.
- Nelson, F., Forsythe, R., & Arit, I. (1994). Ridge collision tectonics in terrane development. *Journal of South American Earth Science*, 7(3-4), 271–278.
- Nelson, S. T., Davidson, J. P., Heizler, M. T., & Kowallis, B. J. (1999). Tertiary tectonic history of the southern Andes: The subvolcanic sequence to the Tatara–San Pedro volcanic complex, Lat. 36°S. *Geological Society of America Bulletin*, 111(9), 1387–1404.
- Ni, H., Keppler, H., & Behrens, H. (2011). Electrical conductivity of hydrous basaltic melts: Implications for partial melting in the upper mantle. *Contributions to Mineralogy and Petrology*, 162(3), 637–650.
- Niemeyer, H. & Muñoz, J. (1983). Laguna de la Laja, Region del Bío Bío. Carta Geológica de Chile, No. 57, Serie Geología Básica.

- Nitschke, F. (2017). *Numerical and experimental characterization of dissolution and precipitation processes in deep geothermal reservoirs*. PhD thesis, Karlsruhe Institute of Technology.
- Nitschke, F., Held, S., Neumann, T., & Kohl, T. (2018). Geochemical characterization of the geothermal system at Villarrica volcano, Southern Chile; Part 2: site-specific re-evaluation of SiO₂ and Na-K solute geothermometers. *Geothermics*, 74, 217–225.
- Nitschke, F., Held, S., Villalón, I., Neumann, T., & Kohl, T. (2017a). Assessment of performance and parameter sensitivity of multicomponent geothermometry applied to a medium enthalpy geothermal system. *Geothermal Energy Journal*, 5(12), 1–20.
- Nitschke, F., Held, S., Villalón, I., Neumann, T., & Kohl, T. (2017b). In-situ temperature determination at the Villarrica geothermal system, Southern Chile: Implications from laboratory experiments for geothermometry. *Proceedings Workshop on Geothermal Reservoir Engineering, Stanford University*, (pp. 1–8).
- NOAA (2015). Combined Chlorofluorocarbon-11 data from the NOAA/ESRL Global Monitoring Division.
- Norabuena, E. (1998). Space geodetic observations of Nazca-South America convergence across the Central Andes. *Science*, 279, 358–362.
- Nur, A. & Ben-Avraham, Z. (1983). Volcanic gaps due to oblique consumption of aseismic ridges. *Tectonophysics*, 99(2-4), 355–362.
- Olhoeft, G. R. (1981). Electrical properties of granite with implications for the lower crust. *Journal of Geophysical Research*, 86(B2), 931–936.
- Oncken, O., Chong, G., Franz, G., Giese, P., Götze, H.-J., Ramos, V., Strecker, M. R., & Wigger, P., Eds. (2006). *The Andes*. Springer-Verlag.
- Ortiz, R. (2003). Villarrica volcano (Chile): characteristics of the volcanic tremor and forecasting of small explosions by means of a material failure method. *Journal of Volcanology and Geothermal Research*, 128(1-3), 247–259.
- Ossandón C., G., Freéaut C., R., Gustafson, L. B., Lindsay, D. D., & Zentilli, M. (2001). Geology of the Chuquicamata mine: A progress report. *Economic Geology*, 96(2), 249–270.
- Oster, H., Sonntag, C., & Münnich, K. O. (1996). Groundwater age dating with chlorofluorocarbons. *Water Resources Research*, 32(10), 2989–3001.
- OVDAS (2015). *Report: 25.03.2015*. Technical report, Observatorio Volcanológico de los Andes del Sur: La Araucanía - Los Ríos.
- Palmer, M. R. & Elderfield, H. (1985). Sr isotope composition of sea water over the past 75 Myr. *Nature*, 314, 526–528.
- Pankhurst, R. J., Hervé, F., Rojas, L., & Cembrano, J. (1992). Magmatism and tectonics in continental Chiloé, Chile. *Tectonophysics*, 205, 283–294.
- Pankhurst, R. J., Weaver, S. D., Hervé, F., & Larrondo, P. (1999). Mesozoic – Cenozoic evolution of the North Patagonian Batholith in Aysén, Southern Chile. *Journal of the Geological Society of London*, 156, 673–694.

- Parada, M.A. López-Escobar, L., Oliveros, V., Fuentes, F., Morata, D., Calderón, M., Aguirre, L., Féraud, G., Espinoza, F., Moreno, H., Figueroa, O., Muñoz Bravo, J., Troncoso Vásquez, R., & Stern, C. R. (2007). Andean magmatism. In: Moreno, T. & Gibbons, W (eds.): *The Geology of Chile*; The Geological Society of London, (pp. 115–146).
- Parada, M., Godoy, E., Hervé, F., & Thiele, R. (1987). Miocene calc-alkaline plutonism in the Andes of Central Chile. *Revista Brasileira de Geociencias*, 17, 450–455.
- Parada, M., Rivano, S., Sepulveda, P., Hervé, M., Herve, F., Puig, A., Munizaga, F., Brook, M., Pankhurst, R., & Snelling, N. (1988). Mesozoic and Cenozoic plutonic development in the Andes of Central Chile (30°30'–32°30'S). *Journal of South American Earth Sciences*, 1(3), 249–260.
- Parasnis (1986). *Principles of applied geophysics*. Springer-Verlag.
- Pardo-Casas, F. & Molnar, P. (1987). Relative motion of the Nazca (Farallon) and South American Plates since Late Cretaceous time. *Tectonics*, 6(3), 233–248.
- Parkhomenko, E. (1967). *Electrical properties of rocks*. Plenum Press.
- Parkinson, W. (1959). Directions of rapid geomagnetic variations. *The Geophysical Journal of the Royal Astronomical Society*, 2(1), 1–14.
- Pearce, C. I. (2006). Electrical and magnetic properties of sulfides. *Reviews in Mineralogy and Geochemistry*, 61, 127–180.
- Pearson, S. C. P. & Prieto, A. (2012). Improved visualization of reservoir simulations: Geological and fluid flow modeling of a high-temperature geotherm field in New Zealand. *Proceedings TOUGH Symposium, Lawrence Berkeley National Laboratory Berkeley, California*, (pp. 319–323).
- Pearson Jr., F., Balderer, W., Loosli, H., Lehmann, B., Matter, A., Peters, T., Schmassmann, H., & Gautschi, A. (1991). *Applied isotope hydrogeology. A case study in Northern Switzerland. Nagra Technical Report NTB 88-01*. Elsevier.
- Pedroza, V., Le Roux, J. P., Gutiérrez, N. M., & Vicencio, V. E. (2017). Stratigraphy, sedimentology, and geothermal reservoir potential of the volcanoclastic Cura-Mallín succession at Lonquimay, Chile. *Journal of South American Earth Sciences*, 77, 1–20.
- Pérez, Y. (1999). Fuentes de aguas termales de la cordillera Andina del Centro-Sur de Chile (39–42°S). *SERNAGEOMIN*, Bol. 54, 68.
- Petit-Breuilh, M. E. & Lobato, J. (1994). Analisis comparativo de la cronologia eruptiva historica de los Volcanes Llaima y Villarrica (38°–39°S). *Actas 7th Congreso Geológico Chileno*, 13, 366–370.
- Pilger, R. H. (1984). Cenozoic plate kinematics, subduction and magmatism: South American Andes. *Journal of the Geological Society*, 141(5), 793–802.
- Pilger, R. H. & Handschumacher, D. (1981). The fixed-hotspot hypothesis and origin of the Easter-Sala y Gomez-Nazca trace. *GSA Bulletin*, 92(7), 437–446.
- Plafker, G. & Savage, J. C. (1970). Mechanism of the Chilean earthquakes of May 21 and 22, 1960. *GSA Bulletin*, 81(4), 1001–1030.
- Plummer, L. N. & Busenberg, E. (2006). Chlorofluorocarbons in aquatic environments. In: *Use of chlorofluorocarbons in hydrology: A guidebooks*; International Atomic Energy Agency.

- Potent, S. (2003). *Kinematik und Dynamik neogener Deformationsprozesse des Südzentralchilenischen Subduktionssystems, nördlichste Patagonische Anden (37°-40°S)*. PhD thesis, University of Hamburg.
- Presnall, D. C., Simmons, C. L., & Porath, H. (1972). Changes in electrical conductivity of a synthetic basalt during melting. *Journal of Geophysical Research*, 77(29), 5665–5672.
- Pérez-Flores, P., Cembrano, J., Sánchez-Alfaro, P., Veloso, E., Arancibia, G., & Roquer, T. (2016). Tectonics, magmatism and paleo-fluid distribution in a strike-slip setting: Insights from the northern termination of the Liquiñe–Ofqui fault System, Chile. *Tectonophysics*, 680, 192–210.
- Pérez-Flores, P., Veloso, E., Cembrano, J., Sánchez-Alfaro, P., Lizama, M., & Arancibia, G. (2017a). Fracture network, fluid pathways and paleostress at the Tolhuaca geothermal field. *Journal of Structural Geology*, 96, 134–148.
- Pérez-Flores, P., Wang, G., Mitchell, T., Meredith, P., Nara, Y., Sarkar, V., & Cembrano, J. (2017b). The effect of offset on fracture permeability of rocks from the Southern Andes Volcanic Zone, Chile. *Journal of Structural Geology*, 104, 142–158.
- Procesi, M. (2014). Geothermal potential evaluation for Northern Chile and suggestions for new energy plans. *Energies*, 7(8), 5444–5459.
- Radic, J. P. (2010). Las cuencas cenozoicas y su control en el volcanismo de los complejos Nevados de Chillán y Copahue-Callaqui (Andes del Sur, 36°-39°S). *Andean Geology*, 37(1), 220–246.
- Radic, J. P., Rojas, J., Carpinelli, A., & Zurita, E. (2002). Evolución tectónica de la cuenca terciaria de Cura-Mallín, región Cordillerana Chileno Argentina. *Congreso Geológico Argentino*, 15(3), 233–237.
- Ramos, M. E., Folguera, A., Fennell, L., Giménez, M., Litvak, V. D., Dzierma, Y., & Ramos, V. A. (2014). Tectonic evolution of the North Patagonian Andes from field and gravity data (39°–40°S). *Journal of South American Earth Sciences*, 51, 59–75.
- Ranero, C. R., von Huene, R., Weinrebe, W., & Reichert, C. (2006). Tectonic Processes along the Chile Convergent Margin? In: Oncken, O., Chong, G., Franz, G., Giese, P., Götze, H.-J., Ramos, V.A., Strecker, M.R. & Wigger, P. (eds): *The Andes—Active Subduction Orogeny*; Springer-Verlag.
- Rapela, C. W. & Pankhurst, R. J. (1992). The granites of Northern Patagonia and the Gastre Fault System in relation to the break-up of Gondwana. *Geological Society, London, Special Publications*, 68(1), 209–220.
- Reutter, K., Scheuber, E., & Wigger, P. (1994). *Tectonics of the Southern Central Andes: Structure and evolution of an active continental margin*. Springer-Verlag.
- Reutter, K.-J. (2001). Le Ande centrali: elemento di un'orogenesi di margine continentale attivo. *Acta Naturalia de l'Ateneo Parmense*, 37(1/2), 5–37.
- Reyes-Wagner, V., Díaz, D., Cordell, D., & Unsworth, M. (2017). Regional electrical structure of the Andean subduction zone in central Chile (35°-36°S) using magnetotellurics. *Earth, Planets and Space*, 69, 1–9.
- Rippe, D., Unsworth, M. J., & Currie, C. A. (2013). Magnetotelluric constraints on the fluid content in the upper mantle beneath the Southern Canadian Cordillera: Implications for rheology. *Journal of Geophysical Research: Solid Earth*, 118(10), 5601–5624.

- Risacher, F., Fritz, B., & Hauser, A. (2011). Origin of components in Chilean thermal waters. *Journal of South American Earth Sciences*, 31(1), 153–170.
- Rittmeyer, C. & Vehlow, J. (1993). Decomposition of organohalogen compounds in municipal solid waste incineration plants. 1. Chlorofluorocarbons. *Chemosphere*, 26(12), 2129–2138.
- Rodi, W. & Mackie, R. L. (2001). Nonlinear conjugate gradients algorithm for 2-D magnetotelluric inversion. *Geophysics*, 66(1), 174.
- Rojas, C., Beck, M., Burmester, R., Cembrano, J., & Hervé, F. (1994). Paleomagnetism of the Mid-Tertiary Ayacura Formation, Southern Chile: Counterclockwise rotation in a dextral shear zone. *Journal of South American Earth Sciences*, 7(1), 45–56.
- Roquer, T., Arancibia, G., Rowland, J., Iturrieta, P., Morata, D., & Cembrano, J. (2017). Fault-controlled development of shallow hydrothermal systems: Structural and mineralogical insights from the Southern Andes. *Geothermics*, 66, 156–173.
- Rosenau, M., Melnick, D., & Echtler, H. (2006). Kinematic constraints on intra-arc shear and strain partitioning in the Southern Andes between 38°S and 42°S latitude. *Tectonics*, 25(4).
- Rowland, J. V. & Sibson, R. H. (2004). Structural controls on hydrothermal flow in a segmented rift system, Taupo Volcanic Zone, New Zealand. *Geofluids*, 4, 259–283.
- Rozanski, K. & Florkowski, T. (1979). Krypton-85 dating of groundwater. In: *Isotope hydrology*; IAEA Vienna, (pp. 949–959).
- Rybach, L. (1976). Radioactive heat production in rocks and its relation to other petro-physical parameters. *Pure and Applied Geophysics*, 114(2), 309–317.
- Sakai, H. (1977). Sulfate-water isotope thermometry applied to geothermal systems. *Geothermics*, 5, 67–74.
- Sánchez, P., Pérez-Flores, P., Arancibia, G., Cembrano, J., & Reich, M. (2013). Crustal deformation effects on the chemical evolution of geothermal systems: The intra-arc Liquiñe–Ofqui fault system, Southern Andes. *International Geology Review*, 55(11), 1384–1400.
- Sánchez-Alfaro, P., Reich, M., Arancibia, G., Pérez-Flores, P., Cembrano, J., Driesner, T., Lizama, M., Rowland, J., Morata, D., Heinrich, C. A., Tardani, D., & Campos, E. (2016). Physical, chemical and mineralogical evolution of the Tolhuaca geothermal system, Southern Andes, Chile: Insights into the interplay between hydrothermal alteration and brittle deformation. *Journal of Volcanology and Geothermal Research*, 324, 88–104.
- Sanjuan, B., Millot, R., Ásmundsson, R., Brach, M., & Giroud, N. (2014). Use of two new Na/Li geothermometric relationships for geothermal fluids in volcanic environments. *Chemical Geology*, 389, 60–81.
- Sanjuan, B., Millot, R., Innocent, C., Dezayes, C., Scheiber, J., & Brach, M. (2016). Major geochemical characteristics of geothermal brines from the Upper Rhine Graben granitic basement with constraints on temperature and circulation. *Chemical Geology*, 428, 27–47.
- Santos, P. A. & Rivas, J. A. (2009). Gravity surveys contribution to geothermal exploration in El Salvador: The cases of Berlín, Ahuachapán and San Vicente areas. *United Nations University: Short Course on Surface Exploration for Geothermal Resources*, (pp. 1–6).

- Sanyal, S. K. (2005). Classification of geothermal systems - A possible scheme. *Proceedings Workshop on Geothermal Reservoir Engineering; Stanford University, California*.
- Scheuber, E. & Gonzalez, G. (1999). Tectonics of the Jurassic-Early Cretaceous magmatic arc of the north Chilean Coastal Cordillera (22°-26°S): A story of crustal deformation along a convergent plate boundary. *Tectonics*, 18(5), 895–910.
- Schill, E., Appel, E., Crouzet, C., Gautam, P., Wehland, F., & Staiger, M. (2004). Oroclinal bending versus regional significant clockwise rotations in the Himalayan arc—Constraints from secondary pyrrhotite remanences. In: Sussman, A. J. & Weil, A. B. (eds.): *Orogenic curvature: Integrating paleomagnetic and structural analyses*; GSA Special Papers, 383, 73–85.
- Schill, E., Geiermann, J., & Kümmitz, J. (2010). 2-D Magnetotellurics and Gravity at the Geothermal Site at Soultz-sous-Forêts. *Proceedings World Geothermal Congress*.
- Schmidt, S. & Götze, H.-J. (2006). Bouguer and isostatic maps of the Central Andes. In: Oncken, O., Chong, G., Franz, G., Giese, P., Götze, H.-J., Ramos, V.A., Strecker, M.R. & Wigger, P. (eds): *The Andes—Active Subduction Orogeny*; Springer-Verlag, (pp. 559–562).
- Schmucker, U. (1973). Regional induction studies: A review of methods and results. *Physics of the Earth and Planetary Interiors*, 7(3), 365–378.
- Schnetzer, F. (2017). *The interaction of water and 2:1 layer silicates*. PhD thesis, Karlsruhe Institute of Technology.
- Schnetzer, F., Thissen, P., Giraudo, N., & Emmerich, K. (2016). Unraveling the coupled processes of (de)hydration and structural changes in Na⁺-saturated montmorillonite. *Journal of Physical Chemistry C*, 120(28), 15282–15287.
- Schulz, R., Angemar, T., Alten, J., Ganz, B., Kuder, J., Schumacher, S., & Tribbensee, K. (2013). *Aufbau eines Internet basierten Informationszentrums für geothermische Energienutzung*. Technical report, Leibniz-Institut für Angewandte Geophysik.
- Seal, R. R., Alpers, C. N., & Rye, R. O. (2000). Stable isotope systematics of sulfate minerals. In: Alpers, C. N., Jambor, J. L. & Nordstrom, D. K. (eds.): *Sulfate Minerals - Crystallography, Geochemistry and Environmental Significance*; Mineralogical Society of America, (pp. 541–602).
- Sepulveda, F., Lahsen, A., Dorsch, K., Palacios, C., & Bender, S. (2005). Geothermal exploration in the Cordón Caulle Region, Southern Chile. *Proceedings World Geothermal Congress*, (pp. 24–29).
- Sepulveda, F., Lahsen, A., & Powell, T. (2006). The Cordón Caulle geothermal area, Chile: Comparison with other geothermal systems based on gas geothermometry. *Proceedings NZ Geothermal Workshop*.
- Shankland, T. J. & Ander, M. E. (1983). Electrical conductivity, temperatures, and fluids in the lower crust. *Journal of Geophysical Research*, 88(B11), 9475.
- Sibson, R. H. (1977). Fault rocks and fault mechanisms. *Journal of the Geological Society*, 133, 191–213.
- Simpson, F. & Bahr, K. (2005). *Practical Magnetotellurics*. Cambridge University Press.

- Smellie, J., Laaksoharju, M., & Wikberg, P. (1995). Äspö, SE Sweden: A natural ground-water flow model derived from hydrogeochemical observations. *Journal of Hydrology*, 172(1-4), 147–169.
- Sánchez-Alfaro, P., Sielfeld, G., van Campen, B., Dobson, P., Fuentes, V., Reed, A., Palma-Behnke, R., & Morata, D. (2015). Geothermal barriers, policies and economics in Chile – Lessons for the Andes. *Renewable and Sustainable Energy Reviews*, 51, 1390–1401.
- Somoza, R. (1998). Updated Nazca (Farallon) -South America relative motions during the last 40 My: Implications for mountain building in the Central Andean region. *Journal of South American Earth Sciences*, 11(3), 211–215.
- Sonier, D., Duran, N., & Smith, G. (1994). Dechlorination of trichlorofluoromethane (CFC-11) by sulfate-reducing bacteria from an aquifer contaminated with halogenated aliphatic compounds. *Applied and Environmental Microbiology*, 60(12), 4567–4572.
- Spalletti, L. A. & Salda, L. H. D. (1996). A pull apart volcanic related tertiary basin, an example from the Patagonian Andes. *Journal of South American Earth Sciences*, 9(3-4), 197–206.
- Spangenberg, J. E., Dold, B., Vogt, M.-L., & Pfeifer, H.-R. (2007). Stable hydrogen and oxygen isotope composition of waters from mine tailings in different climatic environments. *Environmental Science & Technology*, 41, 1870–1876.
- Spichak, V., Geiermann, J., Zakharova, O., Calcagno, P., Genter, A., & Schill, E. (2015). Estimating deep temperatures in the Soultz-sous-Forêts geothermal area (France) from magnetotelluric data. *Near Surface Geophysics*, 13(2089).
- Stern, C. R. (2004). Active Andean volcanism: its geologic and tectonic setting. *Andean Geology*, 31(2), 161–206.
- Stettler, A. (1977). ^{87}Rb - ^{87}Sr systematics of a geothermal water-rock association in the Massif Central, France. *Earth and Planetary Science Letters*, 34, 432–438.
- Stober, I. & Bucher, K. (1999). Deep Groundwater in the crystalline basement of the Black Forest Region. *Applied Geochemistry*, 14(2), 237–254.
- Stober, I. & Bucher, K. (2013). *Geothermal energy: from theoretical models to exploration and development*. Springer-Verlag.
- Suarez, M. & Emparan, C. (1995). The stratigraphy, geochronology and paleophysiography of a Miocene fresh-water interarc basin, Southern Chile. *Journal of South American Earth Sciences*, 8(1), 17–31.
- Suárez, M. & de la Cruz, R. (2001). Jurassic to Miocene K-Ar dates from eastern central Patagonian Cordillera plutons, Chile (45°–48°S). *Geological Magazine*, 138, 53–66.
- Sveinbjörnsson, B. M. (2016). *Medium enthalpy geothermal systems in Iceland - thermal and electric potential*. Technical report, ÍSOR (Iceland Geosurvey).
- Swenson, J. L., Beck, S. L., & Zandt, G. (2000). Crustal structure of the Altiplano from broadband regional waveform modeling: Implications for the composition of thick continental crust. *Journal of Geophysical Research: Solid Earth*, 105(B1), 607–621.
- Swift, C. M. (1967). *A magnetotelluric investigation of an electrical conductivity anomaly in the southwestern United States*. PhD thesis, Massachusetts Institute of Technology.

- Szarka, L. (1988). Geophysical aspects of man-made electromagnetic noise in the earth—A review. *Surveys in Geophysics*, 9(3), 287–318.
- Tajima, M., Niwa, M., Fujii, Y., Koinuma, Y., Aizawa, R., Kushiyama, S., Kobayashi, S., Mizuno, K., & Ohûchi, H. (1996). Decomposition of chlorofluorocarbons in the presence of water over zeolite catalyst. *Applied Catalysis B: Environmental*, 9(1-4), 167–177.
- Tardani, D., Reich, M., Roulleau, E., Takahata, N., Sano, Y., Pérez-Flores, P., Sánchez-Alfaro, P., Cembrano, J., & Arancibia, G. (2016). Exploring the structural controls on helium, nitrogen and carbon isotope signatures in hydrothermal fluids along an intra-arc fault system. *Geochimica et Cosmochimica Acta*, 184, 193–211.
- Tassara, A. & Yáñez, G. (2003). Relación entre el espesor elástico de la litósfera y la segmentación tectónica del margen andino (15°–47°S). *Revista Geológica de Chile*, 30, 159–186.
- Tassi, F., Aguilera, F., Darrah, T., Vaselli, O., Capaccioni, B., Poreda, R. J., & Delgado Huertas, A. (2010). Fluid geochemistry of hydrothermal systems in the Arica-Parinacota, Tarapacá and Antofagasta regions (Northern Chile). *Journal of Volcanology and Geothermal Research*, 192(1-2), 1–15.
- Taylor, S. R. (1964). Abundance of chemical elements in the continental crust - A new table. *Geochimica et Cosmochimica Acta*, 8, 1273–1285.
- Tebbens, S. F., Cande, S. C., Kovacs, L., Parra, J. C., LaBrecque, J. L., & Vergara, H. (1997). The Chile Ridge: A tectonic framework. *Journal of Geophysical Research: Solid Earth*, 102(B6), 12035–12059.
- Telford, W., Geldart, L., & Sheriff, R. (2012). *Applied geophysics*. Cambridge University Press.
- ten Grotenhuis, S. M., Drury, M. R., Spiers, C. J., & Peach, C. J. (2005). Melt distribution in olivine rocks based on electrical conductivity measurements. *Journal of Geophysical Research: Solid Earth*, 110(12), 1–11.
- Thorpe, R. (1984). The tectonic setting of active Andean volcanism. In: Harmin, R.S. & Barreiro, B.A. (eds.): *Andean magmatism: Chemical and Isotopic Constrains*; Birkhauser - Shiva Geology Series, (pp. 4 – 8).
- Tikhonov, A. N. (1950). The determination of the electrical properties of deep layers of the earth's crust. *Dokl. Acad. Nauk*, 73, 295–297. (in russian).
- Tomlinson, A. & Blanco, N. (1997). Structural evolution and displacement history of the West fault system, Cordillera, Chile: Part 1: synmineral history. *Proceedings 8th Congreso Geológico Chileno, Antofagasta*, 3, 1873–1877.
- Torgersen, T. & Clarke, W. (1985). Helium accumulation in groundwater, I: An evaluation of sources and the continental flux of crustal ⁴He in the Great Artesian Basin, Australia. *Geochimica et Cosmochimica Acta*, 49, 1211–1218.
- Türkoğlu, E., Unsworth, M., Bulut, F., & Çağlar, İ. (2015). Crustal structure of the North Anatolian and East Anatolian Fault Systems from magnetotelluric data. *Physics of the Earth and Planetary Interiors*, 241, 1–14.
- Turnadge, C. & Smerdon, B. D. (2014). A review of methods for modelling environmental tracers in groundwater: Advantages of tracer concentration simulation. *Journal of Hydrology*, 519, 3674–3689.

- Tyburczy, J. A. & Waff, H. S. (1983). Electrical conductivity of molten basalt and andesite to 25 kilobars pressure: Geophysical significance and implications for charge transport and melt structure. *Journal of Geophysical Research*, 88(B3), 2413–2430.
- Tzanis, A. & Beamish, D. (1987). Audiomagnetotelluric sounding using the Schumann resonances. *Journal of Geophysics*, 61, 97–109.
- Unsworth, M. (2004). Crustal and upper mantle structure of Northern Tibet imaged with magnetotelluric data. *Journal of Geophysical Research*, 109(B2), B02403.
- Unsworth, M. J., Egbert, G. D., & Booker, J. R. (1999). High-resolution electromagnetic imaging of the San Andreas fault in Central California. *Journal of Geophysical Research*, 104(B1), 1131–1150.
- Unsworth, M. J., Jones, A. G., Wei, W., Marquis, G., Gokarn, S. G., Spratt, J. E., Bedrosian, P., Booker, J., Leshou, C., Clarke, G., Shenghui, L., Chanhong, L., Ming, D., Sheng, J., Solon, K., Handong, T., Ledo, J., & Roberts, B. (2005). Crustal rheology of the Himalaya and Southern Tibet inferred from magnetotelluric data. *Nature*, 438, 78–81.
- Unsworth, M. J., Malin, P. E., Egbert, G. D., & Booker, J. R. (1997). Internal structure of the San Andreas fault at Parkfield, California. *Geology*, 25(4), 359–362.
- Ussher, G., Harvey, C., Johnstone, R., & Anderson, E. (2000). Understanding the resistivities observed in geothermal systems. *Proceedings World Geothermal Congress*.
- Utgé, S., Folguera, A., Litvak, V., & Ramos, V. A. (2009). Geología del sector norte de la Cuenca de Cura Mallín en las lagunas de Epulauquen, Neuquén. *Revista de la Asociación Geológica Argentina*, 64(2), 231–248.
- Vanyan, L., Tezkan, B., & Palshin, N. (2001). Low electrical resistivity and seismic velocity at the base of the upper crust as indicator of rheologically weak layer. *Surveys in Geophysics*, 22(2), 131–154.
- Veizer, J. & Compston, W. (1974). $^{87}\text{Sr}/^{86}\text{Sr}$ composition of seawater during the Phanerozoic. *Geochimica et Cosmochimica Acta*, 38, 1461–1484.
- Velde, B. (1995). *Origin and mineralogy of clays*. Springer-Verlag.
- Vergara, M., Moran, J., & Zentilli, M. (1997). Evolución termotectónica de la cuenca terciaria entre Parral y Chillán: Análisis por trazas de fisión en apatitas. *Proceedings VIII Congreso Geológico Chileno, Antofagasta*, (pp. 1574–1578).
- Verma, M. P. (2000). Revised quartz solubility temperature dependence equation along the water-vapor saturation curve. *Proceedings World Geothermal Congress 2000*.
- Verma, S. P. & Santoyo, E. (1997). New improved equations for Na/K, Na/Li and SiO₂ geothermometers by outlier detection and rejection. *Journal of Volcanology and Geothermal Research*, 79(1-2), 9–23.
- Villalón, I. (2015). Lithological controls influencing the geochemistry of geothermal systems north of the Villarrica Volcano, an experimental approach. B.Sc. Thesis, University of Chile.
- Völker, D., Kutterolf, S., & Wehrmann, H. (2011). Comparative mass balance of volcanic edifices at the Southern Volcanic Zone of the Andes between 33°S and 46°S. *Journal of Volcanology and Geothermal Research*, 205(3-4), 114–129.

- Vozoff, K. (1991). The Magnetotelluric Method. In: Nabihian, M. N. (ed.): *Electromagnetic Methods in Applied Geophysics - Volume 2*; Society of Exploration Geophysicists, 19(2), 281–289.
- Waber, H., Schneeberger, R., Mäder, U., & Wanner, C. (2017). Constraints on evolution and residence time of geothermal water in granitic rocks at Grimsel (Switzerland). *Procedia Earth and Planetary Science*, 17, 774–777.
- Wait, J. R. (1954). On the relation between telluric currents and the earth's magnetic field. *Geophysics*, 19, 281.
- Wang, C.-Y., Rui, F., Zhengsheng, Y. A. O., & Xingjue, S. T. (1986). Gravity anomaly and density structure of the San Andreas fault zone. *Pure and Applied Geophysics*, 124(1), 127–140.
- Wannamaker, P. E. (2000). Comment on “The petrologic case for a dry lower crust” by W.D. Bruce, B.W. Yardley, and J.W. Valley’. *Journal of Geophysical Research*, 105, 6057–6064.
- Wannamaker, P. E., Evans, R. L., Bedrosian, P. A., Unsworth, M. J., Maris, V., & Shane McGary, R. (2014). Segmentation of plate coupling, fate of subduction fluids, and modes of arc magmatism in Cascadia, inferred from magnetotelluric resistivity. *Geochemistry, Geophysics, Geosystems*, 15, 4230–4253.
- Wannamaker, P. E., Jiracek, G. R., Stodt, J. A., Caldwell, T. G., Gonzalez, V. M., McKnight, J. D., & Porter, A. D. (2002). Fluid generation and pathways beneath an active compressional orogen, the New Zealand Southern Alps, inferred from magnetotelluric data. *Journal of Geophysical Research*, 107(B6), 1–21.
- Waxman, M. H. & Smits, L. (1968). Electrical Conductivities in Oil-Bearing Shaly Sands. *Society of Petroleum Engineers*, 8, 107–122.
- Weckmann, U., Ritter, O., Chen, X., Tietze, K., & de Wit, M. (2012). Magnetotelluric image linked to surface geology across the Cape Fold Belt, South Africa. *Terra Nova*, 24(3), 207–212.
- Weidelt, P. (1972). The inverse problem of geomagnetic induction. *Zeitschrift für Geophysik*, 38, 257–289.
- Wiese, H. (1962). Geomagnetische Tiefentelluric Teil II: Die Streichrichtung der Untergrundstrukturen des elektrischen Widerstandes, erschlossen aus geomagnetischen Variationen. *Pure App. Geophys.*, 52, 83–103.
- Wolters, F., Lagaly, G., Kahr, G., Nüesch, R., & Emmerich, K. (2009). A comprehensive characterization of dioctahedral smectites. *Clays and Clay Minerals*, 57(1), 115–133.
- Wood (1992). Geology and hydrology of Rotorua geothermal field. *Geothermics*, 21, 25–41.
- Woodhouse, S. & Meisen, P. (2011). *Renewable energy potential of Chile*. Global Energy Network Institute (GENI).
- Woods, M. T. & Okal, E. A. (1994). The structure of the Nazca Ridge and Sala Y Gomez Seamount Chain from the dispersion of rayleigh waves. *Geophysical Journal International*, 117(1), 205–222.
- Wrage, J., Tardani, D., Reich, M., Daniele, L., Arancibia, G., Cembrano, J., Sánchez-Alfaro, P., Morata, D., & Pérez-Moreno, R. (2017). Geochemistry of thermal waters in the Southern Volcanic Zone, Chile - Implications for structural controls on geothermal fluid composition. *Chemical Geology*, 466, 545–561.

- Yañez, G., Gana, P., & Fernández, R. (1998). Origen y significado geológico de la anomalía Melipilla, Chile central. *Rev. Geol. Chile*.
- Yardley, B. W. D. & Valley, J. W. (1997). The petrologic case for a dry lower crust. *Journal of Geophysical Research*, 102(B6), 12173–12185.
- Yardley, B. W. D. & Valley, J. W. (2000). Reply on Comment on “The petrologic case for a dry lower crust by P.E. Wannamaker. *Journal of Geophysical Research*, 105(B3), 6065–6068.
- Yañez, G., Cembrano, J., Pardo, M., Ranero, C., & Selles, D. (2002). The Challenger-Juan Fernández-Maipo major tectonic transition of the Nazca-Andean subduction system at 33°-34°S: geodynamic evidence and implications. *Journal of South American Earth Sciences*, 15(1), 23–38.
- Yañez, G. A., Ranero, C. R., von Huene, R., & Díaz, J. (2001). Magnetic anomaly interpretation across the Southern Central Andes (32°-34°S): The role of the Juan Fernández Ridge in the late Tertiary evolution of the margin. *Journal of Geophysical Research: Solid Earth*, 106(B4), 6325–6345.
- Yokochi, R., Sturchio, N. C., Purtschert, R., Jiang, W., Lu, Z. T., Mueller, P., Yang, G. M., Kennedy, B. M., & Kharaka, Y. (2013). Noble gas radionuclides in Yellowstone geothermal gas emissions: A reconnaissance. *Chemical Geology*, 339, 42–51.
- Zaffarana, C. B., López de Luchi, M G, Somoza, R., Mercader, R., Giacosa, R., & Martino, R. D. (2010). Anisotropy of magnetic susceptibility study in two classical localities of the Gastre Fault System, central Patagonia. *Journal of South American Earth Sciences*, 30(3-4), 151–166.
- Zeebe, R. E. (2010). A new value for the stable oxygen isotope fractionation between dissolved sulfate ion and water. *Geochimica et Cosmochimica Acta*, 74(3), 818–828.
- Zhang, L., Unsworth, M., Jin, S., Wei, W., Ye, G., Jones, A. G., Jing, J., Dong, H., Xie, C., Le Pape, F., & Vozar, J. (2015). Structure of the Central Altyn Tagh Fault revealed by magnetotelluric data: New insights into the structure of the northern margin of the India–Asia collision. *Earth and Planetary Science Letters*, 415, 67–79.
- Zhonghe, P. (2001). Isotope and chemical geothermometry and its applications. *Science in China*, 44, 16–20.
- Zhou, Z. & Ballentine, C. J. (2006). ⁴He dating of groundwater associated with hydrocarbon reservoirs. *Chemical Geology*, 226, 309–327.
- Zoback, M. D. (2010). *Reservoir geomechanics*. Cambridge University Press.

Appendix

A. Academic Curriculum Vitae

Personal Information

Name **Sebastian Held**
Nationality **German**
Date of Birth **01.12.1984 in Dortmund**

Academic Education

07/04 **Abitur**, Mallinckrodt Gymnasium Dortmund

10/06 - 08/09 **Bachelor of Science**, Karlsruhe Institute of Technology (KIT)
Subject: Applied Geosciences
Thesis: Conceptual studies for the calculation of heat propagation in the subsurface with the help of finite elements

10/09 - 12/11 **Master of Science**, Karlsruhe Institute of Technology (KIT)
Subject: Applied Geosciences
Thesis: Construction of a hydraulic/thermal model and following calculation of economic efficiency of the geothermal power plant at Soultz-sous-Forêts (France)
in collaboration with the EnBW AG

since 01/13 **PhD student**, Karlsruhe Institute of Technology (KIT)
Titel: Multidisciplinary Geothermal exploration at Villarrica geothermal system, southern Chile
Supervisor: Prof. Dr. Thomas Kohl

B. Declaration of authorship

Chapter 4: Geological and Tectonic Settings Preventing High-Temperature Geothermal Reservoir Development at Mt. Villarrica (Southern Volcanic Zone): Clay Mineralogy and Sulfate-Isotope Geothermometry

Citation: Held, S., Schill, E., Sánchez, P., Neumann, T., Emmerich, K., Morata, D. and Kohl, T. (2015): Geological and Tectonic Settings Preventing High-Temperature Geothermal Reservoir Development at Mt. Villarrica (Southern Volcanic Zone): Clay Mineralogy and Sulfate-Isotope Geothermometry; *Proceedings: World Geothermal Congress 2015, Melbourne, Australia*

The first study was funded by German Federal Ministry of Education and Research (BMBF) under the funding number 01DN12126 and is a contribution to the CONICYT-International Relationships Department-Scientific International Cooperation Program-Exchange Project #PCCI130025. This publication benefits from the HGF portfolio project “Geoenergy”.

I organized and managed the geochemical survey in March 2013 and sampled the geothermal fluids and clay minerals at the Villarrica area. I prepared samples for laboratory analysis. In terms of XRD data analysis I used Eva software (© Bruker) to reveal mineralogical composition. I analyzed and interpreted the results. I wrote the manuscript.

Chapter 5: Resistivity distribution from mid-crustal conductor to near-surface across the 1200 km long Liquiñe-Ofqui Fault System, southern Chile

Citation: Held, S., Schill, E., Pavez, M., Díaz, D., Muñoz, G., Morata, D., Kohl, T.(2016): Resistivity distribution from mid-crustal conductor to near-surface across the 1200 km long Liquiñe-Ofqui Fault System, Southern Chile; *Geophysical Journal International*, 207(3), 1387-1400

This study is part of a collaborative research project between Karlsruhe Institute of Technology (KIT) and the Andean Geothermal Center of Excellence (CEGA, Fondap-Conicyt 15090013) funded by the BMBF-CONICYT International Scientific Collaborative Research Program (FKZ01DN14033/PCCI130025). Additional the project benefits from the Helmholtz portfolio project “Geoenergy” in the topic “Geothermal Energy Systems”.

I organized and managed the geophysical research campaign in November and December 2013 and coordinated a four person research team conducting all 31 full sensor measurements. I processed the high-frequency data using the Winglink software (© Schlumberger) while Maximiliano Pavez processed the low-frequency data using the code by Egbert and Booker. I merged both datasets. I analyzed the directionality and dimensionality of subsurface resistivity distribution. Evaluation of vertical magnetic field and phase tensor was done by me. I conducted inversion and forward modeling using the Winglink software (© Schlumberger). I evaluate

resistivity reduction in terms of reduction mechanism. I wrote the manuscript.

Chapter 7: Hydrochemistry of the hot spring fluids of Villarrica geothermal system in the Andes of Southern Chile

Citation: Held, S., Nitschke, F., Schill, E., Morata, D., Eiche, E., Kohl, T. (2017): Hydrochemistry of the hot spring fluids of Villarrica geothermal system in the Andes of Southern Chile; *Geothermal Research Council Transactions*, 41

This study is again part of a collaborative research project between Karlsruhe Institute of Technology (KIT) and the Andean Geothermal Center of Excellence (CEGA, Fondap-Conicyt 15090013). The authors appreciate the support under the BMBF- CONICYT International Scientific Collaborative Research Program (FKZ 01DN14033/ PCCI130025). Additional support under the topic "Geothermal Energy Systems" of the Helmholtz portfolio project "Geoenergy" and by EnBW Energie Baden-Württemberg AG is gratefully acknowledged.

The geochemical survey in March 2014 was organized and managed by me. I sampled the geothermal fluids in the research area and conducted on-site measurements. I analyzed the measurements and investigate the fluid genesis by interpretation of data in terms of fluid origin, genesis and equilibrium state. I wrote the manuscript.

Chapter 8: Geochemical characterization of the geothermal system at Villarrica volcano, Southern Chile; Part 1: Implications of lithology contrasts on fluid genesis

Citation: Held, S., Schill, E., Schneider, J., Nitschke, F., Morata, D., Neumann, T., Kohl, T. (submitted): Geochemical characterization of the geothermal system at Villarrica volcano, Southern Chile; Part 1: Implications of lithology contrasts on fluid genesis; *Geothermics*, 74, 226-239

The study is part of a collaborative research project between Karlsruhe Institute of Technology (KIT) and the Andean Geothermal Center of Excellence (CEGA, Fondap-Conicyt 15090013). The authors appreciate the support under the BMBF- CONICYT International Scientific Collaborative Research Program (FKZ 01DN14033/ PCCI130025). Additional support under the topic "Geothermal Energy Systems" of the Helmholtz portfolio project "Geoenergy" and by EnBW Energie Baden-Württemberg AG is gratefully acknowledged.

The investigations are carried out on data from geochemical fluid surveys of 2013 and 2014. I prepared the rock and fluid samples for laboratory analysis. I developed a Matlab code for subsurface mixing evaluation. I interpret the data in terms of water-rock interaction. I wrote the manuscript.

C. Publications

- Held, S., Genter, A., Kohl, T., Kölbl, T., Sausse, J. and Schoenball, M. (2014): Economic evaluation of geothermal reservoir performance through modeling the complexity of the operating EGS in Soultz-sous-Forêts; *Geothermics*, 51, 270-280 (*peer-reviewed*)
- Held, S., Schill, E., Sánchez, P., Neumann, T., Emmerich, K., Morata, D. and Kohl, T. (2015): Geological and tectonic settings preventing high-temperature geothermal reservoir development at Mt. Villarrica (Southern Volcanic Zone): Clay mineralogy and sulfate-isotope geothermometry; *Proceedings World Geothermal Congress 2015*, Melbourne, Australia
- Held, S., Schill, E., Pavez, M., Diaz, D., Morata, D., Kohl, T. (2015): Tectonic control of the geothermal system at Mt. Villarrica - Insights from geophysical and geochemical surveys; *Proceedings Chilean Geological Conference*, La Serena, Chile
- Kohl, T., Held, S., Schill, E. (2015): Geoscientific challenges for geothermal development in Europe and South America; *Proceedings Chilean Geological Conference*, La Serena, Chile
- Villalón, I., Nitschke, F., Held, S., Morata, D. (2015): Lithological controls influencing the geochemistry of geothermal systems in the vicinity of Villarrica volcano: an experimental approach; *Proceedings Chilean Geological Conference*, La Serena, Chile
- Pavez, M., Diaz, D., Held, S., Schill, E. (2015): Estudio de resistividad eléctrica mediante magnetotelúrica, en la zona de falla Liquiñe-Ofqui entorno al volcán Villarrica; *Proceedings Chilean Geological Conference*, La Serena, Chile
- Held, S., Schill, E., Kohl, T. (2015): Geothermal reservoir characterization using strontium isotopes in a medium-temperature geothermal system at Villarrica volcano, southern Chile; *Proceedings High Temperature Aqueous Chemistry Workshop*, Heidelberg, Germany
- Nitschke, F., Held, S., Mundhenk, N., Villalón, I., Kohl, T., Neumann, T. (2015): Reactivity of Chilean reservoir rocks and the use of geochemical tools for reservoir characterization; *Proceedings European Geothermal Workshop 2015*, Strasbourg, France
- Nitschke, F., Held, S., Himmelsbach, T., Kohl, T. (2015): The application of THC Code TOUGHREACT-Pitzer on failure conditions of geothermal project GeneSys; *Proceedings European Geothermal Workshop 2015*, Strasbourg, France
- Held, S., Schill, E., Pavez, M., Díaz, D., Muñoz, G., Morata, D., Kohl, T. (2016): Resistivity distribution from mid-crustal conductor to near-surface across the 1200 km long Liquiñe-Ofqui Fault System, Southern Chile; *Geophysical Journal International*, 207, 1387-1400 (*peer-reviewed*)
- Watanabe, N., Blöcher, G., Cacace, M., Held, S., Kohl, T. (2016): Geoenergy Modeling III - Enhanced Geothermal Systems; *Springer Briefs in Energy* (**book**)

- Held, S., Schill, E., Pavez, M., Diaz, D., Morata, D., Kohl, T. (2016): Effects of major fault zones on geothermal reservoirs - A case study at Villarrica Volcano, southern Chile; *Proceedings European Geothermal Congress*, Straßbourg, France
- Nitschke, F., Held, S., Villalon, I., Mundhenk, N., Kohl, T., Neumann, T. (2016): Geochemical Reservoir Exploration and Temperature Determination at the Mt. Villarrica Geothermal System, Chile; *Proceedings European Geothermal Congress*, Straßbourg, France
- Meller, C., Bremer, J., Ankit, K., Baur, S., Bergfeldt, T., Blum, P., Canic, T., Eiche, E., Gaucher, E., Hagenmeyer, V., Heberling, F., Held, S., Herfurth, S., Isele, J., Kling, T., Kuhn, D., Mayer, D., Müller, B., Nestler, B., Neumann, T., Nitschke, F., Nothstein, A., Nusiaputra, Y., Orywall, P., Peters, M., Sahara, D., Schäfer, T., Schill, E., Schilling, F., Schröder, E., Selzer, M., Stoll, M., Wiemer, H., Wolf, S., Zimmermann, M., Kohl, T. (2016): Integrated research as key to the development of a sustainable geothermal energy technology; *Energy Technology*, 5, 965-1006 (**peer-reviewed**)
- Nitschke, F., Held, S., Himmelsbach, T., Kohl, T. (2017): THC simulation of halite scaling in deep geothermal single well production; *Geothermics*, 65, 234-243 (**peer-reviewed**)
- Nitschke, F., Held, S., Villalón, I., Neumann, T., Kohl, T. (2017): In-situ temperature determination at the Villarrica geothermal system, Southern Chile: Implications from laboratory experiments for geothermometry; *Proceedings Workshop on Geothermal Reservoir Engineering*, Stanford University, USA
- Held, S., Nitschke, F., Schill, E., Morata, D., Eiche, E., Kohl, T. (2017): Hydrochemistry of the hot spring fluids of Villarrica geothermal system in the Andes of Southern Chile; *Geothermal Research Council Transactions*, 41 (**peer-reviewed**)
- Nitschke, F., Held, S., Villalón, I., Neumann, T., Kohl, T., (accepted): Assessment of performance and parameter sensitivity of multicomponent geothermometry applied to a medium enthalpy geothermal system; *Geothermal Energy Journal*, 5(12), 1-20 (**peer-reviewed**)
- Held, S., Schill, E., Schneider, J., Nitschke, F., Morata, D., Neumann, T., Kohl, T. (submitted): Geochemical characterization of the geothermal system at Villarrica volcano, Southern Chile; Part 1: Impacts of lithology on the geothermal reservoir; *Geothermics*, 74, 226-239 (**peer-reviewed**)
- Nitschke, F., Held, S., Neumann, T., Kohl, T. (submitted): Geochemical characterization of the geothermal system at Villarrica volcano, Southern Chile; Part II: Site-specific Re-evaluation of SiO₂ and Na-K Solute Geothermometers; *Geothermics*, 74, 217-225 (**peer-reviewed**)

D. Presentations with abstracts

Held, S., Genter, A., Kohl, T., Kölbl, T., Sausse, J. and Schoenball, M. (2012): Significance of thermal transport in complex fractured reservoirs for the economic performance; *Geothermiekongress*, Karlsruhe, Germany

Held, S., Kohl, T. and Kölbl, T. (2013): From geological data to economic efficiency calculation - An approach to optimize reservoir management; *International Congress on Enhanced Geothermal Systems*, Potsdam, Germany

Held, S., Nitschke, F., Schill, E., Kohl, T. and Neumann, T. (2017): Advanced geochemical techniques to characterize geothermal fluid circulation patterns, *Goldschmidt Conference*, Paris, France

Held, S., Nitschke, F., Schneider, J. and Kohl, T. (2017): Advances in geochemical exploration - From dilution determination to improvements of geothermometers; *Geothermiekongress*, München, Germany

E. Acknowledgements

Many people accompanied and supported me during the last couple of years I worked on this thesis. I would like to thank all of them.

First of all, I would like to thank my supervisor Thomas Kohl for providing me the opportunity to work on this challenging subject. Thank you for your support during project acquisition and thank you transferring your enthusiasm for Chile and the Chile project. I try to follow your attitude of “Thinking big” to master even greater challenges.

I would like to thank Diego Morata for the fruitful scientific discussion, for support during research area selection and for taking the responsibility of being my co-supervisor.

Many thanks to Eva Schill for the scientific discussions during geophysical processing and interpretation. Also for the good times during field surveys. I don't forget that I still owe you a Curry.

Thank you Fabian for the innumerable scientific discussions, which only enable successful scientific work. And for pushing me on the trails.

A big thank to Jochen Schneider and Gerard Muñoz for the fruitful scientific discussion.

Thank you Daniel Diaz for support during field campaign organization and for providing measurement equipment.

Many thanks to the members of Geothermal working group encouraging me all the time during the thesis. Special thanks to Roman, for fighting Latex with me, to Emmanuel, for improving of my Matlab skills, and to Caro, for proofreading in many cases.

I would like to thank Max Pavez for the good times during the field campaigns and the introduction to Chilean wine making.

I thank my Chilean Colleagues, Ignacio Villalón, Pablo Sánchez, Gerd Sielfeld, Diego Aravena, Daniele Tardani and Gabriel Perez for support during organization and realization of field campaign, many fruitful scientific discussions and insights into Chilean “Cumbia”.

Many thanks to Victor Martinez for his immense engagement for German-Chilean partnership.

Thank you Silke for guiding me through the jungle of KIT administration.

I am thankful to GRACE for supporting my research stays in Chile.

Thank you Silvia and Erik, filling each of my days with 100 smiles and laughs. Finally, I would like thank my family for their tremendous support during all that years.

Muchas Gracias - Vielen Dank

